TESIS DE LA UNIVERSIDAD DE ZARAGOZA

2025 169

Antonio Dionisio Martínez Pérez

Methodologies for passive-polyphase-filter optimization in monolithic transceiver architectures

http://zaguan.unizar.es/collection/Tesis

Director/es
Celma Pueyo, Santiago
Aznar Tabuenca, Francisco

ISSN 2254-7606

Prensas de la Universidad Universidad Zaragoza

Universidad de Zaragoza
Servicio de Publicaciones

ISSN 2254-7606

Universidad Zaragoza
1542

Tesis Doctoral

METHODOLOGIES FOR PASSIVE-POLYPHASE-FILTER OPTIMIZATION IN MONOLITHIC TRANSCEIVER ARCHITECTURES

Autor

Antonio Dionisio Martínez Pérez

Director/es

Celma Pueyo, Santiago
Aznar Tabuenca, Francisco

UNIVERSIDAD DE ZARAGOZA
Escuela de Doctorado

Programa de Doctorado en Tecnologías de la Información y Comunicaciones en Redes Móviles

2025

Repositorio de la Universidad de Zaragoza – Zaguan http://zaguan.unizar.es

Universidad Zaragoza
1542

Tesis Doctoral

METHODOLOGIES FOR PASSIVE-POLYPHASE-FILTER OPTIMIZATION IN MONOLITHIC TRANSCEIVER ARCHITECTURES

Autor

Antonio D. Martínez Pérez

Director/es

Santiago Celma Pueyo
Francisco Aznar Tabuenca

Facultad de Ciencias

2024

Repositorio de la Universidad de Zaragoza – Zaguan http://zaguan.unizar.es

METHODOLOGIES FOR PASSIVE-POLYPHASE-FILTER OPTIMIZATION IN MONOLITHIC TRANSCEIVER ARCHITECTURES

Submitted in fulfillment of the requirements for the Degree of Doctor of Philosophy in Mobile Network Information and Communication Technologies by

Antonio D. Martínez Pérez

Thesis supervisors:

Dr. Santiago Celma Pueyo

Dr. Francisco Aznar Tabuenca

University of Zaragoza

Electronic Design Group (GDE)—I3A

Zaragoza, October 2024

“It’s time to toss the dice”

Methodologies for Passive-Polyphase-Filter Optimization in Monolithic Transceiver Architectures

Antonio D. Martínez Pérez
Supervisors: Dr. Santiago Celma Pueyo and Dr. Francisco Aznar Tabuenca

Abstract

The modern world is saturated with diverse wireless communication systems. Scientific and technological advancements, as well as society, demand the transmission of larger volumes of data, and it must be done faster than ever. Electronic systems must constantly improve to match expectations. Fortunately, the development of integrated circuits (IC) helps, allowing more compact designs—or enhanced performance for an equivalent area consumption—with the evolution of the technological node.

Moreover, this rushed pursuit of improving the performance of the circuits might relegate more classical optimization methods based on the thorough study of the topologies. The traditional approach can provide critical data to increase efficiency. Conversely, simulation strategies might face difficulties in establishing a relationship between the characteristics of devices and system operation; however, the employed models can be more detailed and accurate. Besides, simulations enable statistical studies that would be otherwise too expensive—economically and timely—or complex to implement as experimental tests.

This work focuses explicitly on optimizing passive polyphase filters (PPF). This circuit is a fundamental building block for constructing a long list of transmitter and receiver architectures, especially useful in monolithic implementations, *i.e.*, the whole system comprised of a single IC. The study is included in a project for designing the electronic front-end of a remote antenna unit (RAU) in a TSMC 65-nm standard CMOS technology. Nevertheless, the research adopts a generalist approach, easing the replication of results and methodologies for other applications and technologies.

The apparent simplicity of the PPFs is misleading. These filters are asymmetric networks that only use passive devices (resistors and capacitors). Moreover, the design-variable number is small, as many of the elements are ideally identical. However, two issues obscure PPF use. First, the analytical expressions that describe the key characteristics of the filter are complex. Thus, adjusting the frequency range in which specifications are fulfilled is difficult. Second, the PPFs are very sensitive to the effect of

non-idealities, and their response may suffer massive changes from one sample to another of the same design due to those phenomena. The study of PPF contained in this thesis supposes two different but complementary perspectives.

On the one hand, an exhaustive analysis of the circuit is carried out, studying the potential degradations due to non-idealities. The research focuses on the phenomena that cause an imbalance between the circuit components, mainly mismatch variations. There are several obstacles to achieving the objectives, as the topology operation is based on a particular symmetry. Firstly, to establish a limit, the worst possible mismatch combination must be found among a myriad of potential cases. Then, analytical expressions can be developed to link PPF performance with the potential device variations due to non-idealities. These calculations must be replicated for each of the distinct PPF configurations. Finally, the expressions converge into a simple and efficient limit, which is also common for any potential use of a PPF.

On the other hand, the complete development process of a PPF is done, evaluating the most critical factors for each step and proposing methodologies to optimize the design decisions. Thus, the thesis not only presents a thorough list of guidelines for PPF implementation, but it also includes the tools to adapt it to other technologies and applications, enumerating the required simulations—with the detailed manufactured models—to evaluate the relevance of the different effects. The last stage presents experimental results, proving that a PPF can fulfill the desired specifications in the selected technology.

This work innovates with the quantitative—quick and accurate—limit to narrow down the impact of mismatch. This approach contrasts with the occasional mentions of this effect in the literature, which are qualitative predictions. For the first time, there is a direct relationship between device fabrication tolerances and the main characteristics of the filter. Consequently, the results allow determining design constraints to the PPF components and predicting if a PPF of specific technology can guarantee fulfilling target specifications.

Besides, the proposed methodologies produce better performance than classical implementation and synthesis PPF methods, optimizing the efficiency of the resources invested into the filter. Moreover, the generalist approach has a significant indirect advantage: the strategies have few assumptions. Thus, they can be used in scenarios where the number of stages or particular characteristics impede or discourage the employment of traditional procedures.

Additionally, the thesis concludes with a description of distinct and promising future research lines to continue studying and optimizing high-performance PPFs.

Metodologías de Optimización de Filtros Polifásicos Pasivos en Arquitecturas Monolíticas de Transceptores

Antonio D. Martínez Pérez
Directores: Dr. Santiago Celma Pueyo y Dr. Francisco Aznar Tabuenca

Resumen

Actualmente vivimos en un mundo saturado de diversos sistemas de comunicaciones inalámbricas. Los avances científicos y tecnológicos, así como la sociedad en su conjunto, demandan continuamente transmitir mayores volúmenes de datos en menor tiempo. Para mantener este ritmo, los sistemas electrónicos se hayan en continua mejora para cumplir con las expectativas. Afortunadamente, el desarrollo tecnológico de los circuitos integrados (IC) acompaña, permitiendo producir diseños más compactos —o mejores prestaciones en la misma área— conforme el nodo tecnológico evoluciona.

Ahora bien, esta persecución apresurada por mejorar las prestaciones de los circuitos, en ocasiones, hace olvidar los métodos de optimización más tradicionales en base al minucioso estudio de las topologías. Este enfoque más clásico puede proporcionar información crítica sobre cómo puede obtenerse el máximo rendimiento del circuito. Si bien las relaciones entre dispositivos empleados y prestaciones globales son difíciles de obtener mediante simulación, los modelos empleados pueden ser mucho más complejos y precisos. También permiten realizar estudios estadísticos difícilmente reproducibles experimentalmente por coste en tiempo y económico, o control de las condiciones.

En particular, este trabajo se centra en la optimización de filtros polifásicos pasivos (PPF). Estos son un bloque básico para la implementación de numerosas arquitecturas de transmisores y receptores, y especialmente útil cuando todo el sistema se implementa en el mismo IC (sistemas monolíticos). El desarrollo se realiza dentro de un proyecto de diseño de un *front-end* electrónico para unidades de antena remotas, utilizándose para ello una tecnología TSMC CMOS standard de 65 nm. No obstante, la investigación se realiza con un enfoque generalista, facilitando la extrapolación de resultados y metodologías a otras tecnologías y aplicaciones.

La aparente simplicidad de los PPF resulta engañosa. Estos filtros están compuestos por una red asimétrica de exclusivamente elementos pasivos (resistencias y condensadores). Además, el número de variables de diseño es relativamente reducido

dado que muchos elementos idealmente son idénticos. Sin embargo, aparecen dos problemas. Primero, las expresiones analíticas que describen la característica principal del filtro son complejas y resulta bastante difícil ajustar el rango frecuencial en el que cumple las especificaciones. Y segundo, los PPF son muy sensibles a los efectos de las no idealidades, pudiendo variar enormemente su respuesta de un filtro a otro, incluso en diseños idénticos.

El estudio de los PPF contenido en esta tesis se realiza desde dos perspectivas distintas pero complementarias.

Por un lado, se realiza un minucioso análisis del circuito, estudiando el efecto que las no-idealidades pueden producir. La investigación se centra especialmente en aquellos fenómenos que ocasionan un desequilibrio (*mismatch*) entre los componentes del circuito. Dado que el funcionamiento de la topología se basa en su particular simetría, surgen numerosos obstáculos a superar para alcanzar los objetivos. En primer lugar, debe encontrarse el peor caso posible para acotar el impacto del *mismatch*. Una vez hallado, se desarrollan las expresiones analíticas que relacionan las prestaciones a las que aspira un PPF con las potenciales variaciones de los dispositivos que lo componen. Estos cálculos se realizan para cada una de las distintas configuraciones de un PPF. Finalmente, se logra obtener una cota fácil de calcular y aplicable a todos los usos de un PPF.

Por otro lado, se realiza el proceso de diseño completo de un PPF, evaluando los factores más críticos de cada paso y proponiendo metodologías que optimicen las decisiones de diseño. De este modo, la tesis no solo presenta un recopilatorio exhaustivo de pautas a seguir para el diseño óptimo de PPFs, paso por paso, sino que también introduce las herramientas necesarias para comprobar por simulación la importancia de los diversos efectos en otras tecnologías, pudiendo utilizarse para tal fin los modelos de simulación que proporcionan los fabricantes. Como paso final, se realizan las medidas de los prototipos, probando que pueden obtenerse PPF con las especificaciones deseadas para el proyecto planteado.

Este trabajo innova presentando una cota cuantitativa, concisa y precisa, del efecto que puede producir el *mismatch*, frente a las predicciones cualitativas que aparecen ocasionalmente en la literatura. Por primera vez, podemos establecer una relación directa entre la precisión de los dispositivos y el valor que puede garantizarse en la característica principal del filtro. Como consecuencia, pueden determinarse restricciones de diseño para los componentes e incluso predecir si una tecnología es viable para las especificaciones deseadas.

También, las metodologías planteadas permiten alcanzar prestaciones superiores a los métodos clásicos de implementación y síntesis, sacando el máximo beneficio a los recursos invertidos en el PPF. Además, el enfoque generalista dota de una ventaja indirecta: las estrategias propuestas tienen menos restricciones. Gracias a ello, los procedimientos resultan muy prometedores para su uso en sistemas donde el número de etapas o características particulares impidan o desaconsejen el empleo de las metodologías tradicionales.

Adicionalmente, se describen diversas y prometedoras líneas futuras para continuar profundizando en la investigación y desarrollo de los PPF de altas prestaciones.

Agradecimientos

Dicen que lo importante es el camino y no el destino, y así lo siento en los pasos que me han traído hasta aquí. No obstante, gracias a Dios, llego ya a la meta tras un largo recorrido. Redactar esta tesis, especialmente estas líneas, me han traído a la mente a demasiada gente que directa o indirectamente ha sido fundamental. Me ha emocionado más de lo que reconoceré, y apostaría que podría escribir otro libro, no menor que este, solo de recuerdos inolvidables que he disfrutado desde que empecé la senda del doctorando. Gracias, a todos los que estuvisteis allí y los hicisteis posible. También a los que continuasteis cuando todo se veía negro y me disteis el empuje para acabar. Gracias, incluso si en este limitado espacio —y tiempo, ya conocéis lo mío con los "deadlines"— no he podido mencionaros.

Agradezco, en primer lugar, a mis directores, Santiago y Fran, la oportunidad que me brindaron y que me consideraran para este proyecto. También la paciencia demostrada cuando inevitablemente el tiempo se echaba encima; o cuando planteaba nuevas propuestas a seguir que se salían de lo esperado y eran un tanto enrevesadas de explicar de primeras (¡esos "mapas del tiempo" superpuestos!); o cuando me alargo tanto como estos agradecimientos porque quiero decir demasido. Gracias por el voto de confianza. Vuestra guía durante estos años ha sido esencial e insustituible. Gracias a vosotros, concluyo la tesis algo más sabio que lo que la empecé (¡o eso espero!).

Al GDE, que me acogió. En verdad, el pasillo ha sido más una segunda casa que un puesto de trabajo, y no solo lo digo por Pedro. Es difícil imaginarme estos años sin Óscar, Miguel, Nicolás, Pepe, Carlos, Belén o Concha. Gracias por tantas veces que me habéis ayudado, aconsejado, o dedicado unas palabras de ánimo o humor. Obviamente, tampoco puedo olvidarme de mis compañeros de —además de Cadence— los cafés en mates, las cenas de jóvenes investigadores y demás desventuras predoctorales: Diego, Uxua, Guillermo, Abel, Raúl, Jorge, ... Quiero, también, hacer extensivo mi agradecimiento a tantos otros con los que he coincidido a lo largo de estos años.

Al ICTEAM de la Universidad Católica de Lovaina (UCL) que dio visto bueno a una estancia casi de improviso. A todo el equipo, pero en especial, a Cecilia Gimeno y Denis Flandre, estoy tremendamente agradecido a la atenta supervisión y recibimiento que me brindaron. Lo aprendido con ellos ha resultado tan influyente como diseñador que me cuesta creer que solamente fueran dos meses y medio.

Al Laboratorio di Microsistemi Integrati de la Universidad de Pavía, especialmente a mis supervisores Edoardo Bonizzoni y Franco Maloberti por creer en la propuesta que hicimos para el YITP y ayudarme a desarrollarla. También a su grupo al completo, por aceptarme como uno más de ellos tanto en el trabajo como en los descansos.

A las instituciones que han hecho posible esta investigación. A la DGA por el contrato predoctoral concedido en la convocatoria 2017-2021; y a la Agencia Estatal de Investigación, Fondo Europeo de Desarrollo Regional a través de los proyectos: TEC2017-85867-R y PID2020-114110RA-I00. También al programa Ibercaja-CAI y Young Investigator Training Program (ISCAS 2018) por financiar mis estancias doctorales.

En modo más personal, a mis padres, Pedro y Carmen, por su apoyo incondicional y constante. Sois un ejemplo diario en todos ámbitos de la vida: de la Física a la Metafísica, de los circuitos a la pintura. Gracias por inspirarme a crecer en "sabiduría y virtud", a apasionarme con lo que hago, a dar prioridad a lo que importa y mostrarme que no hay reto grande, y que los talentos no están para enterrarse. También a Blas.

A mi familia, que no podía faltar: me acompañáis a celebrar las victorias y me dais consuelo en las derrotas por mucho que no os hable más que de galimatías. Os tengo más presentes de lo que os digo, a todos. Estoy impaciente por compartir este logro con vosotros.

A los "globalistas", que crecimos hasta ser un "grupo de muchos grupos", quizás el nombre era profético: Antón, Alejandro, Diana, Juan, Andrés, Merino, Wendy, ... Omar, tú tampoco te escapas ya de este equipo. Simplemente no sé qué habría hecho sin vosotros. Solo de momentos importantes que hemos compartido, chapas que me habéis aguantado y anécdotas que me sacan una sonrisa, ya saturaríais un *making-of* de esta tesis. PD: quiero mi pancarta.

A tantos amigos que me enorgullezco de atesorar, aunque no los vea a menudo. A Eli por sus consejos y las partidas "top". A Surya por su conversación y la "musiqueta". De no ser por vosotras, creo que habría vuelto (aún) menos cuerdo de mi exilio. A Miguel Ángel, señor, y a Holland, figura, os advierto que lo de planes pendientes post-tesis es una lista real y no solo mera motivación.

Al Club Esgrima Aragón y todos sus locos tiradores. Sois legión y no os puedo nombrar a todos (si alguno le ofende, que me rete), pero me alegráis el día cuando os veo, incluso cuando preguntabais por la tesis. Esos míticos 30 min de última hora han sido como un respiro para llegar con aliento hasta aquí. Vaya paciencia tienes con nosotros, Moncho. Gracias por hacerlo posible, maestro.

A los que me acompañaron o se apiadaron y recogieron por mis periplos académicos, y quienes debo no menos que una visita: Guilhem (ve requisando el tractor), Arnold y "Platinum", Antoine, Darwin y Julián, Ludovic y Hugo, JPO y Martín, Michel, ... y tantísimos otros a quienes espero volver a ver, por mucho que se encuentren dispersos por el mundo.

A aquellos docentes que me influyeron más de lo que se imaginan, como Arantxa y Vicente, que me "empujaron" —no sé si con o sin comillas— a la microelectrónica y al doctorado. También a la señorita Susana y Guillermo Baylo, que ya no sé de ellos, pero que me enseñaron a tener curiosidad, hacerme preguntas y declararle la guerra al aburrimiento. No sé si es verdad que un maestro deja su huella en la eternidad, pero desde luego todos ellos, y no menos de los que he nombrado, dejaron la suya en mí. Gracias a todos.

A ti, que lees esto, gracias y ánimo.

Antonio D. Martínez Pérez

04 Octubre 2024

Contents

Abstract i

Resumen iii

Agradecimientos vii

Contents x

List of Figures xv

List of Tables xix

Abbreviations xxi

Symbols xxv

1 Introduction 1
- 1.1 A wireless tale of radio communication systems . . . 3
  - 1.1.1 Ancient signals . . . 4
  - 1.1.2 Telegraphing the future . . . 6
  - 1.1.3 The spark of inspiration . . . 9
  - 1.1.4 The many fathers of the 1901 radio . . . 12
  - 1.1.5 The radio we know . . . 14
  - 1.1.6 Once upon a time there was a triode . . . 17
  - 1.1.7 The age of silicon . . . 19
- 1.2 Motivation . . . 22
  - 1.2.1 Issues and opportunities of a continual evolution . . . 23
  - 1.2.2 Research and thesis context . . . 25
- 1.3 Objetives . . . 28
- 1.4 Thesis organization . . . 30
- References . . . 32

2 Theoretical foundations 41
- 2.1 Transceiver architectures . . . 42
  - 2.1.1 Frequency converter block . . . 42
  - 2.1.2 Transmitter architectures . . . 46
  - 2.1.3 Receiver architectures . . . 50

2.2 Complex signals . . . 54
2.2.1 Complexities of the negative spectrum . . . 55
2.2.2 Phasors and polyphase decompositions . . . 58
2.2.3 Complex filters . . . 61
2.3 Technology devices . . . 62
2.3.1 Non-idealities . . . 63
2.3.1.1 Temperature and process variations . . . 64
2.3.1.2 Mismatch variations . . . 65
2.3.1.3 Parasitics . . . 66
2.3.2 Type of devices . . . 67
2.3.2.1 Capacitors . . . 67
2.3.2.2 Resistors . . . 68
References . . . 70

3 Analysis of image rejection ratio for passive polyphase filters 73
3.1 Working principles . . . 74
3.1.1 Basic description . . . 74
3.1.2 PPF types . . . 78
3.1.2.1 IQ filter configuration . . . 79
3.1.2.2 Type I . . . 80
3.1.2.3 Type II . . . 83
3.1.2.4 Comparison . . . 85
3.1.3 Multi-stage filters . . . 86
3.1.4 Non-idealities effects . . . 88
3.1.4.1 Temperature and process variations . . . 89
3.1.4.2 Mismatch . . . 90
3.1.4.3 Parasitics . . . 94
3.2 Mismatch analysis . . . 95
3.2.1 Worst-case search for a 1-stage PPF . . . 96
3.2.2 Worst-case analysis . . . 101
3.2.2.1 Type-I D-IQ conversion . . . 102
3.2.2.2 Type-II D-IQ conversion . . . 106
3.2.2.3 Type-I IQ-D conversion . . . 109
3.2.2.4 Type-II IQ-D conversion . . . 111
3.2.2.5 Quadrature Filter . . . 114
3.2.2.6 Discussion . . . 118
3.2.3 Worst-case search for a multi-stage PPF . . . 120
3.3 Additional effects to PPF performance and analysis . . . 124
3.3.1 Capacitor mismatch impact . . . 124
3.3.2 Load effect . . . 125
3.3.3 Load mismatch . . . 127
References . . . 131

4 Design and implementation of passive polyphase filters 135
4.1 Schematic stage . . . 135
4.1.1 Specifications . . . 136
4.1.2 Minimizing the effect of non-idealities . . . 136

4.1.3 Component selection and sizing . . . 137
4.1.4 Pole splitting . . . 141
4.1.5 Schematic simulations . . . 146
4.1.5.1 Combined simulation disadvantages . . . 146
4.1.5.2 First step: process variations . . . 147
4.1.5.3 Second step: mismatch impact . . . 150
4.2 Layout stage . . . 153
4.2.1 Initial considerations . . . 153
4.2.2 First layout approach . . . 154
4.2.3 Second layout approach . . . 157
4.2.4 Final layout design . . . 160
4.3 Experimental stage . . . 165
4.3.1 Setup . . . 166
4.3.2 Results . . . 168
4.3.3 Discussion . . . 171
References . . . 173

5 Conclusions **177**
5.1 Analytical study . . . 178
5.2 Design and optimization methodology . . . 181
5.3 Future research directions . . . 185
References . . . 189

Appendixes **192**

A Conclusiones **193**
A.1 Estudio analítico . . . 194
A.2 Metodología de diseño y optimización . . . 197
A.3 Líneas futuras de investigación . . . 202
Referencias . . . 207

B Removing telegraphic wires **211**
B.1 Conduction telegraph . . . 211
B.2 Induction telegraph . . . 215
References . . . 217

C Analysis of 1-stage ideal PPF **219**
C.1 Differential to quadrature converter . . . 220
C.1.1 Type I . . . 221
C.1.2 Type II . . . 223
C.2 Quadrature to differential converter . . . 224
C.2.1 Type I . . . 225
C.2.2 Type II . . . 226
C.3 Quadrature filter . . . 228

D Analysis of 1-stage PPF with worst-case mismatch **231**
D.1 Differential to quadrature conversion . . . 232
D.1.1 Type I . . . 233
D.1.2 Type II . . . 237
D.2 Quadrature to differential converter . . . 242
D.2.1 Type I . . . 243
D.2.2 Type II . . . 249
D.3 Quadrature filter . . . 255
D.4 Discussion . . . 261

E Alternative PPF mismatch decomposition **263**
E.1 Redefining mismatch . . . 263
E.2 D-IQ Conversion . . . 265
E.2.1 Type I . . . 265
E.2.2 Type II . . . 267
E.3 Discussion . . . 269

F Alternative PPF mismatch combination **271**

G A systematic analysis method for general PPFs **275**
References . . . 276

H Technology device tolerances **277**
H.1 Capacitors . . . 277
H.2 Resistors . . . 278

I Publications of the author **285**
Publication in journals . . . 285
Contributions to international conferences . . . 286
Contributions to national conferences . . . 288
Contributions to workshops and forums . . . 289

List of Figures

1.1 RF design hexagon 2
1.2 Aeneas Tacticus's communication system 5
1.3 Different RoF RAU approaches 26

2.1 Heterodyne signals in the frequency domain 43
2.2 SQ frequency converter schemes 45
2.3 DQ frequency conversion scheme 46
2.4 Classical superheterodyne TX architecture 47
2.5 SQ SSB TX architecture 48
2.6 Two-step-up TX architecture 49
2.7 Classical superheterodyne RX architecture. 51
2.8 Hartley RX architecture 51
2.9 Hartley-PPF RX architecture 52
2.10 Weaver RX architecture 53
2.11 Weaver-PPF RX architecture 53
2.12 Operation of SQ upconverter 57
2.13 Operation of SQ downconversion 58
2.14 Sets of phasors 59
2.15 Decomposition into symmetrical components 62
2.16 Real and complex filter responses 63

3.1 Schematics for one- and three-stage PPFs 74
3.2 Differential IQ signal with different sequences 75
3.3 PPF behavior at tunned frequency 76
3.4 Different PPF configurations 78
3.5 Standard one-stage PPF block diagram 80
3.6 Decomposition of a Type-I differential signal 82
3.7 Decomposition of a Type-II differential signal 83
3.8 Type-II IQ-D conversion diagram block 84
3.9 *IRR* curves of PPFs with different stage numbers 87
3.10 PPF simulation in different process corners 90
3.11 *IRR* curves of PPFs with mismatch 91
3.12 Mismatch tolerance of devices 92
3.13 *IRR* curves of PPFs with mismatch on different stages 93
3.14 Three-stage PPF with relevant parasitics 94
3.15 Last-stage parasitics impact on the PPF *IRR* 95
3.16 PPF with resistor mismatch 98
3.17 Effect of $\boldsymbol{M}_1$ mismatch combinations 99

3.18 Effect of all possible mismatch combinations for a one-stage PPF 100
3.19 PPF with worst-case mismatch combination 102
3.20 Type-I D-IQ converter PPF *IRR* 105
3.21 Type-II D-IQ converter PPF with worst-case mismatch 107
3.22 Type-II D-IQ PPF *IRR* 109
3.23 Type-I IQ-D converter PPF 110
3.24 Type-II IQ-D converter PPF 112
3.25 Transfer function subcircuits for Type-II IQ-D PPF 112
3.26 Mismatch impact on the *IRR* of D-IQ, ID-D, and IQ-IQ PPFs 117
3.27 Effect of $\boldsymbol{M}_3$ mismatch combinations 121
3.28 Effect of most-harmful $\boldsymbol{M}_3$ mismatch combinations 122
3.29 *IRR* mismatch color map vs. a worst-case simulation 123
3.30 *IRR* mismatch color map vs. calculated limit 124
3.31 RC and CR circuits with load impedance 126

4.1 Mismatch tolerance of technology devices 139
4.2 Area consumption of technology devices 140
4.3 Expected *IRR* in the *BW* versus k_2 (*"rppolywo"*) 145
4.4 Expected *IRR* in the *BW* versus k_2 (*"rnpolywo"*) 145
4.5 *IRR* curves with process variations 148
4.6 Histogram of frequency shift due to process variations 148
4.7 *IRR* curves for the PPF designs (process variations) 149
4.8 *IRR* heat mao for the PPF designs (mismatch) 151
4.9 Histogram of the *IRR* from the designs 152
4.10 Diagram of interdigitated resistor placement 155
4.11 First approach layout design 156
4.12 *IRR* of the first approach layout 157
4.13 Diagram of the second layout approach 158
4.14 Second approach layout placement 158
4.15 Three-stage PPF schematic representations 161
4.16 Diagram of the final layout design 162
4.17 Diagram of the expanded final layout design 163
4.18 Final layout design 163
4.19 Final layout design with pads 164
4.20 Post-layout *IRR* results of the final layout version 165
4.21 Final layout *IRR* histogram 165
4.22 Schematics of the PCB for the PPF experimental measurement 166
4.23 Photograph of the PCB implementation 168
4.24 Experimental *IRR* results of PPF prototype samples 169
4.25 Experimental and simulation *IRR* comparison 170

B.1 Morse's conducted telegraph over water 212
B.2 Ratheanau's experiment 214

C.1 Analyzed PPF configurations 220
C.2 1-stage PPF representation 221
C.3 Block diagram for the PPF 222
C.4 Type-I IQ-D PPF 225

C.5 Type-II IQ-D PPF 226
C.6 Type-II IQ-D PPF equivalent circuits 227

D.1 Analyzed 1-stage PPF with the worst-case mismatch 232
D.2 *IRR* curves from Type-I D-IQ PPF 237
D.3 Type-II D-IQ PPF with worst-case mismatch 238
D.4 *IRR* curves from Type-II D-IQ PPF 242
D.5 Type-I IQ-D with worst-case mismatch 243
D.6 *IRR* curves from Type-I IQ-D PPF 248
D.7 Type-II IQ-D PPF with worst-case mismatch 249
D.8 Equivalent circuits of Type-II IQ-D PPF 249
D.9 *IRR* curves from Type-II IQ-D PPF 254
D.10 *IRR* curves from different PPF configurations 261

F.1 One-stage PPF with mismatch ($\boldsymbol{M}_1$ vector 2) 272

List of Tables

1.1 Comparison between radio-over-fiber RAU alternatives 27

2.1 TX architecture comparative for RAU downlink 50
2.2 RX architecture comparison for RAU downlink 54

3.1 PPF analysis summary results 118

4.1 PPF design specifications 136
4.2 Design values for a three-stage PPF with *"rppolywo"* resistors 144
4.3 Design values for a three-stage PPF with *"rnpolywo"* resistors 144

H.1 Process variations in MIM capacitors 279
H.2 Mismatch variations in MIM capacitors 280
H.3 Process variations in *"rnpolywo"* resistors 281
H.4 Mean error of *"rnpolywo"* resistors (process error) 282
H.5 Standard deviation of *"rnpolywo"* resistors (process error) 282
H.6 Mismatch variations in *"rnpolywo"* resistors 283
H.7 Mean error of *"rnpolywo"* resistors (mismatch error) 284
H.8 Standard deviation of *"rnpolywo"* resistors (mismatch error) 284

Abbreviations

Acronym	Significance
A	Positive sequence symmetrical component
AC	Alternating current, *i.e.*, small-signal conditions
AM	Amplitude modulated
ASIC	Application specific integrated circuit
AT&T	American Telephone and Telegraph
B	Differential collineal symmetrical component
BB	Baseband
BBoF	Baseband over fiber
BiCMOS	Bipolar-CMOS (technology)
BJT	Bipolar-junction transistor
BS	Base Station
C	Negative sequence symmetrical component
CMOS	Complementary metal-oxide-semiconductor
CW	Continuous wave
D	General bias symmetrical component
D-IQ	Differential to IQ (signal converter)

DAS	Distributed antenna system
DC	Direct current
DQ	Double quadrature (scheme)
DUT	Device under test
ELF	Extremely low frequency
FET	Field-effect transistor
ff	Fast-fast (corner)
FM	Frequency modulated
fs	Fast-slow (corner)
GE	General Electric (Company)
HF	High frequency
IC	Integrated Circuit
IEEE	Institute of Electrical and Electronics Engineers
IF	Intermediate frequency
IF_I	Intermediate-frequency in-phase component
IF_Q	Intermediate-frequency quadrature component
IFoF	Intermediate-frequency over fiber
IoT	Internet of Things
IQ	In-phase and quadrature components
IQ-D	IQ to differential (signal converter)
JFET	Junction field-effect transistor
LNA	Low-noise amplifier

LO	Local oscillator
LO_I	Local-oscillator in-phase component
LO_Q	Local-oscillator quadrature component
LTI	Linear time-invariant
MIM	Metal-insulator-metal (capacitors)
M_n	Metal layer n
MOM	Metal-oxide-metal (capacitors)
MOSFET	Metal–oxide–semiconductor field-effect transistor
PCB	Printed circuit board
PLL	Phase-locked loop
PPF	Passive polyphase filter
PVT	Process, voltage and temperature (errors)
Q (factor)	Quality factor of a device, relating parasitic and nominal values
QLO	IQ local oscillator
RAU	Remote antenna unit
RF	Radio frequency
RF_I	Radio-frequency in-phase component
RF_Q	Radio-frequency quadrature component
RFoF	Radio-frequency over fiber
RoF	Radio over Fiber
RX	Receiver
sf	Slow-fast (corner)

SiGe	Silicon–germanium
SMD	Surface mount devices
sms	Short message service
SOI	Silicon on insulator
SQ	Single quadrature (scheme)
ss	Slow-slow (corner)
SSB	Single sideband
TX	Transmitter
tt	Typical (corner)
VNA	Vector network analyzer

Symbols

Symbol	Name	Units
A	Signal amplitude / Phasor magnitude	V or A
A_{BAL}	Amplitude balance	–
A_I	Amplitude of in-phase component	V or A
A_{IF}	Amplitude of IF signal	V or A
A_{LO}	Amplitude of LO signal	V or A
A_Q	Amplitude of quadrature component	V or A
A_{RF}	Amplitude of RF signal	V or A
b	Normalized frequency (ωRC)	–
b_p	Peak normalized frequency	–
BW	Channel bandwidth	Hz
BW_{PPF}	PPF bandwidth	Hz
C	Capacitance	F
C_h	Channel capacity	bits/s
C_{Lmn}	Parasitic capacitance on the node n of the stage m	F
C_L	Load capacitance	F

C_{Tn}	Temperature coefficient of n-order	$1/\mathrm{K}^n$
f	Frequency	Hz
f_0	Filter central frequency	Hz
f_1	First stage pole frequency	Hz
f_2	Second stage pole frequency	Hz
f_3	Third stage pole frequency	Hz
f_{IF}	Intermediate-frequency frequency	Hz
f_{LO}	Local-oscillator Frequency	Hz
f_{RF}	Radio-frequency frequency	Hz
$\mathscr{F}(u(t))$	Fourier transform of $u(t)$	–
$\mathscr{F}^{-1}(U(j\omega))$	Inverse Fourier transform of $U(j\omega)$	–
H	Height	m
H_1	Transfer function of RC circuit	–
H_1'	Transfer function of RC circuit with capacitive load	–
H_{1A}, H_{1B}	Transfer function of RC circuit with mismatch	–
H_2	Transfer function of CR circuit	–
H_2'	Transfer function of CR circuit with resistive load	–
H_{2A}, H_{2B}	Transfer function of CR circuit with mismatch	–
$H(s)$	Transfer function	–
I	In-phase component	V or A
I_{in}	In-phase component of input signal	V or A
IRR	Image rejection ratio	–

$IRR_{A_{BAL}}$	Image rejection ratio with ideal $\Delta\theta$	–
IRR_{max}	Peak image rejection ratio	–
$IRR_{\Delta\theta}$	Image rejection ratio with ideal A_{BAL}	–
k_2	Pole splitting factor	–
K_D	Deviation factor to lower frequencies	–
K_U	Deviation factor to higher frequencies	–
L	Length	m
$\boldsymbol{M}$	Mismatch basis matrix	–
$\boldsymbol{M}_N$	N-stage PPF mismatch basis matrix ($4N \times 4N$)	–
p_n	Phasor n of a composite signal	–
P_o	Power output	W
Q	Quadrature component	V or A
Q_{in}	Quadrature component of input signal	V or A
R	Resistance	Ω
R_L	Load resistance	Ω
$R_\square$	Sheet resistance	Ω per square unit
s_+	Positive sequence	–
s_-	Negative sequence	–
SNR	Signal-to-noise ratio	–
$\boldsymbol{T}$	Natural-to-symmetrical change-of-basis matrix	–
T	Temperature	K or ℃
t	Time variable	s

$\boldsymbol{U}$	Case coordinates in $\boldsymbol{M}$	–
$\boldsymbol{U}_N$	Case coordinates in $\boldsymbol{M}_N$	–
V_{DD}	Supply voltage (DC)	V
v_{in}	Input voltage (AC)	V
v_n	Voltage at input n (AC)	V
v_o	Output voltage (AC)	V
v_{on}	Voltage at output n (AC)	V
v_{o+}	Positive output voltage (AC)	V
v_{o-}	Negative output voltage (AC)	V
W	Width	m
x	Symmetric lineal mismatch tolerance	m
x_c	Load capacitance mismatch tolerance	m
x_r	Load resistance mismatch tolerance	m
y	Symmetric geometric mismatch tolerance	m
z	Common-factor mismatch tolerance	m
γ_c	Capacitance load to capacitor ratio (C_L/C)	–
γ_r	Resistor to resistance load ratio (R/R_L)	–
ΔC	Capacitor variation	–
$\boldsymbol{\Delta E}$	Element deviation vector ($K \times 1$)	–
ΔR	Resistor variation	–
$\boldsymbol{\Delta R}$	Resistor mismatch vector	–
ΔR_k	Variation of resistor k	–

$\Delta\theta$	Phase error	rad
$\delta(x)$	Dirac delta function	–
θ_I	In-phase component phase	rad
θ_Q	Quadrature component phase	rad
λ	Wavelength	m
ρ	Electrical resistivity	Ω·m
σ	Standard deviation	–
ω	Angular frequency	rad/s
ω_{IF}	Intermediate-frequency angular frequency	rad/s
ω_{LO}	Local-oscillator angular frequency	rad/s
ω_{on}	Pole of the stage n	rad/s
ω_{RF}	Radio-frequency angular frequency	rad/s

Chapter 1

Introduction

Just as electricity burst into towns, streets, and homes almost a century ago, wireless communications have done the same in our days. The ability to transmit information by air using electromagnetic signals is nothing new. However, in this first quarter of the millennium, wireless communications have evolved and enabled devices that were unimaginable not so long ago. To the point that not having Internet in those pocket computers that we call smartphones feels strange. Wherever we go, we expect to have Wi-Fi or at least a connection to a mobile network. We have become used to continuous and portable connectivity, which is linked to wireless technology development.

Perhaps the maximum exponent of this concept is the Internet of Things (IoT) [Asl20], which is taken to the extreme to provide objects with new functionalities. According to this strategy, all types of machines or devices can be equipped with a small communications module, which allows them to exchange information with their environment and thus improve their effectiveness. From refrigerators that make your shopping list to optimizing processes in a factory, countless applications can benefit from transmitting additional information.

However, these advantages have significant work behind them. Their operation depends on designing systems that meet increasingly restrictive and opposed specifications. The infamous "design hexagon" [Raz11], Figure 1.1, is an example of this issue. The representation includes six different critical parameters for radio-frequency (RF) electronic circuits. Improving one of them jeopardizes the adjacent ones in the hexagon.

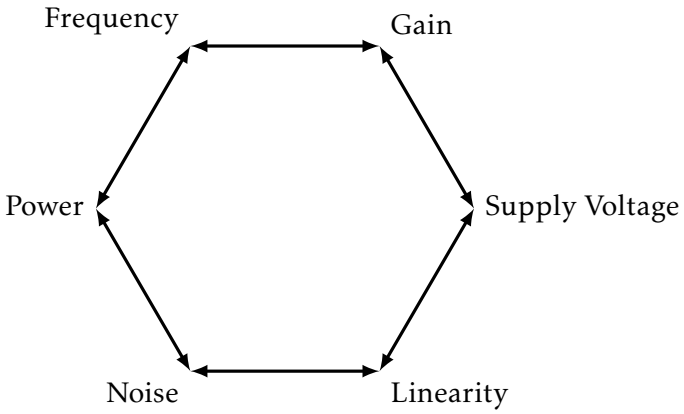

Figure 1.1: RF design hexagon.

For example, a lower supply voltage might allow more suitable or smaller batteries and even reduce power consumption. Nevertheless, it will also impact device biasing. Circuit elements will have a reduced voltage range to achieve larger dynamic operation ranges (linearity) and desirable operation regions of active components (typically translated to losing gain). Another well-known trade-off happens between gain and frequency to the extent that the gain-bandwidth product is a typical parameter for amplifiers with a single-pole dominant.

The evolution of microelectronics has enabled the inclusion of digital circuits everywhere. As a result, even tiny systems can use more complex communication protocols that provide a more efficient sharing of channel resources. Nevertheless, physical front-ends, as well as nature, are in the analog domain [Raz17]. The unique particularities (and issues) of RF electronics exacerbate the roughness of the analog world. There, designers must fiercely fight the mentioned RF hexagon to reach the desired specifications.

Fortunately, circuit integration improves the trade-offs. The device miniaturization implies not only an area reduction but also a better frequency performance, cost, and a reduction of parasitics. Sometimes, integration means the difference between whether lumped-element models remain valid for a particular frequency range. Moreover, a communication system fully integrated on the same chip—a monolithic system—benefits the most from all those advantages. However, it must cope with a dilemma as every system piece will use the same technology. One option for the circuit is to employ an expensive technology for all the parts. That ensures the performance of demanding building blocks. Nonetheless, that would also—notably—increase the cost of simpler

circuits without a worthy improvement in those pieces. Otherwise, the most exigent blocks must perform well without the leverage of specialized technology.

Research of the PhD candidate was encompassed in a project that aimed to design an RAU (Remote Antenna Unit) using standard CMOS technology. More precisely, the studies focus on the antenna front-end blocks (see more details later in the chapter and in Section 2.1). In that context, the main work of these years has been the development of methodologies of design and optimization for critical blocks of heterodyne transceivers. All these circuits are present in the majority of modern communication devices.

Thus, the generalist approach might confer the research a more inspirational interest for any analog designer to attain better performance in their circuits. The ideas also might interest anyone in charge of a top-down design, helping to estimate specifications for a particular technology and topologies. As an engineering saying goes, "The cost of a change grows exponentially with each stage." Consequently, developing tools and methods to relate available resources and parameter limits was an especially attractive project.

More specifically, this memory focuses on researching passive polyphase filters, a fundamental piece of the frequency conversion block for many receivers and transmitters. This part of the research comprises the entire process of a microelectronic design for a particular circuit, from an exhaustive analytical study to the proper design (schematics and layout) and finalizing with the experimental measurement of the prototype.

Bellow, Section 1.1 describes the history of electronics and the rise of electronic wireless communications. Then, Section 1.2 explains the motivation and the relationship of this memory with other studies. Objectives of the thesis are defined in Section 1.3. Section 1.4 presents the thesis organization.

1.1 A wireless tale of radio communication systems

The ability to communicate effectively distinguishes humans from any other animal. We desire and need to express and share ideas, and we can learn and evolve from that

exchange. Since ancient times, the importance of sending and receiving messages by a fast and reliable method has been widely known.

A clear example is the legend of the Athenian herald **Pheidippides**, who died from exhaustion after delivering the critical result of the Battle of Marathon. More than 2500 years later, one of the most famous athletics competitions remains named after his achievement to quickly and dependably carry the message, even at the cost of his life.

Nor would the velocity of a legendary runner be enough for the cravings for improvement. Information had to take off and fly to its target. Delivering messages by hand or voice is not always practical, and just a half-century later, there are indications about Athenian vessels using some visual communication system to coordinate their efforts in the battles during the Peloponnesian War (431–401 BC).

1.1.1 Ancient signals

Around a century later, the first defense structures of what would become the Great Wall of China used beacon fires and drums for communication along the strongholds [Wal98] . The ambitious length of China's border wall forced them to develop a series of codes to transmit messages from one tower to another. It is said that by the Tang dynasty (618–907 AC), a message could travel more than 1100 km in 24 hours [Ste08]. The following dynasties added better or complementary methods and codes, such as artillery signaling (Ming dynasty, 1368–1644 AC). The same infrastructure also had couriers as backups for that ancient telegraphy. However, the record distance achieved in 24 hours this way was around 400 km, quite impressive but inferior to the alternatives.

Although little physical evidence remains, and technical descriptions are lost in time, many early Greek and Roman historians mention different visual signalizing methods used by the Roman armies [Ste08]. The extension of these communication systems—as opposed to sending messengers—is not clear, but there is little doubt about their use of signals in times of war.

Aeneas Tacticus's system is the exception. He was one of the earliest Greek writers (4^{th} century BC) on the art of war, especially on security. The title of his only treatise on

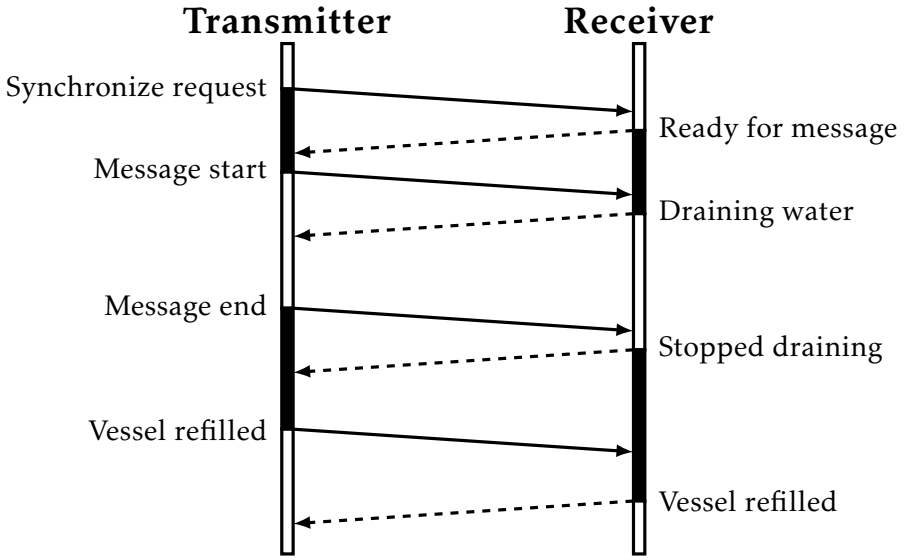

Figure 1.2: Graphic representation of synchronization protocol of Aeneas Tacticus's communication system. Dark segments indicate the torch is up, while light sections imply it is down.

surviving to our days, "How to Survive under Siege," seems to be representative of the topics concerning him.

According to Polybius (circa 200–118 BC), Aeneas wrote a guide to securing military communications and devised a clever hydraulic semaphore system [Pol]. The sender and the receiver have identical recipients filled with water and equal plugs at the bottom to remove the liquid in a controlled manner. Inside the recipient and connecting to a floating device, a stick with marks at distinct heights includes the possible messages (or the alphabet). After pouring the same quantity of liquid—*i.e.*, having both plugs synchronously removed and then placed again—the water level indicates the same mark in both vessels.

Torch signalizing achieved synchronization, as shown in Figure 1.2. The sender team raises the torch to notify of a new message; then, they wait for the receiver team signal that indicates they are ready. After that, the torch is lowered while draining water until the desired mark. The receiver team imitates the operation and stops pouring the water when the transmitting team's torch is up again. The cycle ends with each torch descending when the vessel is refilled.

A pair of vessels per team could neglect refilling time. Also, events or letters should be organized from most to least probable, as some marks are faster to transmit than

others. The system can also provide some basic security: having an identical vessel and knowing the symbol order is mandatory to understand the message.

Recent studies estimate a data transfer rate of 151 letters per hour [Kul24] when used to transmit Ancient Greek text, which is quite impressive compared to similar methods. As a reference, the optical telegraph from 1794 could work at 100 letters per hour. It was not until the development of the electric telegraph and Morse's code (1840s) that the new technologies had an obvious advantage in speed.

1.1.2 Telegraphing the future

Needless to say, as centuries passed, countless inventions were developed and used with a wide range of degrees of success around the world. Among that myriad of innovative solutions to reach further distances, we should focus on a discovery made on "July 2, 1729, about 10 in the morning" (the letter explains the experiments in great detail [Gra31]). **Stephen Gray** successfully transmitted electric force over wires. The result of that particular experiment has significant implications: electricity was not just something static, but wires could conduct it. Moreover, the scientific community proved that metals—previously deemed "no-electric" in the rising age of electrostatic—are better conductors than the packthread wires that Gray employed. However, the application to telecommunications had to wait a couple of decades after this.

In the 1750s, the Spanish physician **Francisco Salvá y Campillo** was probably the first to propose electricity to transmit information. He considered the electrostatic telegraph possible and as fast as the best optical telegraph—in his own words—to send a message from Mataró to Barcelona: "Therefore, electricity must be made to speak if it is to be applied to telegraphy, and this, I believe, is not difficult to achieve" [Rom01].

Salvá's statement proves that he was a visionary, but to be faithful to history, he was not the only one studying the properties and applications of electricity. Several contemporary men of science were making their attempts, proposing new ideas or conducting exciting experiments [Alb54]. Some of those experiments were as colorful and shocking as those of **Jean-Antoine Nollet**, a scientist and *abbé* of the Parisian Grand Convent of the Carthusians. *Abbé* Nollet arranged around two hundred monks in a circle, apart

from their neighbors around 7 meters, but linked to them by metal wires. Without warning, Nollet connected the ends to a big electrostatic battery. The loud and simultaneous exclamations proved that electricity is quite fast indeed [Sta98].

Still, there was a missing piece: **Alessandro Volta**'s key invention, the voltaic pile, was mandatory for opening the practical uses of electricity. Ironically, Volta developed it as an *experimentum crucis* [Rou81], failing to see the great potential of electrochemistry. The capability of generating electrical current enabled innumerable experiments that were not doable with electrostatic generators. A new century truly had begun in the year 1800.

Meanwhile, **George-Louis Lesage** implemented an electrostatic telegraph in 1774, proving the possibility of communication by electricity but with little practical use. A different history was the optical telegraph of **Claude Chappe** in 1791. The invention was critical during the Napoleonic wars (1803-1815), and other countries quickly adopted it [Gua19]. Unfortunately, the harsh criticism from his rivals caused him a deep depression and paranoia, and Chappe did not survive to see his invention flourish right across Europe [Sta98]

By contrast, **Salvá** presented an exciting report on February 22, 1804 [Sal76]. He reviewed state-of-the-art optical telegraphs and concluded that electrical versions would be more suited for long-distance communications in the short future, recognizing the potential of Volta's invention. Moreover, he proposed the electrolysis of water—recently discovered—to detect electrical currents and their direction by the generated hydrogen and oxygen bubbles. Thus, he proposed an electric telegraph using all of that. The system used several circuits with a common return and exploited the capability of distinguishing current direction, *i.e.*, for n signals, only $1+n/2$ wires would be required. Thus, the approach notably reduced the number of wires enough to represent a complete alphabet. It seems that Salvá carried out some experiments before the members of the Academy of Science on the day of the report, becoming the first recorded use of electric current to transmit information [Alb54]. However, it is unknown if he did long-distance trials. He seems to be working on it, but there are indications that he did not have long enough cables on February 22 [Yus10].

Four years later, in 1809, **Samuel von Sömering** experimented with a telegraph design almost identical in description to Salvá's, although the range of the first prototypes was

too short for practical use. In 1812, the system had evolved to include a wire per letter of the alphabet (twenty-four) and had a reach of 12 kilometers [Sar06]. Letters were sent two by two, using the wire of the second one as the return path for the former. He also experimented with water-filled troughs, replacing wires. He noticed the system worked when the troughs were separate but not if electrodes shared the medium. He might have produced the first wireless conduction telegraph if he had tried with wider troughs.

Hans Christian Ørsted's discovery of electromagnetism (1820) [Øer20] enabled new methods of current detection. **Joseph Henry**, **André-Marie Ampère**, **Karl Friedrich Gauss** with **Wilhelm Weber**, and **Karl August von Steinheil**, among many others, improved previous versions. Finally, **William Fothergill Cooke** and **Charles Wheatstone** took notice of the obstacles to the telegraph as a profitable communication system and patented their five-needle device in 1837. [Alb54].

In parallel to Cook and Wheatstone, **Samuel Morse** saw the commercial possibilities of the electric telegraph [Sta98]. He stopped his scheme in Europe—he was doing miniatures of the Louvre's finest paintings, his "Gallery of the Louvre" to exhibit in America and charge admission—, took a fast ship and started his project in his homeland. With the essential technical and economic assistance of Alfred Vail, they also obtained a working long-distance telegraph prototype in 1837.

However, their most significant improvement was the "Morse code" (1844), which could achieve a much faster data transfer rate than previous methods. Telegraph of Gauss and Weber in 1833 could transmit 120 letters per hour (slower than Aeneas's system), although they improved to 420 some years later. On the other hand, the Morse code enables a rate of 40 words per minute, with some experts achieving rates faster than 60 words per minute.

With the deployment of the first lines in the 1840s, the public and governments started to become aware of the importance of the electric telegraph. Before that, it was deemed more like a curiosity. For example, the experiments of **Francis Ronald** were infamously rejected as "wholly unnecessary" by the Admiralty (United Kingdom navy) in 1816, although just in 1832, they tried (unsuccessfully) to acquire the invention of **Baron Pavel Schilling** (later, he became the father of telegraphy in Imperial Russia). To add insult to injury, the first commercial telegraph in the United Kingdom derived from

Ronald's works. Maybe because Ronald was a friend of Cook's father [Sta98], Cook and Wheatstone found their investor in the railway companies instead of the government, as opposed to other European countries around those years. On the other side of the Atlantic, Morse got substantial funds from Congress to deploy the telegraph in the United States once he proved the importance of his patent [Sta98]. His connection with politics—he ran mayor for New York in 1836 and was quite vocal throughout his life in his ideology, quite "controversial" in our days—might help him in this regard.

In a single decade, the electrical telegraph superseded optical telegraph to become the new standard [Sar06]. The following and fast popularization of the system in most developed nations (anyone could use it for a fee) and the deployment of submarine telegraph cables to connect continents greatly impacted society and how people saw the world. As Germans say, the world had become a *kabelsalat* (cable salad), a tangled mass of cables connecting everything. Innumerable researchers, physicists, and engineers kept working to improve the galvanic telegraph and update it with novel discoveries. However, the history of wireless technology takes us to a particular branch of that family tree: we will focus on the children of those initial telegraph systems that were taking their first steps without a cable.

It should be noted that other telegraph approaches [Rob12] did not survive the fierce competition of state-of-the-art communication systems. An example of this creative invention is the device developed by **Francis Whishaw** in 1838 [Whi39]. His apparatus employed water pressure through a pipe to indicate a particular water level in reception. In other words, it was similar to Aeneas's idea, but Whishaw used communicating vessels and more modern hydraulic devices instead of synchronizing by torch signals. The transmission was nearly instantaneous, and Whishaw expected to supersede optical and electrical telegraphy. However, he was unable to deploy it commercially, probably due to complications with water temperature changes. Apparently, freezing weather caused significant issues during his experiments.

1.1.3 The spark of inspiration

There were several attempts to remove wires (Appendix B) for telegraph links. However, neither showed the potential of later systems based on electromagnetic waves. Among the myriad technological advances and intelligent solutions in the golden age

of inventors, the spark of two geniuses—and many essential contributors—ignited a train of unexpected discoveries that would change the world and societies again.

In 1864, **James Clerk Maxwell** produced a set of equations that explained the mysterious electromagnetic fields [Max65]. They were a massive set of twenty expressions and twenty unknowns. His findings and thoughts were reflected in his book *A Treatise on Electricity and Magnetism* (1873) [Max73]. Despite the author's best intentions, this work is infamously known for being especially hard to interpret and understand. His death in 1879, while he was in the review process for a second edition of the book, offered little help in making it more accessible. Nevertheless, Maxwell's *magnum opus* was the seed of the inspiration for a long list of fairly recognized researchers.

The fresh branches were already growing, thanks to those brave readers. They applied the novel discoveries to diverse fields and completed Maxwell's theories. Three of them—**Oliver Heaviside**, **Francis FitzGerald**, and **Oliver Lodge**—were known as "the Maxwellians" for their contribution to the expansion and diffusions of Maxwell's ideas after his demise [Hun05].

Heaviside had not received a formal education since elementary school. Still, his brief work as a telegraph operator and discovery of the recently published Maxwell's book changed his career [Sar06]. His achievements include his telegraph equations [Hea76] and his significant contributions to waveguide development. He is also responsible for the term "impedance," among many other keywords in modern electronics and electromagnetism. In addition to that, he made significant advances in operational calculus and analysis of circuits [Kul91]. Moreover, he reformulated Maxwell's set of equations in a more straightforward and compact form (developed at some point between [Hea92b] and [Hea92a]). These expressions are the ones currently learned and feared by present students.

Maxwell had laid the theoretical foundations for wireless communications; however, science requires experimental verification, which was tricky in this case. Think about modern RF electronics. Sometimes, the field is still jokingly called "the voodoo of electronics" [Joh03] due to the complex behaviors of the systems. Producing a design capable of transmitting and receiving a wireless signal was a titanic task in those days. **Lodge** recorded several ideas about generating light electromagnetically, although the first descriptions of how to produce electromagnetic waves other than light were in

collaboration with **FitzGerald** between 1879 and 1883 [Hun05]. Nevertheless, they were unsuccessful.

Other wireless systems were explored in the meantime. **Alexander Graham Bell** successfully transmitted a voice-modulated light beam to a receptor almost 500 meters from the origin in 1878 [Huu03], just two years after the world's first telephone patent.

Several researchers and inventors come close to proving electromagnetic waves since 1864: **Edison**—twice—with his mistaken "ethereal force" [Edi75; Hou76] and a non-tested patent[Sar06]; **Dolbear** with his electrostatic telephone[Dol86]; and **David Edwards Hughes**, who related sparks and noise in a close speaker without galvanic contact—something similar to interferences caused by 2G and 3G signals that heralded an incoming call or sms in near speakers. Hughes even deduced it must be caused by "aerial electric waves"; however, after an unsatisfactory reunion with the Royal Society, he refused to write a paper on the subject until doing more experiments. When he realized, it was already too late [Fah99].

Finally, **Heinrich Rudolf Hertz** verified Maxwell's theory in 1887 [Her87]. He had no contact with the Maxwellians before publishing his results. However, they seemed to develop a good relationship after that. FitzGerald was instrumental in awarding Hertz the Rumford Medal of The Royal Society [Sar06]. Hertz simplified Maxwell's equation similarly to Heaviside. However, he did not use a vector form; hence, he had 12 expressions instead of the famous four-equation set. Nevertheless, Hertz himself recognized the priority of Heaviside [Nah02]. Hertz's work critically impacted the spread and understanding of electromagnetism.

His experiments [Poz12] proved that electromagnetic waves (called "Hertzian waves" until the 1910s) existed, and they have a finite velocity. Moreover, other predicted behaviors, such as refraction and polarization, were also confirmed. The setup was somewhat crude, but the frequency of the received signal was around 50 MHz (A photograph of the original apparatus exists, although it was taken 15 years later [Bry98]). Note that working with such high frequencies implied significant complexity, but it was mandatory for Hertz due to space and device constraints [Lee04]. This pioneering system was notably power-hungry, as the signal at the receiver must have enough power to produce a visible spark in a little gap between conductors. Spark-gap transmitters were born as electromagnetic wave generators.

1.1.4 The many fathers of the 1901 radio

Soon, many visionaries saw applications to electromagnetic waves [Sar06] despite the lack of adequate detectors. **Richard Threlfall** and **Alexander Pelham Trotter** proposed similar methods of placing a spark gap transmitter in lighthouses; ships could "see" it by Geissler tubes even in poor visibility conditions [Süs69]. However, no one was close to the imagination of **William Crookes** [Cro92]. Some of his claims might not be too realistic, but he was quite accurate in other aspects. For example, his analysis of the critical obstacles to overcome: communications need "more delicate receivers" and better ways to generate and direct the waves, *i.e.*, better devices to improve transmitters and receivers.

The first piece to enhance reception had been already discovered and rediscovered several times and for different applications: **Samuel Alfred Varley** (1866), **Lord Rayleigh** (1879), **Hughes** (1879), and **Temistocle Calzecchi Onesti** (1884) implemented similar devices [Süs69]. Finally, **Edouard Branly** (1890) implemented the coherer: an electrical component that would present a very large impedance unless it received a high-frequency signal [Lee04]. It took some years until Branly's technical paper received deserved attention, as physicists hardly ever read engineering journals [Süs69]. Lodge called it "coherer," although Branly did not like the name, preferring the term "radio conductor" [Phi80]. The coherer was a staple in reception until 1902.

Who sent the first message by "Hertzian waves" is controversial. On the one hand, **Lodge** demonstrated the transmission of signals through walls in 1894 during a commemoration of Hertz [Lod94]. The title, "The Work of Hertz and some of his successors," reflects the expectations of British maxwellians. However, Lodge's demonstration was focused on the theory instead of the application—some argue that Lodge employing a galvanometer instead of a telegraph receiver proves he did not think of that use.

On the other hand, **Guglielmo Marconi**—who just wanted an "invisible line" to replace wires for commercial intent—was unambiguous in his application to telegraph in his first experiment (1896), using **Augusto Righi**'s spark transmitter [Rig04], a version of the Branly and Lodge coherer. Marconi had a very different background from the rest of radio pioneers. He was from a wealthy Italian family, providing him substantial contacts and support. The general public associates his name with wireless and radio,

although he mostly used others' work (not always referencing the source). Nevertheless, his work gave significant publicity to wireless interest for the new century.

The dispute for priority is a complex and exciting topic that involves many details, interests, and arguments [Hon01]. Moreover, other names may deserve a place in the contest. One of them is **Aleksandr Stepanovich Popov**. His work was based on Lodge's advances, and he made a public demonstration in 1896 (three months before Marconi). However, there is significant confusion about the capabilities of his apparatus due to Popov's words just two months before [Huu03]. Again, politics—much later, URSS wanted to revindicate the radio as a Russian invention—and technical similarities with Marconi's work do not help to clarify the facts. In all likelihood, his prototype could not transmit intelligence before Marconi's exhibition in 1896 [Süs62].

Another name is **Nikola Tesla**. He was exceptionally prolific; notwithstanding, his significant contributions to wireless communications are historically neglected, and many of his inventions were "reinvented" by others without referencing him [Sar06], a striking contrast to Marconi's recognition. As soon as 1893, he gave some lectures worldwide, demonstrating that wireless power was possible—his expositions were in dark rooms illuminated by wirelessly powered vacuum lamps [Hon01]. In 1898, he exhibited a radio-controlled boat that did not require a line of vision to operate (even British maxwellians saw electromagnetic waves as rays analogous to light).

In 1892, Tesla had been experimenting with producing high-frequency and high-voltage signals (apparatus later known as "Tesla coils" and widely employed). However, his great stroke of genius was using two tuned circuits in reception and transmission to enable the generation of much more powerful RF signals [Sar06]. The authorship is typically—and erroneously—given to Marconi due to his famous "four seven's" patent. However, Tesla's patent (1897) predates Marconi's (1900).

However, Marconi's system advance seems to have "borrowed" [Sar06] some ideas from **Karl Ferdinand Braun**—inventor also of the phased array antenna (1905) and metal-mineral unilateral conduction (1874), a predecessor of the diode. Contrary to Marconi, Braun avoided publicity and saw his work in terms of scientific advancements. Ironically, they shared a Nobel Prize in 1909 for their contributions to the development of wireless telegraphy.

Finally, in 1901, **Marconi** succeeded in wirelessly sending a message across the Atlantic with an apparatus that included the inventions of **Tesla**, **Braun**, and **Lodge**. Besides, the advice and designs of **John Ambrose Fleming** were critical for the success [Hon01]. Despite the questionable authorship, there is no doubt that Marconi caught the public's attention, showing the great interest and potential applications of wireless communication.

Sadly, this milestone also implied the end of **Tesla**'s most ambitious project: The World Telegraphy [Tes78]. He wanted to use the Earth's resonance frequencies to transmit large distances—first messages, then power. His predicted frequencies were close to the real ones (discovered in the 1960s [Sar06]), and his proposed designs were significantly close to ELF (extremely low frequency) propagation. He started in 1900—which is said to have hastened Marconi's plans of transatlantic communication. However, after the 1901 demonstration, investors lost their interest in favor of simpler devices like Marconi's apparatus.

Nevertheless, Tesla had his *vendetta* in 1943. After a long dispute (delivery was after the death of both), the United States Supreme Court gave priority to a patent of **Teslas**'s circuit—also, to works of **Braun** and **Lodge**—over **Marconi**'s radio. This sentence did not address who invented the radio—a complex and controversial question still in our days[Lee04]. Still, it helped restore credit to some forgotten contributors since then [Sar06].

1.1.5 The radio we know

The coherer enabled previous systems, even transatlantic wireless communication, but their performance was less than ideal. Any electromagnetic event can trigger it without any distinction between signal and noise. Also, coherers require a mechanical reset—they are digital: pulse or no pulse. On top of that, their sensitivity was not enough.

Similar devices appeared. As is the case of the so-called "Italian Navy Coherer", exchanged in 1901 by the Italian army with Marconi—who was allowed to patented under his name [Bla26], being typically attributed to **Luigi Solari** [Hon01]. It was one of the coherers employed in his experiment of that year.

Experimenters were losing their heads in the search for better detectors. The attempt of **Archie Frederick Collins** is probably the best example of the desperate pursuit. He theorized that weather predictions by "bad old legs" were the brain detecting electromagnetic waves caused by storms. Thus, he used (human) brain tissue as an improved—and macabre—coherer. In the article of 1902 [Col02], Collins poses in a photograph listening to electromagnetic waves with his brainy apparatus. Fortunately, nothing came from those macabre studies.

Ernest Rutherford—better known later for his atomic model—had experimented in 1895 with a magnetic detector to measure electromagnetic waves [Bla26]. At some point, **Marconi** became aware and saw promising enough to patent two devices in 1902. They tend to be remembered as Marconi's "hysteresis detectors," but early mentions cite them as "Rutherford-Marconi Magnetic detector", and Rutherford claimed to be the inventor of this particular method [Sar06]. Contrary to coherers, this kind of detector could respond to amplitude-modulated (AM) signals, although not as well as a rectifier detector.

Jagadish Chandra Bose—who had been working from 1895 to 1900 with microwaves up to 60 GHz before realizing that no one was able to replicate his delicate setup [Sar06]—applied a patent for the first point-contact crystal (galena) detector in 1901. It seems to be the first semiconductor detector [Lee04]. These detectors follow the intuition of coherer working due to an intriguing imperfect contact; thus, the new system was implemented as a small wire (the "catwhisker") point contacting a crystal surface. It worked similarly to a Schottky diode, although measurements show discrepancies [Lee04]. However, it was a crude rectifier and the inspiration of the symbol typically used for diodes. In 1906, patents from **Henry Harrison Chase Dunwoody** and **Greenleaf Whittier Pickar** protected similar devices but using carborundum [Tha83] and silicon, respectively. Pickard did not stop there and reported in 1919 having tried at least 31,250 pairs of wire-crystal [Pic19].

Unlike coherers, crystal radios do not require a reset after each reception; thus, they can demodulate AM signals. Soon, better detectors would appear without the problematic contact: the pressure of the catwhisker over the crystal must be very light and precise to operate; thus, readjusting was common, although carborundum detector were more

stables. However, they have maintained (decreasing) niches as they are cheap, can be homemade and portable, and, in some cases, can operate without a power source.

Reginald Aubrey Fessenden was never satisfied with coherers and had already started his search in 1892 [Süs69]. He was convinced that being constantly receptive—no mechanical resets—was mandatory for an adequate detector. He tried dozens of methods until attaining the barretter in 1903. Its operation was unclear, but it would be the standard of sensitivity for a decade. No better claim of its interest is the many infringements of his patent. Fessenden also conceived the heterodyne principle before even the vacuum tube, and he made it work with what was available [Sar06].

Those achievements were only half of his plan [Fes08]. The second part was implementing continuous wave (CW) transmitters. Marconi, Fleming, and many others—almost everyone but Fessenden—thought of Fessenden's attempt as a useless effort. In their mind, the spark was needed due to the so-called whip-lash theory. However, he was right.

Fessenden experimented with **Valdemar Poulsen**'s arc transmitters, based on Thomson's works. However, the device had a pretty unpleasant tendency to explode during the initialization of the arc. In 1904, Fessenden contacted General Electric (GE) Company to order an HF alternator (50–100 kHz). GE engineers under **Ernst Alexanderson** struggled for two years and delivered their best effort (September 1906). A letter signed by the engineering team stated the technology could not operate above 10 kHz. Fessenden took it personally and—as usual—obsessively worked on rebuilding the prototype. By November 1906, he had a working 50–88 kHz alternator. Fessenden later improved its output power to 50 kW. GE Company rose it to 200 kW as the "Alexanderson alternator"; however, incoming technologies soon superseded it.

Finally, **Fessenden** had all the pieces together. Thus, for Christmas Eve 1906, he made the first transmission of a recording (Handel's Largo) and live music, himself playing a Christmas carol with his violin—and singing the last chorus. That first voice-over-radio transmission ended with a Christmas greeting and asking for reports from anyone who would have listened—those using receivers without the need for a reset, *i.e.*, compatible with AM signals. In the words of his assistant: "One can well imagine the feelings of surprise of the lonely ship operators, accustomed to the cold colorless dash and dot of the Morse code, when music suddenly burst upon their ears, to be followed by

understandable speech." [Kin32]. Needless to say, they received many letters from intrigued ship operators all over the North Atlantic.

Sadly, Fessenden did not receive the deserved credit for his invention in life. He even lost control of his patents; he is thought to have produced more than 500 despite being a lone wolf (and hard to work with). Ironically, historians have made him one of the greatest forgotten in the history of radio. Until recently, he had no entry in the Canadian Encyclopedia despite being born in Canada [Sar06].

1.1.6 Once upon a time there was a triode

In the 1880s, **Edison** was trying to improve the life of those first electric lamps. After some time, bulbs suffer from darkening due to soot accumulation. They observed that the crystal was clearer closer to the negative side of the filament. Thus, they added an additional metallic plate to absorb the carbon there instead of going to the glass. However, they found something surprising (1883): a small current would flow from the filament to the electrode if the former were at a higher voltage; otherwise, there would be no current. The "Edison effect" became a curiosity in the scientific community. Probably because of the small currents, Edison failed to see the applications of his rectifier. Nevertheless, he patented it in 1883, considered the first electronic (not electric) patented device. Many researchers, such as **Edwin J. Houston**, **William Spottiswoode**, and **Preece**, were interested in the topic [Hon01].

Fleming also noticed a strange "molecular shadow" and studied it in 1883–1894 [Fle85; Fle95]. Around 1896, the community's excitement changed towards the novel X-rays and natural radioactivity. However, Fleming would remember it again when he found the necessity of RF rectifiers for his work in Marconi's company. That was the basis of the Fleming valve (1905). Those first valves had some issues: they were power hungry, had a poor lifetime, and the comparison with the competence—barreters or crystal detectors—was not good.

Nonetheless, **Lee de Forest** entered the scene. De Forest had probably the most turbulent and controversial career among the radio pioneers, which is not a minor deal. According to him, he made and lost four fortunes. In 1906, he was just saved from

bankruptcy thanks to the legitimate discovery of the carborundum detector; Dunwoody did the work as his consultant. This legitimate success allows him to pay the expenses of **Fessenden**'s infringement suit after the blatant copy of the barreter—he just shaped the contact wire as a spade and called it a day. Moreover, it seems that **Dunwoody** did not receive his payment. Before the end of the year, de Forest announced his novel invention: the audion [Lee04].

Fleming expected someone to implement a similar device eventually; still, de Forest undermined Fleming's contribution—"a laboratory curiosity" (1907), while the audion was "Aladdin's lamp of our new world" (his own words on the first page of his not so-humble autobiography, "The Father of radio"). A not-too-cordial exchange of publications on The Electrician 1906–1907 ignited a lifelong animosity between two men with already opposed commercial interests [Hon01]. In the last de Forest iteration, the audion is a Fleming valve with a zigzag wire electrode (the grid) between filament and plate, a triode. There is significant evidence of him finding that composition after trying different ways of placing additional electrodes—sometimes even outside of the valve—to call the device of his, avoiding Fleming's patent [Lee04]. However, the information and declarations from the first years of audion are confusing.

In any case, de Forest's company (funded in 1906) went bankrupt, and de Forest almost went to prison for fraud. He avoided jail by allowing a reorganization of the company (without him) and relinquishing his patents, all but the audion (lawyers saw it worthless). As the last piece remaining of a former vast treasure, de Forest tried occasionally to improve his device. Eventually, he discovered its amplification capabilities; although they were limited to small signals, otherwise, it would produce significant noise and a weird blue glow. On top of that, reproducibility and durability were far from optimal.

Audions were largely forgotten until 1911. Previous experiences as Tesla's assistant inspired **Fritz Lowenstein** to test the audion in the laboratory of **John Hays Hammond Jr**. Lowenstein expected that the audion had some useful characteristics for his project: a guide system for torpedoes. As a secondary result, Lowenstein obtained a surprising-clear amplifier for long-distance telephone signals [Ham57]. A few months later, one of Lowestein's assistants, **Benjamin F. Miessner**, perceived a howling sound in the device. A close inspection reconfirmed the old saying: "If you want an oscillator, try designing

an amplifier." From that revelation, they produced an efficient oscillator for wireless telephony [Ham57].

Somehow, before long, **de Forest** managed to design his own systems. He could not remove that "annoying" howling sound, but it worked, and he managed to impress **John Stone Stone** and the American Telephone and Telegraph (AT&T) [Ham57]. De Forest rose again thanks to the consequent contract [Hon01].

Lowenstein did not patent his advances, but his amplifier was noticed in GE, more precisely, by **Alexanderson**, who then informed **Irving Langmuir**. Langmuir found that the erratic behavior of audions was due to the ionization of residual gases inside the bulb. This way, the vacuum valves were born.

A young engineer—21-year-old **Edwin Howard Armstrong**—invented the regenerative amplifier/detector in 1913. He attained high gain and selectivity while demodulating the signal with few components [Arm14]. In addition to that, when the output is connected to the input, the circuit becomes a very compact RF oscillator [Arm15]—**Alexander Meissner** independently achieved a similar circuit in Europe at the same time; hence, sometimes the topology is called the Meissner oscillator. Arsmtrong's success caused a bitter and long feud with de Forest and many legal disputes (some with incomprehensible sentences) [Hon01].

Just a few years later, in 1917, **Armstrong** evolved **Fessenden**'s heterodyne principle into the superheterodyne receiver. Instead of a direct demodulation, the system downconverts RF to an intermediate frequency (IF), which is then demodulated. This method improved the sensibility of receivers to unexpected levels—transmitters required one order of magnitude less power. Today, almost all modern receivers still use superheterodyne reception or a variant (Section 2.1).

1.1.7 The age of silicon

Electronic advances exploded during the two following decades. The World War I forced a significant improvement of vacuum tubes, and many clever circuits appeared to challenge the dominance of Armstrong's regenerative receiver: the tuned radio-frequency receiver, the reflex circuit, the superregenerator (also Armstrong in 1922), the differential pair (or "long-tailed" pair), the push-pull amplifier or oscillators such

as Hartley's, dynatron, Colpitts... Many remain in use today and have been adapted to solid-state technologies.

Circuit theory needed to evolve to keep pace with new devices and applications. Countless researchers contribute to developing new tools for designers [Bel62]. The understanding of electronic filters and networks made significant advances with the work of **George Ashley Campbell**, **Otto Julius Zobel**, **Wilhelm Cauer**, and many others. **Hans Ferdinand Mayer** and **Edward Lawry Norton** independently derived (Mayer-) Norton's theorem in 1926. **Jacob Millman** proved his theorem in 1940. A significant step for polyphase filters (and systems) is the contribution of **Charles Legeyt Fortescue** in 1918. He presented the bases of n-phase circuits and decomposition in symmetrical components [For18].

A bit later, **Harold Stephen Black** solved a critical issue of amplifiers: a negative feedback loop can scarify some gain to reduce distortion and enlarge bandwidth in 1927. His publication in 1934 [Bla34] (reprinted by IEEE in 1984 and 1999) is a classical reference. **Harry Nyquist** and **Hendrik Wade Bode** studied stability in that decade and introduced theory and tools for analyzing linear systems—such as Bode plots. Their contribution was critical to attaining stable amplifiers. Another example of theory developments to more complex circuits is the phase-locked loop (PLL) by **David Robertson** (1925) and **Henri de Bellescize** (1932). The invention of the radar, operational amplifiers, and the first digital computers before or during World War II clearly prove how fast electronics progressed.

Also, in those years, information theory was born. **Nyquist** (1924) [Nyq24] and **Ralph V. L. Hartley** (1928) [Har28] laid the foundations for the brilliant work of **Claude Shannon** (1948): "A Mathematical Theory of Communication." Information Theory has helped to develop countless knowledge fields since its creation.

Communication theory also had notable improvements. A series of studies—**Alfred Marshall Mayer** (1871–1875), **John William Strutt** (also known as Lord Rayleigh, 1894), and **Carl Englund** (1914–1916)—culminated in **John Renshaw Carson**'s invention, the SSB (Single Side-Band) modulation (1915). The deployment of a communication system with this optimization of the AM spectrum was as soon as 1918. Moreover, **Hartley** (1928) and **Donald K Weaver** (1956) devised receiver structures for SSB reception (see Section 2.1.3). Similar reasons led **Armstrong** to develop frequency

modulation (FM) in 1936. Henceforward, the majority of the most known modulations made their appearance. The new communication systems also included many brilliant ideas, such as the frequency-hopping spread spectrum (1947) of **George Anheuil** and **Hedy Lamarr** (the Hollywood star had a not-typically-know but exciting life out of the screen).

The vacuum tubes became more complex and acquired additional functionalities. As soon as 1914, **Eric Tigerstedt** modified the geometry to improve collection. **John Milton Miller** discovered the Miller effect (1919), explaining the tendency to oscillate of the first designs. First **Walter Hans Schottky** (1916) and later, **Albert Hull** and **Neal Hooker Williams** (1918) patented different versions of the tetrode, followed by **Gilles Holst** and **Bernardus Dominicus Hubertus Tellegen** inventing the pentode (1926). The vacuum tube technology started to show some limitations due to their basic principles. Thus, researchers and investors took an interest in developing other technologies.

Semiconductors have been known since 1833, and they had moderate use in communications since 1906 (crystal radios). In those first years, **Oleg Losev** is a unique case. He built solid-state receivers (without triodes!) in the 1920s because he had no access to vacuum tubes (they were too expensive around those years in Russia). He made fascinating studies until his demise in the siege of Leningrad: he refused to leave the city because he was conducting some "promising experiments with silicon" [Lee04]. Nevertheless, the development of the transistor started with the analysis of band theory by **Alan Wilson** (1931–1932). It took until 1938 to produce the first model metal-semiconductor, although the milestone was almost simultaneously reached by three researchers: **Schottky**, **Boris Davydov**, and **Nevil Mott**.

In December 1947, **William Shockley**'s team in the Bell Labs—**John Bardeen** and **Walter Brattain**—invented the first point-contact transistor. Excluded from the patent, Shockley isolated himself to work in a new transistor type based on **Russel Ohl**'s works from 1940. In January 1948, **Shockley** conceived the bipolar-junction transistor (BJT). However, the prototype failed to achieve the expected performance and was impractical for mass production. Fortunately, **Gordon Kidd Teal** was much more optimistic than management and developed—with little support—the crystal-growing technique, overcoming one of the main obstacles for BJTs. **Morgan Sparks** used the method to

produce the second generation of BJT (announced in 1951 by Bell Labs). These devices were far superior to point-contact transistors and demonstrated the potential of semiconductors versus vacuum tubes. In the following years, **William Pfann** and **Henry Theurer** (1951) and **Charles Lee** and **Morris Tanenbaum** (1954) significantly improved the performance and mass production potential.

Around that time, the field-effect transistor (FET) appeared. **Julius Edgar Lilienfeld** (1926) and **Oskar Heil** (1934) thought the first concepts; however, their fabrication was impossible yet. **Shockley** presented a new theory in 1952, and the following year, **George Clement Dacey** and **Ian Munro Ross** built the first JFET (1953). Seven years later, **Dawon Kahng** and **John Attala** produced the first working MOSFET, and after a similar period, **Frank Wanlass** (1966) implemented the CMOS.

The second half of the century exhibited the consequences of increasingly compact electronic circuits, enabling an impressive evolution of digital and informatic systems. The path to integrated circuits (IC) began in 1955 with the works of **Jules Andrus** and **Walter Bond** (photolithography) and **Carl Frosch** and **Lincoln Derick** (oxide masking). In 1958, **Jack Kilby** proved the viability of producing integrated circuits (oscillator and amplifier); however, those crude solid circuits required gold "flying wires" to connect the separate devices. It is not hard to suppose that was far from ideal for mass production. The solution came from **Robert Noyce** almost by accident. Company lawyers asked Noyce to find an application for **Jean Hoerni**'s planar manufacturing (1959).

Consequently, the first monolithic IC was built in 1959. It took a short time for the first integrated MOS (1964) and computer-aided design tools specific to IC (1966). It was in 1965 when **Gordon Moore**, co-founder of Fairchild Semiconductor, enunciated the prediction that would be remembered as the "Moore's law." Still today, the number of components keeps growing exponentially with the years, seeding new technological advances for the future.

1.2 Motivation

The history of electronic communications proves the massive impact of components on system performance (in addition to the inherent complexity of wireless transmissions). The vast majority of advances are "born," and the attempts focus on understanding

the basic principles and applications. Then, the infancy stage arrives, and the first working devices are employed. Sometimes, the improvement in this phase is even revolutionary despite a suboptimal performance. Their true potential, however, is not reached until their maturity, when they are not only functioning but also optimal in their performance.

1.2.1 Issues and opportunities of a continual evolution

The continuous downsizing of technological nodes implies an implicit improvement in the performance of designs. At the same time, it also means incessant work to adapt the circuits to the new technological canvas—a blessing and a curse for enthusiasts of this field. The same circuit implemented in more modern technology is expected to have fewer parasitics and more accurate component values. Overall, it should aim for better performance. In addition, software and hardware development has enabled much more powerful simulation programs and tools. Thus, designers can work with device models significantly more complex than those manageable by traditional "pencil and paper" approaches. Fortunately, smaller sizing worsens non-ideal effects.

Nevertheless, it can become a trap for designers. In the race against time to produce designs, we might forget the more traditional (and time-costly) method of analysis and synthesis. Sometimes, waiting is worthwhile. Not only does this process avoid the usual risks of trial-and-error methods, but it is also necessary for circuits to reach the stage of true maturity and harness the opportunities offered by technological progress. In addition to the decrease in size, the evolution of technological nodes implies new trade-offs, new possibilities, and more accurate devices.

Even for standard CMOS technologies, there are *a*) specialized variants focusing on particular applications (*e.g.*, high/low power or RF) and *b*) specialized devices that might be included if needed at the cost of additional masks and the corresponding fabrication steps. These options add to unconventional—and more expensive—technologies, such as SOI, BiCMOS, or SiGe, that present specific performance boosts. It must not be forgotten that technology usually provides different ways to implement a circuit element; each has its pros and cons.

Innovation may also bring new opportunities in the form of renewed devices and topologies that could not previously meet given specifications. Modern (integrated) low-noise amplifiers (LNAs) are a remarkable example. They can be divided *grosso modo* into two families, depending on whether they employ inductors. On the one hand, historically, LNAs with inductors have had issues as the integrated-inductor quality was very poor. Consequently, limitations on inductors translate into constrained specifications. As a result, their use was restricted to microwave designs, where no alternative existed. However, as technology improves, inductors also do, and this kind of LNA has become practical for a wider frequency range.

In contrast, inductorless LNAs were typically limited to relatively low frequencies or when inductors were unavailable. The maximum cut-off frequency of their low-pass behavior is tied to the parasitic capacitances of transistors and resistors. As the technologies improve, those non-idealities decrease; hence, the working frequency range grows to higher frequencies. Technological evolution makes inductorless LNAs a promising option for previously problematic frequencies. As both families widen their operation range, their boundaries become more blurred. Applications restricted to one of the LNA types might now find better performance with the other, or at least an available alternative. In short, the trade-offs may change.

Ultimately, the integration scale reduction might cause the previously overlooked effects to become critical factors. Consequently, more sophisticated simulation models are required to provide the accuracy needed to characterize and analyze the circuits. A notable change happens in the operation region of MOS. In the past, they were invariably biased into strong inversion to amplify, corresponding to the well-known equations. However, an analysis of a recent design will probably find equivalent transistors working—often inadvertently—in moderate or weak inversion; this could be a need for supply voltages as low as 1.2 V or even less. In such cases, the model exhibits a more complex behavior than usual [Tsi11], and simulations can provide a more detailed insight.

In this context, my work over these years has been focused on optimization and design methodologies that combine the advantages of more classical design and synthesis with the powerful simulation tools we have available. In other words, the objective is to benefit from the quickness and accuracy of simulation models while addressing the

old fundamental questions that designers face: is further improvement possible? At what cost?

1.2.2 Research and thesis context

The reference scenario for the methodologies is a project aimed at checking the feasibility of designing a Remote Antenna Unit (RAU) in a standard CMOS technology, in contrast to more expensive ones such as [Ko12] and [Ton19]. RAUs are the fundamental components of a distributed antenna system (DAS).

Typically, the base station (BS) is the element that provides wireless connectivity—from the client to BS (uplink) and vice versa (downlink)—to a region and serves as the link to the outside. The antenna is located on or adjacent to the BS and must have enough range to cover the entire region of interest. This approach has a clear disadvantage in complex environments, such as a house or factory, as the coverage will not be homogeneous due to inevitable obstacles. There will be areas where connectivity is low or non-existent, and signals will leak outside the area of interest, causing interference to neighbors and posing a security risk.

A DAS strategy mitigates these issues by replacing the antenna with multiple RAUs distributed throughout the area of interest. The DAS approach creates a series of picocells that provide more homogeneous coverage and greater control over the connectivity or critical zones. Note that this method also enables frequency reuse techniques between non-overlapping picocells. Thus, DASs are particularly useful for ensuring connectivity in areas of high data traffic demand, such as IoT applications or Industry 5.0 [Asl20].

The evolution of optical fibers encourages techniques such as the Radio over Fiber (RoF) technique [Lim19]. This kind of optical link is promising for DASs to establish high-capacity channels between a BS and several RAUs without interfering with each other. Therefore, the RAUs must convert between optical and antenna signals. Depending on which functions the BS delegates to the RAU, there are three types of RoF schemes [Par20], shown in Figure 1.3.

In a Baseband over Fiber (BBoF) scheme, the RAU (Figure 1.3a) communicates with the BS in the baseband (BB) frequency range. Therefore, the RAU acts as an entire BB-to-RF

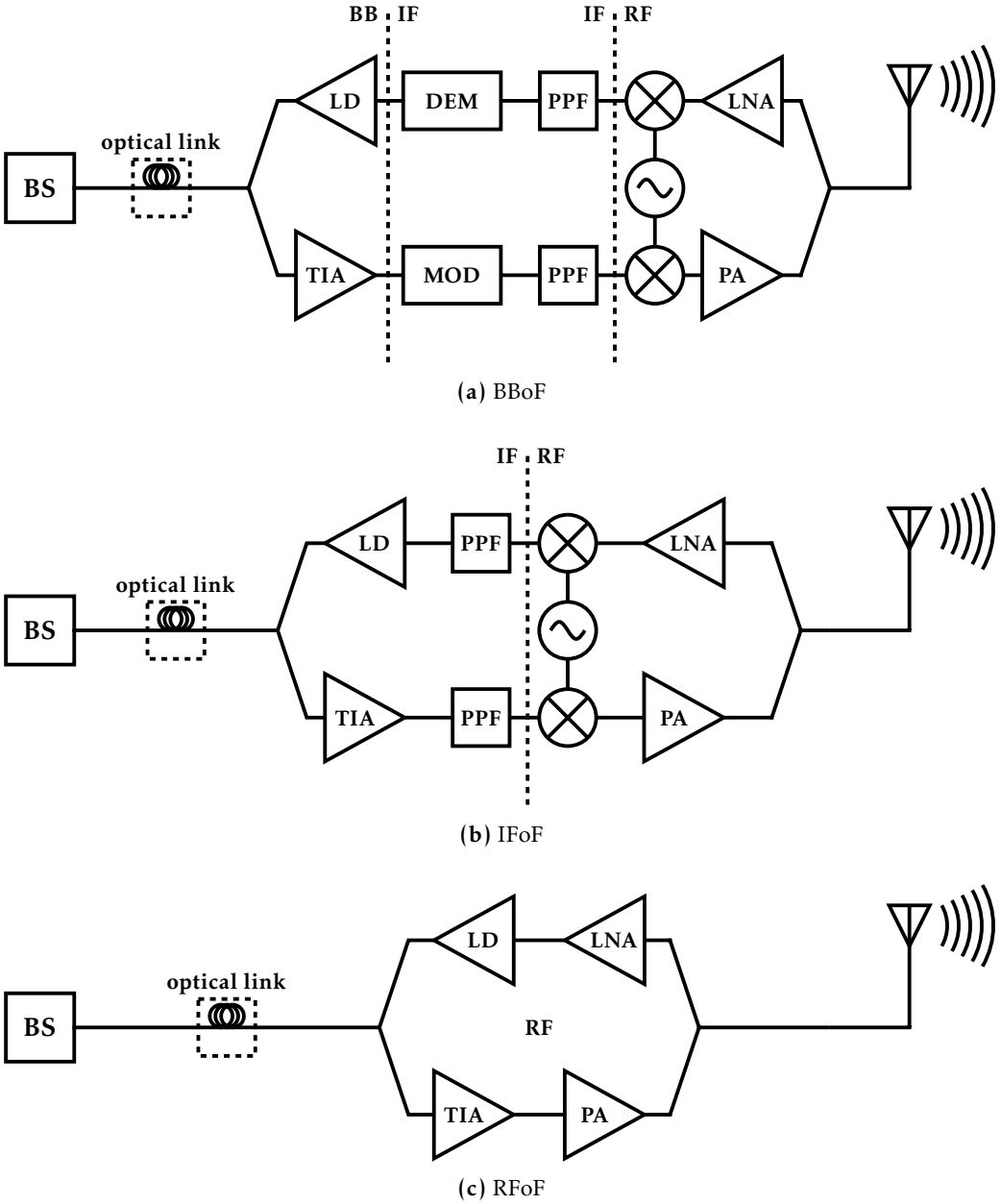

(a) BBoF

(b) IFoF

(c) RFoF

Figure 1.3: Different radio-over-fiber RAU approaches.

receiver for the uplink, downconverting an antenna signal and demodulating it before transmitting it to BS through the optical channel. The received optical signal must be modulated and upconverted for the downlink before being sent to the antenna. In other words, the RAU requires as many devices as a full transceiver.

The opposite strategy is to send an RF signal over fiber (RFoF). In this case, the RAU (Figure 1.3c) is conceptually more straightforward because the same RF signal it receives is transmitted to the other side. However, there is a severe drawback to this alternative. The devices that make up the optical front end must be able to work at

Parameters	BBoF	IFoF	RFoF
Structure complexity	High	Medium	Low
Device requirements	Low	Medium	High
Power consumption	High	Medium	Medium
Overall cost	High	Low	High

Table 1.1: Comparison between radio-over-fiber RAU alternatives.

RF, which significantly complicates this part and makes it more expensive. As a result, what is improved in terms of complexity is made worse regarding device constraints. Similarly, power demands due to working at higher frequencies counteract savings from employing fewer devices.

In between is the option to send the IF signal over fiber (IFoF). In this case, the RAU (Figure 1.3b) implements IF-RF conversion and vice versa, but not the modulation/demodulation. This scheme supposes additional blocks regarding RFoF, but it notably relaxes the circuit specifications of the intermediate blocks and the optical front end. Ultimately, these trade-offs reduce the overall cost compared to BBoF and RFoF, making DAS implementation more promising. Table 1.1 summarizes the pros and cons of the three alternatives.

The optimization methodologies—"maturing" RAU building blocks—are of special interest, as they can clarify whether a conventional CMOS technology can meet the specifications. Also, deep knowledge of these blocks could provide the opposite perspective and establish the requirements that the technology must satisfy to implement an RAU with desired specifications. Thus, they could identify which technologies are valid for the project beforehand instead of evaluating a single one.

The research done during the PhD program focused on the electronic front-end and frequency converter, specifically, the LNA, the mixer stage, and the PPF blocks. However, there were also collaborations on the optical front end [Roy18a; Roy19; Roy18b; Par23a; Par23b].

Inductorless LNA topologies are typically based on two halves that must be balanced

for high performance. It is not possible to optimize the entire circuit without simultaneously modifying both halves to maintain the equilibrium. Therefore, a methodology has been proposed to graphically represent the specifications in a contour map against a variable of each part [Mar22b]. With such information, the design can be improved iteratively without loss. The method has also been refined iteratively, including proposals to significantly improve the robustness of the designs through automatic bias control[Mar21b]. In terms of publications, the LNA has been the most prolific, with one journal article, 6 conferences contributions (5 international), and 6 workshops and forums. In addition, two Bs. and two Ms. thesis were derived from it, which in turn led to 4 contributions to conferences in Greece [Mar22a], Italy [Arc23; Mar23] and Spain [Lóp24].

On the frequency converter side, a study has been published on the effect of non-idealities on different architectures of the mixer stage and the constraints that must be met to perform as intended [Mar21a]. In addition, work has been done to continue this study with the idea of establish a relationship between the specifications of the mixer stage and PPFs separately and together. However, this line of research is still incomplete.

The research on PPFs is presented in this memory. The work in this area is especially appealing for the thesis, as it starts with an analytical study and follows the IC design process until experimental measurements are examined. In addition, our publications on the topic—in a journal [Mar18b] and two congresses [Mar17; Mar18a]—only cover a small part of the final study, so compiling all the published and unpublished material was of particular personal interest too.

1.3 Objetives

In essence, this work aims to study and implement the PPF block. This circuit is crucial to meet transmitter and receiver specifications in most modern communication systems. The apparent simplicity of PPFs is misleading since their performance is not easy to predict a priori, nor is the required number of stages to meet desired specifications.

They are, therefore, a paradoxical case and entirely appropriate for our intent. They are widely employed, and at first sight, they do not have an excessive number of design variables. Nevertheless, the exact calculation of their characteristics can become enormously complex if anything alters the symmetry. Even in the ideal case, accurately estimating the filter bandwidth is difficult [Kau08]. Contrary to other filters, a PPF band pass wider than needed is not harmful—other than the misuse of resources—and PPF performance directly depends on device characteristics, *i.e.*, PPFs passively improve with technological evolution. As a result, they are usually overlooked despite their importance in modern communication systems. Thus, this work aims to provide better quantitative estimations and reveal the relationship between the specifications of devices (resistors and capacitors) and the capabilities a PPF with them can offer.

Moreover, characteristic estimations are of particular interest while designing a PPF. It defines the needed number of filter stages, and it is worth noting that, except for the 2- and 3-stage cases [Kau08], there is little guidance in the literature. Typically, there is no choice but to resort to iterative simulations (even without considering non-idealities). Moreover, in some situations, the feasibility might not be apparent before post-layout simulations, and the design might take much more time because of it.

In short, our study of PPFs has two goals: to understand the impact of non-idealities on it and to perform the complete design process of a PPF, optimizing the method by using what will be learned.

In detail, the analytical study should meet the following requirements:

- It should describe the **effects of the various non-idealities** in the performance. Knowing it is needed to predict achievable filter performance given device characterization. This information is handy in assessing whether a technology can implement the desired system.
- It should pay special attention to those **non-idealities that alter filter balance**. These are the least analyzed in the literature and the most complex. However, they are also responsible for significant changes in the filter response. The main effect that changes in this sense is the mismatch.

- It should be **transparent to the employed technology**. Otherwise, its usefulness would be limited and have little future potential. The work intends to remain helpful for designers as technology evolves.
- Finally, it should cover **the most possible uses and configurations** of a PPF. The usefulness of the analysis is proportional to the cases in which it is valid. Being able to predict the behavior under very specific conditions is not the same as predicting the performance limits in a wide range of scenarios.

In turn, the implementation and design process of the PPF must meet the following requirements:

- It should **fulfill RAU specifications**. More specifically, the proposed application takes Wi-Fi as a reference due to its widespread use. Thus, the PPF must be compatible with IEEE 802.11.
- It should follow a **systematic and comprehensive optimization methodology**. This approach brings two critical advantages: 1) it will identify false optimums, and 2) the same method applied here would provide helpful information in other scenarios.
- It should pay special attention to the **effect of non-idealities** and their impact on the results. Simulations during the design process can provide a second insight into the analysis results, mutually benefiting both main objectives.
- It should cover the **complete design process**, from the schematic stage to the experimental measurements of a prototype. There are two reasons for this: 1) it made useful the work itself within the RAU design project, and 2) different non-idealities appear in each design phase; a reliable performance prediction must cope with all those effects.

1.4 Thesis organization

Chapter 1 begins the thesis with a digest of electronics and wireless communications history. It enumerates the significant milestones from the discovery of electric currents to the implementation of integrated circuits, mentioning the development of electric

communication systems as the technology advanced. This chapter also includes the motivation that drives this work and its context. The objectives and thesis organization are declared at the end of the chapter.

Chapter 2 sets the foundations for the following chapters. The first part focuses on the electronic front-end core of an IFoF RAU: the frequency converter block. The analysis of its operation reveals the interest of a block with the properties of a PPF. Moreover, this section also proposes and compares different transmitter and receiver architectures—analogous to downlink and uplink chains, respectively—that might adapt better to the application. Complex signals are the topic of the second part. It resumes the reasons behind the use of IQ signals and explains the basis and tools for the PPF analysis. Finally, the last section outlines the technology devices that can implement the PPF. It also describes the distinct non-idealities affecting integrated components and how they are modeled.

Chapter 3 analytically describes PPFs and the interaction of the filter with non-idealities. The first part focuses on a formal and intuitive outline of the operation and basic principles of these filters, as well as the main impact of different non-idealities on the filter response. A thorough analysis of performance degradation follows this due to the mismatch. This section starts by finding the worst possible mismatch combination among all possible cases for a 1-stage PPF. Then, that worst case is analyzed for all the five PPF configurations, and a limit is obtained. Moreover, the results are extrapolated to a multi-stage scenario at the end of the section. The last part of the chapter adds additional considerations to the analysis, extending the scenarios in which it remains valid.

Chapter 4 covers the design and optimization process of a PPF. The target specifications are set with the RAU implementation in mind; however, the application and technology are transparent to the proposed methodology, and it can be easily extrapolated to other scenarios. The design focuses on the careful choice of devices, the trade-offs of k_2 selection, and an efficient simulation process to evaluate process and mismatch errors. An alternative k_2-selection method is proposed and compared to the conventional approach during this phase. The suggested strategy can be applied to a broader range of scenarios. Next, the layout is designed, showing different stages of the process to

illustrate the reasoning better. The final section discusses the measurement setup and experimental results.

Chapter 5 draws the final conclusions.

Additional appendixes complete the main content:

- Appendix A includes conclusions translated into Spanish to fulfil a requirement for the doctoral international mention.
- Appendix B describes diverse methods and attempts of wireless electric telegraph before the discovery of electromagnetic waves.
- Appendix C shows the analysis of an ideal one-stage PPF in the different configurations as a reference.
- Appendix D presents the full analysis of the worst-case mismatch combination for a 1-stage PPF. The section details the calculus for each possible PPF configuration.
- Appendix E offers an alternative mismatch decomposition. The terms correspond with the observed effects on the filter response.
- Appendix F develops the mismatch analysis for a combination different from the worst case but interesting for comparison with the results from Chapter 3.
- Appendix G describes a systematic methodology to transform an 8-port network PPF model into a 2-port system. This conversion enables quadrupole techniques to obtain an exact expression for any PPF regardless of the scenario and non-idealities.
- Appendix H presents different tables of capacitors and resistors variations due to mismatch and process.
- Appendix I gathers the list of publications during the doctoral research.

References

[Alb54] A. L. Albert. *Electrical communication, 3rd edition*. John Willey and Sons, 1954.

[Arc23] A. Arcusa-Puente, J. Marqués-García, A. D. Martínez-Pérez, F. Aznar, and S. Celma. "Design approach to CMOS LNA for FR2 band". *24th European Conference on Circuit Theory and Design (ECCTD 2023)*. Torino, Italy, Nov. 2023.

[Arm14] E. H. Armstrong. "Operating features of the audion". *Electrical world* (Dec. 12, 1914), pp. 1149–1152.

[Arm15] E. H. Armstrong. "Some recent developments in the audion receiver". *Proceedings of the Institute of Radio Engineers* 3.3 (1915), pp. 215–238. DOI: 10.1109/JRPROC.1915.216677.

[Asl20] F. Aslam, W. Aimin, M. Li, and K. Ur Rehman. "Innovation in the Era of IoT and Industry 5.0: Absolute innovation management (AIM) framework". *Information* 11.2 (2020). ISSN: 2078-2489. DOI: 10.3390/info11020124.

[Bel62] V. Belevitch. "Summary of the history of circuit theory". *Proceedings of the IRE* 50.5 (1962), pp. 848–855. DOI: 10.1109/JRPROC.1962.288301.

[Bla26] G. G. Blake. *History of radio telegraph and telephony*. Radio Press, 1926.

[Bla34] H. S. Black. "Stabilized feedback amplifiers". *The Bell System Technical Journal* 13.1 (1934), pp. 1–18. DOI: 10.1002/j.1538-7305.1934.tb00652.x.

[Bry98] J. H. Bryant. "Heinrich Hertz's experiments and experimental apparatus: His discovery of radio waves and his delineation of their properties". *Heinrich Hertz: Classical physicist, modern philosopher*. Springer, 1998, pp. 39–58. ISBN: 9789401588553. DOI: 10.1007/978-94-015-8855-3_4.

[Col02] A. F. Collins. "The effects of electric waves on the human brain". *Electrical world and engineer* 39.8 (Feb. 22, 1902), pp. 335–338.

[Cro92] W. Crookes. "Some possibilities of electricity". *Fortnightly Review* (Feb. 1, 1892), pp. 174–176.

[Dol86] A. E. Dolbear. "Bell not the inventor of the speaking telephone". *Scientific American* 54.2 (1886), p. 21.

[Edi75] T. A. Edison. "The discovery of another form of electricity". *Scientific American* 33.26 (Dec. 1875), pp. 400–401.

[Fah99] J. J. Fahie. "Prof. D. E. Hughes's researches in wireless telegraphy". *The Electrician* 43 (May 5, 1899), pp. 40–41.

[Fes08] R. A. Fessenden. "Wireless telephony". *Transactions of the American Institute of Electrical Engineers* 27 (1908), pp. 553–661.

[Fle85] J. A. Fleming. "XVI. On molecular shadows in incandescence lamps". *The London, Edinburgh, and Dublin Philosophical Magazine and Journal of Science* 20.123 (1885), pp. 141–144. DOI: 10.1080/14786448508627735.

[Fle95] J. A. Fleming. "A further examination of the Edison effect in glow lamps". *Proceedings of the Physical Society of London* 14.1 (Oct. 1895), p. 187. DOI: 10.1088/1478-7814/14/1/318.

[For18] C. L. Fortescue. "Method of symmetrical co-ordinates applied to the solution of polyphase networks". *34th annual convention of the American Institute of Electrical Engineers*. AIEE, June 28, 1918, pp. 1027–1140.

[Gra31] S. Gray. "V. A letter to Cromwell Mortimer, M. D. Secr. R. S. containing several experiments concerning electricity by Mr. Stephen Gray". *Philosophical Transactions of the Royal Society of London* 37.417 (1731), pp. 18–44. DOI: 10.1098/rstl.1731.0005.

[Gua19] M. Guarnieri. "Messaging before the Internet - Early electrical telegraphs". *IEEE Industrial Electronics Magazine* 13.1 (2019), pp. 38–53. DOI: 10.1109/MIE.2019.2893466.

[Ham57] J. H. Hammond and E. S. Purington. "A history of some foundations of modern radio-electronic technology". *Proceedings of the IRE* 45.9 (1957), pp. 1191–1208. DOI: 10.1109/JRPROC.1957.278525.

[Har28] R. V. L. Hartley. "Transmission of information". *The Bell System Technical Journal* 7.3 (1928), pp. 535–563. DOI: 10.1002/j.1538-7305.1928.tb01236.x.

[Hea76] O. Heaviside. "XIX. On the extra current". *The London, Edinburgh, and Dublin Philosophical Magazine and Journal of Science* 2.9 (1876), pp. 135–145. DOI: 10.1080/14786447608639176.

[Hea92a] O. Heaviside. *Electromagnetic theory, vol. 1-3*. The Electrician Printing and Publishing Co, 1892–1912. ISBN: 9780828402354.

[Hea92b] O. Heaviside. "XI. On the forces, stresses, and fluxes of energy in the electromagnetic field". *Philosophical Transactions of the Royal Society of London* 183 (1892), pp. 423–480. DOI: 10.1098/rsta.1892.0011.

[Her87] H. Hertz. "On electromagnetic effects produced by electrical disturbances in insulators". *Sitzungsber. d. Berl. Akad. d. Wiss.(10 November 1887)* (1887).

[Hon01] S. Hong. *Wireless: from Marconi's black-box to the audion*. The MIT Press, 2001. ISBN: 0262082985.

[Hou76] E. J. Houston and E. Thomson. "Electrical phenomena. The alleged etheric force, test experiments as to its identity with induced electricity". *Chemical News* 32.857 (Apr. 28, 1876), pp. 173–174.

[Hun05] B. J. Hunt. *The Maxwellians*. Cornell University Press–Ithaca and London, 2005. ISBN: 0801482348.

[Huu03] A. A. Huurdeman. *The worldwide history of telecommunications*. John Wiley and Sons, 2003. ISBN: 9780471205050. DOI: 10.1002/0471722243.

[Joh03] H. Johnson and M. Graham. *High-speed signal propagation: advanced black magic*. Prentice Hall PTR Signal Integrity Library. Prentice Hall PTR, 2003. ISBN: 9780130844088.

[Kau08] J. Kaukovuori, K. Stadius, J. Ryynanen, and K. Halonen. "Analysis and design of passive polyphase filters". *IEEE Transactions on Circuits and Systems I: Regular Papers* 55.10 (Nov. 2008), pp. 3023–3037. DOI: 10.1109/tcsi.2008.917990.

[Kin32] S. Kintner. "Pittsburgh's contributions to radio". *Proceedings of the Institute of Radio Engineers* 20.12 (1932), pp. 1849–1862. DOI: 10.1109/JRPROC.1932.227746.

[Ko12] M. Ko, J.-S. Youn, M.-J. Lee, K.-C. Choi, H. Rucker, and W.-Y. Choi. "Silicon photonics-wireless interface IC for 60-GHz wireless link". *IEEE Photonics Technology Letters* 24.13 (2012), pp. 1112–1114. DOI: 10.1109/LPT.2012.2196034.

[Kul24] M. Kulikova. "Antique hydraulic telegraph: refinement of the data transfer rate in Ancient Greece by an experiment and a mathematical model". *Eurasian Scientific Journal* 1 (2024), pp. 30–33.

[Kul91] P. Kullstam. "Heaviside's operational calculus: Oliver's revenge". *IEEE Transactions on Education* 34.2 (1991), pp. 155–166. DOI: 10.1109/13.81595.

[Lee04] T. H. Lee. *The design of CMOS radio-frequency integrated circuits, 2nd edition*. Cambridge University Press, 2004. ISBN: 0521835399.

[Lim19] C. Lim, Y. Tian, C. Ranaweera, T. A. Nirmalathas, E. Wong, and K.-L. Lee. "Evolution of radio-over-fiber technology". *Journal of Lightwave Technology* 37.6 (2019), pp. 1647–1656. DOI: 10.1109/JLT.2018.2876722.

[Lod94] O. Lodge. *The work of Hertz and some of his successors*. The D. Van Nostrand Company, June 1, 1894.

[Lóp24] G. López-Gómez, F. Aznar, and A. D. Martínez-Pérez. "Diseño y caracterización de amplificador de bajo ruido para banda X en tecnología CMOS 65 nm". *XVI International Conference of Technology, Learning and Teaching of Electronics*. Malaga, Spain: TAEE, June 2024.

[Mar17] A. D. Martinez-Perez, J. Morte, F. Aznar, C. Sanchez-Azqueta, and S. Celma. "Impact of non-idealities on passive polyphase filter performance". *2017 European Conference on Circuit Theory and Design (ECCTD)*. Catania, Italy: IEEE, Sept. 2017. DOI: 10.1109/ecctd.2017.8093256.

[Mar18a] A. D. Martinez-Perez, F. Aznar, G. Royo, C. Sanchez-Azqueta, and S. Celma. "Analysis of the influence of component mismatch on integrated passive polyphase filters". *2018 IEEE International Symposium on Circuits and Systems (ISCAS)*. Fireze, Italy: IEEE, May 2018. DOI: 10.1109/iscas.2018.8351661.

[Mar18b] A. D. Martínez-Pérez, F. Aznar, G. Royo, C. Sánchez-Azqueta, and S. Celma. "Analysis of mismatch impact on image rejection ratio for passive polyphase filters". *International Journal of Circuit Theory and Applications* 46.10 (June 2018), pp. 1838–1847. DOI: 10.1002/cta.2505.

[Mar21a] A. D. Martinez-Perez, F. Aznar, G. Royo, and S. Celma. "Analysis of non-idealities on CMOS passive mixers". *Electronics* 10.9 (2021). ISSN: 2079-9292. DOI: 10.3390/electronics10091105.

[Mar21b] A. D. Martinez-Perez, F. Aznar, G. Royo, P. A. Martinez-Martinez, and S. Celma. "Robust design methodology for RF LNA including corner analysis". *Internacional Conference on Synthesis, Modeling, Analysis and Simulation Methods and Applications to Circuit Design (SMACD)*. Efurt, Germany, July 2021. ISBN: 9783800755882.

[Mar22a] J. Marqués-García, A. Arcusa-Puente, A. D. Martínez-Pérez, and F. Aznar. "Modeling frequency response of gm-boosted inductorless common-gate LNA". *IFIP/IEEE International Conference on Very Large Scale Integration*. Patras, Greece, Oct. 2022.

[Mar22b] A. D. Martinez-Perez, F. Aznar, D. Flandre, and S. Celma. "Design-window methodology for inductorless noise-cancelling CMOS LNAs". *IEEE Access* 10 (2022), pp. 29482–29492. DOI: 10.1109/ACCESS.2022.3158356.

[Mar23] J. Marqués-García, A. D. Martínez-Pérez, F. Aznar, and S. Celma. "An approach to the modeling and design of the gm-boosted common-gate LNA". *24th European Conference on Circuit Theory and Design (ECCTD 2023)*. Torino, Italy, Nov. 2023.

[Max65] J. C. Maxwell. "VIII. A dynamical theory of the electromagnetic field". *Philosophical Transactions of the Royal Society of London* 155 (Jan. 1865), pp. 459–512. DOI: 10.1098/rstl.1865.0008.

[Max73] J. C. Maxwell. *A treatise on electricity and magnetism*. Oxford University Press, 1873.

[Nah02] P. J. Nahin. *Oliver Heaviside: The life, work, and times of an electrical genius of the victorian age, 2nd edition*. John Hopkins University Press, 2002. ISBN: 9780801869099.

[Nyq24] H. Nyquist. "Certain factors affecting telegraph speed". *The Bell System Technical Journal* 3.2 (1924), pp. 324–346. DOI: 10.1002/j.1538-7305.1924.tb01361.x.

[Øer20] J. C. Ørsted. "Experiments on the effect of a current of electricity on the magnetic needle". *Annals of philosophy, or, Magazine of chemistry, mineralogy, mechanics, natural history, agriculture, and the arts* 16.4 (1820), pp. 273–276.

[Par20] D. F. Paredes-Páliz, G. Royo, F. Aznar, C. Aldea, and S. Celma. "Radio over fiber: An alternative broadband network technology for IoT". *Electronics* 9.11 (Oct. 2020). DOI: 10.3390/electronics9111785.

[Par23a] D. F. Paredes-Páliz, A. D. Martinez-Perez, F. Aznar, and S. Celma. "CMOS Linear laser driver for intermediate frequency over fiber (IFoF) links". *Electronics* 12.15 (2023). ISSN: 2079-9292. DOI: 10.3390/electronics12153251.

[Par23b] D. F. Paredes-Páliz, A. D. Martínez-Pérez, F. Aznar, and S. Celma. "Linear laser driver design in 65-nm node CMOS technology for IFoF optical links". *24th European Conference on Circuit Theory and Design (ECCTD 2023)*. Torino, Italy, Nov. 2023.

[Phi80] V. J. Philips. *Early radio wave detectors*. Stevenage, 1980. ISBN: 0906048249.

[Pic19] G. W. Pickard. "How I invented the crystal detector". *Electrical experimenter* 7.4 (Aug. 1919), pp. 325, 360.

[Pol] Polybius. *The Histories*. Vol. 10, pp. 44–45.

[Poz12] D. M. Pozar. *Microwave engineering, 4th edition*. Wiley, 2012. ISBN: 9781118213636.

[Raz11] B. Razavi. *RF microelectronics, 2nd edition*. Prentice Hall, 2011. ISBN: 9780137134731.

[Raz17] B. Razavi. *Design of analog CMOS integrated circuits, 2nd edition*. McGraw-Hill Education, 2017. ISBN: 9780072524932.

[Rig04] A. Righi. *Radio*. Nicola Zanichelli, 1904.

[Rob12] S. Roberts. *Distant writing: A history of the telegraph companies in Britain between 1838 and 1868*. 2012. URL: http://distantwriting.co.uk (visited on 08/14/2024).

[Rom01] J. Romeu and A. Elias. "Early proposals of wireless telegraphy in Spain: Francisco Salva Campillo (1751-1828)". *IEEE Antennas and Propagation Society International Symposium*. Vol. 1. 2001, pp. 10–13. DOI: 10.1109/APS.2001.958781.

[Rou81] R. Routledge. *A popular history of Science*. Routledge and Sons, 1881.

[Roy18a] G. Royo, A. D. Martínez-Pérez, C. Sánchez-Azqueta, C. Aldea, and S. Celma. "Low-EVM CMOS transimpedance amplifier for intermediate frequency over fiber". *2018 IEEE International Symposium on Circuits and Systems (ISCAS)*. May 2018. DOI: 10.1109/ISCAS.2018.8351471.

[Roy18b] G. Royo, C. Sánchez-Azqueta, A. D. Martínez-Pérez, C. Aldea, and S. Celma. "Fully-differential transimpedance amplifier for reliable wireless communications". *Microelectronics Reliability* 83 (2018), pp. 25–28. ISSN: 0026-2714. DOI: https://doi.org/10.1016/j.microrel.2018.02.007.

[Roy19] G. Royo, A. D. Martinez-Perez, C. Sanchez-Azqueta, C. Aldea, and S. Celma. "A highly linear low-noise transimpedance amplifier for indoor fiber-wireless remote antenna units". *Electronics* 8.4 (2019). ISSN: 2079-9292. DOI: 10.3390/electronics8040437.

[Sal76] F. Salvá-y-Campillo. "Memoria segunda sobre el galvanismo aplicado a la telegrafía". *Memorias de la Real Academia de Ciencias Naturales y Artes*. 1876, pp. 41–55. DOI: 10.1109/APS.2001.958781.

[Sar06] T. K. Sarkar, R. J. Mailloux, A. A. Oliner, M. Salazar-Palma, and D. L. Sengupta. *History of wireless*. John Wiley and Sons, 2006. ISBN: 0471718149.

[Sta98] T. Standage. *The Victorian Internet: the remarkable story of the telegraph and the nineteenth Century's on-line pioneers*. Walker and company, 1998. ISBN: 0802713424.

[Ste08] C. H. Sterling. *Military communications: From ancient times to the 21st century*. ABC-Clio, 2008. ISBN: 9781851097326.

[Süs62] C. Süsskind. "Popov and the beginnings of radiotelegraphy". *Proceedings of the IRE* 50.10 (1962), pp. 2036–2047. DOI: 10.1109/JRPROC.1962.288232.

[Süs69] C. Süsskind. "The early history of electronics III. Prehistory of radiotelegraphy". *IEEE Spectrum* 6.4 (1969), pp. 69–74. DOI: 10.1109/MSPEC.1969.5214055.

[Tes78] N. Tesla, A. Marinčić, and V. Popović. *Colorado Springs notes, 1899–1900*. Nolit, 1978. ISBN: 8617073527.

[Tha83] D. P. Thackeray. "When tubes beat crystals: early radio detectors". *IEEE Spectrum* 20.3 (1983), pp. 64–69. DOI: 10.1109/MSPEC.1983.6369844.

[Ton19] Y. Tong, C.-W. Chow, G.-H. Chen, C.-W. Peng, C.-H. Yeh, and H. K. Tsang. "Integrated silicon photonics remote radio frontend (RRF) for single-sideband (SSB) millimeter-wave radio-over-fiber (ROF) systems". *IEEE Photonics Journal* 11.2 (2019), pp. 1–8. DOI: 10.1109/JPHOT.2019.2898938.

[Tsi11] Y. Tsividis and C. McAndrew. *Operation and modeling of the MOS transistor*. The Oxford Series in Electrical and Computer Engineering Series. Oxford University Press, 2011. ISBN: 9780195170153.

[Wal98] A. Waldron. *The Great Wall of China: From history to myth*. Cambridge University Press, 1998. ISBN: 052136518X.

[Whi39] F. Whishaw. "Hydraulic telegraph". *The Railway Magazine and Annals of Science*. Vol. 5. 1839, pp. 9–11.

[Yus10] A. P. Yuste. "Francisco Salva's electric telegraph: Scanning our past". *Proceedings of the IEEE* 98.11 (2010), pp. 1974–1977. DOI: 10.1109/JPROC.2010.2068394.

Chapter 2

Theoretical foundations

Any optimization process requires a complete assimilation of the system to improve. Moreover, comprehending the ideas behind the purpose and operation of a circuit is essential to achieving a deep understanding of it. This fact is especially true for devices as particular as polyphase filters. Thus, this chapter focuses on forming the theoretical foundations.

Most modern communication systems employ architectures that benefit from using sets of signals with varying phase offsets—*i.e.*, polyphase signals. Using complex variables enables exciting possibilities to operate with those signals. However, it also supposes additional difficulties to the calculus and analysis in the form of particularities that should be observed.

Another critical point of polyphase filters is the non-idealities that condition their performance. Thus, describing the concrete phenomena and their models for analysis and simulation is crucial to the optimization. Furthermore, phenomena and models are dependent on the devices available in a standard CMOS technology.

Three sections comprise this chapter. Section 2.1 focuses on the transmitter and receiver architectures that are useful for an IFoF RAU implementation. It also reveals the importance of the polyphase filter as a key block inside those structures. Section 2.2 details the benefits and particularities of complex signals—especially IQ signals—and introduces an analytical tool employed in future chapters. Finally, Section 2.3, enumerates the distinct devices in the technology and the different phenomena that could alter them.

2.1 Transceiver architectures

As soon as the interest in wireless communication exploded, the frequency spectrum became a hostile environment full of noise and interferences that threatened the integrity of messages. The famous Shannon-Hartley theorem holds some valuable clues about the issue:

$$C_{ch} = BW \cdot \log_2\left(1 + SNR\right) \tag{2.1}$$

where C_{ch} is channel capacity, BW is the channel bandwidth, and SNR is the signal-to-noise ratio. In other words, the communication in a section of the spectrum is proportional to the power employed (logarithmically), but that power also contributes to other communication noise. Thus, the capacity of the spectrum is finite.

The impulse to transmit more and more data leads to the imposition of more efficient spectrum use and stringent norms that regulate how much power can be emitted out of the desired signal bandwidth. Consequently, several techniques and schemes optimize receiver (RX) and transmitter (TX) architectures.

2.1.1 Frequency converter block

Perhaps the most critical operation for the IFoF RAU is the transformation of IF into RF (upconverting) in the downlink chain and the opposite conversion (RF to IF, downconverting) in the uplink. The most usual way to shift a signal in frequency is by mixing it with a single tone, typically generated by a local oscillator (LO). The building blocks that perform the multiplication are known as mixers. There are several topologies and techniques to implement the operation according to the particular requirements [Raz11].

Analytically and supposing for clarity IF and LO as sinusoidal signals,

$$A_{IF}\sin\left(\omega_{IF}t\right) \cdot A_{LO}\sin\left(\omega_{LO}t\right) = \frac{A_{IF}A_{LO}}{2}\left(\cos\Big(\left(\omega_{LO} - \omega_{IF}\right)t\Big) - \cos\Big(\left(\omega_{LO} + \omega_{IF}\right)t\Big)\right) \tag{2.2}$$

where ω_{IF} and ω_{LO} are the angular frequency of IF and LO signals with $\omega = 2\pi f$, A_{IF} and A_{RF} are their amplitudes, and t corresponds with the time variable. The initial

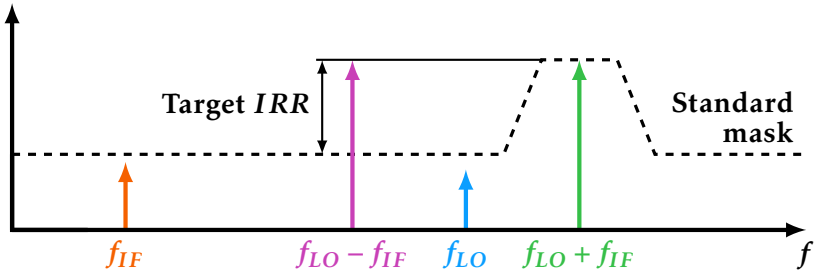

Figure 2.1: Heterodyne signals in the frequency domain: IF (orange), LO (blue), RF (green), and the image (magenta). The dashed black line indicates the emitting power limit imposed by the communication standard. The system should reduce the image by the target IRR to fulfill the standard mask.

phase is considered zero for both signals for simplicity in the expressions. Otherwise, phase offsets are translated into the final trigonometric functions with the same sign as the respective ω.

In other words, the multiplication translates the IF signal from f_{IF} to the desired frequency ($f_{RF1} = f_{LO} + f_{IF}$); however, it also "mirrors" a copy at $f_{RF2} = f_{LO} - f_{IF}$. This undesired signal is the image, and it typically jeopardizes fulfilling the standard mask; otherwise, it would cause interference on other channels. Thus, it must be rejected, suppressed, or prevented. The image rejection ratio (IRR) represents the grade of achievement of this task as the ratio between desired signal power and image power.

If the LO signal is a pure tone—ideally, it should be—, then each frequency from BW_{IF} is independently moved to its respective position in $f_{LO} + f_{IF}$ and $f_{LO} - f_{IF}$. Arbitrarily, the former is considered the desired band, and the latter is the image. Figure 2.1 illustrates this issue. Note that IF and LO signals are less problematic at the output, as they only appear there as leakage due to non-idealities.

A similar occurrence happens in the inverse operation, from RF to IF. Following an analogous development to (2.2),

$$A_{RF}\sin(\omega_{RF}t)\cdot A_{LO}\sin(\omega_{LO}t) = \frac{A_{RF}A_{LO}}{2}\Big(\cos\big((\omega_{RF}-\omega_{LO})t\big) - \cos\big((\omega_{RF}+\omega_{LO})t\big)\Big) \tag{2.3}$$

In this case, distinguishing between RF and LO products is straightforward. They are extremely distant; hence, there is no issue in filtering the undesired. However, another problem exists: for each f_{IR}, two particular frequencies in the RF range produce a

contribution at f_{IR} in combination with f_{LO}. One is the proper RF signal ($f_{IF} + f_{LO}$), and the other is the downconverting image ($f_{LO} - f_{IF}$). Note that frequencies match the ones from (2.2), although input and output—cause and effect—signals are exchanged.

In other words, for a receiver, both the desired RF signal and the image are translated to BW_{IF}. In this case, the image is not an obstacle to fulfilling norms but a significant source of noise and interference obscuring precious information. Image made transmitters culprit and receivers victims. Moreover, as they share BW_{IF}, a passband filter cannot reject the image once they are in the IF range. Thus, the image must be canceled before it is irreversibly combined with desired signal, *e.g.*, by a filter that selects RF and rejects the image. Nevertheless, it could be an issue if $f_{LO} \gg f_{IF}$, as then, desired RF ($f_{LO} + f_{IF}$) signal and image ($f_{LO} - f_{IF}$) are relatively close in frequency.

The IQ signals enable a different approach. Two components—In-phase (I) and Quadrature (Q)—form an IQ signal. Ideally, they have equal amplitude and a phase offset ($\theta_Q - \theta_I$) of 90 degrees ($\pi/2$ radians). A quadrature LO (QLO) is an oscillator that produces an IQ signal, and there are blocks capable of generating an IQ signal from an input one. Supposing that IF and LO are IQ signals and (2.2) corresponds with $\mathrm{IF_I}$ and $\mathrm{LO_I}$ product, then note the difference with $\mathrm{IF_Q}$ and $\mathrm{LO_Q}$ operation,

$$A_{IF}\cos(\omega_{IF}t)\cdot A_{LO}\cos(\omega_{LO}t) = \frac{A_{IF}A_{LO}}{2}\left(\cos\Big((\omega_{LO}-\omega_{IF})\,t\Big)+\cos\Big((\omega_{LO}+\omega_{IF})\,t\Big)\right) \tag{2.4}$$

Both (2.2) and (2.4) results have the same two terms referring to the desired upconverted signal and its image; however, the second term sign is opposed. Thus, one of them can be selected by summing or subtracting both products. This structure is the single-quadrature (SQ) upconversion. Note that a subtraction when using differential signals—recommended in these cases due to noise—is just a sum with exchanged positive and negative connections.

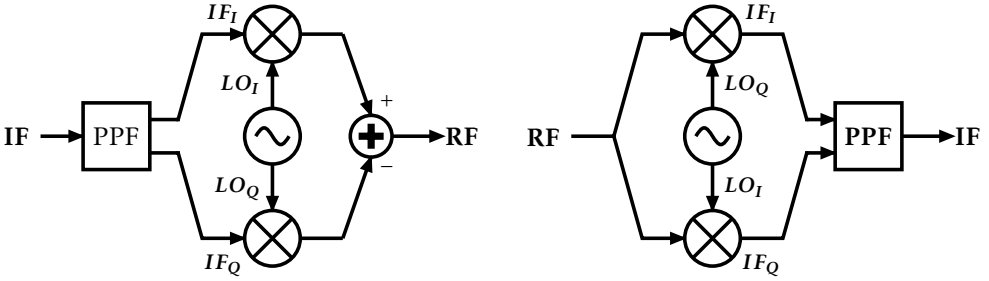

(a) Upconversion **(b)** Downconversion

Figure 2.2: SQ frequency converter schemes.

In downconversion, an equivalent development can be made. If RF-LO_I product results in (2.3), then, RF-LO_Q is

$$A_{RF}\sin(\omega_{RF}t)\cdot A_{LO}\cos(\omega_{LO}t)=\frac{A_{RF}A_{LO}}{2}\left(\sin\Big((\omega_{RF}-\omega_{LO})t\Big)+\sin\Big((\omega_{RF}+\omega_{LO})t\Big)\right) \tag{2.5}$$

Note that $\sin(-x)=-\sin(x)$. Thus, IF IQ signals have a different phase difference (opposite sign in Q component) depending on its origin frequency band, whether it is the RF signal ($f_{RF1}>f_{LO}$) or the image ($f_{RF2}<f_{LO}$). Therefore, a filter based on that distinction can cancel the image even in the IF range. This intent is the origin of the asymmetric networks known as polyphase filters [Gin75]. This thesis focuses on a particular type of those systems, the passive polyphase filters (PPFs), that, according to their configuration, can implement this operation or the IQ generation (Section 3.1.2). Figure 2.2 illustrates block diagrams for upconverting and downconverting with mixers and PPFs.

As usual, when non-idealities enter the scene, errors lead to imperfect image cancellation. Instead, the *IRR* serves as a metric of how successful the scheme is. In most cases, the actual *IRR* values are difficult to predict, as the most impactful errors typically alter system balance. Consequently, expressions become significantly complex; the operation of these circuits relies on symmetry. However, what would we designers do if everything would be easy?

Different strategies exist to cope with those inaccuracies at a diagram block level. For example, a double quadrature (DQ) scheme can correct some of them at the cost of additional devices and complexity [Mar21]. Starting in Figure 2.2a, an extra pair of mixers are included to obtain cross terms (IF_I-LO_Q and IF_Q-LO_I). Their sum produces

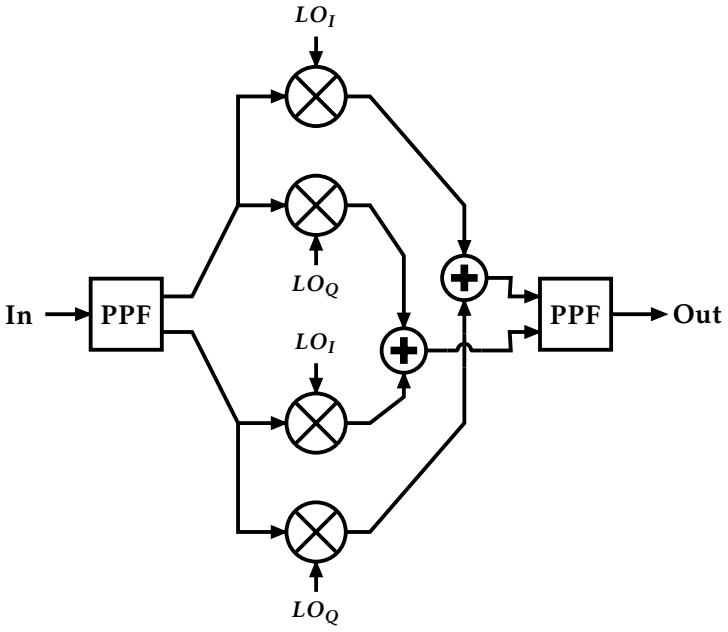

Figure 2.3: DQ frequency conversion scheme.

a quadrature component to the RF signal that a PPF can combine into the final RF. The same scheme achieves the inverse operation, but PPFs exchange their position. In downconversion, the first must work at the RF range, while the second operates in the IF band. Ideally, this structure cancels QLO IQ mismatch and can improve overall performance [Beh01]. The DQ frequency converter diagram is shown in Figure 2.3. Note that PPFs work in this scheme as IQ converters, and they can be removed if following or preceding blocks employ IQ signals.

2.1.2 Transmitter architectures

From the perspective of the RAU electronic front-end, the downlink chain—*i.e.*, transmission from BS to client—is equivalent to a transmitter architecture. It requires the implementation of a frequency upconversion to elevate the IF signal to the RF range before sending it.

A classical superheterodyne approach [Lee04] address this operation with the scheme shown in Figure 2.4. The optical front-end receives the input signal and amplifies it with a transimpedance amplifier (TIA). The TIA converts the electrical current from the detector into a voltage signal. After the TIA, a channel selector filter (CSF) rejects all but the channel bandwidth, removing undesirable harmonics, noise, and DC offset.

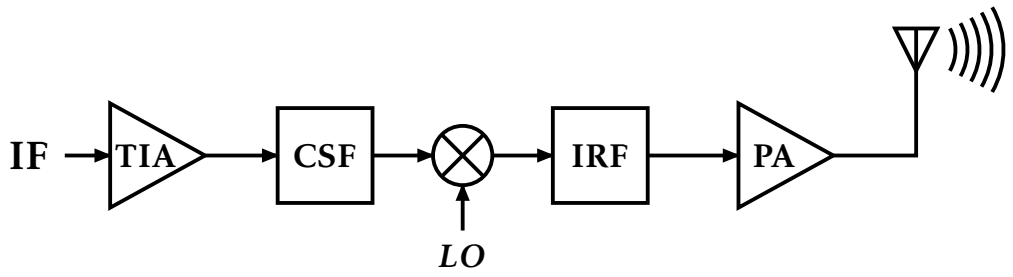

Figure 2.4: Classical superheterodyne TX architecture.

Sometimes, the block might include equalization to cancel the distortion of optical fiber, although it is generally preferred as a preforming before the optical link. Then, the IF signal is multiplied by a LO tone in the mixer to generate the RF signal. A strict filter is mandatory for SSB communication before the power amplifier (PA). The image rejection filter (IRF) must remove the undesired products of the mixer, mainly the image, which has equal power to the desired signal. Between PA and the antenna, additional filters and a matching network are usually needed.

In most approaches, the LO is the element tunable to select the channel. This element typically implements variability more easily without harming performance. It also implies that all IF circuits can be designed with a particular frequency in mind, relaxing the constraints of the most stringent filters.

The main drawback of the superheterodyne transmitter occurs when f_{LO} is much larger than f_{IF}. This relationship is generally desired to ease IF block design. However, under those circumstances, the two replicas in the RF range are very close; hence, IRF must be very selective. Achieving enough IRR to accomplish norm specification might become difficult or even impossible if other relevant conditions worsen the issue (*e.g.*, fully integrating the RAU or covering different communication standards).

The other disadvantage is linked to the power losses. The image comprises half of the output power of the mixer, neglecting some spurious products. Thus, the conversion is far from efficient. The usual solution relies on the PA to achieve the required gain. Consequently, the PA usually employs several stages to achieve the desired amplification, although it tends to become the bottleneck for adequate linearity in the downlink chain.

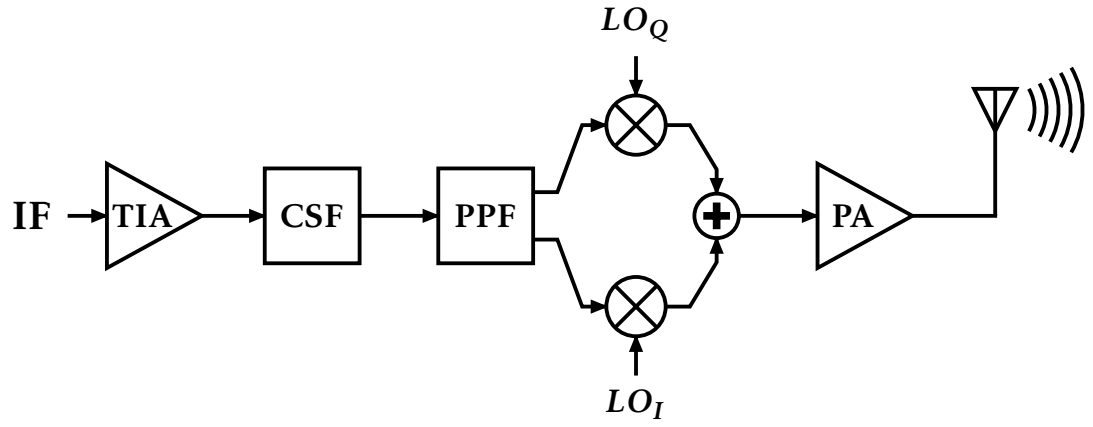

Figure 2.5: SQ SSB TX architecture.

Nevertheless, the long time this scheme has been widely used (see Section 1.1.6) proves its reliability and flexibility to be adapted to different needs even across very distinct technologies.

Moreover, an alternative to improve the conversion power efficiency is employing the upconversion scheme illustrated in Figure 2.2a. This way, the image is not produced, and the mixer stage output is directly the SSB signal. The resultant architecture is the SQ SSB transmitter (see Figure 2.5). It doubles the number of mixers and requires an IQ signal from the LO. This kind of oscillator, a QLO, can be obtained from a special topology that produces I and Q signals or by adding an IQ generator (*e.g.*, a PPF) to the LO output. Besides, specific scenarios may favor schemes that are more robust against non-idealities. In those cases, the system might benefit from using a DQ structure.

In any case, this scheme replaces the IRF with a PPF. Note that, unlike IRF, the PPF is previous in the chain to the mixers. Thus, the change implies that the filter must operate in IF (100 MHz) instead of RF (5 GHz), significantly relaxing the constraints. The substitution is also advantageous to integration. It enables a more compact system and reduces costs.

On the other hand, this architecture has some limitations in flexibility, as the PPF performs better with narrowband signals. This drawback can be more constraining in a scheme with a DQ mixer stage, more precisely in the RF PPF block.

In recent years, low-IF and zero-IF structures have gained popularity in a wide array of applications. Those systems employ a significantly low frequency for IF, which is advantageous for digitalizing some IF blocks, such as IQ generation. However, such a

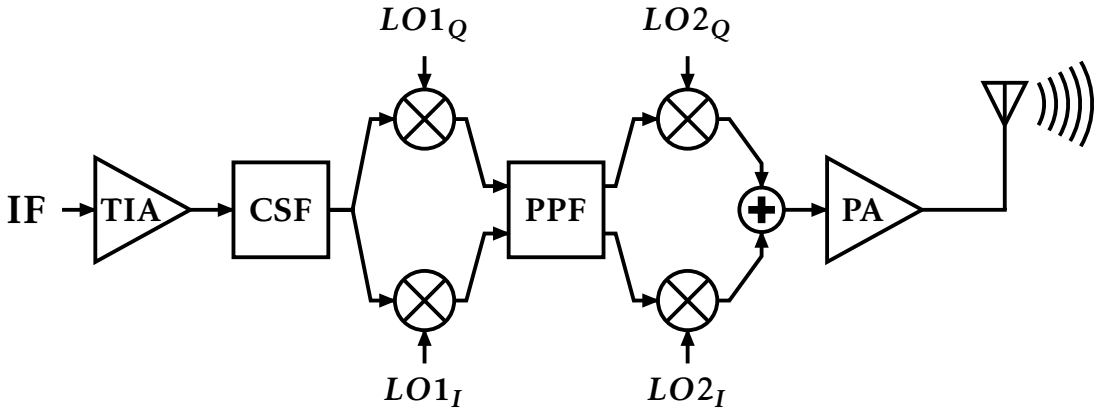

Figure 2.6: Two-step-up TX architecture.

low frequency can hamper filtering the DC offset before the mixer stage. Thus, they are prone to suffering from carrier leakage ($f_{LO} \pm 0$). Schemes from Figure 2.4 and Figure 2.5 might have issues blocking that leakage if f_{IF} is too low.

Nevertheless, other transmitter architectures can solve this problem [Mak07]. The two-step-up transmitter scheme (Figure 2.6)—based on the Weaver receiver [Wea56], see Section 2.1.3—cancels carrier leakage if an adequate combination of f_{LO1} and f_{LO2} is selected. Its BW is typically more flexible than the SQ/DQ SSB approach. It can be wider as the scheme is less demanding to the PPF. Even PPF could be replaced by pass-band filters to increase BW at the cost of IRR. An array of PPF for different standards can be included, although control circuits may be challenging to implement.

Besides the evident increment in complexity, a two-step-up scheme requires two QLOs and a DQ configuration is advised for the first mixer stage [Mak07]. There are two mixer stages, so the designer must be careful with where images lie. The two-step-up approach reaches its full potential if the RAU scheme uses some digital blocks in the downlink chain or an IF close to a BBoF strategy.

Table 2.1 summarizes the comparison between the three presented architectures. In the case of the IFoF RAU application, a SQ SSB approach presents the best trade-off. Compared to the classical superheterodyne scheme, it notably improves integrability. The constraint reduction of some other blocks, such as the IRF, mitigates the drawback of using additional blocks. The Two-step-up scheme has a great trade-off in capabilities, but the increased complexity in design offsets the marginal flexibility regarding the SQ

	Superheterodyne	**DQ/SQ SSB**	**Two-step-up**
Power efficiency	Low	High	High
Freq. flexibility	High	Medium	Medium
Carrier leakage	Low*	Low*	Vulnerable**
Cost	High	Low	Medium
Integrability	Low	High	High
Number of mixers	1	2–4	4–8
Number of LOs	1 LO	1 QLO	2 QLOs

*Very low or Zero IF might present carrier leakage

**it requires careful f_{LO} selection

Table 2.1: Transmitter architecture comparative for RAU downlink implementation.

SSB architecture. A more straightforward design is preferred when implementing less expensive RAUs.

2.1.3 Receiver architectures

Analogous to the relationship between the downlink chain and transmitter architectures, the schemes for the uplink are equivalent to receiver structures. Thus, the strategies are similar to the transmitter approaches.

Once again, the superheterodyne scheme is the most straightforward architecture to understand [Raz11]. The operation of the superheterodyne receiver (shown in Figure 2.7) is analogous to the transmitter, but it follows a reverse order. A low-noise amplifier (LNA) acts as the first stage, as the received signal power is minimal. This amplifier must provide gain without degrading the SNR—note expression (2.1). The LNA must match the antenna impedance or include a matching network. Similarly, some band-selection filtering is typically done by antenna response, LNA selectivity, actual filters, or a combination of them.

However, the image remains unfiltered after LNA, as it usually falls too close to the desired signal. For this reason, a specific IRF is also required for SSB reception. Implementing the IRF is one of the biggest drawbacks of the receiver integration. The relatively close frequencies of IRF pass and reject bands require step filter response,

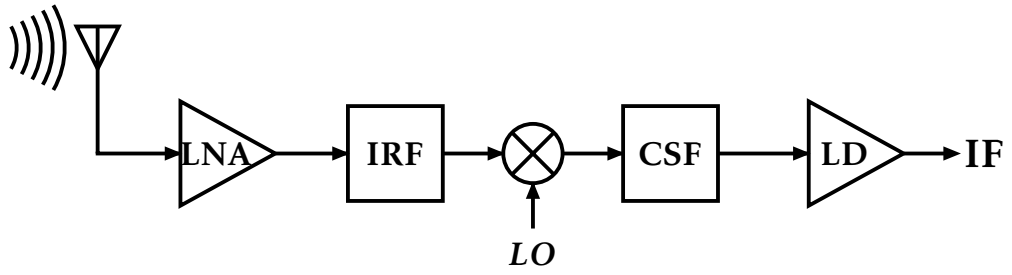

Figure 2.7: Classical superheterodyne RX architecture.

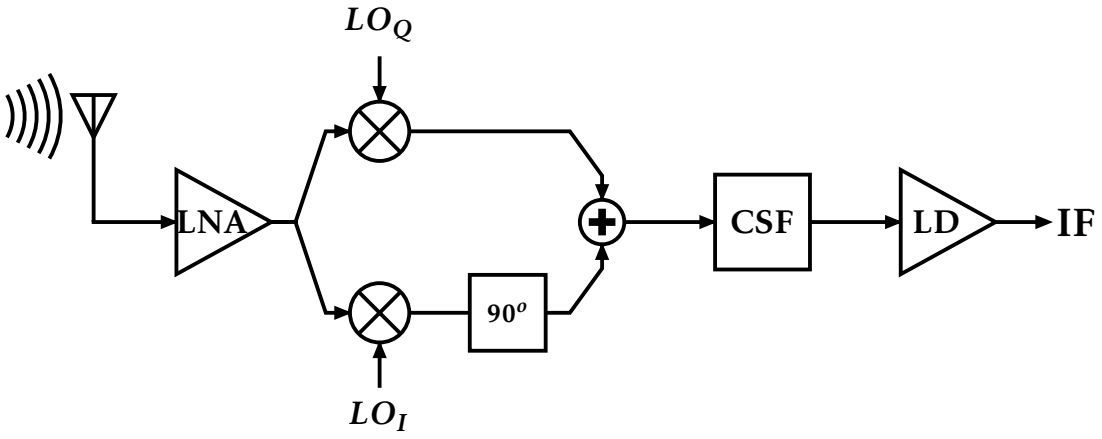

Figure 2.8: Hartley RX architecture.

and it is difficult to achieve on-chip. Nevertheless, this block is critical to avoid image interference overlapping the desired signal.

After the IRF, the RF signal is multiplied by a LO tone in the mixers, producing the IF signal. Then, the signal goes into a CSF to remove unwanted frequencies that could appear due to spurious signals, interferences, or non-idealities. Finally, a laser driver (LD) significantly enhances signal power to generate the optical variations that are transmitted through the optical fiber.

A simple scheme is often synonymous with reliance and flexibility, and the superheterodyne receiver is no exception. However, the limitations imposed by IRF notably increase the economic cost and system size. An attractive solution is employing signal cancellation to remove the image, as Hartley proposed in its [Har28]. Figure 2.8 depicts its application to RAU uplink chain.

The scheme multiplies the RF signal by an IQ signal—thus, it requires a QLO—and introduces a 90-degree phase shifter in one of the branches. Consequently, summing both products, desired-signal contributions are constructively added, but the image

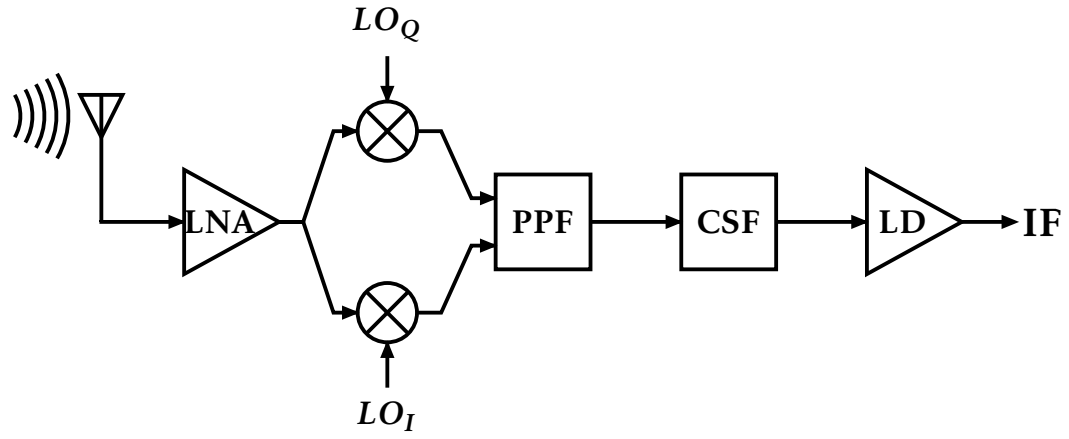

Figure 2.9: Hartley-PPF RX architecture.

ones cancel each other. There are two main drawbacks to the strategy. First, the non-idealities constrain the *IRR* achievable in the practice. Mixer inaccuracies can have a considerable impact, but LO errors can also significantly harm *IRR* performance. Second, the 90-degree phase shifter is problematic. Typical implementations have a very narrow *BW*, and they might be expensive. Also, it should not alter the amplitude mismatch with the other branch, which might be tricky to obtain.

Later issues are sometimes overcome by employing a ±45-degree phase shift block in each branch. This strategy improves balance, and the implementation can be as straightforward as RC and CR filters. The solution is compact but limited in performance. However, a PPF can provide a similar behavior, as later detailed in Section 3.1.1. Moreover, the PPF block can perform the sum operation. Thus, Figure 2.9 replaces the phase shifter and the adder with a PPF, resulting in the frequency converter from Figure 2.2b.

The PPF is a very efficient replacement for the IRF or alternative phase shifters in terms of integrability. Besides, its behavior as a complex filter improves *IRR*, passively mitigating image and making the scheme significantly more reliable. It also gains some flexibility in the bandwidth, although it remains dependent on the PPF constraints.

The Weaver receiver (Figure 2.10) aims to broaden bands [Wea56]. This scheme replaces the problematic phase shifter, but the overheads are the additional mixers and QLO. A pair of low-pass filters are also encouraged to remove undesirable frequencies. The second mix generates the phase shift between branches to cancel the image in the sum [Raz11]. In this structure, the sign is opposed to Figure 2.8, but signs are omitted

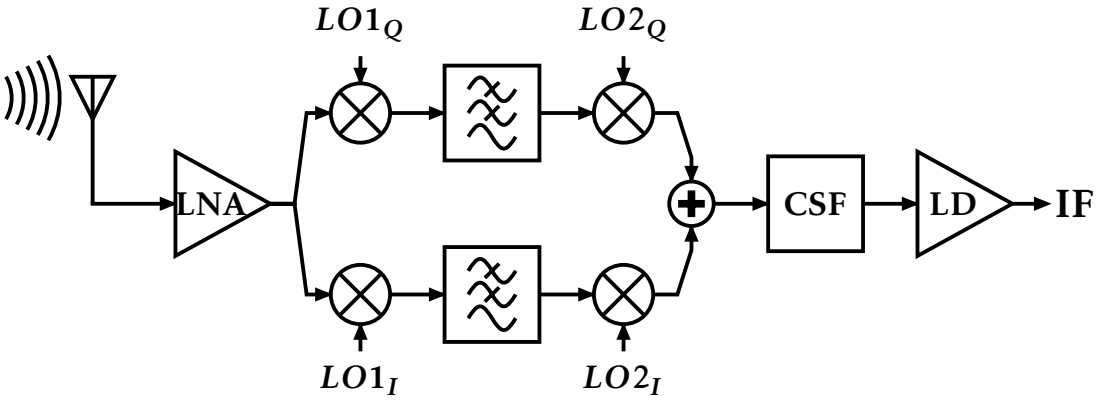

Figure 2.10: Weaver RX architecture.

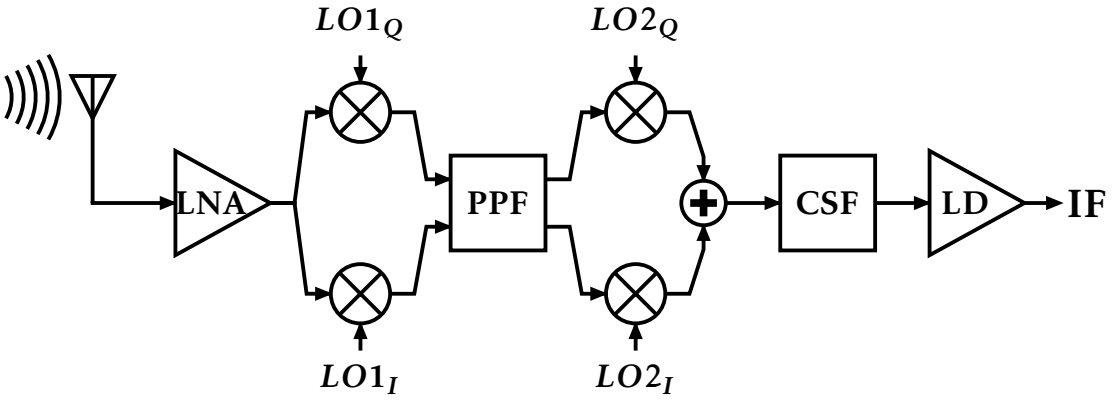

Figure 2.11: Weaver-PPF RX architecture.

in the diagrams for clarity. In essence, the system is more flexible and easier to implement than the Hartley approach. However, the performance is heavily impaired by the mismatch between both branches.

A PPF can improve *IRR* at the cost of limiting BW to this filter. The resultant scheme is the Weaver-PPF receiver from Figure 2.11. The structure is similar to the Hartley-PPF scheme, but the polyphase filter does not convert the IQ signal but enhances *IRR* in a particular frequency range. The second pair of mixers and the adder implement the operation of transforming the complex IQ signal into a real one.

The true potential of the structure is unlocked in the scenario of mixed-signal [Mak07] or BBoF RAUs. In the case of using digital blocks, part of the blocks can be included in the digital part, hence mitigating its main drawback. Note that a careful selection of f_{LO1} and f_{LO2} avoids issues of low-IF or zero-IF approaches, such as the DC offset due to leakages [Raz11]. Thus, the IF can be lowered for an easier A/D conversion than

	Superhet.	**Hartley**	**Hartley-PPF**	**Weaver**	**Weaver-PPF**
Reliability	High	Medium	High	Low	High
Freq. flexibility	High	Medium*	Medium*	High	Medium*
Cost	High	Medium	Lowest	Low	Low
Integrability	Low	Medium	High	High	High
Number of mixers	1	2–4	2–4	4–8	4–8
Number of LOs	1 LO	1 QLO	1 QLO	2 QLO	2 QLO

*High for narrowband

Table 2.2: Receiver architecture comparison for RAU downlink implementation.

other schemes. Similarly, the two sets of mixers can provide the two-step conversion (RF-IF and then IF-BB) without additional blocks.

Table 2.2 summarizes the advantages and disadvantages of the different approaches. In general, the Harley-PPF scheme presents the best trade-offs for an analog IFoF RAU as it performs similarly to Weaver-PPF but uses less number of devices. Notably, all the schemes can replace any pair of mixers for a DQ scheme to mitigate the impact of non-idealities, especially in the tone from QLOs.

2.2 Complex signals

An IQ signal is complex in the mathematical sense. Ideally, the I and Q components have equal amplitude, but a second variable exists: the phase difference between them. Its complex nature means that real and imaginary parts can describe it, although the polar form (magnitude and phase) is typically more intuitive.

The key aspect of IQ signals is that phase becomes a main factor. Thus, signals with equal frequency can be distinguished if they differ in phase. Needless to say, that capacity is quite valuable for those scenarios where the image is inconvenient and should be rejected.

In essence, a (complex) signal IQ is implemented by two tangible components (two "wires"), I and Q. Neglecting the initial phase,

$$s_{IQ}(t) = I + j \cdot Q = A_I \cdot \cos(\omega t) - j \cdot A_Q \cdot \sin(\omega t) \tag{2.6}$$

where $s_{IQ}(t)$ is the IQ signal and j is the imaginary unit.

Consequently, most schemes employ pairs of branches in their structure—which could be considered a single IQ signal. The previous section provides plenty of examples in its figures. In practice, the actual number of branches is usually doubled, as balanced signals mitigate several critical issues [Gra09]. Thus, real signals employ two components with opposed signs (180-degree phase offset), while complex ones rely upon a set of four, a proper polyphase system. From an ideal and theoretical perspective, balanced signals have the same variables and information as an equivalent single-ended signal. However, device mismatch, errors, and non-idealities might imply additional variables when they break the circuit symmetry.

2.2.1 Complexities of the negative spectrum

Any student of electronics soon faces the frequency response of systems. That is a fundamental part of the analysis and synthesis of circuits. Indeed, in the communication field, we are more used to the small-signal frequency domain than the temporal one. However, while the analysis in the frequency domain becomes a routine tool, we tend to forget the actual basis of the Fourier transform:

$$F(j\omega) = \mathscr{F}\Big(f(t)\Big) = \int_{-\infty}^{\infty} f(t) e^{-j\omega t} dt \tag{2.7}$$

where $F(j\omega)$ is the Fourier transform ($\mathscr{F}$) of $f(t)$, and the inverse operation is described as,

$$f(t) = \mathscr{F}^{-1}\Big(F(j\omega)\Big) = \frac{1}{2\pi} \int_{-\infty}^{\infty} F(j\omega) e^{j\omega t} d\omega \tag{2.8}$$

Although frequency is strictly complex and described by $F(j\omega) = |F(\omega)|e^{j\theta}$, with θ being the phase, for simplicity, we assume $F(j\omega) = F(\omega)$ [Svo14]. Also, we define signals

as complex or real according to their nature in the temporal domain; all of them are complex in the transformed domain.

Be $u_1(t) = \cos(\omega_0 t)$, then,

$$\begin{aligned} U_1(j\omega) = \mathscr{F}\Big(u_1(t)\Big) &= \int_{-\infty}^{\infty} \cos(\omega_0 t) e^{-j\omega t} dt = \int_{-\infty}^{\infty} \left(\frac{e^{-j\omega_0 t}}{2} + \frac{e^{j\omega_0 t}}{2}\right) e^{-j\omega t} dt = \\ &= \frac{1}{2}\Big(\mathscr{F}\Big(e^{-j\omega_0 t}\Big) + \mathscr{F}\Big(e^{j\omega_0 t}\Big)\Big) = \frac{1}{2}\Big(2\pi\delta(\omega-\omega_0) + 2\pi\delta(\omega+\omega_0)\Big) = \\ &= \pi\Big(\delta(\omega-\omega_0) + \delta(\omega+\omega_0)\Big) \end{aligned} \tag{2.9}$$

where δ is the Dirac delta function.

Note that the cosine is translated into two points in the frequency axis: one positive and another negative. Moreover, 1) both points have equal amplitude, and 2) any periodic signal can be decomposed into a series of trigonometric signals; hence, the spectrum of real signals is symmetrical. As a result, negative frequencies are often redundant and omitted.

Consider now a second signal with a 90-degree offset, *i.e.*, $u_2(t) = \sin(\omega_0 t)$, then,

$$\begin{aligned} U_2(j\omega) = \mathscr{F}\Big(u_2(t)\Big) &= \int_{-\infty}^{\infty} \sin(\omega_0 t) e^{-j\omega t} dt = \int_{-\infty}^{\infty} \left(\frac{e^{-j\omega_0 t}}{2j} - \frac{e^{j\omega_0 t}}{2j}\right) e^{-j\omega t} dt = \\ &= \frac{1}{2j}\Big(\mathscr{F}\Big(e^{-j\omega_0 t}\Big) - \mathscr{F}\Big(e^{j\omega_0 t}\Big)\Big) = \frac{1}{2j}\Big(2\pi\delta(\omega-\omega_0) - 2\pi\delta(\omega+\omega_0)\Big) = \\ &= -j\pi\Big(\delta(\omega-\omega_0) - \delta(\omega+\omega_0)\Big) \end{aligned} \tag{2.10}$$

For this signal, there is also symmetry $|U_2(j\omega)| = |U_2(-j\omega)|$, although the phase of positive and negative points are opposed. Indeed, the Fourier transform of any real signal always fulfills that $H(j\omega) = H^*(-j\omega)$, where H is an arbitrary transformed function (real in the time domain) and H^* is its complex conjugate.

As Fourier transform has the linearity property, then the transform of an IQ signal is

$$\begin{aligned} S_{IQ}(jw) = \mathscr{F}\Big(s_{IQ}(t)\Big) &= \mathscr{F}\Big(A_I \cdot u_1(t) - j \cdot A_Q \cdot u_2(t)\Big) = A_I \mathscr{F}\Big(u_1(t)\Big) - j \cdot A_Q \mathscr{F}\Big(u_2(t)\Big) = \\ &= A_I \pi\Big(\delta(\omega-\omega_0) + \delta(\omega+\omega_0)\Big) - A_Q \pi\Big(\delta(\omega-\omega_0) - \delta(\omega+\omega_0)\Big) = \\ &= \Big(A_I - A_Q\Big)\pi\delta(\omega-\omega_0) + \Big(A_I + A_Q\Big)\pi\delta(\omega+\omega_0) \end{aligned} \tag{2.11}$$

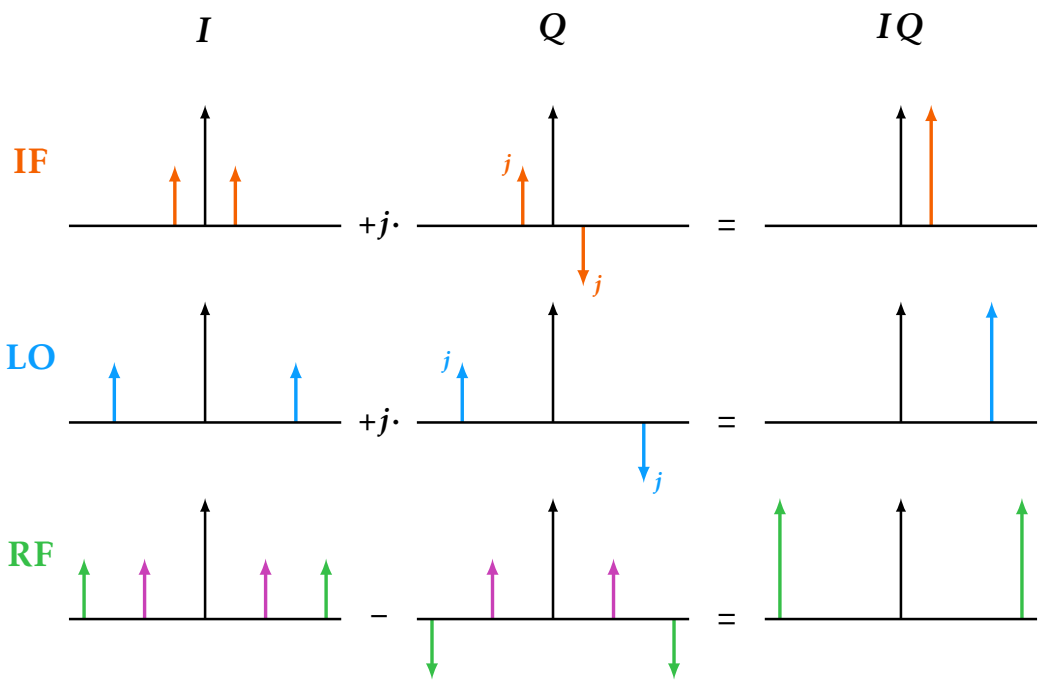

Figure 2.12: Operation of SQ upconverter. The first and second columns represent the I and Q components, respectively. The corresponding IQ signal is shown on the right side. In the last row, the image is presented in magenta.

In other words, if $A_I \neq 0$ and $A_Q \neq 0$, then symmetry is broken, which is only possible due to $s_{IQ}(t)$ being a complex signal. Even more, if $A_I = A_Q$, *i.e.*, an ideal IQ signal, the signal is only projected in the positive or negative frequency instead of both.

Thus, multiplying IQ signals—remember that multiplication in time is convolution in the frequency domain [Svo14]—can avoid image generation. See the operation of the SQ frequency upconverter scheme (Figure 2.2a). According to it, IF_I and IF_Q compose IF as an IQ signal. LO_I and LO_Q do the same with LO. The output produces a single tone (RF). Figure 2.12 illustrates the operation in detail. Terms with imaginary amplitude include a j to indicate the 90-degree phase offset.

Moreover, a couple of details from Figure 2.12 are noteworthy. Firstly, although IQ signals are asymmetrical, the actual electric signal—the ones on the wires must be. A complex signal is a useful abstraction of the combination of pairs of I and Q signals (the actual and tangible ones). Secondly, the sign of the RF combination selects the desired signal and the image to cancel. A substration implies $f_{RF} > f_{LO}$, while a sum means $f_{RF} < f_{LO}$.

The operation of the SQ downconversion scheme (Figure 2.2b) is shown in Figure 2.13.

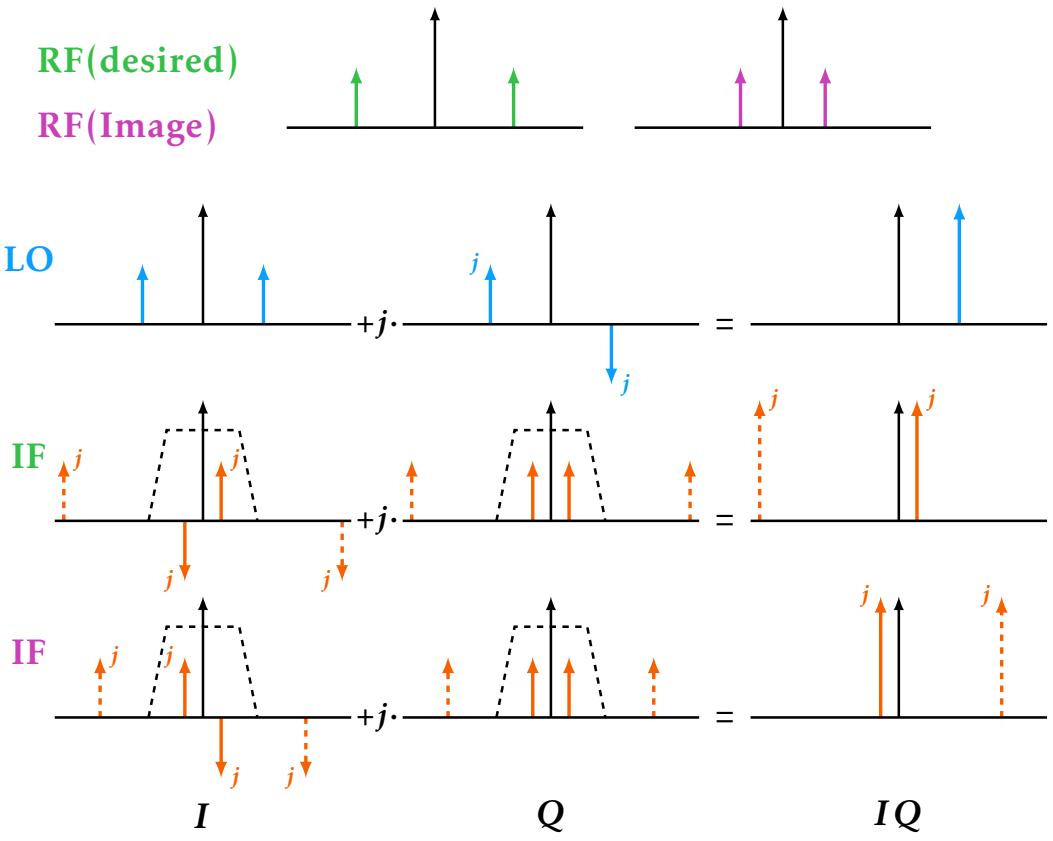

Figure 2.13: Operation of SQ downconversion. The third and fourth rows represent the response of the desired signal and the image, respectively.

In this case, two distinct input frequencies (green and magenta) can produce f_{IF} in combination with f_{LO}. Although another tone is produced in each case, it lies far away from f_{IF}. Thus, a straightforward filter (black dashed line) can easily remove those copies (orange dashed arrows). The final IQ signal lies at f_{IF} or $-f_{IF}$, depending on whether the desired signal or the image produces it. That sign means a different sequence (see the following section), a characteristic the subsequent PPF can differentiate.

2.2.2 Phasors and polyphase decompositions

A phasor or phase vector is a helpful tool for distinguishing signals of different phases and working with them [Hor15]. Signals should have equal frequency. Otherwise, as frequency is the derivative of phase with respect to time, phase offset would vary with time.

However, signals of equal frequency—invariant or steady-state responses—can be defined by their amplitude and (relative) phase. A phasor represents the signal as a

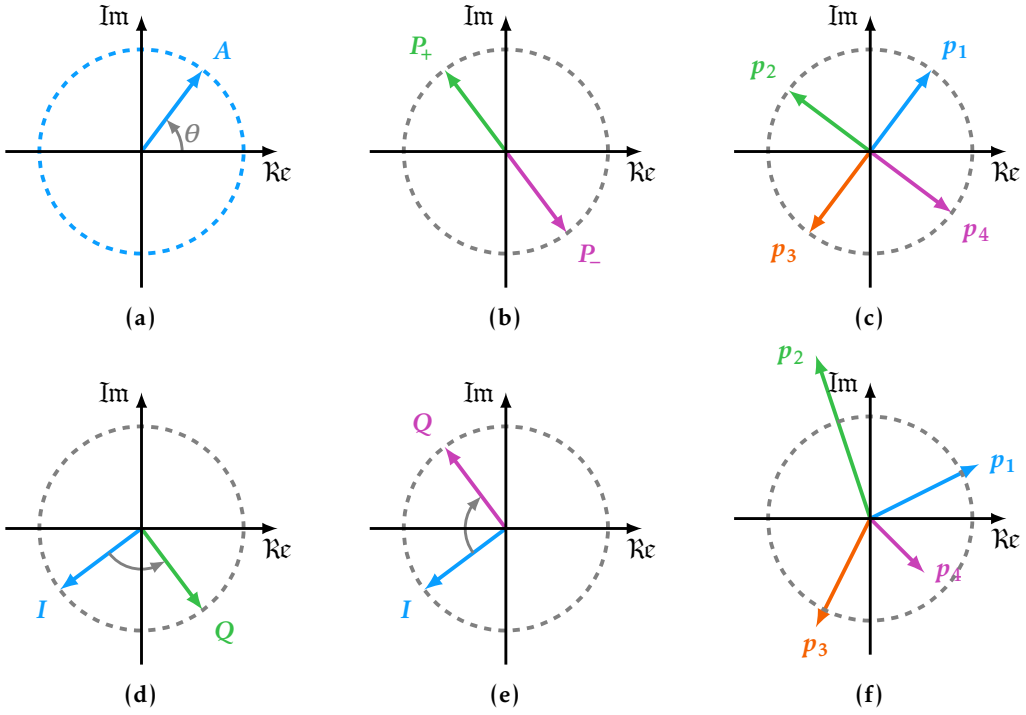

Figure 2.14: Sets of phasors for (a) single-ended signal; (b) balanced signal; (c) balanced IQ signal; (d) IQ signal (positive sequence); (e) IQ signal (negative sequence); and (f) an arbitrary four-phase signal.

complex number. Analytically, it can be considered a particular (and simpler) case of Laplace transform [Svo14]. The usual representation is in polar form with the notation $A\angle\theta$ to describe $A\cos(\omega t + \theta)$.

Graphically, Figure 2.14 shows different sets of phasors. The length of the vector indicates the magnitude (A), whereas the angle is the phase offset (θ). Horizontal and vertical axes correspond to real and imaginary parts, respectively, with the usual meaning in the frequency domain. More precisely, the imaginary unit (j) supposes a 90-degree phase shift.

The phasor representation is advantageous to represent sets of related signals, *e.g.*, balanced (Figure 2.14b), IQ (Figure 2.14d and Figure 2.14e), and balanced IQ (Figure 2.14c) signals. The case of Figure 2.14e is noteworthy. The amplitude of the phasor must be positive; it is a module—hence, $-A\angle\theta = A\angle\theta + 180°$. Thus, the "sequence" of desired signal and image is opposed. See Figure 2.13, the desired image and the image have opposite signs in the IF_I component, hence, the image presents a −90-degree phase offset between I and Q instead of the 90 from desired-signal IF. Notably, the graph can also depict the inaccuracies (Figure 2.14f).

Once the factors that break symmetry appear, each phasor of a composite signal is an independent variable. Hopefully, they maintain some of the desired correlations, but the new terms remove the strict dependencies that allow for a lower number of relevant variables. Thus, a balanced signal with errors depends on two (complex) variables instead of one: the differential-mode component remains characterized by a single variable, but the potential errors (common mode) demand another one. IQ signals (balanced or not) have a similar issue.

In essence, a polyphase system of n signals (aka phases) is an n-dimensional complex vector space V . Thus, any signal of those characteristics can be described by the standard basis of V, *i.e.*, by each of the separate phasors. Nevertheless, this form has little use for IQ signals, as the critical information is contained in the combination of phasor.

Incidentally, another approach, the method of symmetrical components, is widely employed to analyze a three-phase unbalanced system. However, Charles Legeyt Fortescue devised it for an arbitrary number of phases in his extensive paper [For18]. As its name suggests, the method uses symmetrical sets of phasors as alternative basis vectors.

The decomposition in symmetrical phasors is especially beneficial in evaluating the characteristics and quality of an IQ signal. Components that ideally translate into the desired signal and the image have that form. Two collinear components [Beh01] should complete the basis.

For clarity, they use the amplitude unit, and the first phasor ($p1$, typically $I+$) is the phase reference ($\theta_{p1} = 0$), then:

- Positive-sequence IQ signal (A): phasors are uniformly distributed counterclockwise, *i.e.*, $p_1 = +1$; $p_2 = +j$; $p_3 = -1$; and $p_4 = -j$.
- Differential-mode collineal (B): I phasors in phase but opposed to Q phasors, *i.e.*, $p_1 = p_3 = +1$ and $p_2 = p_4 = -1$.
- Negative-sequence IQ signal (C): phasors are uniformly distributed clockwise, *i.e.*, $p_1 = +1$; $p_2 = -j$; $p_3 = -1$; and $p_4 = +j$.
- Common-mode collineal (D): all phasors equal, *i.e.*, $p_1 = p_2 = p_3 = p_4 = 1$.

Note that weights on these terms are complex, but the phase is typically negligible—it only represents the common phase offset. However, the module indicates the component power and the IRR can be obtained from the relationship between A and C weights.

As the initial basis is the standard, the change-of-basis matrix $\boldsymbol{T}$, from the natural basis to the symmetrical components approach, comprises the complex conjugate of second basis vectors (they are placed as rows in $\boldsymbol{T}$). According to their descriptions, $\boldsymbol{T}$ is

$$\begin{pmatrix} a \\ b \\ c \\ d \end{pmatrix} = \frac{1}{4} \cdot \boldsymbol{T} \cdot \boldsymbol{P} = \frac{1}{4} \cdot \begin{pmatrix} +1 & -j & -1 & +j \\ +1 & -1 & +1 & -1 \\ +1 & +j & -1 & -j \\ +1 & +1 & +1 & +1 \end{pmatrix} \cdot \begin{pmatrix} p_1 \\ p_2 \\ p_3 \\ p_4 \end{pmatrix} \tag{2.12}$$

where a, b, c, and d are the weights in A, B, C, and D symmetrical components, respectively, and $\boldsymbol{P}$ is the coordinates on a standard basis. The factor 1/4 appears to balance of weights between basis [Beh01].

Figure 2.15 illustrates the decomposition of the signal from Figure 2.14f into symmetrical components. As expected, A is the main component—the example signal resembles a balanced IQ signal—, while the opposite sequence contribution (C) is much reduced (although it exists). Collinear components can be seen as the unbalance between opposed phasors (B) and a general bias (D).

2.2.3 Complex filters

The usefulness of complex filters is evident from the application of complex signals to communication systems. Analogous to signals, a complex filter presents an asymmetrical frequency response. The Hilbert transform [Beh01] is a typical method of synthesizing a complex filter. From a high-pass filter, the Hilbert transform can shift its response in frequency without requiring symmetry between the positive and negative sides of the spectrum.

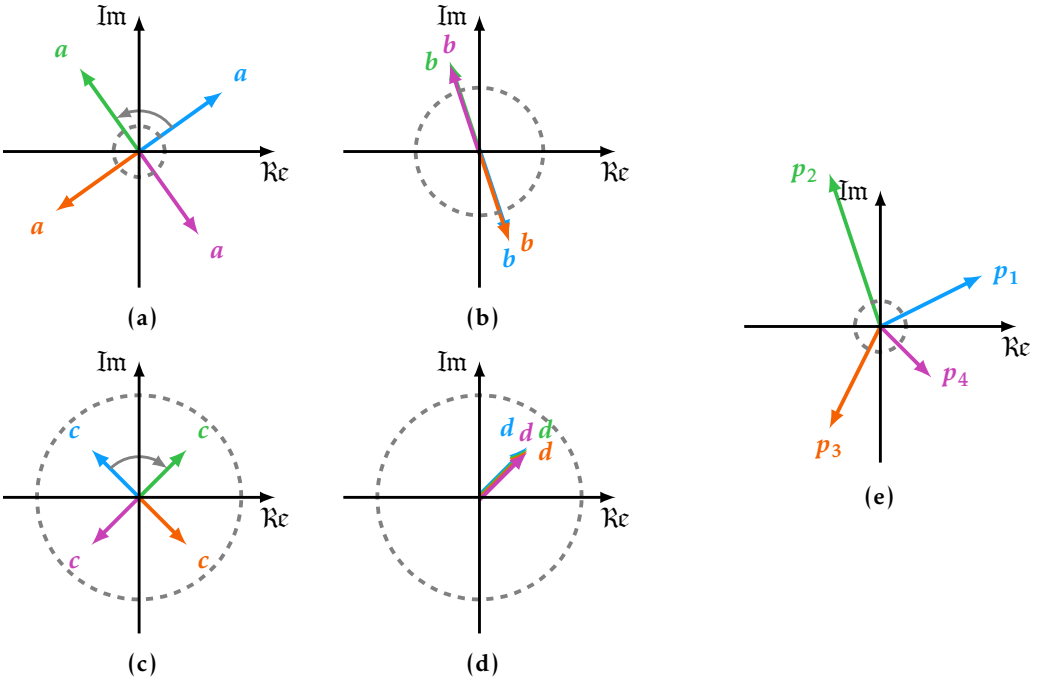

Figure 2.15: Decomposition of an arbitrary non-ideal balanced IQ signal (e) into A, B, C, and D symmetrical components. Gray dashed circle has equal value in the five graphs, indicating the relative sizes.

Translated into phasors, it means the filter distinguishes between sequences or symmetrical components. This distinction is a critical difference from the usual frequency filters. In this kind of complex filter, as opposed to typical ones, the passband and the stopband overlap, sharing the frequency range. However, *IRR* measures the difference between the desired and rejected signals. Consequently, especially in passive filters, the *IRR* curve might present strong variations that nonetheless do not affect the passing signal. They appear due to alterations in the image cancellation. Besides, passive *IRR* filters do not typically have an upper limit; the more *IRR* they have, the better. Figure 2.16 outlines the characteristics of a typical high-pass filter and a complex polyphase one.

2.3 Technology devices

Non-idealities inevitably alter the performance of electronic circuits, and ICs are no exception. Indeed, the PPFs are especially sensitive to those variables despite neglecting some MOS-related issues, such as linearity restrictions or channel effects. The

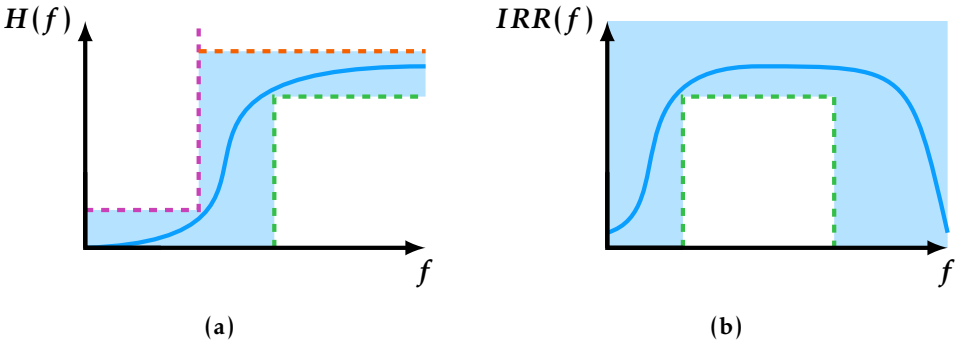

Figure 2.16: Example responses (blue line) of (a) a real high pass filter and (b) a complex *IRR* filter. Magenta and green lines show limitations of the stop and pass bands, respectively. The orange line shows the ripple limit. The blue area summarizes the valid region for the filter curve.

main non-idealities affecting PPFs result from different inaccuracies during fabrication; hence, they are random variables that cause differences with the expected values. They may imply that, ideally, identical devices are distinct or that the same filter design will perform differently in each fabricated sample.

Fortunately for designers, foundries provide detailed models of the available devices in each technology and their potential non-idealities, including statistical information. Those models have proven their usefulness in simulation, and they are becoming incrementally more critical while the technological node evolves and more non-idealities appear.

2.3.1 Non-idealities

There are two primary sources of non-idealities. On the one hand, they appear as discrepancies between the abstract component (*e.g.*, resistor, capacitor, transistor, or inductor) and the physical device that emulates the abstract operation. Section 2.3.2 enumerates different alternatives to construct resistors or capacitors. Transistor second-order effects—especially in nanometer MOS technologies—are a clear example of these phenomena [Raz17]. Mercifully, except for some parasitics, these non-idealities have little impact on the resistors or capacitors required for our filter. However, in the most extreme—and unrecommended—sizings might be noticeable. Variations in the mean value in the tables of the Appendix H are a consequence of these non-idealities.

On the other hand, the other non-idealities impact the expected characteristics of the devices. Moreover, those variations are random and unpredictable. Some techniques

can be applied to mitigate their presence or effect. Statistical models are quite helpful to evaluate their influence on the design. The Monte Carlo analysis method is an essential tool in the simulation of random variables [Jae15]. This algorithm simulates the circuit, selecting a different set of values for the varying factors for each sample according to a provided probability distribution.

2.3.1.1 Temperature and process variations

Temperature affects the electrical characteristics of the materials that compose the microelectronic devices. Consequently, temperature variations can produce noticeable changes in component values. As IC dimensions are minimal, all devices on the silicon can be considered at the same temperatures. This assumption is valid, except maybe for topologies working with high-power densities. However, they are out of the scope of our topic. In essence, the particular temperature of the circuit has a uniform influence on devices.

Conversely, the cluster of phenomena denominated as process variations does not depend on the current circuit situation but on the concrete conditions in which it was fabricated. Technological processes involve delicate procedures and numerous steps [Bak19]; hence, some deviations are unavoidable even under the most stringent control. Because of process variations, some devices can suffer massive deviations from their expected (typical) values. For example, a resistor can present a ±40 % variation. A significant characteristic of process variations is that they equally affect similar devices.

Despite the different origins and timings—one depends on the instant scenario, and the other is fixed once fabricated—both effects are usually summarized as one. Note that for a designer, both suppose a very similar obstacle to overcome. Typically, voltage supply deviations are also considered in the circuit evaluation. Process, voltage, and temperature variations are known as PVT errors. Nevertheless, the PPF is entirely passive and unaffected by any discrepancies in the supply voltage.

Simulation models represent temperature and process variations as changes in the variables that define the values of the different devices. Thus, identical components vary

to the same degree. The potential differences—*e.g.*, due to suffering error gradients instead of a constant one—are included in the mismatch variations.

The simulations can be carried out using the statistical models–i.e., applying random variations—in a Monte Carlo analysis. This method is computationally intensive but provides a histogram of the key parameters and an estimation of the chances the circuit will fulfill specifications despite these variations.

Alternatively, a corner analysis is a worst-case approach. A corner is a scenario that sets certain extreme variations. If the circuit can cope with those changes, the design is considered robust enough against evaluated phenomena. As process variations are approximated to a Gaussian distribution, the corners usually employ a variation equal to 3σ (being σ the standard deviation).

Ultimately, corner parameters depend on the application, technology, and topology. The designers are encouraged to search the most challenging corners to guarantee IC performance after fabrication.

However, the most usual are typical (*tt*), fast (*ff*) and slow (*ss*). The first one describes an ideal situation, *i.e.*, the operation without variations, while the others alter technology characteristics to opposite tolerances of carrier mobilities. The first letter refers to the speed of N regions while the second concerns to P regions; hence, designs that mix devices based on opposed regions might be interested in the *sf* or *fs* corners.

The temperature can be a parameter of the corners, as commercial, industrial, and military products must be capable of operating under certain frequency ranges: from 0 to 70 ℃, from −40 to 85 ℃, and from −55 to 125 ℃, respectively.

2.3.1.2 Mismatch variations

Accuracy in fabrication is limited. Thus, supposedly identical devices will have some differences in practice. This potential discrepancy between two devices is defined as mismatch, which can be critical to the operation of many circuits. Indeed, this dependency is intentional as the precision in making two similar devices is much higher than controlling process variations. In other words, mismatch typically implies a lesser variation than process deviation; hence, systems whose characteristics depend on relative values (instead of absolute magnitudes) are more robust to variations.

Nevertheless, the mismatch is challenging to mitigate. Most of the strategies [All12] imply using symmetrical layouts to maximize the likeness of matched components and their environment. Matching techniques commonly exploit the division of devices into sections, interspersing both components to cancel gradient errors. Also, dummy cells benefit most designs. These cells are disconnected duplicates of a section and are placed at the end of an array (or similar layout distribution) to equalize the surroundings of endings and middle parts.

Moreover, the composition of the device—how it is built and which materials are employed—and the sizing are also critical factors in the equation. Thus, a careful selection of the technology option might drastically benefit performance. A larger size makes border inaccuracy less significant; therefore, area consumption can be exchanged to reduce mismatch to some extent. Tables from Appendix H show this relationship.

One of the main issues, and the first step, in coping with mismatch is identifying the critical pairs [Raz17]. Sometimes it is not evident but heavily dependent on the topology—the particular issue of PPF is explained in Section 3.2. Consequently, a general method to simulate the strict definition is not feasible; devising an algorithm capable of detecting pairs among all circuit devices is impractical and sometimes impossible in a reasonable computational time. As a fitting solution, simulation mismatch models ingeniously adapt the definition: it becomes an independent random deviation to each device. While process variations produce the same effect on each element, the mismatch model applies the changes independently. Thus, potential differences are necessarily applied event to unknown critical pairs.

As an indirect result, most mismatch simulations rely upon Monte Carlo analyses. However, if critical pairs are known, their differences can be included in the corners, or parametric curves can be drawn.

2.3.1.3 Parasitics

Parasitics, typically parasitic impedances, are effects out of the original intent for the device; however, their impact can be expressed as additional abstract elements. For

example, the structure of most IC resistors implies a parasitic capacitance effect between the resistor body and the substrate (two parallel and isolated conductors); consequently, a capacitor between resistor nodes and substrate supposes a better approximation to the behavior when the frequency is high enough than only the resistor. Models of technology devices internally include more complex topology—usually described in documentation—than the represented symbol. However, some problematic parasitics appear due to physical connections and wires. Contrary to mismatch and process, parasitics are better estimated from layout design. The physical distribution plays a vital role in the impact of this non-ideality.

2.3.2 Type of devices

During the design, choosing the particular technology device to implement an element might be as crucial as selecting its value. Distinct alternatives have different advantages and disadvantages. Also, not all technologies have the same options, as many may require additional fabrication steps or more expensive processes.

Two elements are of interest in the PPF design: capacitors and resistors.

2.3.2.1 Capacitors

There are several methods to implement a capacitance. However, analog circuits require several characteristics: good matching accuracy, low voltage and temperature dependence, and high capacitance per unit area [All12]. Thus, some practical arrangements for digital circuits, such as accumulation MOS capacitors, do not satisfy the criteria [All12]. In modern analog processes, there are two kinds of capacitors: metal-oxide-metal (MOM) and metal-insulator-metal (MIM) capacitors.

MOM capacitors use metal layers to implement the capacitor plates. The most direct way is employing different layers for each plate, often interconnecting even and odds layers to maximize capacitance (M1–M3–M5–... vs. M2–M4–...). The capacitance per unit area is low in this way, as the distance between metal layers is relatively large. Thus, another solution is employing fingers in the same layer and interleaving them. Note that both approaches are not mutually exclusive, and a MOM capacitor can use fingers in different layers.

On another note, MIM capacitors are built in special layers much closer to each other than metal ones. Consequently, they present much higher capacitance per area than MOM capacitors (5-10 times), but they are also more expensive; particular MIM layers require specific fabrication processes and masks. Additionally, deviations in MIM capacitors are significantly accurate compared to most standard IC devices. Tables from Appendix H are proof of this. The only drawback of MIM capacitors compared to MOM ones—apart from the economical cost—is a lower Q factor that can jeopardize their use in some RF applications.

2.3.2.2 Resistors

A resistor is typically implemented by a section of a conductor that presents some opposition to the electric current. In other words, it is a piece of material with adequate resistivity. As it depends on the section plane—and the height (H) is fixed and conditional to technology—, the width (W) and the length (L) define resistance value [All12]. The typical expression is as follows,

$$R = \rho \frac{L}{W \cdot H} = R_{\square} \frac{L}{W} \tag{2.13}$$

where ρ is the resistivity, and $R_{\square}$ is the sheet resistance, measured in ohms per square.

Thus, $R/R_{\square}$ is the required "number of squares" to implement that resistor of value R. In other words, 1) L and W are scalable, and 2) the number of squares depends on the resistor type.

Moreover, simulation models typically include additional terms into (2.13),

$$R(T) = R(T_0) \cdot \Big(1 + C_{T1} \cdot \big(T - T_0\big)\Big) \tag{2.14}$$

Or even, with a quadratic relationship [Bak19],

$$R(T) = R(T_0) \cdot \Big(1 + C_{T1} \cdot \big(T - T_0\big) + C_{T2} \cdot \big(T - T_0\big)^2\Big) \tag{2.15}$$

where T is the temperature, T_0 is the room temperature, and C_{T1} and C_{T2} are the coefficients of first-order and quadratic dependencies.

Similar expressions can be found with applied voltage, although linearity is usually high in passive devices. The notable exception is the implementations employing an MOS that is biased in triode. The main weakness of this configuration is its poor linearity, although there are some techniques to improve it [Tsi86].

"Diffusion" resistor uses heavily doped layers—N+ or P+—as the material. Consequently, the sheet resistance is low. Their minimal width is usually large compared with alternatives; thus, they might become expensive in terms of area consumption. Their matching accuracy is good [All12]; however, they can exhibit piezoelectric behavior [Tsi02] and have relatively high temperature and voltage coefficients, resulting in linearity issues. Thus, other resistors might suit better signal paths.

The boundary between diffusion and substrate works is reverse-biased; hence, only a tiny leak current exists. However, this condition causes a relatively large parasitic capacitance and makes the resistor vulnerable to substrate noise. Double- and triple-well structures can act as an imperfect shield. The P and N diffusion resistors present similar characteristics, although the sheet resistance of the P version is usually higher due to the slower carriers.

Polysilicon layers are usually the best option for a resistor as they are affected the least by voltage coefficient and parasitic capacitance [All12]. Moreover, their matching accuracy is excellent; they are very close in that aspect to diffusion devices without their drawbacks. Their sheet resistance is in the tens or hundreds of ohms, although there are some processes to increment it to the thousands at the cost of worsening the temperature coefficients [Tsi02].

Well resistors are made using the N-well layer. These devices provide the largest sheet resistance (thousands of ohms), as N-well is less doped than diffusion. However, voltage and temperature coefficients are significantly larger, although the former can be mitigated if the resistor is wide enough. A great width reduces the relevance of depletion regions on the sides [Tsi02].

Special technologies can enable other kinds of resistors. Although some of them can provide excellent performance, their use is restricted to well-justified cases due to the additional costs.

References

[All12] P. E. Allen and D. R. Holberg. *CMOS analog circuit design, 3rd edition*. Oxford University Press, 2012. ISBN: 9780199765072.

[Bak19] R. J. Baker. *CMOS circuit design layout and simulation, 4th edition*. IEEE Press–Wiley, 2019. ISBN: 9781119481515.

[Beh01] F. Behbahani, Y. Kishigami, J. Leete, and A. Abidi. "CMOS mixers and polyphase filters for large image rejection". *IEEE Journal of Solid-State Circuits* 36.6 (June 2001), pp. 873–887. DOI: 10.1109/4.924850.

[For18] C. L. Fortescue. "Method of symmetrical co-ordinates applied to the solution of polyphase networks". *34th annual convention of the American Institute of Electrical Engineers*. AIEE, June 28, 1918, pp. 1027–1140.

[Gin75] M. J. Gingell. "The synthesis and application of polyphase filters with sequence asymmetric properties". PhD thesis. 1975.

[Gra09] P. R. Gray, P. J. Hurst, S. H. Lewis, and R. G. Meyer. *Analysis and design of analog integrated circuits, 5th edition*. Wiley, 2009. ISBN: 9780470245996.

[Har28] R. V. L. Hartley. "Modulation system". U.S. patent 1666206. Apr. 17, 1928.

[Hor15] P. Horowitz and W. Hill. *The art of electronics, 3rd edition*. Cambridge University Press, 2015. ISBN: 9780521809269.

[Jae15] R. C. Jaeger and T. N. Blalock. *Microelectronic circuit design, 5th edition*. McGraw-Hill Education, 2015. ISBN: 9780073529608.

[Lee04] T. H. Lee. *The design of CMOS radio-frequency integrated circuits, 2nd edition*. Cambridge University Press, 2004. ISBN: 0521835399.

[Mak07] P.-I. Mak, S.-P. U, and R. P. Martins. "Transceiver architecture selection: Review, state-of-the-art survey and case study". *IEEE Circuits and Systems Magazine* 7.2 (2007), pp. 6–25. DOI: 10.1109/MCAS.2007.4299439.

[Mar21] A. D. Martinez-Perez, F. Aznar, G. Royo, and S. Celma. "Analysis of non-idealities on CMOS passive mixers". *Electronics* 10.9 (2021). ISSN: 2079-9292. DOI: 10.3390/electronics10091105.

[Raz11] B. Razavi. *RF microelectronics, 2nd edition*. Prentice Hall, 2011. ISBN: 9780137134731.

[Raz17] B. Razavi. *Design of analog CMOS integrated circuits, 2nd edition*. McGraw-Hill Education, 2017. ISBN: 9780072524932.

[Svo14] J. A. Svoboda and R. C. Dorf. *Introduction to electric circuits, 9th edition*. Wiley, 2014. ISBN: 9781118477502.

[Tsi02] Y. Tsividis. *Mixed analog-digital VLSI devices and technology*. World Scientific, 2002. ISBN: 9812381112.

[Tsi86] Y. Tsividis, M. Banu, and J. Khoury. "Continuous-time MOSFET-C filters in VLSI". *IEEE Journal of Solid-State Circuits* 21.1 (1986), pp. 15–30. DOI: 10.1109/JSSC.1986.1052478.

[Wea56] D. K. Weaver. "A third method of generation and detection of single-sideband signals". *Proceedings of the IRE* 44.12 (1956), pp. 1703–1705. DOI: 10.1109/JRPROC.1956.275061.

Chapter 3

Analysis of image rejection ratio for passive polyphase filters

Modern communication systems are usually heterodyne, or at least based on this kind of architecture [Raz11], and typically, they are also SSB (Single Side-Band). This approach implies dealing with quadrature (IQ) signals [Hor15]. The advantages of this strategy for many applications are undeniable, as evidenced by the mixer architectures shown in Section 2.1. However, the theory around these structures usually assumes the ideal generation of or conversion to IQ signals, neglecting a relevant source of errors in the system operation. Note that an accurate estimation of such inaccuracies is often not a straightforward task, but in practice, it can enable significant system optimization or at least reduce circuit performance uncertainty [Gal00].

One of the main methods of converting from or to IQ signals implies using polyphase filters, particularly passive ones [Gin73], commonly referred to by their acronym PPF (Polyphase Passive Filter). The Image Rejection Ratio (IRR) is an important performance measure for these filters [Kau08]. However, reaching high IRR values is problematic in practice, as several non-idealities strongly impact the actual performance of the PPF [Beh01].

This chapter is divided into three sections. The first section (Section 3.1) describes the operation of a PPF and an overview of non-idealities impact on these filters. The second section (Section 3.2) presents a detailed analytical study of the effects of mismatch between the devices in the circuit, covering two interesting challenges: finding

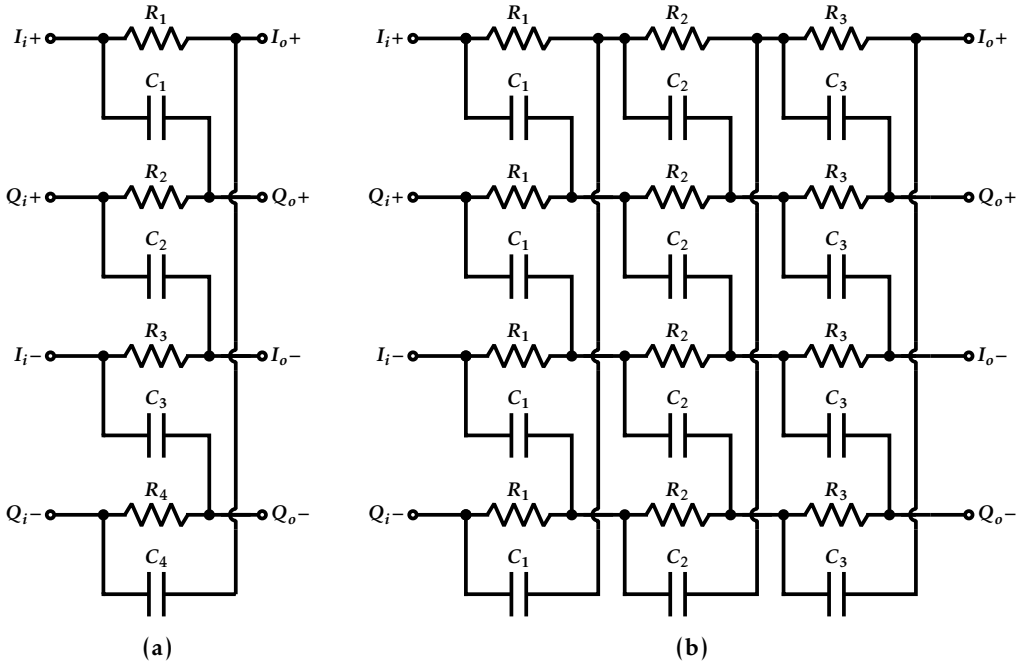

Figure 3.1: Schematics for (a) one-stage and (b) three-stage PPFs.

the worst possible mismatch combination for a given tolerance and obtaining the relationship between the tolerance of the components and the maximum achievable IRR. The third section (Section 3.3) expands on the previous analysis, adding the potential effects of unbalanced loads and suggesting a systematic methodology. The complete analysis provides very relevant information for modeling cases that push the limits of the technology or aim to obtain a very high IRR; in short, to establish a relationship between the potential variations of the elements and the overall performance.

3.1 Working principles

3.1.1 Basic description

A PPF is a passive electronic network that allows quadrature signals to pass while rejecting those with the opposite phase difference [Gin73]. It favors incoming signals with a phase difference of 90 degrees ($\pi/2$ radian) between the I and Q components while canceling those with a phase difference of 270 or −90 degrees.

These filters are constructed using simple stages entirely composed of resistors and capacitors. The elements of these stages are arranged in an asymmetrical but balanced

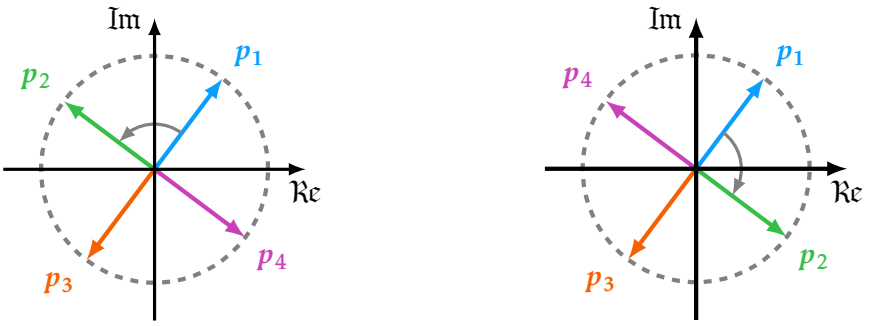

(a) Positive sequence

(b) Negative sequence

Figure 3.2: Differential IQ signal with different sequences. Each vector represents the phasor of each single-ended component of the complex signal.

network. Each input is connected by a resistor to the output of the equivalent phase and by a capacitor to the subsequent output, according to the desired sequence. Figure 3.1 shows examples of this structure with one and three stages.

When the filter operation is analyzed by source superposition [Dor10], the signal at each output results from the corresponding and following (according to the sequence) input signals. One passes through a low-pass RC filter, and the other through a high-pass CR filter [Gal00]. Since RC and CR filters shift the phase of input signals at the cut-off frequency by respectively +45 and −45 degrees, a 90-degree phase-difference input signal (Figure 3.2a, positive sequence) combines constructively (same phase). On the other hand, when their phase difference is −90 degrees (Figure 3.2b, negative sequence), they combine destructively (opposite phase) [Beh01]. Figure 3.3 shows this effect graphically. Section 2.2 discusses IQ signals in more detail.

This behavior implies that at the cut-off frequency, the signal rotates its phase $-\pi/4$ radians ($-45°$) after each stage. This output phase also depends on the frequency and is very sensitive to device variations. However, the critical information of the complex signal is not contained in the absolute phase but in the relative phase between its components, *i.e.*, the phase differences between the single-ended signals that compound the complex one and the corresponding sequence. In practice, phasor I (or $I+$) usually acts as the phase reference for each complex node, and the remaining phases are described in terms of this value. For clarity, outputs are named according to the input in phase at low frequency. Again, Chapter 2 (Section 2.2.2) contains additional details about this in the symmetrical sequence decomposition.

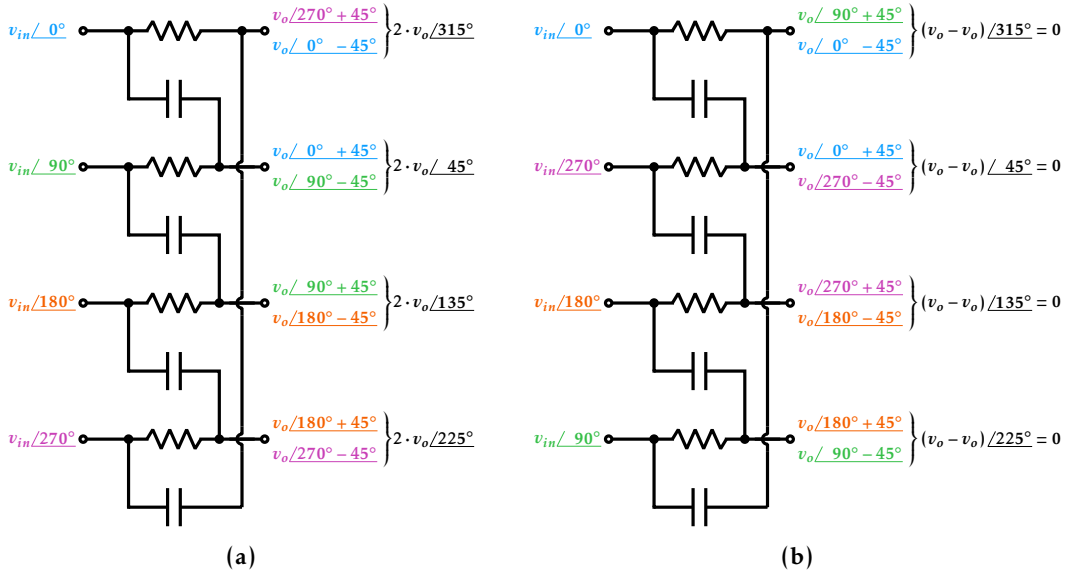

Figure 3.3: PPF behavior at tunned frequency ($\omega = 1/RC$). Contributions from input signals (a) constructively or (b) destructively combine according to the IQ sequence. Output components are shown in their respective input color.

The main parameter that serves as a figure of merit for these filters and describes their response is the IRR. In its usual form, this parameter represents the power ratio between the desired signal and its image (or potential effect, in a receiver case). However, IRR can be generalized as a quality measure for a PPF since the desired signal and the image are respectively translated as the positive (s_+) and negative (s_-) sequences of the complex signal. Consequently, the IRR of a PPF can be calculated as the power ratio of the effect produced by the two sequences. This magnitude, in turn, is equivalent to the ratio of the squares of the corresponding voltages, since the impedances do not vary with the sequence. Analytically,

$$IRR = \frac{P_o|_{s_+}}{P_o|_{s_-}} \equiv \frac{|v_o|^2_{s_+}}{|v_o|^2_{s_-}} \tag{3.1}$$

where P_o and $|v_o|$ are the power and voltage amplitude at the output, respectively.

However, the usefulness of a PPF is not limited to improving the quadrature of a complex signal but also allows the implementation of differential (D) to quadrature (IQ) converters and vice versa. There are two classes of such converters. Both configurations involve different ways of introducing or extracting the differential signal, and their operation is based on the fact that a differential signal can be decomposed as two ideal IQ signals of equal amplitude and opposite sequence.

Unlike the other configurations, a PPF as a D-IQ converter will not be able to have two signals with different sequences at its input. Of particular interest, therefore, are the expressions that relate the IRR to the ideality of the signal [Nor56; Kau08], described in terms of phase error ($\Delta\theta$) and amplitude balance (A_{BAL}). That is,

$$IRR = \frac{1 + 2 \cdot \cos(\Delta\theta) \cdot A_{BAL} + A_{BAL}^2}{1 - 2 \cdot \cos(\Delta\theta) \cdot A_{BAL} + A_{BAL}^2} \tag{3.2}$$

where A_{BAL} is the amplitude ratio between I and Q, and $\Delta\theta$ is the deviation from the ideal phase difference (ideally, $\theta_I - \theta_Q = -\pi/2$ and $\Delta\theta = 0$).

If one of the magnitudes is ideal, *i.e.*, $A_{BAL} = 1$ or $\Delta\theta = 0$, (3.2) results in two possible partial IRR expressions:

$$IRR|_{\Delta\theta=0} = IRR_{A_{BAL}} = \frac{1 + 2A_{BAL} + A_{BAL}^2}{1 - 2A_{BAL} + A_{BAL}^2} = \left(\frac{1 + A_{BAL}}{1 - A_{BAL}}\right)^2 \tag{3.3}$$

$$IRR|_{A_{BAL}=1} = IRR_{\Delta\theta} = \frac{1 + 2 \cdot \cos(\Delta\theta) + 1}{1 - 2 \cdot \cos(\Delta\theta) + 1} = \frac{1 + \cos(\Delta\theta)}{1 - \cos(\Delta\theta)} \tag{3.4}$$

However, these filters have two main disadvantages. First, because they are passive, the desired signal at the output necessarily has power losses (insertion loss), which are highly dependent on the load impedances. This downside makes it convenient to use drivers at the output to compensate for the attenuation suffered in the PPF or preceding stages. Also, they can be mandatory to achieve enough signal-to-noise ratio (SNR) along the signal chain. On the other hand, the sole use of capacitors and resistors also implies a much higher linearity than the achievable with active components [Hir20].

In addition, since the operation is based on the behavior at the exact point of the cut-off frequency, perfect cancelation (even in the ideal case) only occurs at the poles of the system defined by the RC sets of each stage. In other words, the PPF will not ideally reject the IQ signal with a negative sequence at any different frequency. This behavior has two consequences: 1) the system will be very sensitive to effects that change the values of the resistors and capacitors, and 2) the bandwidth of a filter with poles at

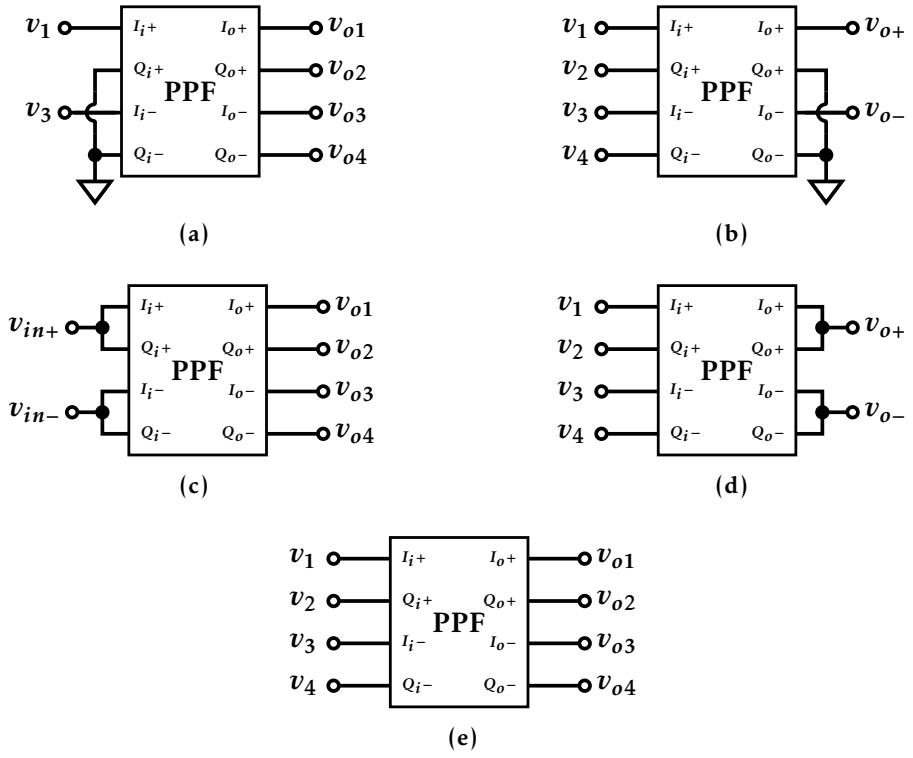

Figure 3.4: Different PPF configurations: (a) Type I as D-IQ converter; (b) Type I as IQ-D converter; (c) Type II as D-IQ converter; (d) Type II as IQ-D converter; and (e) IQ filter.

the same single frequency will be unhelpfully narrow for the great majority of applications. Both problems are alleviated by carefully selecting poles and designing to minimize non-idealities. Chapter 4 details the selection and design process for a practical case.

3.1.2 PPF types

According to how the connection is made at the differential end, the classification distinguishes two types of PPF: Type I and Type II [Kau08]. Each option conditions the kind of error (amplitude or phase) assumed in the differential signal if considered an IQ signal. Each type is usable for both classes of converters (D-IQ and IQ-D). In addition, the PPF can be used as an IQ filter, being both terminations IQ signals in this application. All these five possible configurations are shown in Figure 3.4.

3.1.2.1 IQ filter configuration

In this application, both the input and the output of the PPF are IQ signals; hence, no conversion is performed, but the filter aims to pass the desired sequence while canceling the undesired one (typically, the image).

Transfer functions of simple RC and CR circuits (labeled H_1 and H_2, respectively) can describe the filter behavior,

$$\begin{aligned} H_1 &= \frac{1}{1+sCR} = \frac{1}{1+jb} = \frac{1-jb}{1+b^2} \\ H_2 &= \frac{sCR}{1+sCR} = \frac{jb}{1+jb} = \frac{b(j+b)}{1+b^2} \end{aligned} \tag{3.5}$$

where C is the value of capacitors, R is the value of resistors, and b is the product ωRC, equivalent to the normalized frequency, *i.e.*, the frequency referred to the one that the stage is tunned ($\omega_0 = 1/RC$, $b = \omega/\omega_0$). As usual, j refers to the imaginary unit and s to the complex frequency domain variable.

The block diagram of Figure 3.5 depicts the relationship between outputs and outputs as a function of H_1 and H_2. In this way, and defining v_o as the output signal, in-phase v_o component (I) and quadrature v_o component (Q) are

$$\begin{aligned} I &= H_1 \cdot (v_1 - v_3) - H_2 \cdot (v_2 - v_4) \\ Q &= H_1 \cdot (v_2 - v_4) + H_2 \cdot (v_1 - v_3) \end{aligned} \tag{3.6}$$

As previously mentioned, the IRR outlines the relationship between the output power with a positive and negative input. The positive or desired sequence (s_+) implies that $v_1 = v_{in}/2$; $v_2 = jv_{in}/2$; $v_3 = -v_{in}/2$; and $v_4 = -jv_{in}/2$; while the image or negative sequence (s_-) suppose a sign switch between v_2 and v_4 ($v_1 = v_{in}/2$; $v_2 = -jv_{in}/2$; $v_3 = -v_{in}/2$; and $v_4 = jv_{in}/2$).

Substituting, simplifying, and exploiting I and Q orthogonality, then,

$$IRR|_{IQ\to IQ} = \frac{|v_o|^2_{s_+}}{|v_o|^2_{s_-}} = \frac{|I|^2_{s_+} + |Q|^2_{s_+}}{|I|^2_{s_-} + |Q|^2_{s_-}} = \frac{2 \cdot \frac{(1+b)^2}{1+b^2} \cdot v_{in}^2}{2 \cdot \frac{(1-b)^2}{1+b^2} \cdot v_{in}^2} = \frac{(1+b)^2}{(1-b)^2} \tag{3.7}$$

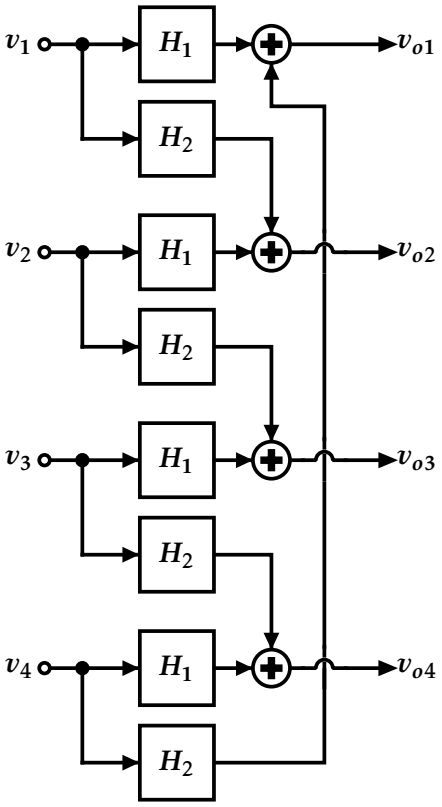

Figure 3.5: Standard one-stage PPF block diagram.

where this is the IRR expression for an ideal one-stage PPF with a pole at $\omega = 1/RC$ in the IQ filter configuration. Section C.3 of Appendix C presents the complete analytical development for this case.

3.1.2.2 Type I

In Type I, the differential signal is connected to two non-adjacent terminals of the four input terminals (typically $I+$ and $I-$), while the other two are open or grounded. It can be shown that the circuit nodes corresponding to the non-excited terminals are virtual grounds for the differential mode and, hence, both alternatives are equivalent [Kau08]. As a consequence of the above, the differential signal can be described as an IQ signal that has no phase error but suffers from maximum amplitude error ($|Q| = 0$).

When used as a D-IQ converter (Figure 3.4a), the filter tends to correct the amplitude error at the input. The PPF perfectly achieves the correction at the pole. In other words, the filter produces an ideal IQ signal with the desired sequence at that frequency.

Analytically, the relationship between inputs and outputs is (3.6), but now $v_2 = v_4 = 0$, that is,

$$I = H_1 \cdot v_{in} = \frac{v_{in}}{1+jb} = \frac{1-jb}{1+b^2} \cdot v_{in} \tag{3.8}$$

$$Q = H_2 \cdot v_{in} = \frac{jb \cdot v_{in}}{1+jb} = \frac{b(j+b)}{1+b^2} \cdot v_{in} \tag{3.9}$$

where I and Q are the in-phase and quadrature components of v_o, respectively. Note that $jb \cdot I = Q$, so 1) the amplitude balance varies with b and 2) both components are in quadrature ($\theta_Q = \theta_I + \arctan(1/0) \Rightarrow \theta_I - \theta_Q = -\pi/2$), *i.e.*, there is no phase shift error. In other words, the PPF does not alter the input phase difference. Thus, the expression (3.2) can be simplified as

$$IRR = \frac{1 + 2 \cdot \cos(\Delta\theta) \cdot A_{BAL} + A_{BAL}^2}{1 - 2 \cdot \cos(\Delta\theta) \cdot A_{BAL} + A_{BAL}^2} = \left(\frac{1+A_{BAL}}{1-A_{BAL}}\right)^2 = \frac{(1+b)^2}{(1-b)^2} \tag{3.10}$$

Note that the final expression for this case is identical to (3.7).

The decomposition into symmetric components (Section 2.2.2), together with the expected behavior of the PPF, allows a more intuitive qualitative view of the phenomenon. This is graphically illustrated in Figure 3.6. Starting with the input signal in Type I configuration ($v_2 = v_4 = 0$ and $v_1 = v_3$), this signal can be described as the sum of two ideal IQ signals of equal amplitude (half the original) and opposite sequence [Beh01]. The figure shows how the p_1 and p_3 components of the two sequences are combined, while p_2 and p_4 cancel each other out.

Nevertheless, each component will have a different response in the filter, with the negative sequence ideally canceling at the filter output. Therefore, an ideal IQ signal ($A_{BAL} = 1$, $\Delta\theta = 0$) is obtained at the output. However, the unwanted component canceling is not perfect outside the pole frequency. Its influence causes the amplitudes of phasors corresponding to I_{in} (p_1 and p_3) to increase while those of Q_{in} (p_2 and p_4) decrease, thus altering the amplitude balance.

In the case of reverse conversion (IQ-D), the positive signal (v_{o+}) of the differential output signal (v_o) is taken at v_{o1}, while the negative signal (v_{o-}) is taken at v_{o3}. The configuration also implies that $v_{o2} = v_{o4} = 0$, and consequently, the stage is divided

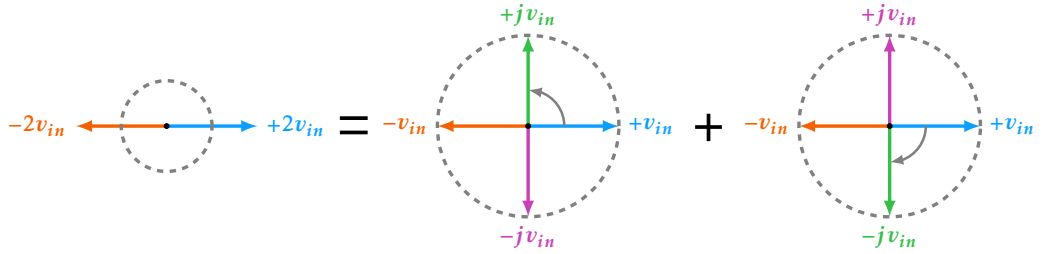

Figure 3.6: Decomposition of a Type-I differential signal into 4-phasor symmetric components. Colors describe the four different phasors: P_1 (blue), P_2 (green), P_3 (orange), and P_4 (magenta).

into two subcircuits described by the following pair of equations,

$$\left.\begin{aligned} v_{o+} &= H_1 \cdot v_1 + H_2 \cdot v_4 = \tfrac{v_1 + jb \cdot v_4}{1+jb} \\ v_{o-} &= H_1 \cdot v_3 + H_2 \cdot v_2 = \tfrac{v_3 + jb \cdot v_2}{1+jb} \end{aligned}\right\} v_o = \frac{(v_1 - v_3) - jb \cdot (v_2 - v_4)}{1 + jb} \tag{3.11}$$

Substituting for each sequence,

$$\left.\begin{aligned} v_o|_{s_+} &= \tfrac{1+b}{1+jb} \cdot v_{in} \Rightarrow |v_o|^2_{s_+} = \tfrac{(1+b)^2}{1+b^2} \cdot v_{in}^2 \\ v_o|_{s_-} &= \tfrac{1-b}{1+jb} \cdot v_{in} \Rightarrow |v_o|^2_{s_-} = \tfrac{(1-b)^2}{1+b^2} \cdot v_{in}^2 \end{aligned}\right\} IRR = \frac{|v_o|^2_{s_+}}{|v_o|^2_{s_-}} = \frac{(1+b)^2}{(1-b)^2} \tag{3.12}$$

Again, the IRR expression obtained is identical to the previous configurations.

From a qualitative point of view, a differential IQ signal (four phasors) is composed of two differential ones (two phasors each). Thus, the differential output signal is proportional to the IQ output. Moreover, under ideal conditions, the PPF does not change the IQ sequence of the signal. Therefore, the v_o comparison of the expression (3.12) is equivalent to comparing how much IQ signals are attenuated due to their sequences. In other words, the PPF will produce a differential signal only if the input IQ signal has the desired sequence.

In addition, all four outputs should have equal loads. This way, the circuit becomes as balanced as possible and avoids unwanted effects degenerating its performance.

The complete analytical developments for Type I as D-IQ and IQ-D converters can be found in sections C.1.1 and C.2.1 of Appendix C, respectively.

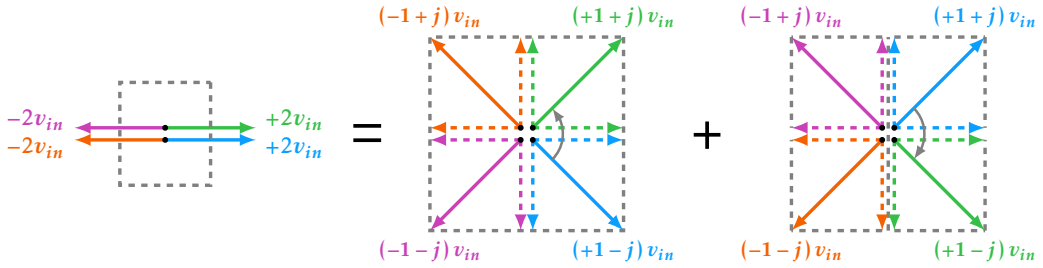

Figure 3.7: Type II differential signal decomposed into symmetrical IQ components. Note that the differential signal has no projection in the collinear components, although it may seem similar at first glance.

3.1.2.3 Type II

In Type II, each end of the differential signal is connected to two adjacent terminals of the filter, leaving the four terminals connected in pairs. This connection produces a complementary effect to the previous one regarding error cancellation. That is, the amplitudes of I and Q at this point are necessarily identical ($v_1 = v_2$ and $v_3 = v_4$; or $v_{o1} = v_{o2}$ and $v_{o3} = v_{o4}$), so $A_{BAL} = 1$, but the phase error is only avoided at the pole. Another effect of this configuration is that the input impedance presented by the filter is lower than in Type I [Kau08]. In other words, the PPF type influences the selection of R and C values.

When used as a D-IQ converter (see Figure 3.4c), the inputs are short-circuited two by two to receive the differential signal. In this configuration, the applied input signal is composed of four phasors (one for each input) of equal amplitude but zero (P_1 and P_2) or π (P_3 and P_4) phase. Each phasor can be split into two identical components of equal amplitude and phase. Then, opposite contributions can be added to each half phasor, both of the same amplitude of the half phasors but orthogonal to them ($\pi/2$ and $3\pi/2$ phase). In short, this means that a differential signal in a Type-II approach can be described as two symmetrical IQ signals of opposite sequence and amplitude $\sqrt{2}$ times smaller than the original. Figure 3.7 illustrates the explanation.

Analytically, output I and Q signals are obtained from v_{in} as

$$I = (H_1 - H_2) \cdot v_{in} = \frac{1 - jb}{1 + jb} \cdot v_{in} = \frac{(1 - jb)^2}{1 + b^2} \cdot v_{in} \tag{3.13}$$

$$Q = (H_1 + H_2) \cdot v_{in} = \frac{1 + jb}{1 + jb} \cdot v_{in} = v_{in} \tag{3.14}$$

where H_1 and H_2 are the transfer functions defined in (3.5).

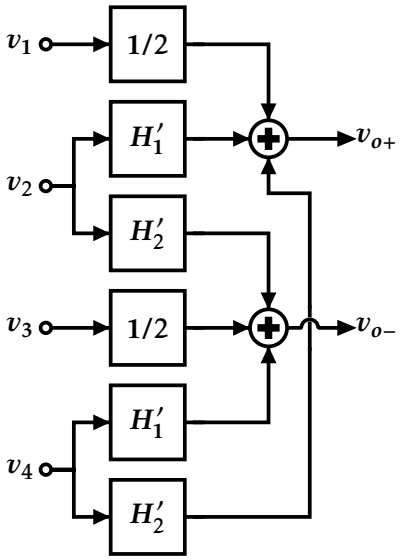

Figure 3.8: Type-II IQ-D conversion diagram block.

The comparison of the penultimate forms of (3.13) and (3.14) shows that the modulus of both is identical ($|1 - jb| = |1 + jb|$), since b is real. Consequently, A_{BAL} is also ideal, *i.e.*, $A_{BAL} = 1$ for any b. However, this will not be the case for the phase. Considering v_{in} as the reference signal,

$$\cos(\Delta\theta) = \cos\left(-\frac{\pi}{2} - \theta_I + 0\right) = \sin\left(\arctan\left(\frac{2b}{1-b^2}\right)\right) = \frac{2b}{1+b^2} \tag{3.15}$$

Substituting in (3.4) and benefiting from $A_{BAL} = 1$,

$$IRR = \frac{1+\cos(\Delta\theta)}{1-\cos(\Delta\theta)} = \frac{\left(1+b^2\right)+2b}{(1+b^2)-2b} = \frac{(1+b)^2}{(1-b)^2} \tag{3.16}$$

Once again, the analysis obtains the same expression for the IRR.

The Type-II IQ-D conversion has the particularity of using a different transfer function set due to the effect of connecting pairs of outputs. These connections imply the

diagram from Figure 3.8. And the expressions are

$$H_0 = \frac{R \,/\!/\, \frac{1}{sC}}{R \,/\!/\, \frac{1}{sC} + R \,/\!/\, \frac{1}{sC}} = \frac{1}{2} \tag{3.17}$$

$$H_1' = \frac{\frac{R}{1+2sCR}}{R + \frac{R}{1+2sCR}} = \frac{1}{2} \cdot \frac{1}{1+jb} = \frac{1}{2} \cdot \frac{1-jb}{1+b^2} \tag{3.18}$$

$$H_2' = \frac{\frac{sCR/2}{1+sCR/2}}{1 + \frac{sCR/2}{1+sCR/2}} = \frac{1}{2} \cdot \frac{jb}{1+jb} = \frac{1}{2} \cdot \frac{b(j+b)}{1+b^2} \tag{3.19}$$

Expanding the expressions from the diagram and substituting v_n for each input sequence,

$$\left.\begin{aligned} v_o|_{s+} &= \tfrac{(1+b)^2+j\left(1-b^2\right)}{2(1+b^2)} \cdot v_{in} \Rightarrow |v_o|^2_{s+} = \tfrac{(1+b)^2}{1+b^2} \cdot \tfrac{v_{in}^2}{2} \\ v_o|_{s-} &= \tfrac{(1-b)^2}{1+b^2} \cdot \tfrac{v_{in}^2}{2} \Rightarrow |v_o|^2_{s-} = \tfrac{(1-b)^2}{1+b^2} \cdot \tfrac{v_{in}^2}{2} \end{aligned}\right\} IRR = \frac{|v_o|^2_{s+}}{|v_o|^2_{s-}} = \frac{(1+b)^2}{(1-b)^2} \tag{3.20}$$

Once more, the IRR expression is equivalent to the previous configurations. Sections C.1.2 and C.2.2 of Appendix C present the complete analytic development for an ideal Type-II PPF.

3.1.2.4 Comparison

The IRR metric is equivalent for all configurations, even if each IRR definition is slightly different. Whether the goal of the PPF is to produce an IQ signal or the inverse transformation to differential mode, the ability of the filter to remove the unwanted IQ sequence component ultimately determines the quality of the operation.

In turn, Type I and Type II are two strategies for solving the same problem: connecting a differential signal (two physical components) to a differential IQ port (four physical terminals). These approaches suppose sacrificing the ideality (at all frequencies but the pole) of one of the quantities that define these signals, *i.e.*, amplitude or phase. Any error in these quantities (or a combination of both) leads to a deterioration in the ratio between the desired sequence signal and its image, as shown in (3.2). In other words, in the vast majority of cases, both types will give the same IRR result.

However, there are some differences. The different connection means that input and output impedances are distinct for both types, which determine the values of the devices in the circuit [Kau08]. In turn, type selection may affect the specifications of the available components for implementation. Moreover, the additional ports in a Type-II configuration typically mean a 3 dB improvement in insertion loss, making this configuration more desirable on equal terms.

In short, the primary IRR expression for a single-stage PPF under ideal conditions is

$$IRR = \left(\frac{1+b}{1-b}\right)^2 = \left(\frac{\omega_0+\omega}{\omega_0-\omega}\right)^2 \tag{3.21}$$

Where ω_0 is the pole frequency ($1/RC$), and b is the normalized frequency.

3.1.3 Multi-stage filters

Due to its characteristics, a single-stage PPF is rarely employed in practice because the filter will only obtain a virtually infinite IRR at the tuned frequency. The PPF bandwidth (BW_{PPF}), defined as the range of frequencies over which the filter achieves the desired IRR, is very narrow. Thus, it would limit the desired signal bandwidth (BW). Some non-idealities exacerbate this problem, requiring the addition of some margin to mitigate such effects. In integrated PPFs, device constraints tend to aggravate this problem.

Since each stage of a PPF includes a new pole in the IRR function [Had10], for N poles, the IRR can be expressed as

$$IRR = \prod_{n=1}^{N}\left(\frac{\omega_{0n}+\omega}{\omega_{0n}-\omega}\right)^2 \tag{3.22}$$

where ω_{0n} is the pole of the stage n.

It is not difficult to observe then that, for multiple equal poles, the IRR value will be higher than for a single pole, and consequently, the BW_{PPF}, as defined, will increase. However, the benefit of this strategy (equal poles) is marginal, and non-idealities further impair it in practice.

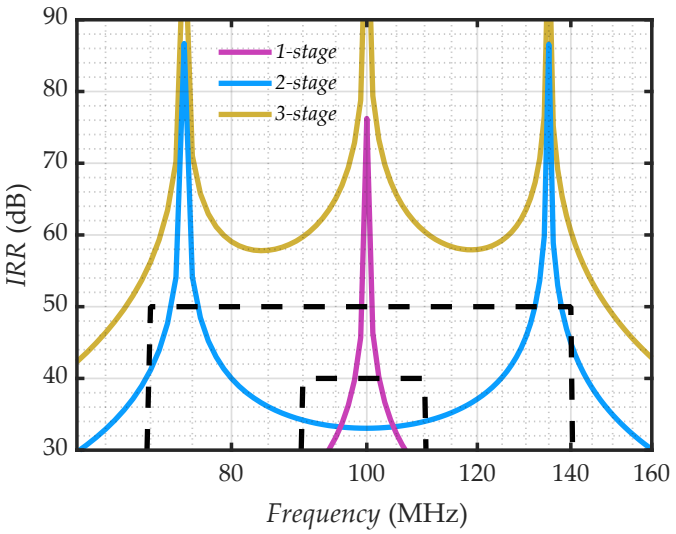

Figure 3.9: IRR curves of PPFs with different stage numbers. The interior black dashed rectangle represents the desired IRR and BW; thus, the IRR curve must be above the rectangle. The exterior black dashed line describes the actual specifications of BW_{PPF} and IRR with realistic margins.

Instead, spreading the poles across the frequency range of interest is much more beneficial. Adding multiple poles in this way means that bandwidth and IRR increase, with the enhancement of the former or the latter depending on the pole separation. However, this also presents a disadvantage: each extra pole requires an additional stage, hence a 3 dB increase in the insertion loss. Figure 3.9 shows the simulation results for three PPFs centered at 100 MHz with different stages. Chapter 4 includes more quantitative details about these trade-offs. Still, for qualitative reference, filter constraints and additional margins (both in IRR and BW_{PPF}) are shown in advance in these graphs to illustrate the required compensation for non-idealities in practice. Figure 3.9 clearly shows how adding a second pole at separate frequencies greatly extends the filter frequency range. Adding the third pole between the other two, on the other hand, means a significant increase in the complementary magnitude, the IRR.

The main difference between the last two PPFs is the separation between the poles, which is a critical variable in the PPF design. This distance determines a trade-off between BW_{PPF} and the achievable IRR. The closer they are, the higher the IRR in the pole vicinity, but the range in which poles have a significant impact will be narrower. The further each other they are, the opposite effect occurs: the filter will cover a broader range at the expense of a less ambitious IRR. In addition to the direct implication (controlling the trade-off between BW_{PPF} and IRR within the range of interest), it is

also an important tool to optimize the relationship between nominal results and PPF robustness to variations.

Moreover, obtaining the minimum number of poles to guarantee a given IRR in the bandwidth of interest is not a trivial task [Gin75; Nik15]. The trade-offs and the complex impact of non-idealities on the PPF make accurate estimation difficult *a priori* [McG87; Nis11; Kau08]. Therefore, initial design requires generous margins added to the specifications to fulfill the desired characteristic when more complex (and closer to reality) simulations are carried out, especially when including random parameters. For example, in Figure 3.9, the simulated design aims to 50-dB IRR from 70 to 140 MHz to achieve final specifications of 40 dB from 90 to 110 MHz.

Section 4.1 shows a practical case of pole selection optimization and suggests strategies to ease initial design decisions, anticipating non-idealities impact to improve accuracy and reduce risks.

3.1.4 Non-idealities effects

When designing a PPF, considering the non-idealities of the filter components is essential. These effects restrict the maximum archivable IRR and may produce significant frequency shifts in the frequency response. Moreover, most of these degradations are not easily predictable, introducing a hazardous uncertainty in the IRR of implemented PPFs.

As previously mentioned, the filter performance is based on its network balance. Some authors [Kau08; Tan13] typically focus on effects that equally alter all components (for example, process or temperature variations). On the other hand, the study of non-idealities that unbalance the filter has not been reported in such detail due to their difficulty [Beh01], although their impact is by no means less relevant; calculating it is complex because those non-idealities disturb the own filter working principles. Section 3.2 discusses the effects of PPF unbalance in more detail, while following subsections describe the main non-idealities that can alter a PPF performance [Mar17].

Simulation results from the three-stage PPF illustrate the distinct non-idealities, using a Type-I D-IQ converter configuration by default. Those graphs provide qualitative information to understand the ensuing sections and chapters better. Nevertheless, those

sections will offer analytical results and details about their relevance to the design process.

3.1.4.1 Temperature and process variations

Both variations have an identical effect on PPFs; hence, for simplicity, the text hereafter refers to the sum of them as process variations.

Although temperature and process variations depend on the time of operation or are fixed at the time of fabrication, both are global variables that, outside designers control, uniformly alter similar element of the physical circuit. Thus, their models and methods to compensate for them are almost identical from the perspective of a designer. More details on these variations and how to model them can be found in Section 2.3, while Section 4.1 deeps into methods to mitigate their impact.

In a PPF, these variations affect all resistors and capacitors, altering the frequency response of the filter. However, since each resistor is equally affected, and the same is true of capacitors, the poles change but their (geometric) spacing does not vary. In other words, the shape of the IRR curve remains identical but frequency-shifted [Kau08].

Figure 3.10 shows the effect of this type of variation on a three-stage PPF simulation, with the shift toward higher frequencies in blue: lower component values and typically lower temperature, *ff* corner in the employed technology models; and toward lower frequencies in red: higher component values and typically higher temperature, *ss* corner in the used technology models. The graph uses the extreme temperature values of the industrial range, *i.e.*, 80 and −40 °C.

As mentioned in Section 2.3.1, the potential variations of microelectronic devices may be massive, reaching even 40 % variations for some kinds of integrated resistors, and reducing them below a 20 % tolerance might require significant sacrifices in area, frequency, or economic cost. In short, the effect is severe but predictable.

This non-ideality is the main reason why a PPF must cover a frequency range (BW_{PPF}) much larger than the actual BW of the signal. In some cases, tunable elements might be available to address this issue, but the performance of these tunable devices is usually insufficient for the demanding communication field, or their cost is too expensive.

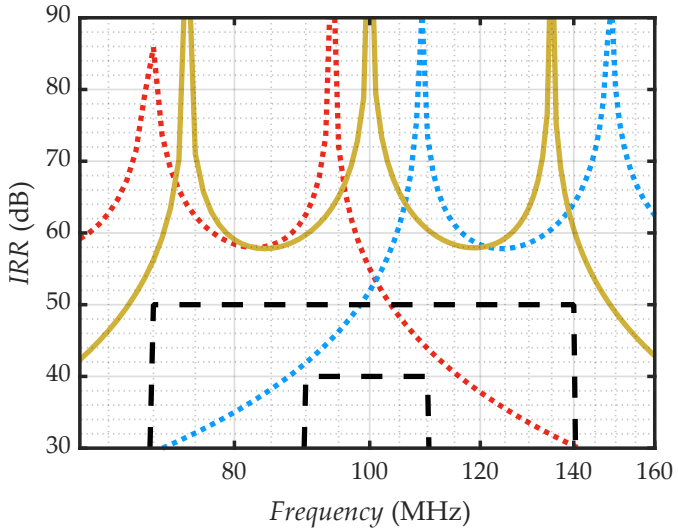

Figure 3.10: Three-stage PPF simulation in different process variation corners: typical (yellow), *ss* (red), and *ff* (blue). The *ss* and the *ff* corners include process fabrication variations in the narrowest sense as global variable and temperature effects.

Figure 3.10 depicts the global process variation impact on the BW_{PPF} specification: while the signal BW is the interior black dashed rectangle (90-110 MHz), the PPF must cover from 70 to 140 MHz to guarantee the operation after these variations. Note that red and blue lines almost entirely consume the BW margin despite being several times larger than the signal BW.

3.1.4.2 Mismatch

Differences between ideally equal elements are the mismatch variations. They appear due to gradients of process variations and inevitable imperfections of the fabrication, and because of them, devices supposed to be identical differ from each other. These deviations are especially dangerous for PPFs, as they upset the balance of the filter.

Figure 3.11 shows a comparison of the impact of mismatch in a three-stage PPF. The data in the figure have been obtained through Monte Carlo analyses of 500 samples, using the mismatch statistical models of resistors and capacitors (Section 2.3.1.2 for more details). Simulations evaluate two types of PPF (Type I and II) under these conditions, as well as two sets of component values, one using 200 fF capacitors and the other 500 fF. The resistances in such cases are sized to maintain the same poles, and global process variations are neglected.

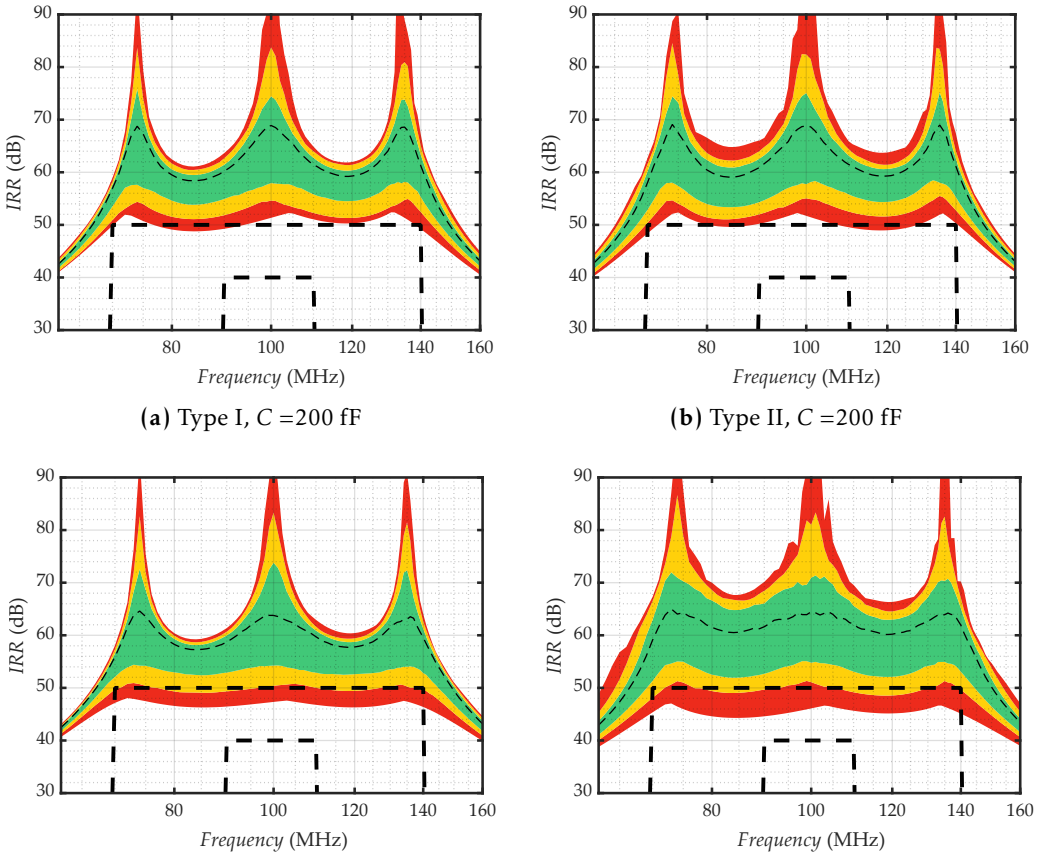

(a) Type I, C =200 fF

(b) Type II, C =200 fF

(c) Type I, C =500 fF

(d) Type II, C =500 fF

Figure 3.11: *IRR* curves of PPFs with mismatch for different types and component values. The thin dashed line is the median value for each frequency. Additive green, yellow, and red areas correspond to the 70, 95, and 100 % percentiles centered on the median *IRR*, respectively.

The disparate deformation produced by each mismatch combination makes the direct representation of the analysis curves unclear. However, a heat map allows for a more intuitive visualization. The green region encapsulates the median value and 35 % percentiles upper and lower that value, *i.e.*, the 70 % center cases. The percentage extends to 95 % with the inclusion of the yellow areas. Each red zone implies a 2.5 % of most extreme results to the best or worst *IRR*. Note that each frequency has its own percentiles, and they are independent of each other.

Although each frequency is evaluated in isolation and the *IRR* curve of each specific sample is lost, the three poles remain clearly identifiable throughout the heat map. This detail is significant given the irregular deformation suffered by each particular case, being deduced that 1) the mismatch tends to degrade the *IRR*, but the degradation can be significantly less severe from one mismatch combination to another, and 2) poles do not move without suffering a strong *IRR* attenuation.

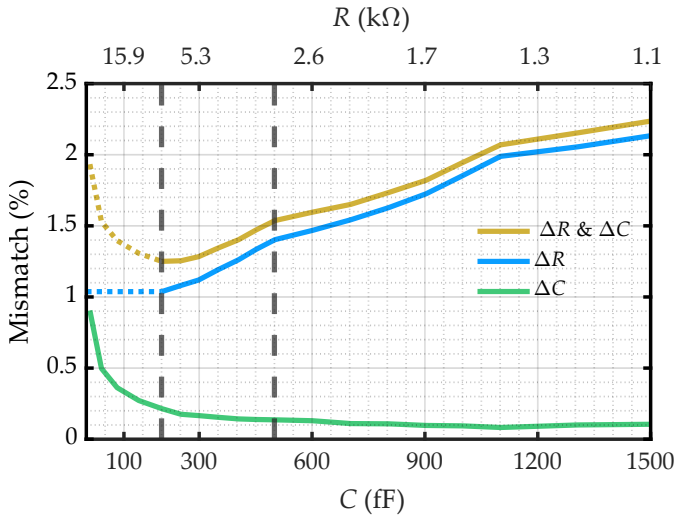

Figure 3.12: Mismatch tolerance of devices from the employed technology to produce a 100-MHz pole. Vertical dashed black lines marks resistor-capacitor values from Figure 3.11

Moreover, mismatch impact may combine with frequency shifts of global process variations, thus aggravating the IRR decrease on the BW of interest. Consequently, a certain margin of IRR must be left to fulfill specifications. Also, a BW additional margin may become mandatory if mismatch tolerance is of the same order of global process variations.

Figure 3.11 also reveals a better performance, i.e., less variance, with 200 fF than 500 fF; Figure 3.12 deeps in the causes. The graph presents maximum mismatch variations (mismatch tolerances) in 1024-sample Monte Carlo analyses for resistors and capacitors. Values of both devices (the upper and the lower horizontal axes) are aligned to produce a 100-MHz pole. Also, the yellow curve shows the combined mismatch, *i.e.*, $(1-\Delta R)(1-\Delta C)$. Note that it is mainly described by resistor variations as capacitor mismatch is negligible by comparison. Resistor sizing is restricted to 1.5 μm wide to optimize mismatch and a maximum of 100 μm length. Variations in resistors are more significant than potential deviations in capacitors. This fact is not unusual in integrated technologies [Has01]. Nevertheless, Type-I and Type-II PPFs do not present significant differences in this aspect, although Type II seems to increase its variability slightly.

On the other hand, Figure 3.13 shows that the mismatch effect largely depends on the stage position. Since the mismatch produces an error in the quadrature, but its absence corrects it, distortions due to mismatch in the first stages might be restored, as

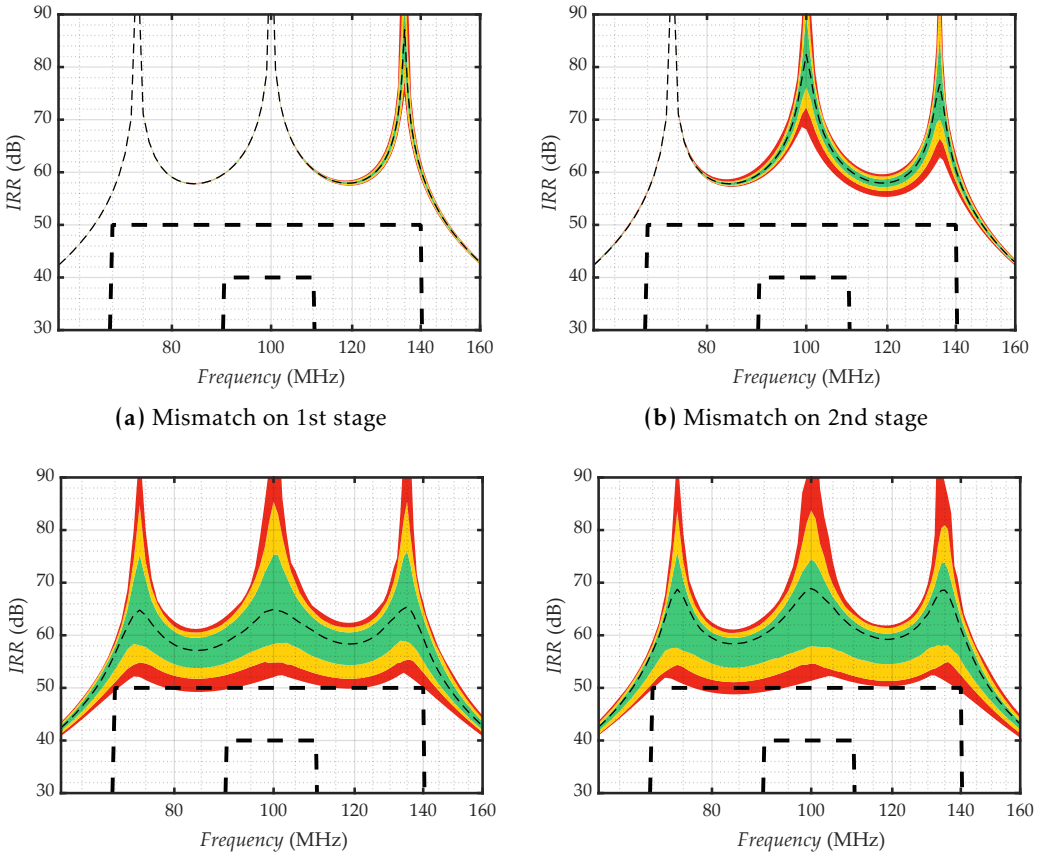

(a) Mismatch on 1st stage

(b) Mismatch on 2nd stage

(c) Mismatch on 3rd stage

(d) Mismatch on all stages

Figure 3.13: *IRR* curves of PPFs with mismatch on different stages. The thin dashed line is the median value for each frequency.

opposed to the caused due to later stages errors. Furthermore, subsequent ideal stages can alleviate the variations caused in the vicinity of its pole. However, when there is any mismatch, the effect is the opposite, and the imbalance degrades the performance in the pole vicinity.

In this way, if only the first stage suffers the mismatch effect (3.13a), its impact is negligible; however, when the last stage (Figure 3.13c) has this non-ideality, the result is almost equivalent to having it in all stages (Figure 3.13d). The case of evaluating mismatch in the second stage (Figure 3.13b), which corresponds to the central pole, is also worth mentioning; significant variations appear in the area close to the pole of the stage with mismatch and the one of the previous stage. However, the vicinity of the last-stage pole is barely affected.

Note that despite mismatch tolerances being typically smaller than global process variations, they may cause more severe and less predictable effects; hence, the importance

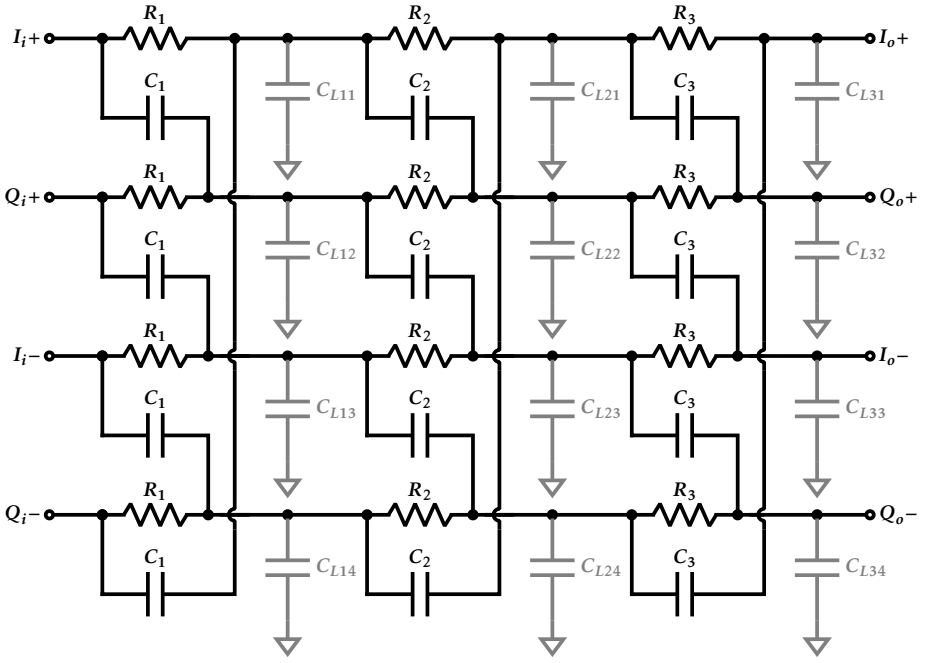

Figure 3.14: Three-stage PPF. The most relevant parasitics are shown in grey.

of the study comprised in the Section 3.2 of this chapter, despite the difficulty of obtaining or finding quantitative information in the bibliography.

3.1.4.3 Parasitics

Since reducing capacitor values and increasing resistor is advisable to minimize IRR degradation due to mismatch, the resistive parasitics have a marginal impact and can be neglected. Therefore, the dominant effects can be modeled as a grounded capacitor at each node, as shown in Figure 3.14. It is known that if all parasitic capacitors of each stage are equal, the IRR is not altered, although they increase insertion loss [Kau08].

However, differences between parasitic capacitances may critically affect the IRR. Discrepancies may cause a similar phenomenon to mismatch, and for the same reasons, this is especially critical for the last stage.

Besides, mismatch alike, those variations that produce dissimilarity between I and Q branches ($C_{Ln1} = C_{Ln3} \neq C_{Ln2} = C_{Ln4}$ in Figure 3.14) will cause a more significant IRR degradation. At the same time, those that alter other pairs while not altering the I-Q balance (for example, $C_{Ln1} = C_{Ln2} \neq C_{Ln3} = C_{Ln4}$) have negligible impact on the IRR. Figure 3.15 illustrates the different effect that last stage load balance has in IRR.

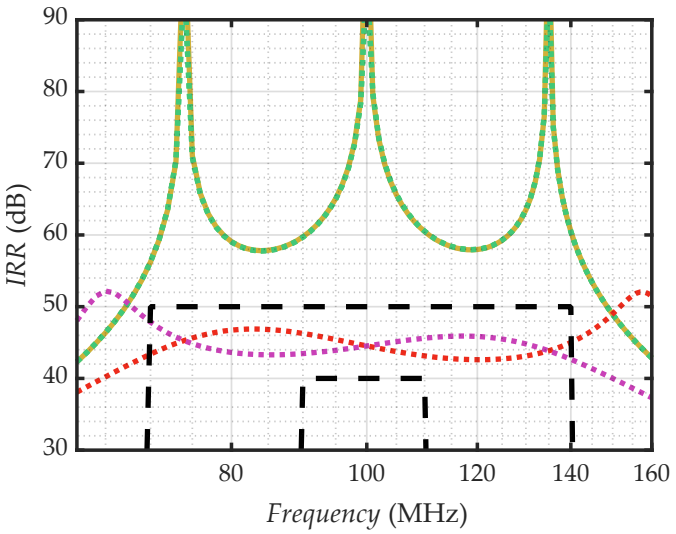

Figure 3.15: Last-stage parasitics impact on the PPF *IRR*. In green and overlapped with the ideal case (yellow) is the I and Q symmetric parasitics deviation case ($C_{L31} = C_{L32} \neq C_{L33} = C_{L34}$). Red and magenta lines are the *IRR* when parasitics of each branch are unbalanced ($C_{L31} = C_{L33} \neq C_{L32} = C_{L34}$).

3.2 Mismatch analysis

As previously mentioned, the circuit balance is a critical factor for the design and optimization of PPF. Among the non-idealities, the mismatch effect describes the primary deviations that unbalance the filter. Therefore, a PPF designer undoubtedly benefits from knowing the relationship between this non-ideality and the *IRR* degeneration it produces. Based on this information, PPF specifications translate as a list of device requirements even before any simulation.

Despite the potential usefulness for designing, authors could not find an in-depth analytical study of the mismatch impact on the literature [Mar18b]. Thus, an exploration of this effect has been done, and it is presented here. The analysis of this non-ideality is not easy to perform. On the one hand, the endless possibilities notably obscure a simulation approach and conclude anything from its results. On the other hand, the network complexity causes the analytical expressions to become completely unmanageable when the circuit is not in perfect balance. That condition is opposite to the mismatch definition.

Consequently, an analysis strategy combining both methods is applied to overcome both issues. First, an algebraic basis is defined to cover the space of possible mismatch

combinations for a one-stage PPF. This way, the properties of the selected basis vectors allow to narrow down the space that contain the worst case. Once determined, an analytical development under the worst-case mismatch scenario produces interesting expressions and limits depending on the device mismatch. Finally, the results are extrapolated and tested for multi-stage situations.

3.2.1 Worst-case search for a 1-stage PPF

Analyzing the effect of mismatch requires studying how severe its impact may be on the PPF performance, *i.e.*, finding the worst possible combination of individual component variations for a given device tolerances. Since IRR is the metric of merit, the worst-case definition is the one that causes the most extreme IRR degradation.

The infinite number of possible combinations makes a purely analytical method infeasible (or at least impractical) for this purpose. Since the variables of each element are independent, it would be necessary to use as many mismatch variables as circuit elements to model all possible cases, and each of those variables is continuous. This path inevitably leads to expressions that are overly complex to obtain and difficult to interpret. And since the number of options increases with the number of stages, the case space (and thus the problem) grows exponentially.

On the other hand, knowing which is the worst case is very advantageous. When applied to a circuit simulation, this knowledge enables testing the reliability of a design with a single simulation rather than resorting to a statistical analysis with hundreds of simulations. Designers also benefit from being aware of which is the worst mismatch as it provides them with guidelines to minimize the effects of mismatch.

However, how can we identify that helpful worst case among such a vast case space?

The deviation of each device can be described by a variable that is independent by definition. Therefore, all possible cases suppose a K-dimensional system, where K is the number of potentially mismatched elements. Consequently, a linear combination of K linearly independent K-dimensional vectors can describe any possible case. In other words, creating a generating set (a basis) for all mismatch case space is possible, and thus, that basis can produce the most detrimental case with the appropriate coefficients.

Analytically, the set of variations can be described as

$$\boldsymbol{\Delta E} = \boldsymbol{M} \cdot \boldsymbol{U} \tag{3.23}$$

where $\boldsymbol{\Delta E}$ is a column vector ($K \times 1$) that contains each element deviation for the case, $\boldsymbol{M}$ is the basis matrix ($K \times K$ size), and $\boldsymbol{U}$ ($K \times 1$) are the coordinates of the case deviations referred to $\boldsymbol{M}$.

In the employed technology, the resistor mismatch variation is much more severe than the capacitor one. Indeed, the error of the latter is usually negligible in comparison [Mar17; All12]. Appendix H shows statistical simulation results for different technology devices.

Furthermore, a vector degrades the PPF IRR because it affects the IQ balance in amplitude (A_{BAL}) or phase ($\Delta\theta$). The discrepancies have a direct relation to IRR as complete or partial expressions show in (3.2), (3.3), and (3.4). In other words, an increase in the difference between I and Q means that the projection into the ideal desired sequence decreases in favor of different components. From one perspective to the other, the conclusion is the same: the components of the worst-case set must be extreme variations. Also, to cover cases where the impact of a specific element is negligible, zero is added as a possible "deviation." Consequently, considering a symmetric tolerance x in devices, the worst-case vector elements are necessarily $+x$, $-x$, or 0.

Because of this, the continuous infinite space is reduced to a discrete (and finite) number of combinations, 3^K, being K equal to the number of resistors, *i.e.*, four times the number of stages (N). Also, as all deviations are extreme or null values (and assuming symmetrical tolerances for clarity and custom), normalization can be done by taking out the tolerance as a common factor.

With these changes, the following expression can describe the PPF mismatch:

$$\boldsymbol{\Delta R} = x \cdot \boldsymbol{M}_N \cdot \boldsymbol{U}_N = \left[\, \Delta R_1 \;\; \Delta R_2 \;\cdots\; \Delta R_K \,\right]^T \tag{3.24}$$

where $\boldsymbol{M}_N$ is the normalized basis matrix for the N-stage PPF (dimension $4N \times 4N$), $\boldsymbol{U}_N$ ($4N \times 1$) is the weight of each vector of the basis $\boldsymbol{M}_N$, x is the tolerance, and $\boldsymbol{\Delta R}$ is the vector containing the variation of each resistor (ΔR_i).

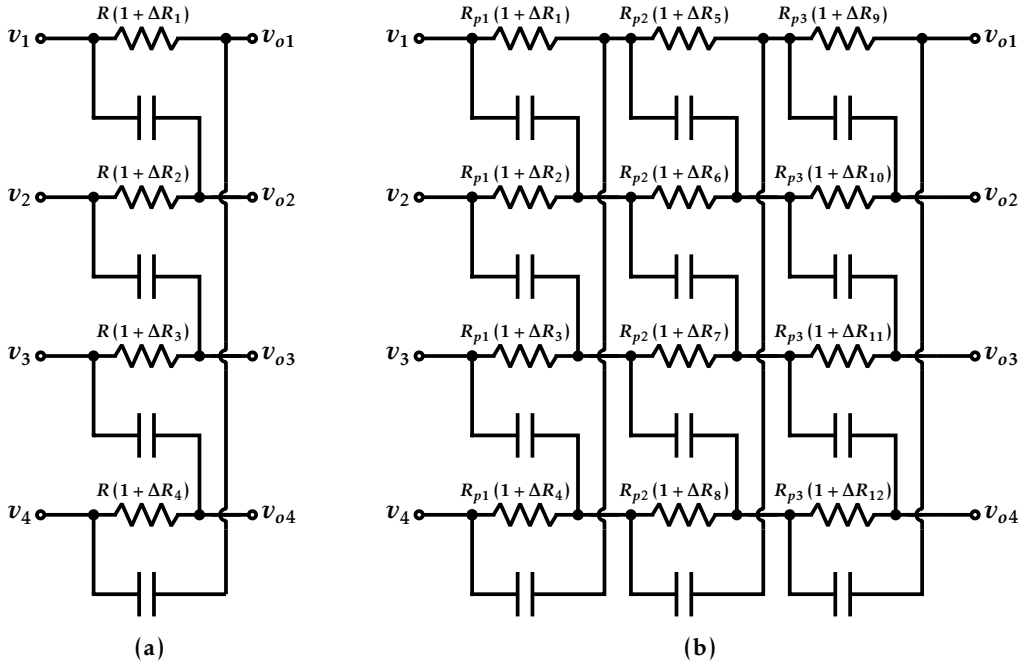

Figure 3.16: PPF with resistor mismatch: (a) single-stage and (b) three-stage case.

For consistency, the resistors are numbered analogously to the voltages, as shown in Figure 3.16 for single-stage and multi-stage PPFs. Note that absolute deviation values depend on the nominal quantities; however, the effects at different stages can be normalized by comparing the deviations as a percentage of the typical value. Thus, they become comparable and independent of absolute resistor values.

Returning to the single-stage PPF case, $\boldsymbol{M}_1$ is such that

$$\boldsymbol{M}_1 = \begin{pmatrix} m_{11} & m_{12} & m_{13} & m_{14} \\ m_{21} & m_{22} & m_{23} & m_{24} \\ m_{31} & m_{32} & m_{33} & m_{34} \\ m_{41} & m_{42} & m_{43} & m_{44} \end{pmatrix} = \begin{pmatrix} +1 & +1 & +1 & +1 \\ +1 & +1 & -1 & -1 \\ +1 & -1 & +1 & -1 \\ +1 & -1 & -1 & +1 \end{pmatrix} \tag{3.25}$$

where the first subscript of m_{nk} is the vector number of the basis (n), and the second is the affected ΔR_i.

The choice of basis vectors is made according to 1) the linear independence criteria, 2) the three possible states (+1, −1, or 0, after clearing x) of worst-case weights, and 3) favoring vectors that separate resistors by pairs. There are four resistors, so the

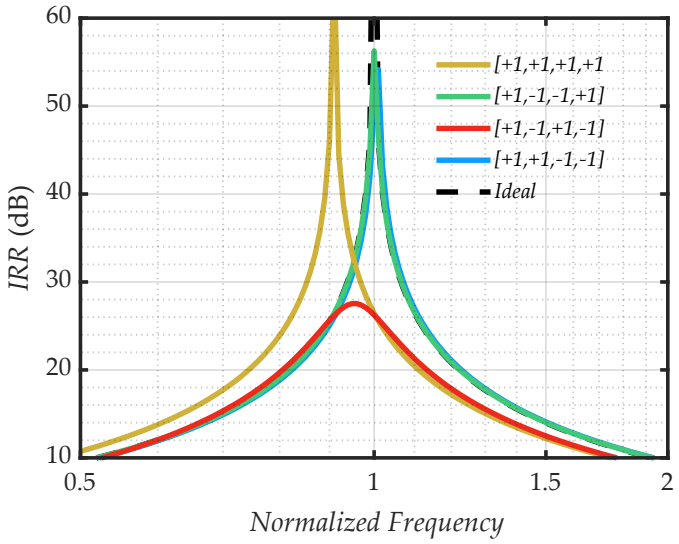

Figure 3.17: Effect of the different mismatch combinations described by each vector of $\boldsymbol{M}_1$. Tolerance is set to ±8 %.

number of different pair combinations is three. If ΔR_1 is defined as positive and the reference, then the three cases are basis vectors 2, 3, and 4, respectively, $[+1\ +1\ -1\ -1]^T$, $[+1\ -1\ +1\ -1]^T$ and $[+1\ -1\ -1\ +1]^T$. Vector 1, on the other hand, covers the case where all deviations are identical ($[+1\ +1\ +1\ +1]^T$). While it is questionable whether this particular variation can be considered strictly as a mismatch or whether it would be part of the global and uniform process deviations, the vector is orthogonal to the other three and hence completes the basis. It also provides an interesting comparison, especially when modeling mismatch between stages.

Note that the distance—defined as the sum of the squares of the elements since the nominal case is the null vector—is also equal in all basis vectors for a fair comparison of their respective effect.

Figure 3.17 shows the impact of the mismatch described by each $\boldsymbol{M}_1$ vector on the same one-stage PPF. The influence of two vectors is negligible (2 and 4, *i.e.*, $[+1\ +1\ -1\ -1]^T$ and $[+1\ -1\ -1\ +1]^T$), while the other two cause substantial changes. The first vector, $[+1\ +1\ +1\ +1]^T$, produces a frequency shift analogous to the process and temperature errors [Mar18a], which was expected as it describes the same kind of variation: all components equally vary. However, the third vector ($[+1\ -1\ +1\ -1]^T$) mainly causes a significant reduction of the peak IRR.

From this information, basis vectors 2 and 4 are far from related to the worst-case. Thus, discarding them can narrow down the space that contains the worst case. In other

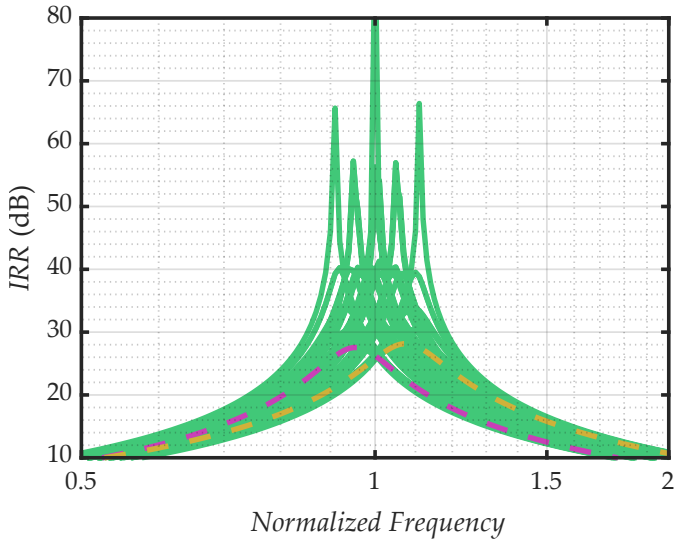

Figure 3.18: Effect of all possible mismatch combinations for a one-stage PPF under the maximum or null deviation criteria. In magenta and yellow, the worst cases, *i.e.*, $[+1\ -1\ +1\ -1\ ]^T$ and $[-1\ +1\ -1\ +1\ ]^T$, respectively.

words, the worst-case vector must be $\boldsymbol{M}_1$ vector 1, 3, or a combination of both. Two additional observations are worth mentioning. First, the basis vector 1 does not strictly describe a mismatch. Thus, it is not a good candidate for the worst-case mismatch despite having a slightly lower IRR than any other in a certain range. Second, the effects produced by vectors 1 and 3 are orthogonal to each other. Vectors with projections in both basis vectors experience proportional peak reduction and frequency shift to the respective $\boldsymbol{U}$ values. Since variations cannot exceed the tolerance value by definition (thus, $m_{kn} \leq 1$), no vector produces a frequency shift larger than $\boldsymbol{M}_1$ vector 1 or a flattening more harmful than $\boldsymbol{M}_1$ vector 3.

Consequently, $[+1\ -1\ +1\ -1\ ]^T$ is the worst mismatch combination. This conclusion confirms the intuition that the most detrimental scenario happens when I and Q elements differ from the other branches. As a demonstration, Figure 3.18 shows the result of the worst-case chosen vector (and its negative equivalent), comparing it to the rest of the 81 possible combinations of maximum-distance mismatch for the given tolerance.

Finally, note two details applied for the sake of clarity. Graphs only cover the Type-I D-IQ converter configuration, although the results can be extrapolated to the other PPF applications. Secondly, the worst-case vector produces a slight frequency shift of the peak beside the notorious IRR reduction. This deviation is observable in Figure 3.17 and 3.18 and seems to reveal a slight correlation with vector $[+1\ +1\ +1\ +1\ ]^T$, so the effects

of the first and third vectors of $\boldsymbol{M}_1$ are not strictly independent. Indeed, the chosen vector can be decomposed as a linear combination of $[\,[+1\ +1\ +1\ +1\,]^T$ and the actual vector responsible for the IRR degradation. As this vector does not fulfill the symmetric tolerances requirement, $[\,+1\ -1\ +1\ -1\,]^T$ has the largest projection into it. Section 3.2.2.6 and Appendix E contain details about this decomposition.

3.2.2 Worst-case analysis

After determining the worst mismatch combination, the five possible PPF configurations can be analyzed. As mentioned above and shown in Appendix C, the IRR expression for all of these cases is identical in the ideal case; however, will this remain valid for all the five different configurations?

The analytical development of each of the possible applications of a PPF is carried out to answer this question. For clarity, load and parasitic effects are ignored; otherwise, expressions would be unnecessarily complex due to unrelated and indirect additional terms. Systematic methods, like the one presented in the Appendix G, can obtain the expressions under any conditions but might be too obscure to draw any conclusion. For this reason, the mismatch effect in its worst combination is the only non-ideality considered. Thus, the filter experiences opposite deviations in its I and Q resistances, *i.e.*, $\Delta R_1 = \Delta R_3 = x$ and $\Delta R_2 = \Delta R_4 = -x$ (see Figure 3.19a).

Ideally, the relationships between inputs and outputs are described by functions H_1 and H_2, which model equivalent RC or CR circuits. With the addition of the mismatch, there are two variants for each. We will call them A when the resistance increases to $R(1+x)$ and B when it decreases to $R(1-x)$. The variable x is considered real, positive,

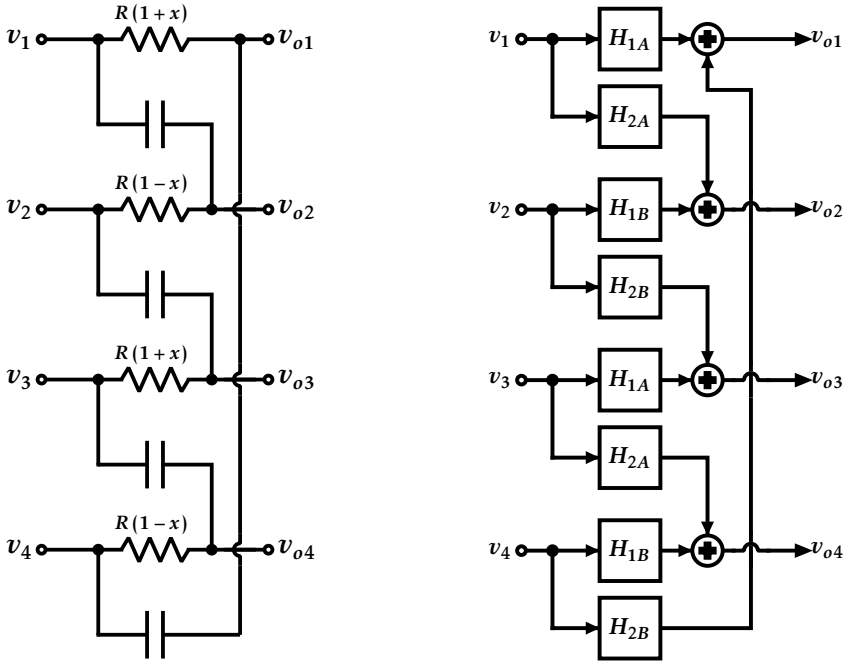

(a) Schematics **(b)** Block diagram

Figure 3.19: PPF with worst-case mismatch combination.

and significantly smaller than one. Analytically,

$$H_{1A} = \frac{1}{1+sCR(1+x)} = \frac{1}{1+jb(1+x)} = \frac{1-jb(1+x)}{1+b^2(1+x)^2}$$

$$H_{1B} = \frac{1}{1+sCR(1-x)} = \frac{1}{1+jb(1-x)} = \frac{1-jb(1-x)}{1+b^2(1-x)^2}$$

$$H_{2A} = \frac{sCR(1+x)}{1+sCR(1+x)} = \frac{jb(1+x)}{1+jb(1+x)} = \frac{b^2(1+x)^2+jb(1+x)}{1+b^2(1+x)^2}$$

$$H_{2B} = \frac{sCR(1-x)}{1+sCR(1-x)} = \frac{jb(1-x)}{1+jb(1-x)} = \frac{b^2(1-x)^2+jb(1-x)}{1+b^2(1-x)^2} \tag{3.26}$$

3.2.2.1 Type-I D-IQ conversion

In this application, the input signal is differential, and the PPF must produce an IQ signal with the desired sequence. Consequently, the deviation from the ideal can evaluate the output signal quality. Amplitude balance (A_{BAL}) and phase error ($\Delta\theta$) imply an interesting metric for the D-IQ converter evaluation. Once these factors are obtained, equation (3.2) calculates the IRR.

From the block diagram in Figure 3.19b, the following relationships can be extracted,

$$\begin{aligned} v_{o1} &= H_{1A} \cdot v_1 + H_{2A} \cdot v_4 \\ v_{o2} &= H_{1B} \cdot v_2 + H_{2B} \cdot v_1 \\ v_{o3} &= H_{1A} \cdot v_3 + H_{2A} \cdot v_2 \\ v_{o4} &= H_{1B} \cdot v_4 + H_{2B} \cdot v_3 \end{aligned} \tag{3.27}$$

where v_k and v_{ok} are inputs and ouputs, respectively, as shown in Figure 3.4a and Figure 3.19a.

The Type-I configuration implies that $v_1 = -v_3 = v_{in}/2$ and $v_2 = v_4 = 0$. Thus, the I and the Q components from the output signal are such that

$$\begin{aligned} I &= H_{1A} \cdot v_{in} \\ Q &= H_{2B} \cdot v_{in} \end{aligned} \tag{3.28}$$

where $I = v_{o1} - v_{o3}$, the in-phase component, and $Q = v_{o2} - v_{o4}$, the quadrature component.

Substituting and transforming to polar form, then,

$$|I| = \frac{\sqrt{1 + b^2(1+x)^2}}{1 + b^2(1+x)^2} = \frac{1}{\sqrt{1 + b^2(1+x)^2}}$$

$$\theta_I = \arctan(-b(1+x)) \tag{3.29}$$

$$|Q| = \frac{b(1-x)\sqrt{1 + b^2(1-x)^2}}{1 + b^2(1-x)^2} = \frac{b(1-x)}{\sqrt{1 + b^2(1-x)^2}}$$

$$\theta_Q = \arctan\left(\frac{1}{b(1-x)}\right) \tag{3.30}$$

From it, A_{BAL} and $\Delta\theta$ are calculated as

$$A_{BAL} = \frac{|I|}{|Q|} = \frac{1}{b(1-x)} \cdot \sqrt{\frac{1 + b^2(1-x)^2}{1 + b^2(1+x)^2}} \tag{3.31}$$

$$\Delta\theta = -\frac{\pi}{2} - \theta_I + \theta_Q \Rightarrow \cos(\Delta\theta) = \frac{1 + b^2(1-x^2)}{\sqrt{(1 + b^2(1-x)^2)(1 + b^2(1+x)^2)}} \tag{3.32}$$

Partial IRR expressions are noteworthy. They serve as the theoretical IRR due to one of the two errors if the other one were ideal (*i.e.*, $A_{BAL} = 1$ or $\Delta\theta = 0$). These metrics contain relevant information about the complete IRR curve and the separate degradation that each of these factors cause. Note that Type I and II differ due to the distinct predominance of one error over the other. Thus,

$$IRR_{A_{BAL}} = \left(\frac{1 + A_{BAL}}{1 - A_{BAL}}\right)^2 = \left(\frac{1 + \frac{1}{b(1-x)} \cdot \sqrt{\frac{1+b^2(1-x)^2}{1+b^2(1+x)^2}}}{1 - \frac{1}{b(1-x)} \cdot \sqrt{\frac{1+b^2(1-x)^2}{1+b^2(1+x)^2}}}\right)^2 \tag{3.33}$$

$$IRR_{\theta} = \frac{1 + \cos(\Delta\theta)}{1 - \cos(\Delta\theta)} \frac{1 + \frac{1+b^2(1-x^2)}{\sqrt{(1+b^2(1-x)^2)(1+b^2(1+x)^2)}}}{1 - \frac{1+b^2(1-x^2)}{\sqrt{(1+b^2(1-x)^2)(1+b^2(1+x)^2)}}} \tag{3.34}$$

The $IRR_{A_{BAL}}$ expression has a pole when the denominator cancels out, *i.e.*, when $A_{BAL} = 1$. Moreover, this pole coincides with the maximum of the complete IRR curve; since the $IRR_{A_{BAL}}$ value tends to infinity at that point, the other factor, IRR_{θ}, defines the IRR peak value. The denominator of (3.34) never cancels out; hence its value is much less sensitive to b. This behavior is consistent with the qualitative description of the Type-I D-IQ converter in Section 3.1.2 and the analytical development in Appendix C. Contrary to the ideal case, the mismatch produces an error in the phase difference, constraining IRR. On the other hand, $IRR_{A_{BAL}}$ still presents a pole function behavior, but mismatch causes a subtle frequency shift.

Figure 3.20 compares the complete and partial IRR curves of this configuration and a 4 % mismatch. The graph also includes the maximum peak calculated by both following methods.

From previous observations, partial IRR expressions can approximate the complete IRR peak value. Starting at (3.33), the maximum value is placed at the function pole (b_p), *i.e.*, $b = b_p$, such that $A_{BAL}(b_p) = 1$. Then,

$$1 = \frac{1}{b_p(1-x)} \sqrt{\frac{1 + b_p^2(1-x)^2}{1 + b_p^2(1+x)^2}} \Rightarrow b_p = \frac{1}{\sqrt{1-x^2}} \tag{3.35}$$

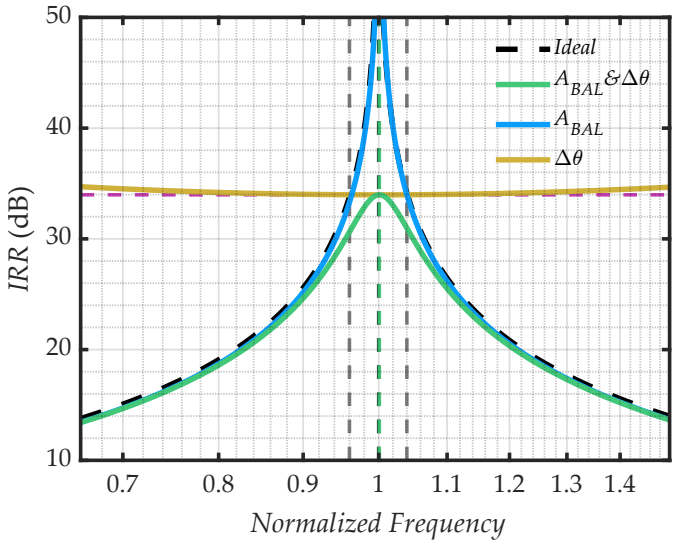

Figure 3.20: Type-I D-IQ converter PPF *IRR*. The dashed green vertical line marks the new pole position, slightly larger than $b = 1$. Grey dashed lines indicate a ±4 % deviation from 1. On the other hand, the dashed horizontal magenta line signals the obtained *IRR* limit due to mismatch tolerance ($x = 0.04$).

And substituting $b = b_p$ in (3.34),

$$IRR_{max} = IRR_{\Delta\theta}(b = b_p) = \frac{1+\sqrt{1-x^2}}{1-\sqrt{1-x^2}} = \frac{\left(1+\sqrt{1-x^2}\right)^2}{x^2} \approx \frac{4}{x^2} \tag{3.36}$$

A similar conclusion is obtained by developing and simplifying the complete *IRR* expression, validating the estimation. For clarity, $a = (1+x)$ and $c = (1-x)$, then substituting (3.31) and (3.32) in (3.2),

$$\begin{aligned} IRR &= \frac{1+2\cdot\frac{1}{bc}\cdot\sqrt{\frac{1+b^2c^2}{1+b^2a^2}}\cdot\frac{1+b^2ac}{\sqrt{(1+b^2a^2)(1+b^2c^2)}}+\frac{1}{b^2c^2}\cdot\frac{1+b^2c^2}{1+b^2a^2}}{1+2\cdot\frac{1}{bc}\cdot\sqrt{\frac{1+b^2c^2}{1+b^2a^2}}\cdot\frac{1+b^2ac}{\sqrt{(1+b^2a^2)(1+b^2c^2)}}+\frac{1}{b^2c^2}\cdot\frac{1+b^2c^2}{1+b^2a^2}} = \\ &= \frac{(1+b(1-x))^2+b^2(1-x)^2(1+b(1+x))^2}{(1-b(1-x))^2+b^2(1-x)^2(1-b(1+x))^2} \end{aligned} \tag{3.37}$$

This option also provides some information about the dependence on b and x by comparison with the ideal case, see (3.21). Contrary to the ideal version, there are two summands in both the numerator and the denominator. Besides, the mismatch affects different to each of these terms. As a result, the denominator cannot be zero, and the peak value becomes finite.

Analyzing the function shows a global maximum at $b = 1/\sqrt{1-x^2}$. Thus, substituting,

$$IRR\left(b = \frac{1}{\sqrt{1-x^2}}\right) = \frac{\left(1+\frac{\sqrt{1-x}}{\sqrt{1+x}}\right)^2 + \frac{(1-x)(1-x)}{(1-x)(1+x)}\left(1+\frac{\sqrt{1+x}}{\sqrt{1-x}}\right)^2}{\left(1-\frac{\sqrt{1-x}}{\sqrt{1+x}}\right)^2 + \frac{(1-x)(1-x)}{(1-x)(1+x)}\left(1-\frac{\sqrt{1+x}}{\sqrt{1-x}}\right)^2} = \frac{\left(1+\sqrt{1-x^2}\right)^2}{x^2} \approx \frac{4}{x^2} \quad (3.38)$$

The obtained expression is equivalent to (3.36). Note that as $x \ll 1$, then, $1+\sqrt{1-x^2} \approx 2$.

In other words, given an x mismatch tolerance between resistors, the worst-case mismatch degrades peak IRR to a maximum of $4/x^2$ (as opposed to the infinite value of the ideal case). From another point of view, the PPF could not guarantee an IRR better than $4/x^2$, even if all other non-idealities were negligible or had been counterbalanced.

In addition to the flattened peak, worst-case mismatch shifts IRR frequency in a $1/\sqrt{1-x^2}$ factor. For the typical low values of x, this displacement remains negligible in the evaluated mismatch combination. However, out of the worst case, the mismatch can increase the frequency shift from process variations. Nevertheless, the impact of mismatch on this aspect is usually not as severe as process variations due to the significant difference between respective tolerance values. Thus, the main danger of the mismatch effect comes from the potential decrease to peak IRR.

3.2.2.2 Type-II D-IQ conversion

In the Type-II D-IQ converter configuration, inputs are connected in adjacent pairs, typically $v_1 = v_2$ and $v_3 = v_4$. As shown in Figure 3.21a, this implies that under the conditions imposed for clarity, there are two closed loops without potential differences (colored parts in the schematics). Therefore, those nets have no current, and all their nodes have the same voltage; hence, v_{o2} and v_{o4} will equal v_1 and v_3, respectively. The circuit equivalent is shown in Figure 3.21b.

A critical consequence is the influence of devices on the filter performance. Since colored elements have equal voltage in both nodes, they have no effect. And non-colored resistors suffer equal deviation according to worst-case mismatch. Thus, the actual outcome is analogous to global process variations, not a mismatch error. However, it should be noted that a frequency shift in the mismatch factor $(1 + x)$ produces a very close IRR result to peak degradation at the ideal pole ($b = 1$). Starting from the ideal

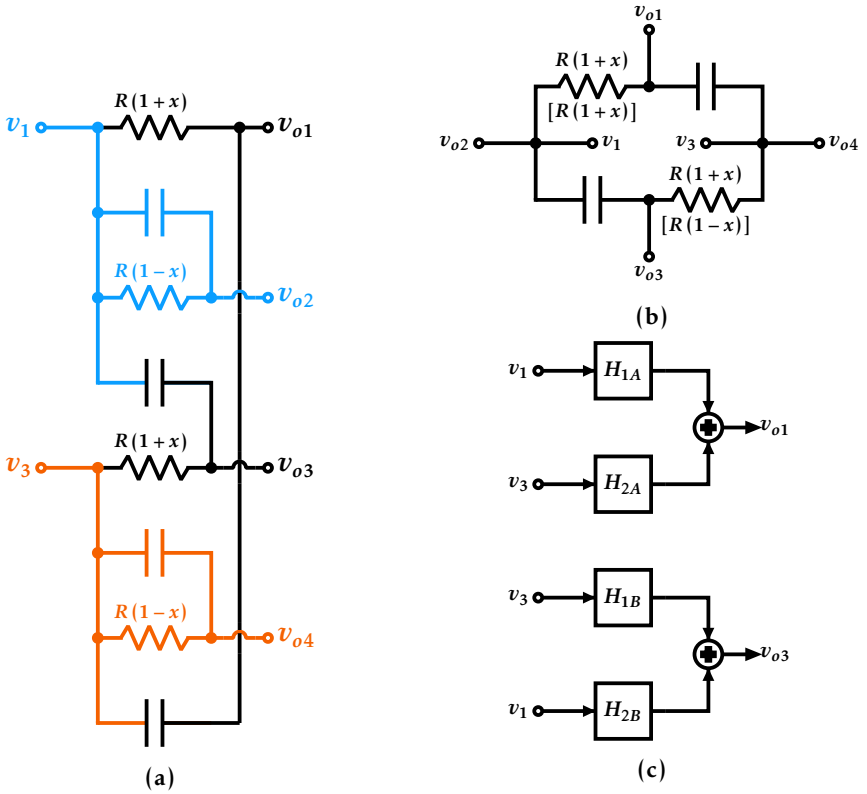

Figure 3.21: Type-II D-IQ converter PPF with worst-case mismatch: (a) Schematics, nets in the same color necessarily have equal voltage, thus colored elements are disposable; (b) Simplified equivalent circuit with the worst-case mismatch (no brackets) and with a mismatch between relevant resistor (brackets); and (c) Block diagram for the former mismatch combination. Note that in (c), $v_{o2} = v_1$ and $v_{o4} = v_3$ are omitted for clarity.

case of (3.21), substituting $b = (1+x)b'$, and considering b' as the reference, *i.e.*, $b' = 1$, then,

$$\left(\frac{1+b}{1-b}\right)^2\Bigg|_{b'=1} = \left(\frac{1+(1+x)}{1-(1+x)}\right)^2 = \frac{(2+x)^2}{x^2} \approx \frac{4}{x^2} \tag{3.39}$$

This similarity between both undesirable impacts, *IRR* degradation and frequency shifting, is also shown in Figure 3.20. The vertical dashed lines ($b = 1-x$ and $b = 1+x$) intersect with the ideal-PPF *IRR* curve at $4/x^2$ of *IRR*.

However, the analysis of this configuration has further interest. Since only two elements are simultaneously *a*) susceptible to mismatch and *b*) capable of affecting performance, there is only one possible combination with mismatch in the strict sense: the one in which relevant resistors have opposite deviations. Thus, this is the only mismatch combination evaluable under the given conditions.

Figure 3.21c shows the relationships to obtain v_{o1} and v_{o3}, assuming that the two resistors of interest suffer opposite deflections. In Figure 3.21b, bracketed notations represent this alternative case. Developing I and Q analogously to the previous configuration and assuming Type-II differential input ($v_1 = v_2 = v_{in}/2$ and $v_3 = v_4 = -v_{in}/2$), A_{BAL} and $\Delta\theta$ are obtained as

$$A_{BAL} = \frac{|I|}{|Q|} = \frac{\left(ac+b^2\right)\sqrt{(ac-b^2)^2 + b^2(a+c)^2}}{(a^2+b^2)(c^2+b^2)} = \frac{ac+b^2}{\sqrt{(a^2+b^2)(c^2+b^2)}} \tag{3.40}$$

$$\cos(\Delta\theta) = \frac{\frac{b(a+c)}{ac-b^2}}{\sqrt{\frac{b^2(a+c)^2}{(ac-b^2)^2}+1}} = \frac{b(a+c)}{\sqrt{(a^2+b^2)(c^2+b^2)}} \tag{3.41}$$

where $a = 1/(1+x)$ and $c = 1/(1-x)$.

Consequently, partial IRRs are

$$IRR_{A_{BAL}} = \left(\frac{1+\frac{ac+b^2}{\sqrt{(a^2+b^2)(c^2+b^2)}}}{1-\frac{ac+b^2}{\sqrt{(a^2+b^2)(c^2+b^2)}}}\right)^2 \tag{3.42}$$

$$IRR_{\Delta\theta} = \frac{1+\frac{b(a+c)}{\sqrt{(a^2+b^2)(c^2+b^2)}}}{1-\frac{b(a+c)}{\sqrt{(a^2+b^2)(c^2+b^2)}}} \tag{3.43}$$

This case presents the inverse situation to Type-I configuration as seen in Figure 3.22. Regarding Type-I, $\Delta\theta$ and A_{BAL} exchange roles when determining IRR. The $IRR_{\Delta\theta}$ as a function of b has a pole at $1/\sqrt{1-x^2}$. By evaluating $IRR_{A_{BAL}}$ at that point, the maximum IRR can be obtained as

$$IRR_{max} = IRR_{A_{BAL}}\left(b = b_p\right) = \left(\frac{1+\frac{ac+ac}{\sqrt{(a^2+ac)(c^2+ac)}}}{1-\frac{ac+ac}{\sqrt{(a^2+ac)(c^2+ac)}}}\right)^2 = \left(\frac{\left(1+\sqrt{1-x^2}\right)^2}{x^2}\right)^2 \approx \left(\frac{4}{x^2}\right)^2 \tag{3.44}$$

As $x \ll 1$, the IRR peak approaches the square of the worst-case results. This result

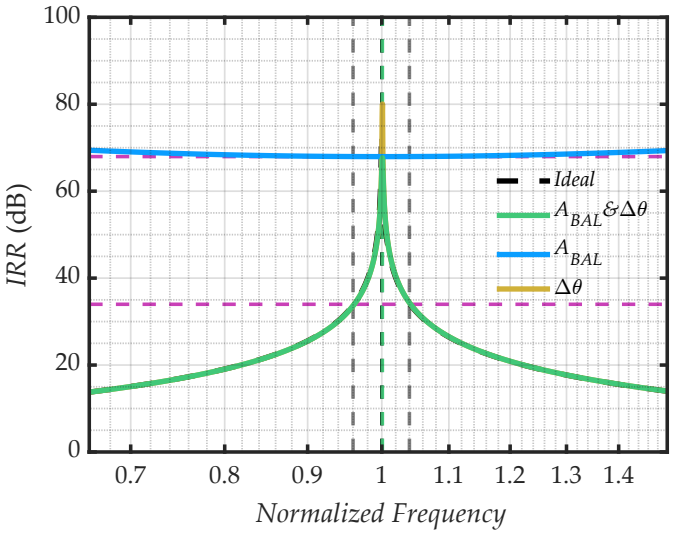

Figure 3.22: Type-II D-IQ PPF *IRR*. Dashed horizontal magenta lines indicate the $(4/x^2)^2$ and $4/x^2$ limits. Note the similitude of $IRR_{A_{BAL}}$ and $IRR_{\Delta\theta}$ with the other partial *IRR* from the Type-I configuration study.

means that the only evaluable mismatch combination for the Type-II D-IQ configuration is not equivalent to the worst case but its squared value, a much less severe limit. Indeed, this result is expected from other $\boldsymbol{M}_1$ vectors compatible with the alternative deviations (see Appendix F). Also, Appendix D contains more details of the Type-II D-IQ PPF analysis.

3.2.2.3 Type-I IQ-D conversion

The Type-I IQ-D converter configuration suffers from a similar problem to Type-II PPF in the reverse conversion mode. Blue elements from Figure 3.23a do not affect the *IRR*. Thus, neither of those resistor mismatch have any impact. Consequently, in the worst-case scenario, the mismatch degradation entirely depends on a pair of resistors with equal deviations. Figure 3.23b shows the equivalent circuit with the worst-case mismatch.

Like the previous configuration, there is only one possible mismatch combination (shown bracketed in Figure 3.23b). The change in the sign for one of the relevant variations results in the block diagram from Figure 3.23c.

In this case, the *IRR* depends on the output power ratio between both input IQ sequences, *i.e.*, (3.1). From the block diagram of Figure 3.23c, the output voltage when input is a positive-sequence (s_+) IQ signal ($v_1 = v_{in}/2$; $v_2 = jv_{in}/2$; $v_3 = -v_{in}/2$; $v_4 =$

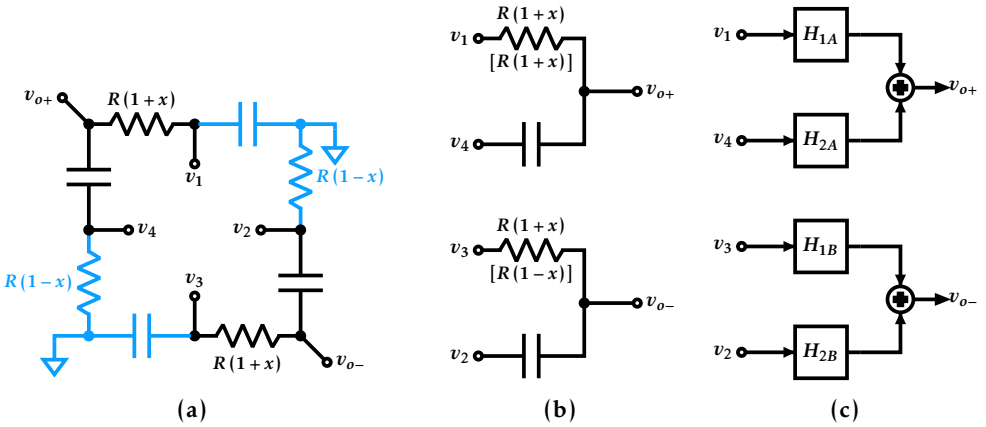

Figure 3.23: Type-I IQ-D converter PPF: (a) schematics, blue elements do not affect v_o; (b) Simplified equivalent circuit for the worst-case mismatch (non-bracketed) and opposite deviations in the relevant resistors (bracketed); and (c) block diagram of the PPF performance with the mismatch between relevant resistors.

$-jv_{in}/2$),

$$v_o|_{s_+} = (H_{1A} + H_{1B} - jH_{2A} - jH_{2B})\frac{v_{in}}{2} = \\ = \frac{\Big(1+ba\Big)B_2 + \Big(1+bc\Big)B_1 - jb\Big(a(1+ba)B_2 + c(1+bc)B_1\Big)}{B_1 B_2} \cdot \frac{v_{in}}{2} \tag{3.45}$$

where $B_1 = 1 + b^2a^2$, $B_2 = 1 + b^2c^2$, $a = (1+x)$ and $c = (1-x)$.

After simplification, the squared modulus is such that

$$|v_o|^2_{s_+} = \frac{\Big((1+ba)B_2 + (1+bc)B_1\Big)^2 + b^2\Big(a(1+ba)B_2 + c(1+bc)B_1\Big)^2}{4B_1^2B_2^2} \cdot v_{in}^2 = \\ = \frac{(1+b)^2 + b^2\Big(1+b(1-x^2)\Big)^2}{B_1B_2} \cdot v_{in}^2 \tag{3.46}$$

Similarly, the squared modulus of v_o when the input signal has a negative sequence is

$$|v_o|^2_{s_-} = \frac{\Big((1-ba)B_2 + (1-bc)B_1\Big)^2 + b^2\Big(a(1-ba)B_2 + c(1-bc)B_1\Big)^2}{4B_1^2B_2^2} \cdot v_{in}^2 = \\ = \frac{(1-b)^2 + b^2\Big(1-b(1-x^2)\Big)^2}{B_1B_2} \cdot v_{in}^2 \tag{3.47}$$

Thus, IRR can be calculated as

$$IRR = \frac{|v_o|^2_{s_+}}{|v_o|^2_{s_-}} = \frac{(1+b)^2 + b^2\Big(1 + b(1-x^2)\Big)^2}{(1-b)^2 + b^2\Big(1 - b(1-x^2)\Big)^2} \tag{3.48}$$

The final expression is similar to (3.37). However, the position of mismatch factors is different from the reverse conversion. Note also the correspondence between the first term of (3.48) and (3.21), the ideal IRR, in their respective numerator and denominator.

The minimum of (3.48) appears at the geometric mean summands of the denominator, *i.e.*, $1/\sqrt{1-x^2}$. Computer-assisted analysis tools can verify this. Thus, evaluating the function at this point,

$$IRR_{max} = IRR\left(b = \frac{1}{\sqrt{1-x^2}}\right) = \left(\frac{\left(\sqrt{1-x^2}+1\right)^2}{x^2}\right)^2 \approx \left(\frac{4}{x^2}\right)^2 \tag{3.49}$$

The obtained result is identical to the Type-II D-IQ converter configuration; therefore, the same implications arise in this case. The developments omitted to synthesize, especially the tedious calculation of $|v_o|^2_{s_+}$ and $|v_o|^2_{s_-}$, are detailed in Section D.2.1 of Appendix D.

3.2.2.4 Type-II IQ-D conversion

As the D-IQ conversion requires a Type-I configuration to evaluate the mismatch effect properly, the responsibility falls to the Type-II case when the PPF works as an IQ-D converter. Schematics resulting from these connections are shown in Figure 3.24a.

The short-circuit of output pairs results in the block diagram from Figure 3.24b, which takes advantage of the transfer functions of Figure 3.25 subcircuits.

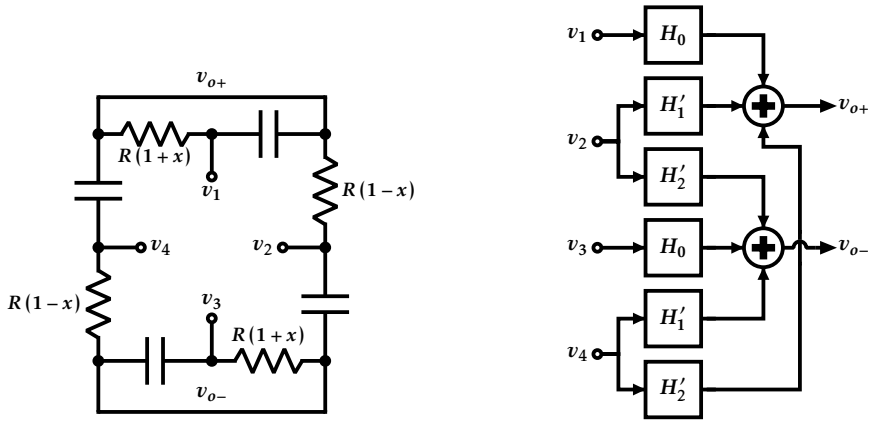

(a) Schematics **(b)** Block diagram

Figure 3.24: Type-II IQ-D converter PPF.

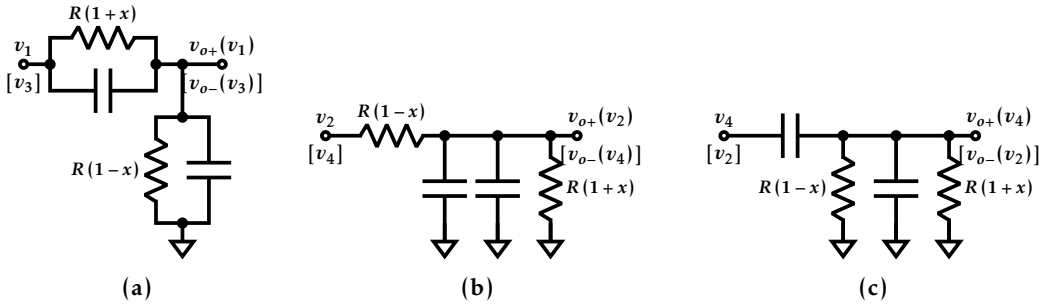

Figure 3.25: Transfer function subcircuits of (a) H_0; (b) H_1'; and (c) H_2'.

Defining $a = \frac{1}{(1+x)(1-x)}$ and having other elements their usual meaning, then,

$$H_0 = \frac{\frac{\not{R}(1-x)}{1+sCR(1-x)}}{\frac{\not{R}(1-x)}{1+sCR(1-x)} + \frac{\not{R}(1+x)}{1+sCR(1+x)}} = \frac{1}{2} \cdot \frac{\frac{1}{1+x} + jb}{a+jb} = \frac{1}{2} \cdot \frac{\frac{a}{1+x} + b^2 + jba - j\frac{b}{1+x}}{a^2+b^2} \tag{3.50}$$

$$H_1' = \frac{\frac{\not{R}(1-x)}{1+2sCR(1-x)}}{\frac{\not{R}(1-x)}{1+2sCR(1-x)} + \not{R}(1-x)} = \frac{1}{2} \cdot \frac{\frac{1}{1-x}}{a+jb} = \frac{1}{2} \cdot \frac{\frac{a}{1-x} - j\frac{b}{1-x}}{a^2+b^2} \tag{3.51}$$

$$H_2' = \frac{\frac{\frac{R}{2a}}{1+\frac{sCR}{2a}}}{\frac{1}{sC} + \frac{\frac{R}{2a}}{1+\frac{sCR}{2a}}} = \frac{1}{2} \cdot \frac{sCR}{a+sCR} = \frac{1}{2} \cdot \frac{jb}{a+jb} = \frac{1}{2} \cdot \frac{b^2+jba}{a^2+b^2} \tag{3.52}$$

From the block diagram of Figure 3.24b, v_o is deduced as

$$\begin{aligned} v_o =& v_{o+} - v_{o-} = H_0 \cdot v_1 + H_1' \cdot v_2 + H_2' \cdot v_4 - H_2' \cdot v_2 - H_0 \cdot v_3 - H_1' \cdot v_4 = \\ =& H_0(v_1 - v_3) + H_1'(v_2 - v_4) + H_2'(v4 - v_2) = H_0(v_1 - v_3) + (H_1' - H_2')(v_2 - v_4) \end{aligned} \tag{3.53}$$

Particularizing (3.53) to the positive sequence case (s_+),

$$\begin{aligned} v_o|_{s_+} =& \frac{\frac{a}{1+x} + b^2 + jba - j\frac{b}{1+x}}{a^2+b^2} \cdot \frac{v_{in}}{2} + \frac{\frac{b}{1-x} + ba + j\frac{a}{1-x} - jb^2}{a^2+b^2} \cdot \frac{v_{in}}{2} = \\ =& \frac{a\left(\frac{1}{1+x}+b\right) + b\left(\frac{1}{1-x}+b\right) + ja\left(\frac{1}{1-x}+b\right) - jb\left(\frac{1}{1+x}+b\right)}{2\left(a^2+b^2\right)} \cdot v_{in} \end{aligned} \tag{3.54}$$

Thus,

$$|v_o|^2_{s_+} = \frac{1}{4} \cdot \frac{\left(a^2+b^2\right)\left(\left(\frac{1}{1+x}+b\right)^2 + \left(\frac{1}{1-x}+b\right)^2\right)}{\left(a^2+b^2\right)^2} \cdot v_{in}^2 = \frac{1}{4} \cdot \frac{\left(\frac{1}{1+x}+b\right)^2 + \left(\frac{1}{1-x}+b\right)^2}{a^2+b^2} \cdot v_{in}^2 \tag{3.55}$$

Analogously, the negative sequence case (s_-) is

$$\begin{aligned} v_o|_{s_-} =& \frac{\frac{a}{1+x} + b^2 + jba - j\frac{b}{1+x}}{a^2+b^2} \cdot \frac{v_{in}}{2} - \frac{\frac{b}{1-x} + ba + j\frac{a}{1-x} - jb^2}{a^2+b^2} \cdot \frac{v_{in}}{2} = \\ =& \frac{a\left(\frac{1}{1+x}-b\right) + b\left(\frac{1}{1-x}-b\right) + ja\left(\frac{1}{1-x}-b\right) - jb\left(\frac{1}{1+x}-b\right)}{2\left(a^2+b^2\right)} \cdot v_{in} \end{aligned} \tag{3.56}$$

$$|v_o|^2_{s_-} = \frac{1}{4} \cdot \frac{\left(a^2+b^2\right)\left(\left(\frac{1}{1+x}-b\right)^2 + \left(\frac{1}{1-x}-b\right)^2\right)}{\left(a^2+b^2\right)^2} \cdot v_{in}^2 = \frac{1}{4} \cdot \frac{\left(\frac{1}{1+x}-b\right)^2 + \left(\frac{1}{1-x}-b\right)^2}{a^2+b^2} \cdot v_{in}^2 \tag{3.57}$$

As impedance remains the same for both sequences, then, power ratio is equivalent to the quocient of voltage squared modulus. Thus,

$$IRR = \frac{|v_o|^2_{s_+}}{|v_o|^2_{s_-}} = \frac{\frac{1}{4} \cdot \frac{\left(\frac{1}{1+x}+b\right)^2 + \left(\frac{1}{1-x}+b\right)^2}{a^2+b^2} \cdot v_{in}^2}{\frac{1}{4} \cdot \frac{\left(\frac{1}{1+x}-b\right)^2 + \left(\frac{1}{1-x}-b\right)^2}{a^2+b^2} \cdot v_{in}^2} = \frac{\left(\frac{1}{1+x}+b\right)^2 + \left(\frac{1}{1-x}+b\right)^2}{\left(\frac{1}{1+x}-b\right)^2 + \left(\frac{1}{1-x}-b\right)^2} \tag{3.58}$$

Evaluating (3.58) in its maximum, *i.e.*, $\frac{\sqrt{1+x^2}}{1-x^2}$,

$$IRR\left(b = \frac{\sqrt{1+x^2}}{1-x^2}\right) = \frac{\left(\frac{1}{1+x} + \frac{\sqrt{1+x^2}}{1-x^2}\right)^2 + \left(\frac{1}{1-x} + \frac{\sqrt{1+x^2}}{1-x^2}\right)^2}{\left(\frac{1}{1+x} - \frac{\sqrt{1+x^2}}{1-x^2}\right)^2 + \left(\frac{1}{1-x} - \frac{\sqrt{1+x^2}}{1-x^2}\right)^2} = \frac{\left(1+\sqrt{1+x^2}\right)^2}{x^2} \approx \frac{4}{x^2} \tag{3.59}$$

The IRR limit is approximately $4/x^2$ since $x \ll 1$. This result equals the obtained in (3.37) from the inverse converter analysis. The presented analytical development might not feel intuitive without some tedious steps omitted to synthesize. However, Section D.2.2 from Appendix D contains the full version of the studies.

3.2.2.5 Quadrature Filter

The last application of a PPF has IQ signals in both input and output. Its schematics and block diagram are identical to the first-case ones (Figure 3.19b). However, the IRR calculation is more complex, especially with a non-negligible mismatch.

The IQ-filter IRR calculus faces a combination of the problems from previous cases. On the one hand, since the input is an IQ signal, the IRR must measure the ratio between the effect produced by each of the two sequences. On the other hand, an IQ output implies that evaluating the "ideality" of each of these IQ signals is necessary.

Because the input is an IQ signal, the expression (3.2) cannot be easily used as a quality measure. However, the output projection onto the desired sequence can evaluate the signal quality. In other words, the comparison can be made by means of the signal coefficients in terms of symmetric sets of phasors (see Section 2.2.2).

The portion of the desired sequence signal that reaches the output (while keeping the sequence) defines the numerator of the IRR expression. This value is equivalent to the power of the projection of v_o onto the desired sequence component (A) when the input is an ideal IQ signal with a positive sequence (s_+). That result is proportional to $|v_o|^2_{A,s_+}$. On the other hand, the denominator is the non-canceled part of the image at the output, *i.e.*, both the projection onto the negative sequence component (C) and, due to the mismatch, A. Note that this last term is indistinguishable from the actual desired signal for future stages. Analytically, this can be expressed as

$$IRR = \frac{|v_o|^2_{A,s_+}}{|v_o|^2_{A,s_-} + |v_o|^2_{C,s_-}} \tag{3.60}$$

Without mismatch, output I and Q phasors are necessarily orthogonal. Thus, the signal squared modulus equals the sum of I and Q squared moduli. However, this assumption is not satisfied if $\Delta\theta \neq 0$, as in this case.

Transfer function terms can be rearranged as follows to simplify further calculations,

$$
\begin{aligned}
H_{1A} &= \frac{1}{1+jb(1+x)} = \frac{\frac{1}{1+x}}{\frac{1}{1+x}+jb} = \frac{a}{a+jb}\cdot\frac{a-jb}{a-jb}\cdot\frac{B_2}{B_2} = \frac{a(a-jb)B_2}{B_1B_2} \\
H_{1B} &= \frac{1}{1+jb(1-x)} = \frac{\frac{1}{1-x}}{\frac{1}{1-x}+jb} = \frac{c}{c+jb}\cdot\frac{c-jb}{c-jb}\cdot\frac{B_1}{B_1} = \frac{c(c-jb)B_1}{B_1B_2} \\
H_{2A} &= \frac{jb(1+x)}{1+jb(1+x)} = \frac{jb}{a+jb}\cdot\frac{a-jb}{a-jb}\cdot\frac{B_2}{B_2} = \frac{b(b+ja)B_2}{B_1B_2} \\
H_{2B} &= \frac{jb(1-x)}{1+jb(1-x)} = \frac{jb}{c+jb}\cdot\frac{c-jb}{c-jb}\cdot\frac{B_1}{B_1} = \frac{b(b+jc)B_1}{B_1B_2}
\end{aligned}
\tag{3.61}
$$

where $a = \frac{1}{1+x}$; $c = \frac{1}{1-x}$; $B_1 = a^2 + b^2$; and $B_2 = c^2 + b^2$.

The projection of v_o onto A can be obtained by multiplying each of the outputs by the indicated factors, *i.e.*, a change of base using (2.12). Developing this expression,

$$
\begin{aligned}
v_o|_A =& \frac{v_{o1} - jv_{o2} - v_{o3} + jv_{o4}}{2} = \frac{(H_{1A}\cdot v_1 + H_{2A}\cdot v_4) - j\,(H_{1B}\cdot v_2 + H_{2B}\cdot v_1)}{2} + \\
&+ \frac{-(H_{1A}\cdot v_3 + H_{2A}\cdot v_2) + j\,(H_{1B}\cdot v_4 + H_{2B}\cdot v_3)}{2} = \\
=& \frac{(H_{1A} - jH_{2B})(v_1 - v_3)}{2} - \frac{(H_{2A} + jH_{1B})(v_2 - v_4)}{2}
\end{aligned}
\tag{3.62}
$$

The factor 1/2 equals both basis power. Note that this value differs from the usual 1/4 as v_{in} refers to the voltage difference in pairs instead of each phasor voltage separately.

Substituting v_{in} with the conditions of a positive input sequence ($v_1 = -v_3 = v_{in}/2$; $v_2 = -v_4 = jv_{in}/2$), then,

$$
\begin{aligned}
v_o|_{A,s_+} =& \frac{(H_{1A} - jH_{2B})\cdot v_{in}}{2} - \frac{(H_{2A} + jH_{1B})\cdot jv_{in}}{2} = \\
=& \frac{a(a+b)B_2 + c(c+b)B_1 - jb\Big((a+b)B_2 + (c+b)B_1\Big)}{B_1B_2}\cdot\frac{v_{in}}{2}
\end{aligned}
\tag{3.63}
$$

Thus, the squared modulus is

$$|v_o|^2_{A,s_+} = \frac{\Big(a(a+b)B_2 + c(c+b)B_1\Big)^2 + b^2\Big((a+b)B_2 + (c+b)B_1\Big)^2}{B_1^2 B_2^2} \cdot \frac{v_{in}^2}{4} = \\ = \frac{(1+b)^2 + b^2\Big(1 + b(1-x^2)\Big)^2}{B_1 B_2 (1+x)^2 (1-x)^2} \cdot v_{in}^2 \tag{3.64}$$

Similarly, the $|v_o|^2_{A,s_-}$ can be obtained from (3.62) under negative-sequence input conditions ($v_1 = -v_3 = v_{in}/2$; $v_2 = -v_4 = -jv_{in}/2$) and squared,

$$|v_o|^2_{A,s_-} = \frac{\Big(a(a-b)B_2 - c(c-b)B_1\Big)^2 + b^2\Big((a-b)B_2 - (c-b)B_1\Big)^2}{B_1^2 B_2^2} \cdot \frac{v_{in}^2}{4} = \\ = \frac{(a-b)^2 B_2 + (c-b)^2 B_1 - 2(ac+b^2)(a-b)(c-b)}{B_1 B_2} \cdot \frac{v_{in}^2}{4} \tag{3.65}$$

Analogously to (3.62), v_o projection onto C when input has also a negative sequence is

$$v_o|_{C,s-} = \frac{v_{o1} + jv_{o2} - v_{o3} - jv_{o4}}{2} = \frac{H_{1A} \cdot v_1 + H_{2A} \cdot v_4}{2} + j\frac{H_{1B} \cdot v_2 + H_{2B} \cdot v_1}{2} - \\ - \frac{H_{1A} \cdot v_3 + H_{2A} \cdot v_2}{2} - j\frac{H_{1B} \cdot v_4 + H_{2B} \cdot v_3}{2} = \\ = \frac{a(a-b)B_2 + c(c-b)B_1 - jb(a-b)B_2 - jb(c-b)B_1}{B_1 B_2} \cdot \frac{v_{in}}{2} \tag{3.66}$$

Consequently, the squared modulus becomes

$$|v_o|^2_{C,s_-} = \frac{\Big(a(a-b)B_2 + c(c-b)B_1\Big)^2 + b^2\Big((a-b)B_2 + (c-b)B_1\Big)^2}{B_1^2 B_2^2} \cdot \frac{v_{in}^2}{4} = \\ = \frac{(a-b)^2 B_2 + (c-b)^2 B_1 + 2(ac+b^2)(a-b)(c-b)}{B_1 B_2} \cdot \frac{v_{in}^2}{4} \tag{3.67}$$

After obtaining all its terms, the IRR is obtained as

$$IRR = \frac{|v_o|^2_{A,s_+}}{|v_o|^2_{A,s_-} + |v_o|^2_{C,s_-}} = \frac{(1+b)^2 + b^2\Big(1 + b(1-x^2)\Big)^2}{(1-b)^2 + b^2\Big(1 - b(1-x^2)\Big)^2 + 2b^2x^2} \tag{3.68}$$

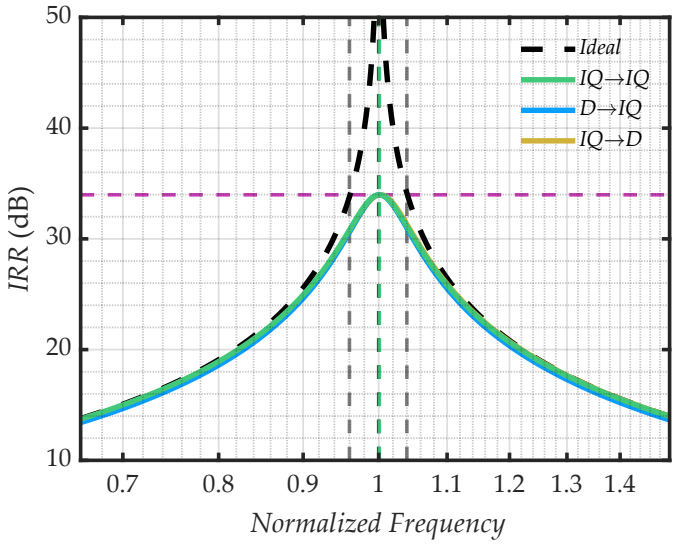

Figure 3.26: Mismatch impact on the *IRR* of D-IQ, ID-D, and IQ-IQ PPFs. The three curves are almost entirely overlapped. Their peak values approximate to $4/x^2$.

At first glance, there is a close correspondence between (3.48) and (3.68). However, adding a third term in the denominator varies maximum value, although it remains at $b = 1/\sqrt{1-x^2}$. Thus, the peak value *IRR* is

$$\begin{aligned} IRR\left(b=\frac{1}{\sqrt{1-x^2}}\right) = \\ =&\frac{\left(1+\frac{1}{\sqrt{1-x^2}}\right)^2+\left(\frac{1}{\sqrt{1-x^2}}\right)^2\left(1+\frac{1}{\sqrt{1-x^2}}(1-x^2)\right)^2}{\left(1-\frac{1}{\sqrt{1-x^2}}\right)^2+\left(\frac{1}{\sqrt{1-x^2}}\right)^2\left(1-\frac{1}{\sqrt{1-x^2}}(1-x^2)\right)^2+2\left(\frac{1}{\sqrt{1-x^2}}\right)^2x^2} = \\ =&\frac{1}{2}\cdot\frac{\left(\sqrt{1-x^2}+1\right)^3}{x^2}\approx\frac{1}{2}\cdot\frac{8}{x^2}=\frac{4}{x^2} \end{aligned} \tag{3.69}$$

Figure 3.26 shows the *IRR* figure for all three configurations for which it is possible to evaluate the worst-case mismatch. Each curve represents a possible PPF application (D-IQ and IQ-D converter and IQ filter), although their curves almost entirely overlap, showing their similitude. Also, the graph reveals that $4/x^2$ is a reasonably accurate estimation for a general PPF *IRR* peak value.

As in previous configurations, Appendix D.3 includes the complete calculus.

	Type	IRR	b_p	IRR_{max}
$D \rightarrow IQ$	I	$\frac{(1+b(1-x))^2+b^2(1-x)^2(1+b(1+x))^2}{(1-b(1-x))^2+b^2(1-x)^2(1-b(1-x))^2}$	$\frac{1}{\sqrt{1-x^2}}$	$\frac{4}{x^2}$
	II	$\left(\frac{1+b(1+x)}{1-b(1+x)}\right)^2$	$1+x$	$\infty \mid \frac{4}{x^2}$
	II'	$\frac{(1+b)^2+b^2(1+b(1-x^2))^2}{(1-b)^2+b^2(1-b(1-x^2))^2}$	$\frac{1}{\sqrt{1-x^2}}$	$\frac{16}{x^4}$
$IQ \rightarrow D$	I	$\left(\frac{1+b(1+x)}{1-b(1+x)}\right)^2$	$1+x$	$\infty \mid \frac{4}{x^2}$
	I'	$\frac{(1+b)^2+b^2(1+b(1-x^2))^2}{(1-b)^2+b^2(1-b(1-x^2))^2}$	$\frac{1}{\sqrt{1-x^2}}$	$\frac{16}{x^4}$
	II	$\frac{\left(\frac{1}{1+x}+b\right)^2+\left(\frac{1}{1-x}+b\right)^2}{\left(\frac{1}{1+x}-b\right)^2+\left(\frac{1}{1-x}-b\right)^2}$	$\frac{\sqrt{1+x^2}}{1-x^2}$	$\frac{4}{x^2}$
$IQ \rightarrow IQ$	-	$\frac{(1+b)^2+b^2(1+b(1+x^2))^2}{(1-b)^2+b^2(1-b(1-x^2))^2+2b^2x^2}$	$\frac{1}{\sqrt{1-x^2}}$	$\frac{4}{x^2}$

Table 3.1: PPF analysis summary results.

3.2.2.6 Discussion

In short, the above calculations result in an effortless expression that can relate the desired IRR and the maximum permissible mismatch on the circuit devices. The study is limited to single-stage PPF, but the following subsection aims to overcome this constraint and extrapolate to multiple-stage filters.

Table 3.1 summarizes the results, showing the IRR expression under the worst-case mismatch, normalized frequency peak (b_p), and maximum IRR value (IRR_{max}) for each of the configurations.

The complete results confirm some relevant points, but it can benefit from other clarifications. Type II in D-IQ conversion and Type I in IQ-D conversion imply a frequency

shifting analogous to the produced by global process variations. As a consequence, their IRR is infinite at $(1+x)$, and thus, for a fair comparison, Table 3.1 also shows $IRR(b=1)$ for those two cases. Note that both cases suffer a deviation equivalent to $\boldsymbol{M}_1$ vector 1, $[+1\ +1\ +1\ +1]^T$, instead of worst-case mismatch, $[+1\ -1\ +1\ -1]^T$, because all relevant devices have identical deviation under analysis conditions. D-IQ Type-II' and IQ-D Type-I' use opposite signs for the relevant devices.

In the rest of the cases, the frequency displacement is insignificant compared to the peak attenuation. The former appears from the discrepancy between the usual mismatch description as symmetric and linear, *i.e.*, extreme cases are $(1+x)$ and $(1-x)$, and symmetrical geometric tolerances, *i.e.*, $(1+y)$ and $1/(1+y)$. Mismatch in terms of $(1+y)$ describes IRR peak degradation without moving it. The difference with the linear case can be modeled by a common factor $(1+z)$, the inverse frequency shift value. Analytically,

$$\left.\begin{aligned}(1+x)&=(1+z)\cdot(1+y)\\(1-x)&=(1+z)/(1+y)\end{aligned}\right\}\Rightarrow\begin{cases}(1+y)=\sqrt{(1+x)/(1-x)}\\(1+z)=\sqrt{(1+x)\cdot(1-x)}\end{cases}\tag{3.70}$$

This decomposition separates the terms corresponding to the two distinct mismatch impacts on the IRR curve: peak attenuation and frequency shift. Appendix E provides more details on and constraints of this decomposition. Besides, it includes analyses of both types of PPF as D-IQ converters as examples of use and benefit.

The significant difference in IRR_{max} for the modified cases is also noteworthy. The only possible mismatch combination was applied as analysis conditions prevent the worst-case evaluation. However, those deviations correlate with $\boldsymbol{M}_1$ vectors 2 and 4, *i.e.*, $[+1\ +1\ -1\ -1]^T$ and $[+1\ -1\ -1\ +1]^T$. Consequently, IRR peaks have a much larger value for equal mismatch, as previously observed in Figure 3.17; more precisely, the peak value of those vectors in the figure is $(4/x^2)^2$. Appendix F analytically confirms this by studying a Type-I D-IQ PPF with this mismatch combination. The substantial IRR difference between mismatch combinations reaffirms the choice of the $\boldsymbol{M}_1$ vector 3 as the most detrimental case.

3.2.3 Worst-case search for a multi-stage PPF

In previous sections, the analysis of the mismatch impact on PPF performance has a significant limitation: it only considers a single-stage PPF, whereas these filters usually have at least three stages [Had15]. This section study proposes a generalization to cover multi-stage PPF cases.

The problem of finding the worst case among all the possible mismatch combinations grows exponentially, making it impossible to obtain directly. For an N-stage system (without considering capacitor non-idealities), there are 3^{4N} combinations. Thus, even a relatively small N would produce many possible mismatch sets. For example, there are 531,441 combinations for $N = 3$.

However, two points can simplify the problem. First, similar to the 1-step case, if there is a generator system (a basis that defines all case space), then a finite number of simulations can narrow down the most detrimental mismatch combination. Secondly, according to simulation results (see Figure 3.13), the mismatch effect heavily depends on the stage order [Mar17]. Therefore, an independent mismatch model for each stage can provide more comprehensible results. In other words, each basis vector should affect a single PPF stage. This strategy also has the advantage of scaling with N.

Based on the above considerations, a basis for an N-stage case can be created by replicating N times the one-stage basis, *i.e.*, the matrix $\boldsymbol{M}_N$ ($4N \times 4N$ size) uses $\boldsymbol{M}_1$ matrixes (4×4 size) on its diagonal and zeros in the rest of elements. By this method, $\boldsymbol{M}_3$ is obtained such that

$$\boldsymbol{M}_3 = \begin{pmatrix} \boldsymbol{M}_1 & 0 & 0 \\ 0 & \boldsymbol{M}_1 & 0 \\ 0 & 0 & \boldsymbol{M}_1 \end{pmatrix} = \begin{pmatrix} +1 & +1 & +1 & +1 & 0 & 0 & 0 & 0 & 0 & 0 & 0 & 0 \\ +1 & +1 & -1 & -1 & 0 & 0 & 0 & 0 & 0 & 0 & 0 & 0 \\ +1 & -1 & +1 & -1 & 0 & 0 & 0 & 0 & 0 & 0 & 0 & 0 \\ +1 & -1 & -1 & +1 & 0 & 0 & 0 & 0 & 0 & 0 & 0 & 0 \\ 0 & 0 & 0 & 0 & +1 & +1 & +1 & +1 & 0 & 0 & 0 & 0 \\ 0 & 0 & 0 & 0 & +1 & +1 & -1 & -1 & 0 & 0 & 0 & 0 \\ 0 & 0 & 0 & 0 & +1 & -1 & +1 & -1 & 0 & 0 & 0 & 0 \\ 0 & 0 & 0 & 0 & +1 & -1 & -1 & +1 & 0 & 0 & 0 & 0 \\ 0 & 0 & 0 & 0 & 0 & 0 & 0 & 0 & +1 & +1 & +1 & +1 \\ 0 & 0 & 0 & 0 & 0 & 0 & 0 & 0 & +1 & +1 & -1 & -1 \\ 0 & 0 & 0 & 0 & 0 & 0 & 0 & 0 & +1 & -1 & +1 & -1 \\ 0 & 0 & 0 & 0 & 0 & 0 & 0 & 0 & +1 & -1 & -1 & +1 \end{pmatrix} \tag{3.71}$$

When simulating these 12 basis vectors (see Figure 3.27), one of them, $[\,0 \cdots 0 \; +1 \; -1 \; +1 \; -1\,]^T$, has a more detrimental impact on PPF performance than any other. This result was expected after observing the effect of the $\boldsymbol{M}_1$ vectors in Section 3.2.1

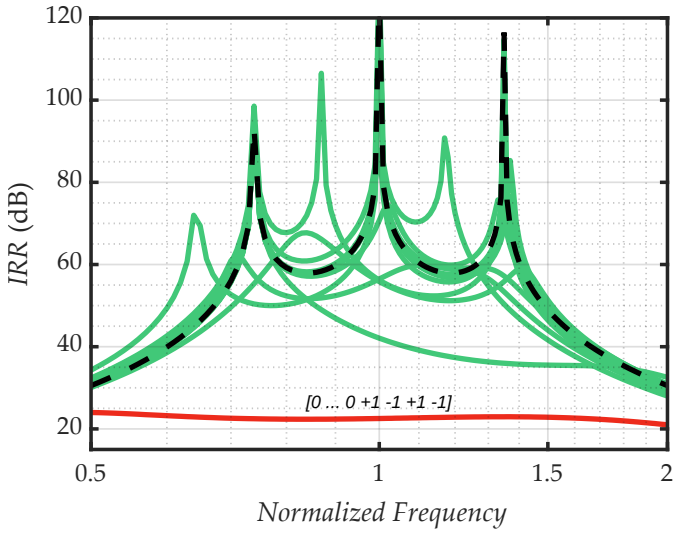

Figure 3.27: Three-stage PPF *IRR* for each one of the mismatch combinations described by $\boldsymbol{M}_3$ vectors (green). Worst case (red) and ideal response (black dashed) are highlighted.

and the different importance of mismatch according to the particular stage (see Figure 3.13), the effect is more severe the later the mismatched stage is.

By the definition of the basis, the worst-case mismatch must have a projection on one or more basis vectors. Since such a case is detrimental to the *IRR*, the degradation must also be present on the corresponding basis vector or be a consequence of their combination. Since $[\,0 \cdots 0\ +1\ -1\ +1\ -1\,]^T$ doubtless causes the most significant impact, it is the worst case, or at least a close approximation.

To verify the previous statement, all the 256 possible combinations containing the deviation described by this vector and maximum normalized deviations for all the rest, *i.e.*, +1 or −1 in the previously null elements, are simulated. Figure 3.28 shows them in red, and their similarity is apparent compared to the other cases. Analogous combinations for the successive three most harmful basis vectors complete the graph, each in a different color. Note that, for clarity, each case discards curves previously included in worse basis vectors. This representation makes evident the notorious difference in the influence of each basis vector.

Therefore, the most damaging mismatch vector is the one that supposes the maximum difference between I and Q resistors of the last stage, or at least such vector is a reasonable estimation of the effect of the potential worst-case mismatch.

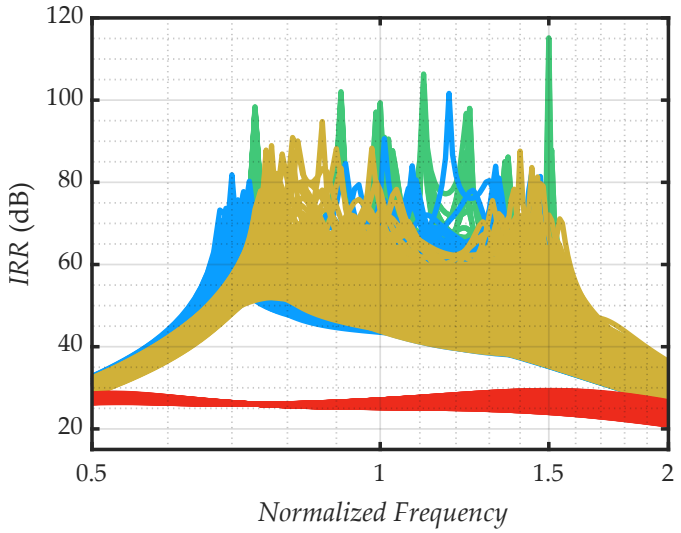

Figure 3.28: Three-stage PPF *IRR* suffering mismatch combinations derived from the three most harmful $\boldsymbol{M}_3$ vectors. They are shown red, yellow and blue from most detrimental to least detrimental. The rest of combinations are in green.

Intuitively, one would expect the mismatches in the remaining stages to have a more extensive influence (which would result in a larger scatter of the red curves in Figure 3.28); however, the nature of the network avoids the accumulation of mismatch errors as each stage recombines I and Q branches. In addition, subsequent stages tend to correct errors of previous stages. This behavior is evident in Figure 3.28, where the smaller green curve corresponds to the worst variation applied in the second stage. In this case, the *IRR* is noticeably limited compared to the rest, but the pole added by the later stage (the one with the lowest frequency) maintains its ideality. On the contrary, the earlier stages are significantly affected since they imply an imbalance in the load impedances they observe. For more details, Section 3.3.3 discusses the effects of the load mismatch.

In addition, Figure 3.29 shows the results of a Monte Carlo analysis (1000 simulations) for a three-stage PPF using devices from a TSMC 65nm technology versus single simulations (black dashed lines) of the same design with ideal elements suffering worst-case mismatch deviations in the last PPF stage, vector $[+1\ -1\ +1\ -1]^T$ or its inverse. The ideal simulation uses the resistor mismatch tolerance given in the technology documentation to configure the deviations. On the other hand, Monte Carlo analysis requires a considerable number of detailed simulations and statistical models that describe variations of the device parameters. Note that the cost of each of these simulations is significantly higher than single ones with the simpler ideal elements.

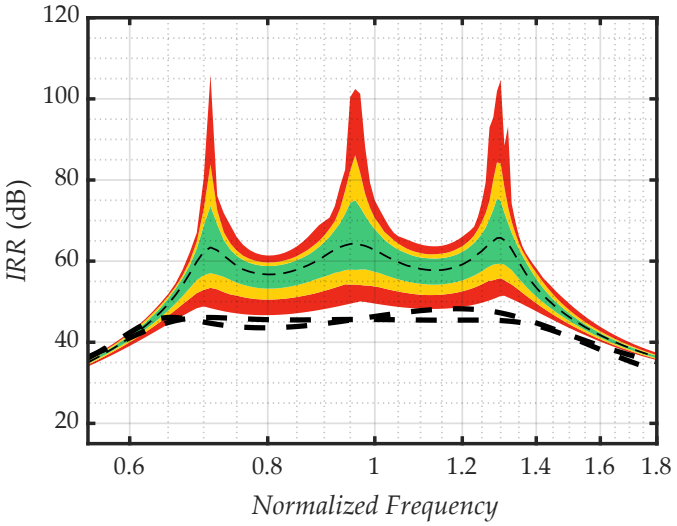

Figure 3.29: *IRR* color map for a three-stage PPF from a mismatch 1000-sample Monte Carlo analysis with devices from the technology library. Black dashed lines mark two worst-case mismatch simulations with ideal models.The green area includes the 70 % percentile with the least distance to the mean for each particular frequency. The yellow region extends to 95 %. The red area covers the extreme values.

As each sample in the Monte Carlo analysis entails a set of random variations, raw results are a confusing mass of *IRR* curves, quite challenging to interpret. To solve this issue, Figure 3.29 colors different percentiles calculated separately for each frequency. Thus, the green area range covers 70 % less extreme cases. This percentile rises to 95 % when including the yellow area. The red area represents the upper and lower 2.5 % percentiles, *i.e.*, the extreme cases.

Figure 3.30 again shows the color map of the Monte Carlo analysis. However, the reference this time is the limit from the analytical result of the one-stage PPF (the guaranteeable *IRR* approximates $4/x^2$). Obtaining this value is even less computationally intensive than an ideal single simulation. This simple fraction corresponds closely with the worst results for each frequency in the whole range of interest. Consequently, it offers a crucial advantage to the designer: the expression establishes a simple relationship between the device tolerance and the *IRR*, enabling the estimation of one of them if the other is known. This association means that a desired *IRR* can set the mismatch constraint for the PPF devices, and this is possible without even needing a prior simulation. Thus, the worst-case *IRR* in the frequency band of interest is

$$IRR_{BW} \approx \frac{4}{x^2} \tag{3.72}$$

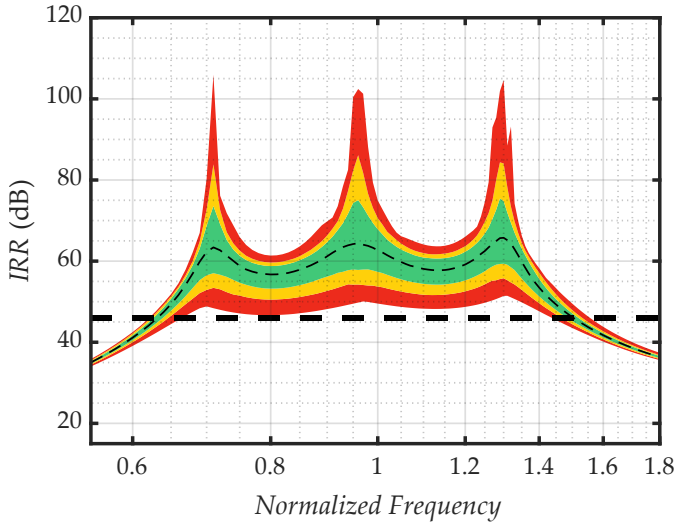

Figure 3.30: *IRR* color map for a three-stage PPF from a mismatch 1000-sample Monte Carlo analysis with devices from the technology library. The black dashed line is $IRR = 4/x^2$, where x is the employed resistor mismatch tolerance.

3.3 Additional effects to PPF performance and analysis

The above developments take advantage of two considerations: only the mismatch affects the circuit, and only resistors present this non-ideality. The last diagrams show that these two analysis conditions are perfectly valid in the employed technology. Also, they facilitate drawing conclusions that otherwise might be obscured by other influences.

However, as the main effects of mismatch have been stated, going deeper into additional considerations helps cover a broader range of scenarios and provides new information on higher-order non-idealities.

3.3.1 Capacitor mismatch impact

In the case of study, capacitor mismatch tolerances are negligible compared to the resistor deviations (see Figure 3.12 and Appendix H). However, other technologies are less fortunate, and capacitor mismatch deviations might become significant. Note that this is not dependent on the node size but, typically, on target specifications and the particular fabrication process. In addition, a thorough optimization process—as done in Section 4.1—might improve resistor mismatch at the cost of worse capacitor deviations. Consequently, with enough dedication, resistor variations might be of the

same order of magnitude as the capacitor mismatch. Additionally, significant parasitics may decide whether the balance is tipped, although they heavily depend on the layout design. Regardless of the underlying reason, deduced expressions can include the capacitor mismatch with this substitution,

$$\begin{aligned}
H_{1A} &= \frac{1}{1+sRC(1+x_R)(1+x_C)} = \frac{1}{1+jb(1+x_1)} \\
H_{1B} &= \frac{1}{1+sRC(1-x_R)(1-x_C)} = \frac{1}{1+jb(1-x_2)} \\
H_{2A} &= \frac{sCR(1+x_R)(1+x_C)}{1+sRC(1+x_R)(1+x_C)} = \frac{jb(1+x_1)}{1+jb(1+x_1)} \\
H_{2B} &= \frac{sCR(1-x_R)(1-x_C)}{1+sRC(1-x_R)(1-x_C)} = \frac{jb(1-x_2)}{1+jb(1-x_2)}
\end{aligned} \tag{3.73}$$

where x_R is the resistor tolerance, x_C is the capacitor tolerance, and x_1 and x_2 define the maximum positive and negative total deviation, respectively. From this, development is equivalent to the previously presented, and it can also be decomposed into $(1+y)$ and $(1+z)$ forms, as described in Appendix E.

Note that the worst-case mismatch is one in which capacitors and resistors from the same I or Q branches have deviations with the same sign. In this form, both effects add their impact on the PPF behavior. Any other combination would imply a lesser pole displacement since each capacitor is always associated with the same resistance. This is also evident from the transfer functions of (3.73).

However, there is an additional effect to consider. Increasing the number of elements (from four to eight) reduces the probability of the sample being an outlier. Therefore, the more optimistic approximation $x^2 \approx x_R^2 + x_C^2$ may be enough for some applications as similar but less accurate results reported in the literature. They are obtained by other methods [Gal00; Had10; Kau08], but data and expressions are consistent with our study.

3.3.2 Load effect

The effect of loads, ignored in the mismatch analysis for clarity, is interesting for two reasons: it improves the estimation of chaining real stages and can model the effects

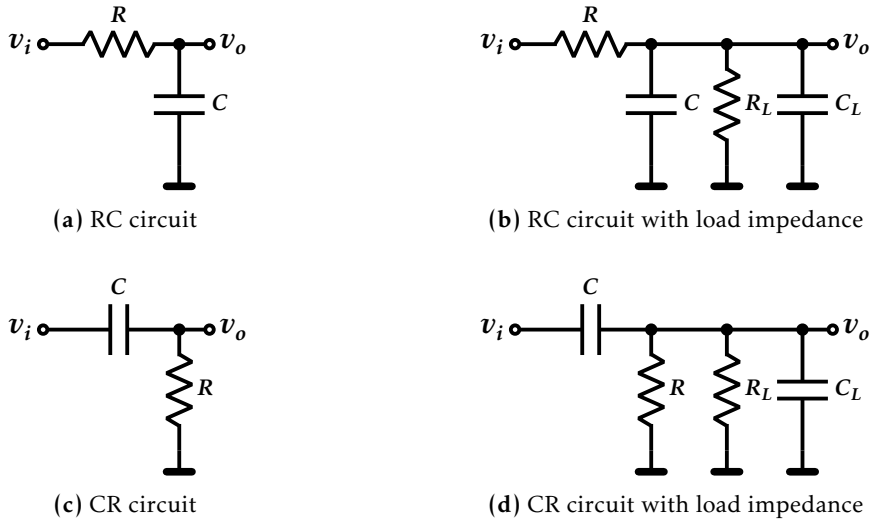

(a) RC circuit

(b) RC circuit with load impedance

(c) CR circuit

(d) CR circuit with load impedance

Figure 3.31: Changes in the equivalent circuit schematic to include load impedances.

of parasitics. In essence, this non-ideality inclusion completes the study of effects that can reduce the IRR of the stage.

In turn, the existence of loadings has two effects. First, the existence of loadings implies new terms in the PPF expressions, even if all loads are identical. This results in additional variables in the IRR and tolerance relationship. On the other hand, the imbalance between circuit loads is another mismatch source that can affect performance and IRR. Since both effects, *i.e.*, mismatch on circuit elements and loads, are independent, they have been presented separately for simplicity.

The expressions are obtained by repeating the procedure shown in Section 3.2.2. However, including the loads slightly modifies the circuits with two terms that depend on the relationship between the value of the PPF devices and the load (or parasitics). Figure 3.31 shows how the new elements modify the equivalent RC and CR circuits.

Load effect expressions use factors $\gamma_r = \frac{R}{R_L}$ and $\gamma_c = \frac{C_L}{C}$, where C_L and R_L are the capacitive and resistive loads, respectively, and R and C are the values of the PPF components. In the absence of mismatch, symmetrical loads only cause power dissipation and do not change the IRR of the stages. More specifically, the transfer functions H_1 and H_2 become

$$H_1 = \frac{1}{(1+\gamma_r)+jb(1+\gamma_c)} = \frac{(1+\gamma_r)-jb(1+\gamma_c)}{(1+\gamma_r)^2+b^2(1+\gamma_c)^2} \tag{3.74}$$

$$H_2 = \frac{jb}{(1+\gamma_r)+jb(1+\gamma_c)} = \frac{b^2(1+\gamma_c)+jb(1+\gamma_r)}{(1+\gamma_r)^2+b^2(1+\gamma_c)^2} \tag{3.75}$$

3.3.3 Load mismatch

The transfer function can be rewritten for a scenario with load mismatch. The worst effects occur when I and Q signals differ, and each load corresponds with one output node. Thus, the worst mismatch combination on loads resembles the case space when applying the mismatch to circuit elements. In other words, the worst case follows the diagram from Figure 3.19b, and the expressions are

$$\begin{aligned}
H_{1A} &= \frac{1}{\left(1+\frac{\gamma_r}{1+x_r}\right)+jb\left(1+\gamma_c(1+x_c)\right)} = \frac{A_1-jbB_1}{A_1^2+b^2B_1^2} \\
H_{1B} &= \frac{1}{\left(1+\frac{\gamma_r}{1-x_r}\right)+jb\left(1+\gamma_c(1-x_c)\right)} = \frac{A_2-jbB_2}{A_2^2+b^2B_2^2} \\
H_{2A} &= \frac{jb}{\left(1+\frac{\gamma_r}{1+x_r}\right)+jb\left(1+\gamma_c(1+x_c)\right)} = \frac{b^2B_1+jbA_1}{A_1^2+b^2B_1^2} \\
H_{2B} &= \frac{jb}{\left(1+\frac{\gamma_r}{1-x_r}\right)+jb\left(1+\gamma_c(1-x_c)\right)} = \frac{b^2B_2+jbA_2}{A_2^2+b^2B_2^2}
\end{aligned} \tag{3.76}$$

where x_c and x_r are the mismatch between resistors (R_L) and capacitors (C_L), respectively. Note that these expressions are easily deduced from (3.74) considering that $\gamma_r = \frac{R}{R_L}$ and $\gamma_c = \frac{C_L}{C}$. $A_1 = 1+\frac{\gamma_r}{1+x_r}$, $A_2 = 1+\frac{\gamma_r}{1-x_r}$, $B_1 = 1+\gamma_c(1+x_c)$, and $B_2 = 1+\gamma_c(1-x_c)$ are defined for simplicity.

The set of transfer functions allows the calculus of the different configurations analogously to Section 3.2.2. For example, in a Type-I D-IQ PPF case, I and Q are

$$I = \frac{A_1-jbB_1}{A_1^2+b^2B_1^2}\cdot v_{in} \Rightarrow \begin{cases} |I| = \frac{\sqrt{A_1^2+b^2B_1^2}}{|A_1^2+b^2B_1^2|}|v_{in}| = \frac{|v_{in}|}{\sqrt{A_1^2+b^2B_1^2}} \\ \theta_I = -\arctan\left(\frac{bB_1}{A_1}\right) \end{cases} \tag{3.77}$$

$$Q = \frac{b^2B_2+jbA_2}{A_2^2+b^2B_2^2}\cdot v_{in} \Rightarrow \begin{cases} |Q| = |b|\frac{\sqrt{A_2^2+b^2B_2^2}}{|A_2^2+b^2B_2^2|}|v_{in}| = |b|\frac{|v_{in}|}{\sqrt{A_2^2+b^2B_2^2}} \\ \theta_Q = -\arctan\left(\frac{A_2}{bB_2}\right) \end{cases} \tag{3.78}$$

Thus, $\Delta\theta$ and $\cos(\Delta\theta)$ are calculated as

$$\Delta\theta = -\frac{\pi}{2} - \theta_I + \theta_Q = -\frac{\pi}{2} + \arctan\left(\frac{\frac{bB_1}{A_1} + \frac{A_2}{bB_2}}{1 - \frac{bB_1A_2}{bA_1B_2}}\right) = -\frac{\pi}{2} + \arctan\left(\frac{b^2B_1B_2 + A_1A_2}{b(a_1B_2 - B_1A_2)}\right) \quad (3.79)$$

$$\begin{aligned}\cos(\Delta\theta) &= \sin\left(\arctan\left(\frac{b^2B_1B_2 + A_1A_2}{b(a_1B_2 - B_1A_2)}\right)\right) = \\ &= \frac{b^2B_1B_2 + A_1A_2}{\sqrt{b^2(A_1B_2 - A_2B_1)^2 + (b^2B_1B_2 + A_1A_2)^2}} = \frac{b^2B_1B_2 + A_1A_2}{\sqrt{\left(A_2^2 + b^2B_2^2\right)\left(A_1^2 + b^2B_1^2\right)}}\end{aligned} \quad (3.80)$$

And A_{BAL} results in

$$A_{BAL} = \frac{1}{|b|} \cdot \frac{\sqrt{A_2^2 + b^2B_2^2}}{\sqrt{A_1^2 + b^2B_1^2}} = \frac{1}{|b|} \cdot \frac{\sqrt{\left(1 + \frac{\gamma_r}{1+x_r}\right)^2 + b^2\left(1 + \gamma_c(1 - x_c)\right)^2}}{\sqrt{\left(1 + \frac{\gamma_r}{1-x_r}\right)^2 + b^2\left(1 + \gamma_c(1 + x_c)\right)^2}} \quad (3.81)$$

Thus, substituting in the expression (3.2),

$$\begin{aligned}IRR &= \frac{1 + 2\frac{b^2B_1B_2 + A_1A_2}{\sqrt{A_1^2 + b^2B_1^2}\sqrt{A_2^2 + b^2B_2^2}} \cdot \frac{1}{b} \cdot \frac{\sqrt{A_2^2 + b^2B_2^2}}{\sqrt{A_1^2 + b^2B_1^2}} + \frac{1}{b^2} \cdot \frac{A_2^2 + b^2B_2^2}{A_1^2 + b^2B_1^2}}{1 - 2\frac{b^2B_1B_2 + A_1A_2}{\sqrt{A_1^2 + b^2B_1^2}\sqrt{A_2^2 + b^2B_2^2}} \cdot \frac{1}{b} \cdot \frac{\sqrt{A_2^2 + b^2B_2^2}}{\sqrt{A_1^2 + b^2B_1^2}} + \frac{1}{b^2} \cdot \frac{A_2^2 + b^2B_2^2}{A_1^2 + b^2B_1^2}} = \\ &= \frac{b^2\left(A_1^2 + b^2B_1^2\right) + 2b\left(b^2B_1B_2 + A_1A_2\right) + A_2^2 + b^2B_2^2}{b^2\left(A_1^2 + b^2B_1^2\right) - 2b\left(b^2B_1B_2 + A_1A_2\right) + A_2^2 + b^2B_2^2} = \\ &= \frac{(A_2 + bA_1)^2 + b^2(B_2 + bB_1)^2}{(A_2 - bA_1)^2 + b^2(B_2 - bB_1)^2} = \\ &= \frac{\left(1 + \frac{\gamma_r}{1-x_r} + b\left(1 + \frac{\gamma_r}{1+x_r}\right)\right)^2 + b^2\left(1 + \gamma_c(1 - x_c) + b\left(1 + \gamma_c(1 + x_c)\right)\right)^2}{\left(1 + \frac{\gamma_r}{1-x_r} - b\left(1 + \frac{\gamma_r}{1+x_r}\right)\right)^2 + b^2\left(1 + \gamma_c(1 - x_c) - b\left(1 + \gamma_c(1 + x_c)\right)\right)^2}\end{aligned} \quad (3.82)$$

The IRR expression is more complex in the load mismatch scenario than the component mismatch because there are more involved variables. Instead of a single variable (x), there are two separate mismatch variables (x_r and x_c). Their respective impact also depends on the relationship between circuit elements and loads; mismatch between loads is more significant the larger loads are in comparison to the circuit devices.

There are two distinct summands on numerator and denominator. As in (3.58) or (3.68), each summand can become zero but at a different b (unless γ_r or x_r equals zero, and also γ_c or x_c does). In other words, contrary to balanced loads, loads with mismatch might constrain the IRR response.

Due to the four different independent variables, the IRR frequency response is not easy to estimate. However, as $\frac{a}{b} < \frac{c}{d} \Rightarrow \frac{a}{b} < \frac{a+c}{b+d} < \frac{c}{d}$, then $IRR(b) \in \left[\min\left(g_1(b), g_2(b)\right), \max\left(g_1(b), g_2(b)\right)\right]$, where

$$g_1(b) = \left(\frac{A_2 + bA_1}{A_2 - bA_1}\right)^2 = \left(\frac{1 + b\alpha}{1 - b\alpha}\right)^2 \tag{3.83}$$

$$g_2(b) = \left(\frac{B_2 + bB_1}{B_2 - bB_1}\right)^2 = \left(\frac{\beta + b}{\beta - b}\right)^2 \tag{3.84}$$

where g_1 and g_2 are terms that depend on resistor or on capacitor loads, $\alpha = \frac{A_1}{A_2}$ and $\beta = \frac{B_2}{B_1}$. As they are analogous to (3.21) but shifted in frequency, dominating factor depends on b and the load variables. Although dependencies are obscure, the lower limit is known at each pole,

$$g_1(b_A) = \infty \Leftrightarrow b_A = \frac{1}{\alpha} = \frac{1 + \frac{\gamma_r}{1 - x_r}}{1 + \frac{\gamma_r}{1 + x_r}} \geq 1 \tag{3.85}$$

$$g_2(b_B) = \infty \Leftrightarrow b_B = \beta = \frac{1 + \gamma_c(1 - x_c)}{1 + \gamma_c(1 + x_c)} \leq 1 \tag{3.86}$$

Note that $\gamma_r, \gamma_c \geq 0$, and $0 < x_r, x_c \ll 1$.

Thus, evaluating IRR at b_B,

$$IRR(b_B) \geq g_1(b_B) = \left(\frac{1 + \alpha\beta}{1 - \alpha\beta}\right)^2 \tag{3.87}$$

As necessarily $\alpha, \beta \in [0,1]$, then,

$$\beta \geq \alpha \Rightarrow \frac{1+\alpha\beta}{1-\alpha\beta} \geq \frac{1+\beta^2}{1-\beta^2} = \frac{\left(1+\gamma_c(1+x)\right)^2 + \left(1+\gamma_c(1-x)\right)^2}{\left(1+\gamma_c(1+x)\right)^2 - \left(1+\gamma_c(1-x)\right)^2} =$$
$$= \frac{1+\gamma_c^2(1+x^2)+2\gamma_c}{2x_c\gamma_c(1+\gamma_c)} = \frac{(1+\gamma_c)^2+x_c^2\gamma_c^2}{2x_c\gamma_c(1+\gamma_c)} =$$
$$= \frac{1+\gamma_c}{2x_c\gamma_c} + \frac{x_c\gamma_c}{2(1+\gamma_c)} \geq \frac{1}{2}\cdot\frac{1+\frac{1}{\gamma_c}}{x_c} \Rightarrow IRR(b_B) \geq \frac{1}{4}\cdot\frac{(1+\frac{1}{\gamma_c})}{x_c^2} \tag{3.88}$$

An analogous development is obtained if $\alpha \geq \beta$. In that case, $\frac{1}{\gamma_c}$ and x_c must be substituted for $\frac{1-x_r^2}{\gamma_r}$ and x_r. Moreover, $IRR(b_A)$ calculous is equivalent. Note that the limit and conditions do not depend on b for both cases. Thus, both have the same lower limit, although $IRR(b_A)$ and $IRR(b_B)$ are not necessarily equal.

The third point of interest (b_C) is the b such that g_1 equals g_2,

$$g_1(b_C) = g_2(b_C) \Rightarrow \left(\frac{1+b_C\alpha}{1-b_C\alpha}\right)^2 = \left(\frac{1+\frac{b_C}{\beta}}{1-\frac{b_C}{\beta}}\right)^2 \Rightarrow \frac{1+b_C\alpha}{|1-b_C\alpha|} = \frac{\beta+b_C}{|\beta-b_C|} \tag{3.89}$$

Denominator signs depend on the relationship of α and β with b_C. That is,

$$b \in (0,\beta) \Rightarrow \begin{cases} 1-b\alpha > 0 \\ \beta - b > 0 \end{cases} \quad b \in (\beta, \frac{1}{\alpha}) \Rightarrow \begin{cases} 1-b\alpha > 0 \\ \beta - b < 0 \end{cases} \quad b \in (\frac{1}{\alpha}, \infty) \Rightarrow \begin{cases} 1-b\alpha < 0 \\ \beta - b < 0 \end{cases} \tag{3.90}$$

Assuming $b_C \in (0,\beta) \cup (\frac{1}{\alpha}, \infty)$, then,

$$\frac{1+b_C\alpha}{1-b_C\alpha} = \frac{\beta+b_C}{\beta-b_C} \Rightarrow b_C\alpha\beta = b_C \tag{3.91}$$

The equation implies that b_C is zero, or $\beta = \frac{1}{\alpha}$, which means $b_A = b_B$. This condition would be only possible at $b = 1$ as $b_A \geq 1$ and $b_B \leq 1$, but if $b_A = b_B = 1$, there is no load mismatch.

On the other hand, if $b \in (\beta, \frac{1}{\alpha})$,

$$\frac{1+b_C\alpha}{1-b_C\alpha} = \frac{\beta+b_C}{-\beta+b_C} \Rightarrow b_C^2\alpha = \beta \Rightarrow b_C = \sqrt{\frac{\beta}{\alpha}} \tag{3.92}$$

In this case, a single ($b > 0$) solution is reached, and IRR can be evaluated at b_C,

$$IRR(b_C) = \left(\frac{1+b_C\alpha}{1-b_C\alpha}\right)^2 = \left(\frac{1+\sqrt{\alpha\beta}}{1-\sqrt{\alpha\beta}}\right)^2 \begin{cases} \alpha > \beta \Rightarrow IRR(b_C) > \left(\frac{1+\beta}{1-\beta}\right)^2 \\ \alpha < \beta \Rightarrow IRR(b_C) > \left(\frac{1+\alpha}{1-\alpha}\right)^2 \end{cases} \tag{3.93}$$

where

$$\left(\frac{1+\alpha}{1-\alpha}\right)^2 = \frac{\left(1+\frac{1-x_r^2}{\gamma_r}\right)^2}{x_r^2} \approx \frac{\left(1+\frac{1}{\gamma_r}\right)^2}{x_r^2} \tag{3.94}$$

$$\left(\frac{1+\beta}{1-\beta}\right)^2 = \left(\frac{1+\gamma_c(1+x_c)+1+\gamma_c(1-x_c)}{1+\gamma_c(1+x_c)-1-\gamma_c(1-x_c)}\right)^2 = \frac{\left(1+\frac{1}{\gamma_c}\right)^2}{x_c^2} \tag{3.95}$$

In other words, $IRR(b_C)$ must be larger than the most restrictive relationship between (3.94) and (3.95), and each one of those expressions resembles the mismatch equation $IRR = \frac{4}{x^2}$. However, there is a relationship factor between load elements in this case. If their values were equal ($\gamma = 1$), the numerator is also 4. However, γ_c and γ_r typically have a lower value than circuit elements; thus, their impact is less significant.

References

[All12] P. E. Allen and D. R. Holberg. *CMOS analog circuit design, 3rd edition*. Oxford University Press, 2012. ISBN: 9780199765072.

[Beh01] F. Behbahani, Y. Kishigami, J. Leete, and A. Abidi. "CMOS mixers and polyphase filters for large image rejection". *IEEE Journal of Solid-State Circuits* 36.6 (June 2001), pp. 873–887. DOI: 10.1109/4.924850.

[Dor10] R. C. Dorf and J. A. Svoboda. *Introduction to electric circuits*. John Wiley & Sons, 2010. ISBN: 9780470521571.

[Gal00] S. H. Galal, H. F. Ragaie, and M. S. Tawfik. "RC sequence asymmetric polyphase networks for RF integrated transceivers". *IEEE Transactions on Circuits and Systems II: Analog and Digital Signal Processing* 47.1 (2000), pp. 18–27. DOI: 10.1109/82.818891.

[Gin73] M. J. Gingell. "Single sideband modulation using sequence asymmetric polyphase network". *Electrical Communication* 48.1 (1973), pp. 21–25.

[Gin75] M. J. Gingell. "The synthesis and application of polyphase filters with sequence asymmetric properties". PhD thesis. 1975.

[Had10] F. Haddad, L. ZaIumld, W. Rahajandraibe, and O. Frioui. "Polyphase filter design methodology for wireless communication applications". *Mobile and Wireless Communications Network Layer and Circuit Level Design*. InTech, Jan. 2010. DOI: 10.5772/7707.

[Had15] F. Haddad, W. Rahajandraibe, and A. Slimane. "Design of an optimal layout RF passive polyphase filter for large image rejection". *2015 IEEE International Symposium on Circuits and Systems (ISCAS)*. IEEE, May 2015. DOI: 10.1109/iscas.2015.7168622.

[Has01] R. A. Hastings. *The art of analog layout*. Prentice Hall, 2001. ISBN: 9780130870612.

[Hir20] A. Hirai, T. Fujiwara, M. Tsuru, K. Mori, and M. Shimozawa. "Vector-sum phase shifter using a tunable active g_m polyphase filter". *IEEE Transactions on Microwave Theory and Techniques* 68.10 (Oct. 2020), pp. 4091–4102. DOI: 10.1109/tmtt.2020.2991738.

[Hor15] P. Horowitz and W. Hill. *The art of electronics, 3rd edition*. Cambridge University Press, 2015. ISBN: 9780521809269.

[Kau08] J. Kaukovuori, K. Stadius, J. Ryynanen, and K. Halonen. "Analysis and design of passive polyphase filters". *IEEE Transactions on Circuits and Systems I: Regular Papers* 55.10 (Nov. 2008), pp. 3023–3037. DOI: 10.1109/tcsi.2008.917990.

[Mar17] A. D. Martinez-Perez, J. Morte, F. Aznar, C. Sanchez-Azqueta, and S. Celma. "Impact of non-idealities on passive polyphase filter performance". *2017 European Conference on Circuit Theory and Design (ECCTD)*. Catania, Italy: IEEE, Sept. 2017. DOI: 10.1109/ecctd.2017.8093256.

[Mar18a] A. D. Martinez-Perez, F. Aznar, G. Royo, C. Sanchez-Azqueta, and S. Celma. "Analysis of the influence of component mismatch on integrated passive polyphase filters". *2018 IEEE International Symposium on Circuits and Systems (ISCAS)*. Fireze, Italy: IEEE, May 2018. DOI: 10.1109/iscas.2018.8351661.

[Mar18b] A. D. Martínez-Pérez, F. Aznar, G. Royo, C. Sánchez-Azqueta, and S. Celma. "Analysis of mismatch impact on image rejection ratio for passive polyphase filters". *International Journal of Circuit Theory and Applications* 46.10 (June 2018), pp. 1838–1847. DOI: 10.1002/cta.2505.

[McG87] W. F. McGee. "Cascade synthesis of RC polyphase networks". *Proc. 1987 IEEE International Symposium on Circuits and Systems, Philadelphia, PA, USA*. 1987, pp. 173–176.

[Nik15] Y. Niki, S. Sasaki, N. Yamaguchi, J. Kang, T. Kitahara, and H. Kobayashi. "Flat passband gain design algorithm for 2nd-order RC polyphase filter". *2015 IEEE 11th International Conference on ASIC (ASICON)*. IEEE, Nov. 2015. DOI: 10.1109/asicon.2015.7516933.

[Nis11] T. Nishi, H. Tanimoto, and S. Oishi. "Cascade synthesis of RC polyphase one-ports". *2011 20th European Conference on Circuit Theory and Design (ECCTD)*. IEEE, Aug. 2011. DOI: 10.1109/ecctd.2011.6043287.

[Nor56] D. Norgaard. "The phase-shift method of single-sideband signal reception". *Proceedings of the IRE* 44.12 (Dec. 1956), pp. 1735–1743. DOI: 10.1109/jrproc.1956.275065.

[Raz11] B. Razavi. *RF microelectronics, 2nd edition*. Prentice Hall, 2011. ISBN: 9780137134731.

[Tan13] H. Tanimoto. "Exact design of RC polyphase filters and related issues". *IEICE Transactions on Fundamentals of Electronics, Communications and Computer Sciences* E96.A.2 (2013), pp. 402–414. DOI: 10.1587/transfun.e96.a.402.

Chapter 4

Design and implementation of passive polyphase filters

While Chapter 3 focuses on the analytical study and operation principle of passive polyphase filters (PPFs), this chapter presents their implementation. It covers the whole design process, from selecting adequate specifications to the prototype experimental measurement. The development includes a proposed method to establish the pole-splitting factor quickly—and, hence, hasten the device sizing—and a layout structure to improve the physical circuit symmetry for less harmful parasitics.

This chapter is organized as follows. Section 4.1 develops the schematic design and the optimal values obtention to reach a high IRR that fulfills specifications. A method for improving IRR according to process variations is proposed. Section 4.2 focuses on the layout design. Guidelines are inferred from the process until a final design is reached, which uses a significantly different approach to usual placement. Section 4.3 collects the experimental results and considerations for measuring the implemented PPF.

4.1 Schematic stage

Determining the required specifications and topology is the first step in any design. In this case, as the title suggests, the circuit is a PPF due to the significant advantage in terms of area for the operation frequency range [Raz11].

Parameter	Value
IRR	40 dB
f_0	100 MHz
BW	20 MHz

Table 4.1: PPF design specifications.

The transceiver architectures from Section 2.1 typically uses drivers at the input and output of the polyphase filter to compensate for the stage power loss and make noise impact negligible by preamplifying the signal. Thus, the system generally works with voltage signals. Also, as the filter is passive, it does not compromise the global linearity. The critical design parameter is the image rejection ratio (IRR), as defined in Chapter 3.

In short, the target design is a PPF for conversion between quadrature and differential signals in the up- and down-conversion chains of an integrated monolithic transceiver. As indicated in the architecture descriptions, the PPF should work in the intermediate frequency (IF) range—*i.e.*, 100 MHz—to improve output IRR at radio frequency (RF), *i.e.*, 5 GHz for the application.

4.1.1 Specifications

The application demands some specifications for the desired global operation. On the one hand, the IF selection fixes the filter central frequency (f_0). On the other hand, system capabilities should be comparable to the Wi-Fi standard [IEE97]. Thus, the filter must provide a minimum of 40-dB IRR in a 20 MHz band (channel bandwidth, BW) to fulfill the objective. The employed technology is 65-nm standard CMOS from TSMC [TSM13]. Table 4.1 summarizes the target specifications.

4.1.2 Minimizing the effect of non-idealities

Previously, Section 3.1.4 analyzes the effect of the main four non-idealities that alter the filter response. This knowledge supposes a series of guidelines to reduce their impact on the design at schematic and layout levels:

- Widening the filter bandwidth (BW_{PPF}) can compensate for effects that imply a frequency shifting. Process and temperature variations are the main culprits, although mismatch and parasitics might contribute to the problem to a lesser extent. In practice, these effects cause the required BW_{PPF} to be significantly larger than the target signal BW. Consequently, this issue heavily influences the number of poles and the pole-splitting factor of the PPF.

- The RC products determine the poles. Thus, there is one degree of freedom in the component sizing. Typically, minimizing capacitors and maximizing resistors imply better robustness against device magnitude variations (as previously shown in Figure 3.11), but other effects—*e.g.* parasitic capacitances or thermal noise—restric the strategy.

- In a similar line, wider resistors reduce fabrication variations. Appendix H includes mismatch and process variation tables for a resistor model. The drawback of increasing its width is that the device might require a significant length to have the same resistance value. Thus, parasitic capacitances, which depend on the device area, will also increase. However, submicron widths suffer from high process and mismatch variations; hence, minimal size resistors are not recommended.

- The study from the previous chapter reveals that the last stage is the most critical to the impact of mismatch. Thus, the symmetry of that stage is essential to achieve good performance. In other words, that stage must have priority in the layout techniques to reduce non-idealities. Also, the I and the Q branches must be as similar as possible to maximize IRR in the band of interest.

In short, careful device selection and sizing are the keys to cancel undesirable effects from non-idealities.

4.1.3 Component selection and sizing

PPF design requires resistors and capacitors. Although using MOS as resistors is usual in integrated circuits out of the RF range, passive devices are preferred to minimize potential variations, especially mismatch. This choice also benefits linearity of the system; almost ideal with this kind of element.

The employed technology [TSM13] allows MIM (Metal Insulator Metal) capacitors, which are more advantageous than the alternative MOM (Metal Oxide Metal) ones [All12] for our system in terms of lesser variance and area consumption. Thus, the choice is evident.

As stated in Section 3.1.4, reduced capacitors and large resistors can offer a better mismatch performance. In other words, sheet resistance must be large enough to implement corresponding resistors. Additionally, devices should also perform well against process variations. Both conditions set the potential candidates among technology resistors [TSM13]: "*rnpolywo*" and "*rppolywo*."

They are polysilicon resistances (see Section2.3.2.2 for additional details) but differ in their N or P wells. In practice, the P-well polysilicon resistor ("*rppolywo*") presents lower tolerance; however, the N-well version has more adequate sheet resistance to implement layout techniques for mismatch reduction, such as common centroid [All12; Bak19]. Thus, if the results were similar, the "*rnpolywo*" would be more promising.

Values of both kinds of devices depend on each other to set a pole. For this reason, Figure 4.1 has upper and lower horizontal axes for resistor and capacitor values, respectively. Both axes are arranged such that the combination of each vertical pair would set the pole at 100 MHz. The graph represents each device mismatch and the combined effect of capacitor-resistor pairs on the RC pole. All capacitors of the study are squares (minimum perimeter-area ratio), and resistors have a width of 2 μm to avoid additional mismatch [TSM13].

Moreover, resistor curves are restricted to a single segment for consistency with the manufacturer characterization [TSM13]. Capacitor and resistor mismatch curves are calculated from statistical data from twenty analyses of Monte Carlo distributed along the range of interest. Each of the analyses uses a set of 1024 samples. The combined curves (dashed lines) employ the equations from Section 3.3.1 and the results of the Monte Carlo analyses.

Greater resistor values decrease their variability at the cost of reduced capacitors that, in turn, suffer from a more considerable mismatch. In the case of "*rnpolywo*", the resistor is always the dominant factor within reasonable values. Note that excessively high

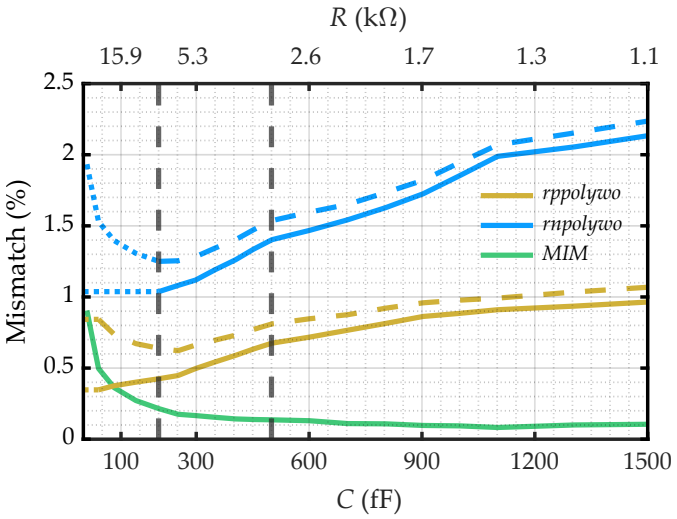

Figure 4.1: Mismatch tolerance of MIM capacitors and possible resistors from the technology, aligned to compose a 100-MHz pole. Dashed lines show the mismatch of the capacitor-resistor pairs.

resistances might cause issues in the driver impedance design, be a significant noise source, or increase signal losses.

On the other hand, the P-well resistors present a notable improvement in mismatch compared with similar values of the N-well alternative. To the extent that large-resistor variations become comparable to deviations of corresponding capacitors. Consequently, the combined curve becomes flattened in the 150–350 fF (10–4.5 kΩ, approximately) range.

Another critical factor is shown in Figure 4.2: the area consumption. As the resistor width is uniform, the area is proportional to the resistance. Similarly, the value of capacitors depends linearly on their area consumption. Consequently, the area of the capacitors is directly proportional to the required capacitance ($f_C(x) = cte \cdot x$). In contrast, the resistor area is inversely dependent on the same value (required capacitance) due to their opposed dependency ($f_R(x) = cte/x$). Device characteristics affect each relationship by different constants. Thus, optimal area points are heavily dependent on technology and employed devices.

Considering these trade-offs, the capacitor sizing is 10×10 μm, translating into 208 fF capacitance. First, this value lies in the minimum mismatch area for both types of resistors; second, it implies a compact design for the two resistor devices; and third, it remains above the range where the capacitance would become comparable to parasitics.

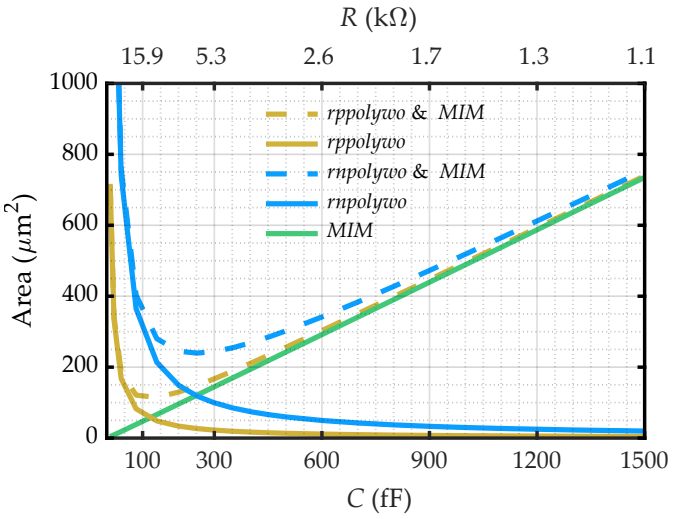

Figure 4.2: Area consumption of technology devices
Area consumption estimation of PPF elements.

The capacitor value and required poles fix the value of resistors: $R_n = 1/(2\pi f_n C_n)$, where R_n, f_n, and C_n are stage-n resistor, pole, and capacitor values, respectively. Nevertheless, note the circular logic in the resistor sizing: required resistor values define sizing, sizing determines process variations, process variations mark the required poles, and the poles defines the desired resistor values. Also, each type of resistor in the technology presents different results.

An approximation is made to break the circularity: resistor variations will be similar to the one for a 100-MHz pole, *i.e.*, 7630 Ω for selected C. Also, a 1.5-μm resistor width is chosen in the end as a trade-off between minimizing statistical errors and parasitic capacitances. Appendix H contains detailed tables of how the sizing affects process and mismatch variations for technology resistors and capacitors.

Monte Carlo analyses with 7630 Ω resistors reveal a ±0.8 % and ±0.4 % mismatch for N-well and P-well alternatives, respectively. Thus, according to (3.72), the 40-dB IRR limit is not compromised due to mismatch. Worst cases would reach at least 48 and 54 dB for N-well and P-well resistors, respectively.

The other issue, frequency shifting due to extreme temperature and process errors, can be estimated by corner simulations under those circumstances. Results show a +20.5 %/−21 % variation for "*rnpolywo*" and +13 %/−14 % for "*rppolywo*". Note that the potential frequency shift due to mismatch is negligible by comparison. On the other hand, capacitors might suffer a +13.5 %/−14.5 % variation.

4.1.4 Pole splitting

Already in the 1970s, Gingell [Gin75] established the conditions for an optimal 3-stage PPF design: a geometrical-ratio pole splitting. After him, some techniques confirmed the result to an arbitrary number of stages by numerical methods [Wad03; Tan06] or synthesis procedures [McG87; Nis11]. However, the number of poles and the distance between them (k_2) remains challenging to estimate without a careful iterative procedure by simulation.

Intuitively, a higher density of poles produces a larger IRR, although the BW_{PPF} will be more constrained than a filter with the same pole number but an increased k_2. In other words, additional poles improve IRR and BW_{PPF}; however, a large number of poles means a higher area consumption, complexity, and, especially, greater signal losses. Thus, an optimal design should use the minimal poles that guarantee the desired IRR over the BW_{PPF}, considering potential variations due to non-idealities. In our design, approximate equations of [Kau08], and preliminary simulations indicate that no less than three poles are mandatory to fulfill the specifications of Table 4.1.

The k_2 optimization is a complex and delicate choice. Proof of this are the few systematic methods present in the literature, such as [Kau08; Nik15; Tan13; McG87]. The classical procedure estimates a normalized BW_{PPF}—*i.e.*, the effective BW (BW_{ef})—from normalized signal BW (BW_{rel}) and a potential deviation factor (BW_{dev}). In our case of study and "*rppolywo*" resistors,

$$BW_{rel} = f_{max}/f_{min} = 1.22 \tag{4.1}$$

$$BW_{dev} = (R_{max} \cdot C_{max})/(R_{min} \cdot C_{min}) = 1.73 \tag{4.2}$$

$$BW_{ef} = BW_{rel} \cdot BW_{dev} = 2.12 \tag{4.3}$$

where f_{max} and f_{min} are the maximum and minimum signal frequencies, and variables from (4.2) refer to the extreme values of filter resistor and capacitor values due to process and temperature.

Finally, the k_2 (for a 3-stage PPF) is obtained from BW_{ef} by solving a second-order equation:

$$BW_{ef,3-stages} \approx 2k_2^2 - 1.9k_2 + 0.9 = 2.22 \tag{4.4}$$

The equation is valid for k_2 equal to 1.39 or −0.46, dismissing the latter for obvious reasons. The same method gives 1.48 for k_2 if PPF employs "*rnpolywo*" resistors.

However, another more straightforward procedure is proposed in this thesis. This alternative design process takes advantage of 1) the signal BW being reasonably narrow compared to expected BW_{PPF}, and 2) assumed deviations are a pessimistic prediction for most cases.

On the one hand, BW approximates to a single frequency, *i.e.*, f_0. The assumption results from significant device tolerances that enlarge BW_{PPF} and the distribution of available spectrum in several channels [IEE97]. Note that the LO controls the channel selection in the heterodyne architectures from Section 2.1, and only the chosen channel is frequency converted to IF. Thus, IF blocks only require a fraction of the operating frequency range: a BW equivalent to a single channel.

On the other hand, the relationship between k_2 and BW_{PPF} is complex due to the IRR function sideways. A strict BW_{PPF} calculation requires obtaining the local minimum IRR between poles and finding where the function first reaches that value (before the first pole) and when it decreases under that value (after the last pole). However, those zones are irrelevant to IRR in the band of interest to all but the most extreme statistical variations. Simplifying BW_{PPF} to be the frequency range between the first and the last poles supposes little error but considerably eases the calculations.

Moreover, both errors oppose each other. While the BW_{PPF} is a pessimistic approach (the actual BW_{PPF} is larger than the estimated), the BW simplification could be too optimistic. Thus, both approximations together are closer than their separate results.

Consequently, the requirement of BW_{PPF} covering signal BW for any deviations transforms into the condition of the f_0 remaining between poles after the effect of variations. Thus, the proposed method for a three-stage PPF:

1. **The first pole (lower frequency)** must be at a frequency f_1 such that the maximum potential deviation to higher frequencies makes it equal to f_0, *i.e.*, 100 MHz in the application of interest.

2. **The last pole (higher frequency)** follows an analogous procedure, and it must be at an f_3 frequency such that it equals f_0 under the most extreme shifting to lower frequencies.

3. **The central pole** is placed at f_2, which must be the geometrical mean of f_1 and f_3. This way, poles are geometrically distributed, and local minimums between poles (both valleys) are balanced. A closer placement of f_2 to one of the other poles would improve IRR between them at the cost of worsen the other half of the BW_{PPF}.

Analytically,

$$f_1 = f_0 \cdot K_U \tag{4.5}$$

$$f_3 = f_0 \cdot K_D \tag{4.6}$$

$$f_2 = \sqrt{f_1 \cdot f_3} = f_0 \cdot \sqrt{K_U \cdot K_D} \tag{4.7}$$

where K_D and K_U are the filter response shifting down and up in frequency, respectively, due to tolerances, *i.e.*,

$$K_D = \frac{1}{(1+\Delta R_+)(1+\Delta C_+)} \tag{4.8}$$

$$K_U = \frac{1}{(1+\Delta R_-)(1+\Delta C_-)} \tag{4.9}$$

where ΔR_+ and ΔC_+ are the tolerances to higher values, and ΔR_- and ΔC_- represent the lower ones.

From these expressions, appropriate values are quickly obtained for each stage resistor. Table 4.2 and Table 4.3 show pole frequency and correspondent resistances for PPF with "*rppolywo*" and "*rnpolywo*," respectively. Capacitors remain at 208 fF.

More notably, k_2 by this method ($\sqrt{K_U/K_D}$) produces a more compact pole distribution than the classical synthesis [Kau08], *i.e.*, 1.32 and 1.43 instead of 1.39 and 1.48, respectively. As a result, overall IRR improves in addition to the procedure simplification.

Pole	Frequency	Resistance	Value
f_1	77 MHz	R_3	9.91 $k\Omega$
f_2	102 MHz	R_2	7.48 $k\Omega$
f_3	135 MHz	R_1	5.65 $k\Omega$

Table 4.2: Design values for a three-stage PPF with "*rppolywo*" resistors.

Pole	Frequency	Resistance	Value
f_1	73 MHz	R_3	10.45 $k\Omega$
f_2	104.3 MHz	R_2	7.31 $k\Omega$
f_3	149 MHz	R_1	5.12 $k\Omega$

Table 4.3: Design values for a three-stage PPF with "*rnpolywo*" resistors.

Nevertheless, a Monte Carlo analysis set with different k_2 can cast a new light on this parameter selection. Figure 4.3 and Figure 4.4 show results for "*rppolywo*" and "*rnpolywo*" PPFs, respectively. The study describes IRR as the minimum IRR between 90 and 110 MHz after process variations are applied according to the statistical models provided by the manufacturer. Green, blue, and magenta lines show the maximum, mean, and minimum value for the Monte Carlo analysis at that k_2. Black dashed lines indicate the k_2 obtained by both methods. Additionally, the yellow dashed line represents the standard deviation (σ) of each sample. Each analysis uses 1024 samples to guarantee convergence without compromising computational cost. For fair comparison and graph legibility, all analyses share the random seed.

First, curves confirm the intuitive idea that close poles achieve larger IRR at the cost of a higher risk of process deviations shifting BW_{PPF} out of BW. More interestingly, the maximum IRR is not at $k_2 = 0$ but at a slightly larger value, as equal poles can not cover all the BW even in the absence of variations. That minimum k_2 optimizes PPF to reach maximum IRR in the most favorable conditions. However, this is not a recommended point in practice, as the PPF would be quite delicate to process variations: slight variations would misalign BW_{PPF} and BW, and filter sideways would define the

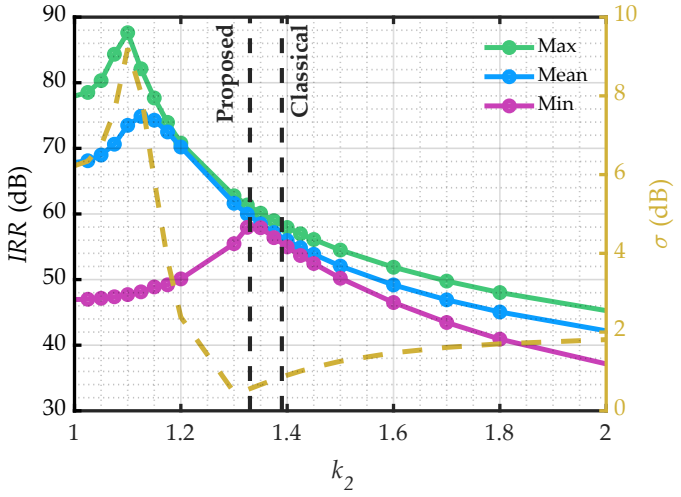

Figure 4.3: Expected IRR in the BW versus k_2 for a PPF with *"rppolywo"* resistors. Curves are interpolated from each Monte Carlo analysis (dots).

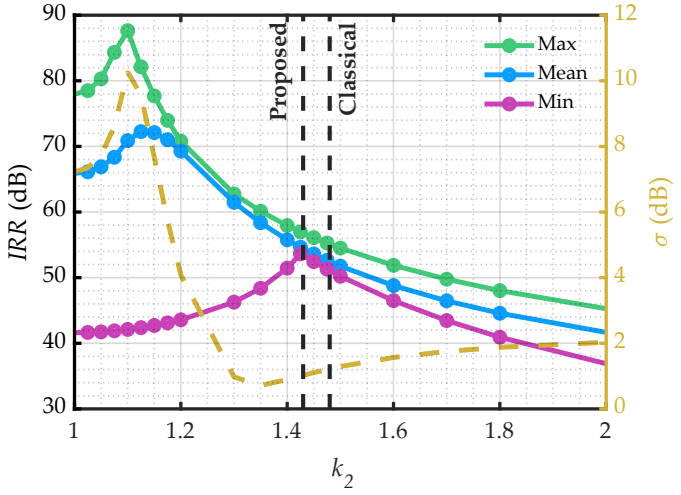

Figure 4.4: Expected IRR in the BW versus k_2 for a PPF with *"rnpolywo"* resistors. Curves are interpolated from each Monte Carlo analysis (dots).

IRR. Note that the mean value is also high due to achieving a large IRR when conditions are favorable. Nevertheless, σ is also maximized, and uncertainty is not a desired characteristic for this kind of filter.

A slight k_2 increment optimizes IRR in terms of mean value. It happens at a point that balances the risk of shifting BW_{PPF} out of BW range and the opportunity cost of IRR due to separate poles. However, this option remains inadequate from a design perspective, as in the previous case, yield can not satisfy most applications. Reliability is usually a key aspect of an image filter, and it will increase with k_2 until the worst sample curve (magenta) peak occurs. That point defines the limit where BW_{PPF} is large enough to keep BW inside for any 1024 variations. From that k_2, IRR decreases due to

the increasing separation of the poles, making IRR valleys between them deeper.

Thus, the curve of minimum IRR for each analysis provides a vital piece of information. It shows the optimal k_2 to maximize reliability. Note that both methods might be considered pessimistic in their estimation, although the proposed one is closer to that value. Note that this difference improves IRR (poles are closer) for all cases at the cost of a little disadvantage in cases rarer than one each 15000 (around 4σ), assuming a normal distribution.

4.1.5 Schematic simulations

Full schematic simulations are mandatory for a more realistic comparison of circuit performances after k_2 selection. This way, more accurate IRR results can be obtained for the different possible PPFs. These simulations complement the process variation data with the deviations due to the mismatch effect. Following the statistical information provided by the manufacturer. The measurement also requires Monte Carlo analysis but presents some additional and significant complexities. Nevertheless, a procedure is proposed to substantially hasten simulations with both non-idealities by taking advantage of their effect on a PPF.

4.1.5.1 Combined simulation disadvantages

Simultaneously evaluating two effects—such as mismatch and process variations—that are random and independent by definition and impact may not be ideal. First, the result of the Monte Carlo analysis would be hardly interpretable. Each case would have undergone disparate frequency shifts and deformations. Consequently, the analysis graphs would become a bewildering tangle of curves. Even if a straightforward and clear metric were used (such as the lowest IRR value within the BW), the results would be unintuitive. While metric histograms might be drawn and specifications verified, the causes of such results would be too challenging to deduce.

Second, the required sample number for meaningful data in a Monte Carlo analysis geometrically increases with each additional stochastic variable. The number of samples needed to obtain reliable results will be the product of the necessary ones for each

effect separately. Thus, simulating the combination supposes a massive increment in computation and processing costs.

For completeness, simulation libraries typically contain only one kind of deviation and are mutually exclusive. Therefore, default libraries might be insufficient in technologies like the one used here, and a custom library combining the models of each non-ideality would be required. Although this task is not complex, it is time-consuming. Also, it requires a deep dive into the simulator operation and model libraries, addressing issues usually inaccessible to most Electronic Design Automation (EDA) software users.

However, the very source of the problem, *i.e.*, the independence between effects, generates a possible solution for the PPFs by applying a "divide and conquer" strategy. According to this technique, the frequency shift caused by the process variations can be analyzed separately, later adding its potential effect to a second simulation with the deformations caused by the mismatch.

4.1.5.2 First step: process variations

As the first step, only process variations are evaluated. This way allows for much more detailed measurements of the potential frequency shifts that the PPF can suffer in the four competing alternatives, *i.e.*, the combinations of resistor types and k_2 selection methods. To ensure the test reliability, each Monte Carlo analysis (one per PPF) employs 1024 samples with the same random seed but a different one from the device and k_2 studies.

Even without mismatch effects, direct plots of the results are problematic to interpret. Figure 4.5 illustrates this issue. However, it is known that all these curves are almost identical but frequency-shifted. Considering that fact, the deviation of each sample can be calculated from the position of their peaks.

Histograms in Figure 4.6 show the frequency shift for both types of resistors. Vertical dashed lines indicate the limit deviations to place f_1 or f_3 into the BW. These values are quickly calculated as the ratio of the pole in question to the nearest BW frequency,

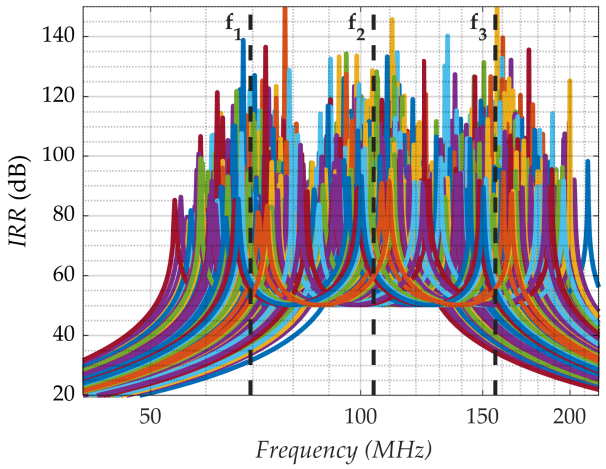

Figure 4.5: *IRR* curves of a process-variation Monte Carlo analysis (1024 samples). The PPF uses *"rnpolywo"* resistors and classical k_2 selection.

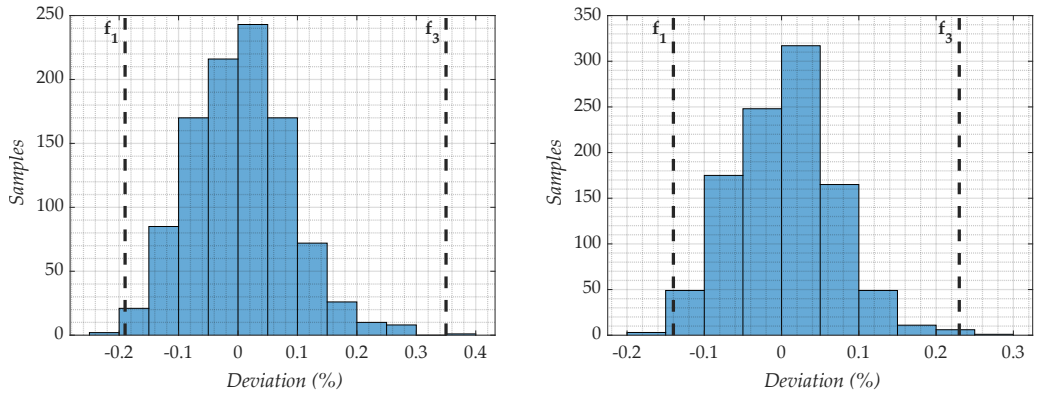

(a) *"rnpolywo"* **(b)** *"rppolywo"*

Figure 4.6: Histogram of the PPF response frequency shift due to process variations. The horizontal axis expresses deviation as a percentage of the *BW* center frequency. Black dashed lines indicate proposed pole positions to *BW*.

which is +35 %/−19 % for *"rnpolywo"* and +23 %/−14 % for *"rppolywo."* Both histograms show that most, if not all, cases lie within the specified limits. In other words, the deviations obtained are consistent with those expected in the k_2 selection.

Note that, despite BW_{PPF} being slightly wider than the frequency range between f_1 and f_3, those poles are a more straightforward reference for the impact of deviations on the filter response. Also, there are only two histograms in Figure 4.6 as there is no significant dependency with the k_2 selection method; differences in the resistor size are negligible to this effect. Nevertheless, proposed and classical methods would differ on the f_1 and f_3 values. The former would be more separated than the ones shown (proposed), although they are not included for clarity.

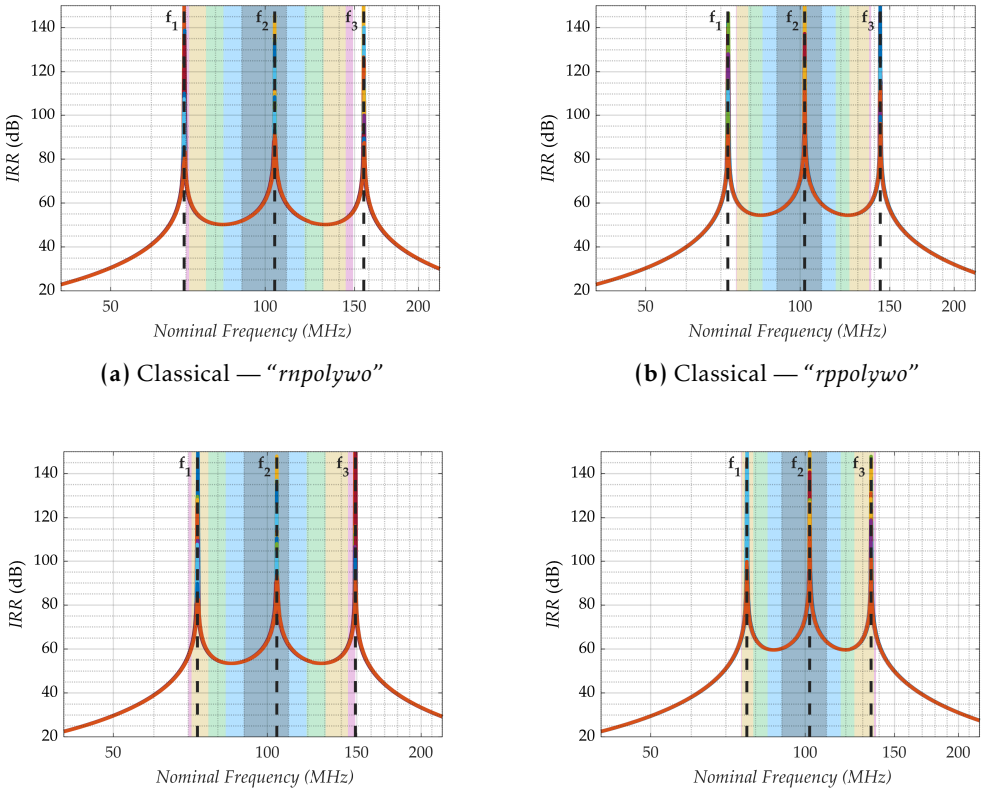

(a) Classical — *"rnpolywo"*

(b) Classical — *"rppolywo"*

(c) Proposed — *"rnpolywo"*

(d) Proposed — *"rppolywo"*

Figure 4.7: *IRR* curves of Monte Carlo analyses for the four PPF designs. Black dashed lines indicate nominal poles. Frequency shifts have been compensated, but the statistical information is shown as *BW* extending in color grey (nominal value), blue (σ), Green (2σ), yellow (3σ), and magenta (most extreme cases).

In addition, the information from each sample enables "aligning" the *IRR* curves of the samples, as Figure 4.7 shows. Note that the curves practically overlap, and the three peaks perfectly fit with the poles. Only the peak heights differ due to the discrete sampling of the simulation.

This alignment is analogous to changing the reference system to the nominal frequencies of the PPF response. Thus, relative positions are maintained, but the BW_{PPF} remains constant under this perspective while the *BW* undergoes an inverse frequency shift. Since the changes are random, so is the position of the *BW*. Therefore, a cautious assumption is considering that the *BW* expands to cover the whole potential range where it might be. Thus, the gray regions in Figure 4.7 show the original *BW* position, *i.e.*, 90–110 MHz. At the same time, the blue, green, and yellow areas cover the potential *BW* enlargement, considering variations of σ, 2σ, and 3σ, respectively. On the other hand, the magenta area covers the cases above three σ that appear in the analysis.

These results confirm, from another perspective, what was observed in Figure 4.3 and Figure 4.4. The wider BW almost fills the entire BW_{PPF} in the proposed method k_2 PPFs, benefiting the filter performance. A fitted but non-overflowed BW_{PPF} is more efficient as closer poles improve IRR. Note that even the worst cases of Figure 4.7d do not exceed the BW_{PPF} since it extends until the peak side fall below the valley IRR.

Moreover, the results provide an essential piece of quantitative data: the range covered by the relative BW if accounting for potential frequency shifts due to process variations. Although this metric is pessimistic because it assumes the relative BW is at all possible locations, it allows the combination with other non-idealities, such as mismatch. Specifically, these ranges are 71–144 MHz and 76–137 MHz for PPFs with "*rnpolywo*" and "*rppolywo*," respectively. It is worth mentioning that those frequencies are similar but different from BW_{PPF} and pole positions.

4.1.5.3 Second step: mismatch impact

As process variation translates into a BW enlargement, the mismatch impact is equivalent to its usual degradations as an independent effect, but considering the new BW range. In other words, the mismatch degradation matters on a broader frequency band instead of just the BW specification. This way, the worst non-ideality combinations are evaluated without relaying in an exponential-increased sample number. Moreover, this strategy allows intuitive representation of the mismatch (Figure 4.8) without compromising final IRR results (Figure 4.9).

Graphs from Figure 4.8 show the impact of mismatch on the PPF IRR in function of the frequency. The representation follows the same guidelines as Figure 3.11, and they reveal two impact factors on the mismatch. On the one hand, the PPF with "*rnpolywo*" resistors presents more variation than the same method but using "*rppolywo*" devices. This uncertainty is visible as an increment of the IRR range for each frequency.

On the other hand, there are also some differences between the results of the k_2 selection methods. More precisely, the analyses of the proposed k_2 seem to present a more significant variance in the IRR valleys than their corresponding classic designs, a logical result considering the pole proximity. However, carefully looking at the most extreme cases (red areas from the figure 4.8) reveals the trade-off.

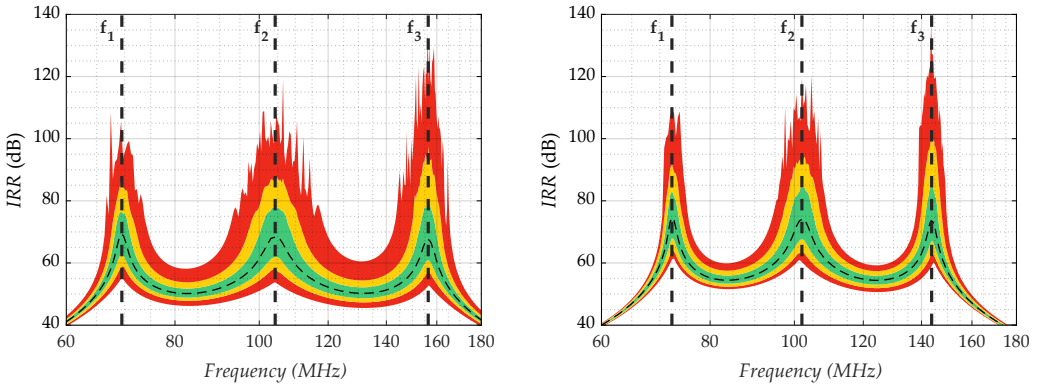

(a) Classical — *"rnpolywo"*

(b) Classical — *"rppolywo"*

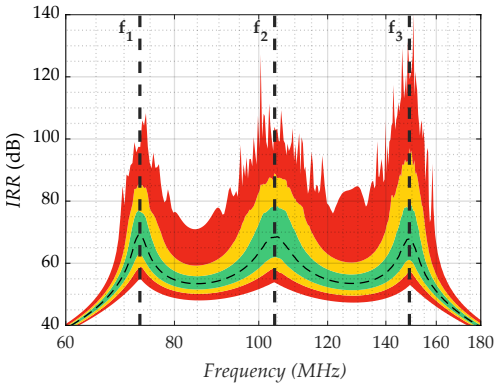

(c) Proposed — *"rnpolywo"*

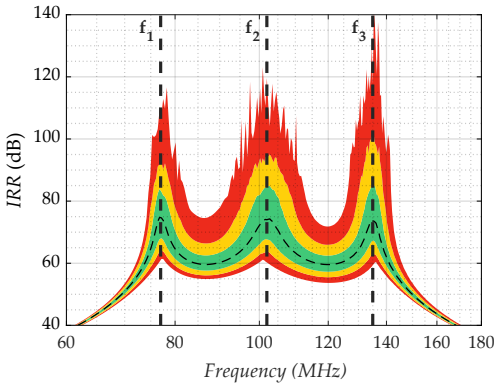

(d) Proposed — *"rppolywo"*

Figure 4.8: *IRR* heat map of PPFs with mismatch variations. The thin dashed line connects the median values of each frequency. The green area comprises 70 % of samples closer to that value. The yellow extent expands it to the 95 % of cases. The most extreme results are in the red region. Additionally, vertical dashed black lines mark the poles.

Most of the extreme-variations range appears in the upper region because a mismatch combination has displaced a pole into valleys. However, this might even be advantageous if the shifted BW ends here: IRR would be larger than usual. Nevertheless, the actual desirability of these cases is uncertain due to two motives: *a*) the random nature of the BW displacements and *b*) the lack of knowledge of how the shifted peak might alter the rest of the curve. Note that this kind of representation focuses on the statistical variation of the IRR for each frequency; hence, the correlations across frequencies are lost.

Nevertheless, the lower red regions are of great interest. They compile the worst case for each frequency, with those minimums typically corresponding to different analysis samples. Those red areas seem similar, although the closer proximity of the proposed poles implies an IRR offset for the proposed k_2 designs.

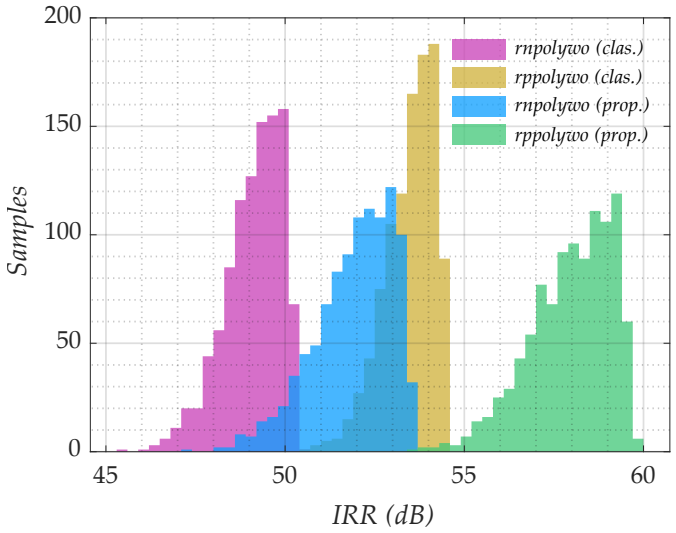

Figure 4.9: Histogram of the *IRR* from the four potential designs. Results are obtained from 1024-sample Monte Carlo analyses, applying mismatch and process variations.

Figure 4.8 shows a great perspective of the variations due to mismatch; however, it omits critical statistical information, such as the minimum value of each sample (as opposed to the minimum value of each frequency). Neither the different *BW* ranges are represented for clarity. For these reasons, the *IRR* histograms of Figure 4.9 provide a better comparison between PPF design performances, showing a common metric ("how much") at the cost of losing perspective of the variation ("what changes").

The *IRR* measurement follows the definition of the minimum *IRR* value within *BW*. Thus, the *IRR* of each sample is described by the minimum inside the previously calculated frequency ranges, *i.e.*, 71–144 MHz and 76–37 MHz for the "*rnpolywo*" and "*rppolywo*", respectively).

The slightly better robustness against variations of "*rppolywo*" implies significant—around 5 dB—*IRR* improvement versus the "*rnpolywo*" alternative. Also, the differences mentioned due to k_2 are projected into the histogram. The broader classical distance means a more predictable *IRR*, while proposed poles admit worse variance as the cost of introducing a beneficial *IRR* offset. Ultimately, the performance advantage vastly outweighs this little sacrifice.

In conclusion, the PPF with "*rnpolywo*" resistors and the proposed k_2 performs best. Thus, that is the design that will be implemented in the layout.

4.2 Layout stage

After carefully sizing the devices, the following design stage is the physical design or layout. The PPF layout performance heavily relies on an adequate balance between the I and Q signal paths and reducing the mentioned non-idealities. Not paying enough attention to the layout wiring might jeopardize the design optimization.

The immediate step is studying the placement and simulating the effects it adds. These post-layout simulations use more complex models (again, provided by the manufacturer) to verify the physical configuration before production.

4.2.1 Initial considerations

The layout design decisions do not escape from having a vast impact on non-idealities that might alter filter balance, such as mismatch or parasitics. Thus, good practice rules and guidelines for the employed technology are critical to achieving desired performance in the design. Seemingly trivial changes like the layer or width of connections might significantly affect performance [All12]; the contrasting IRR curves of following designs evidence this.

From the PPF studies, a series of guidelines are deduced:

1. The symmetry between the **I and Q paths** is essential. Any difference implies an effect equivalent to mismatch, which is known to limit the achievable IRR. On the other hand, the lack of symmetry between balanced paths is not as problematic (Section 3.2.1).

2. The balance of **the last stage** is the most critical one. That stage must have priority over the rest of the circuit to reduce the impact of non-ideal effects (see Figure 3.13c).

3. **The device mismatch** restricts IRR, as demonstrated in Chapter 3. Techniques that reduce it might benefit final performance. Thus, splitting elements for a common-centroid placement or reducing distances between identical elements is desirable. Unfortunately, their actual advantage is hard to evaluate as the complex behaviors of mitigated factors are not included in the simulation models.

In the experimental part, the results would also lack enough reproducibility to evaluate the methods even if the cost and means were not a limitation. Nevertheless, the circuit benefits from mitigation techniques despite being troublesome to quantify.

4. **Proximity between devices** increases parasitic capacitances, typically causing imbalance or signal loss, especially at high frequencies [Raz11]. Note that this issue directly opposes the previous point; thus, the designer must reach a trade-off.

5. The other primary source of parasitics inside the chip is the **wire size** [Bak19]. Reducing their width and using higher metal layers minimize the capacitor effect. However, those recommendations raise series parasitic resistors in the form of larger L/W ratios and the increment of the required series vias, respectively.

However, two considerations should be mentioned about the last point. First, if the paths are perfectly symmetrical, the consequent parasitics would be ideally identical. Thus, despite some signal losses, IRR would be unaffected (negligible effect in practice). Second, PPF uses much larger resistance values than capacitances to optimize device mismatch. As a consequence, capacitors become more vulnerable to parasitics. Hence, enlarging parasitic resistances to reduce parasitic capacitance tends to be more convenient than otherwise.

4.2.2 First layout approach

As mismatch restricts PPF performance in terms of IRR and resistors are the most vulnerable device, the first approach aims to minimize their differences by the common-centroid technique [All12]. Following this strategy, each resistor is divided into four segments, distributed to give each resistor the same geometric center. This way, any gradient error will affect the interdigitated resistors in a similar factor.

In our case, each resistor is split into four parts, and each segment is placed in a different block of the column, as shown in Figure 4.10. Note that each block is a different permutation of the four resistors to give them a shared centroid. In other words, if column positions are enumerated from one to sixteen, the sum of segment positions of each resistor must equal 34.

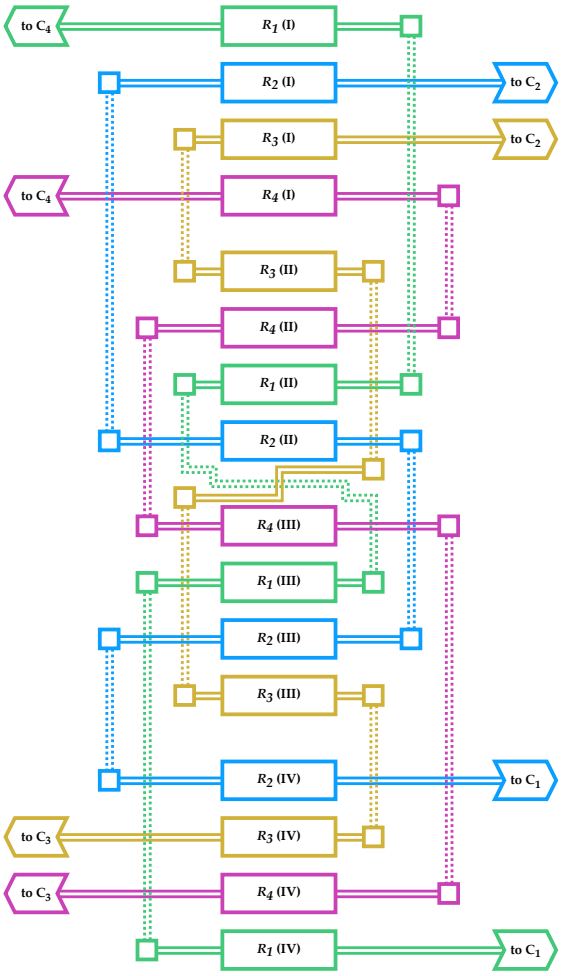

Figure 4.10: Diagram of interdigitated resistor placement and capacitor position for the first layout approach. Each color represents a different resistor. Solid and dotted lines mean two different metal layers; squares are the vias between them.

Additionally, the four groups fulfill an order that allows symmetrical pathing to the middle point. The design only requires two different metals (solid and dotted lines in the diagram) and three levels of horizontal separation on each side. Path with more extended wires or metal layer changes are prioritized to reduce the difference between layout parasitics.

Capacitors are placed after resistors. They are distributed in the quadrant corresponding to the resistor terminal positions: C_1, southeast; C_2, northeast; C_3, southwest; and C_4, northwest. After one stage has been designed, the same scheme can be easily adapted to all the rest. The only difference is just a slight change in the width distance between the east and west metal paths of Figure 4.10 to accommodate the resistor segment lengths of that stage. Figure 4.11 shows the 3-stage design using this

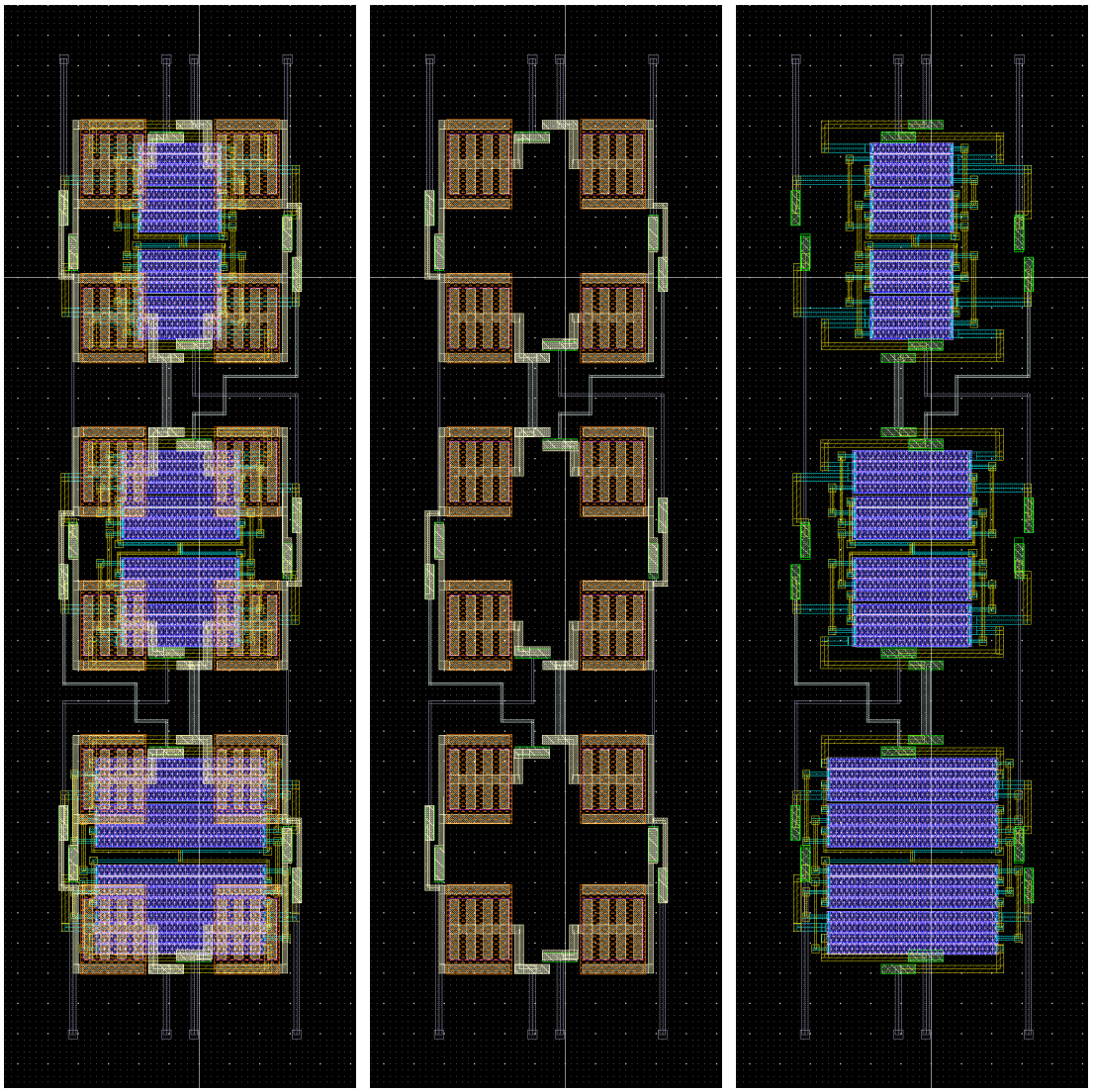

(a) Complete design **(b)** No resistors **(c)** No capacitors

Figure 4.11: First approach layout design. The pale yellow layer is a high metal layer that connects capacitor-specific layers (orange and pink, overlapped). Blue and yellow are the lowest metal layers, hence, the closest to resistors. Vias between high and low metal layers can be seen in green in the no-capacitors view. Light and dark grey are middle metal layers that link stages.

approach. For clarity, the complete version is supplemented with a version without capacitors and a version without resistors.

In this technology, resistors can be placed under the capacitors thanks to the presence of several layers between them. Employed resistors are created over the substrate. In contrast, MIM capacitors are implemented on the highest metal layers. The technology even includes some MIM capacitor implementations with shielding from lower layers if required. These tools help compact the physical design and decoupling stage size from resistor sizing—capacitors remain equal across stages and are significantly larger

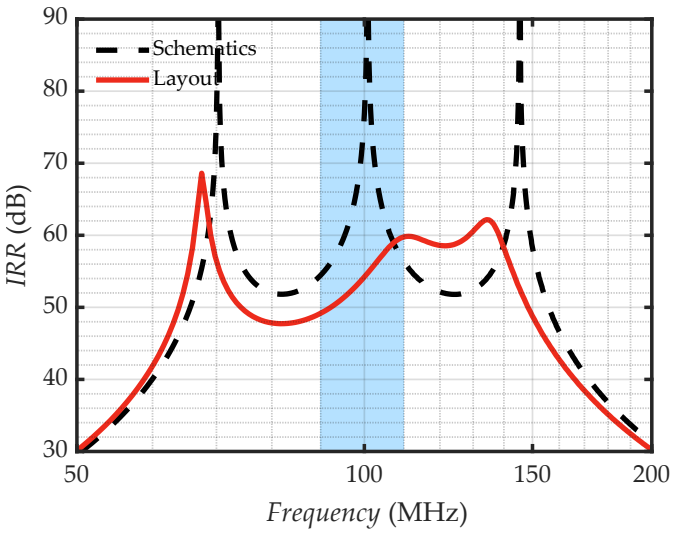

Figure 4.12: *IRR* of the first approach layout.

devices—simplifying implementation after the first stage design is done. The following layouts benefit from these strategies to a greater or lesser extent.

However, simulations reveal the issues of this first approach. Although the common-centroid technique should have reduced the resistor mismatch, its restrictions cause a non-negligible asymmetry [Cro95] between I (R_1 and R_3) and Q (R_2 and R_4) resistors. Consequently, post-layout simulations show a significant *IRR* degradation in Figure 4.12. The graph presents a notable deviation in the poles, translating into a worse *IRR* in most of *BW*. The minimum *IRR* decreases when considering the BW_{PPF} or the extended *BW* range. In other words, the process deviations might exacerbate the issue.

4.2.3 Second layout approach

The study from Section 3.2 concluded that mismatch impact dramatically depends on the particular mismatch combination. Differences between I and Q resistors are much more harmful than distinctions inside the differential signal paths. Thus, this strategy focuses on the similitude between two pairs of resistors from different branches instead of the four resistors. More precisely, the particular pairs are R_1-R_4 and R_2-R_3. If $R_1 = R_4$ and $R_2 = R_3$, the difference between the pairs would cause an error in the collinear components of the IQ signal, but it would not affect the desired sequence or the image.

In this way, pairs are placed by common-centroid columns. This split significantly eases the segment connections. Figure 4.13 shows the resultant distribution diagram.

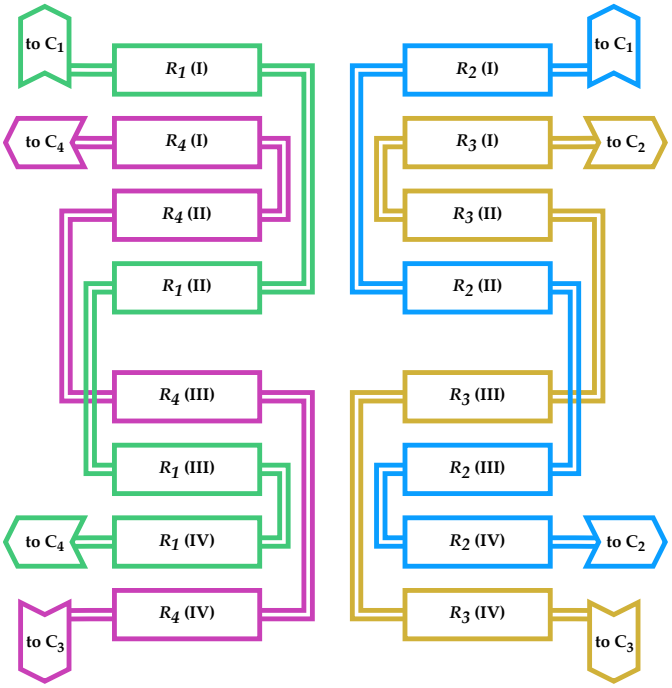

Figure 4.13: Diagram of the second layout approach.

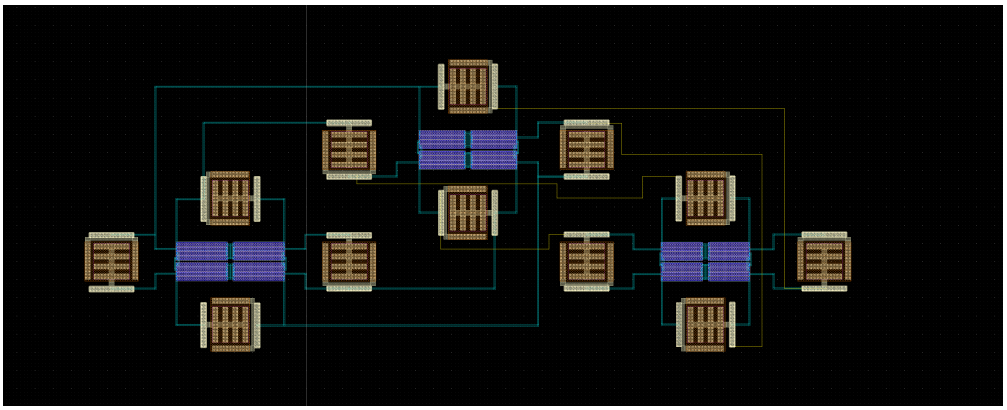

Figure 4.14: Second approach layout placement. The design was dismissed at an early stage as the initial placement reveals issues for reaching the desired symmetry.

Note that the wiring of this placement is more straightforward, as the split significantly eases the segment connection. Thus, this approach reduces the risk of potentially harmful parasitics compared to the previous design.

In this design, capacitors are placed according to the direction of the correspondent terminal. The expansion to several stages is simple but presents a relevant disadvantage: capacitor placement does not allow efficient area consumption or inter-stage path symmetry. Figure 4.14 shows a 3-stage PPF layout.

The layout of Figure 4.14 can be optimized by using higher-layer metals as connection

layers, moving some devices closer to minimize area, or even iteratively improving the balance of parasitics. All those actions would undoubtedly enhance the performance after a significant effort and dedication. However, simulations reveal that this approach is hardly symmetrical enough for our *IRR* ambitions. Thus, relinquishing this strategy in favor of new methods seems more promising.

Nevertheless, this attempt reveals some critical aspects to consider for the final placement:

- **Linear placement of signal paths** is inconvenient for PPF physical design. Ideally, the four phases should be equidistant to their "neighbors." However, parallel pathing implies that the northmost and southmost wires (supposing they follow a typical west-to-east orientation) are not physically adjacent. While dummy placement can solve some issues, other aspects—like parasitics between adjacent wires—might still affect the circuit symmetry.

- **Connections between stages** are problematic. In the two previous versions, reaching similar characteristics between the four phase signals from one stage to the following one was tedious. Moreover, that optimization is highly vulnerable to falling into a false optimum due to potential variations not considered in the models (would two paths keep equivalent characteristics after fabrication if they are geometrically distinct?). To this extent, inter-stage connections should be considered in the stage design to maximize the similitude between the pathing of signals.

- **Capacitors** have a particular relevance in the physical design. Although they are notably more robust against mismatch variations than resistors, the low capacitance makes them susceptible to imbalance due to parasitics. Thus, similitude between adjacent capacitors becomes critical for an adequate physical design (see Section 3.3.1. One crucial problem of the last design is that C_1 and C_3 presented more parasitic capacitances than C_2 and C_4, as wires are closer, *e.g.*, R_1(I)-R_1(II) and R_2(I)-R_2(II) vs. R_4(I)-R_4(II) and R_1(III)-R_1(IV) in the Figure 4.13.

- **The common centroid technique** is inefficient for our particular case. As resistors are implemented in the substrate, their metal connections are in the lower metal layer. Thus, splitting these devices into segments significantly increases

parasitic capacitances. Even if higher metals are employed for the intra-resistor pathing, vias require some area in each associated metal to fulfill design rules, and each segment connection would imply a set of vias. Thus, although the technique undoubtedly improves resistor mismatch, the cost would jeopardize other factors that alter the circuit balance.

Therefore, searching for a new approach considering all those key points can greatly benefit post-layout results and improve system performance.

4.2.4 Final layout design

The final design method is significantly distinct from previous versions and the layouts of the literature, for example [Beh01]. Only [Mil16] uses a similar concept, although the signal flow is opposite, and component placement is distinct from our proposal. The final approach focuses on solving the issues cited in the last attempt.

First, the asymmetry in the four phases adjacencies can be seen in the usual representation of the PPF schematics (Figure 4.15a). One of the connections of each stage—C_{i4} to R_{i1}—is different from the other phases in needing to cross all the rest of the signals. On the other hand, the less usual "circular" representation of the schematics (Figure 4.15b) forego the crossings with an alternative distribution of the diagram elements. Thus, this device organization is highly promising as a start for the physical placement instead of a more classical approach.

The circular placement also solves the second issue: the interstage connections. According to the schematics idea, signals go from the inside to the outside or vice versa. This approach differs from the typical right-to-left planning, and it removes the asymmetries due to a linear arrangement of the stages. In previous cases, the routing between stages was challenging to balance due to the asymmetrical starting and ending points; however, a circular distribution enables perfect radial symmetry, and hence, all phases have equal distances between stages. Moreover, the routing does not require any crossing.

Another critical change from previous attempts is that capacitors become the main factors in each stage and global PPF placement. On one hand, they are the largest

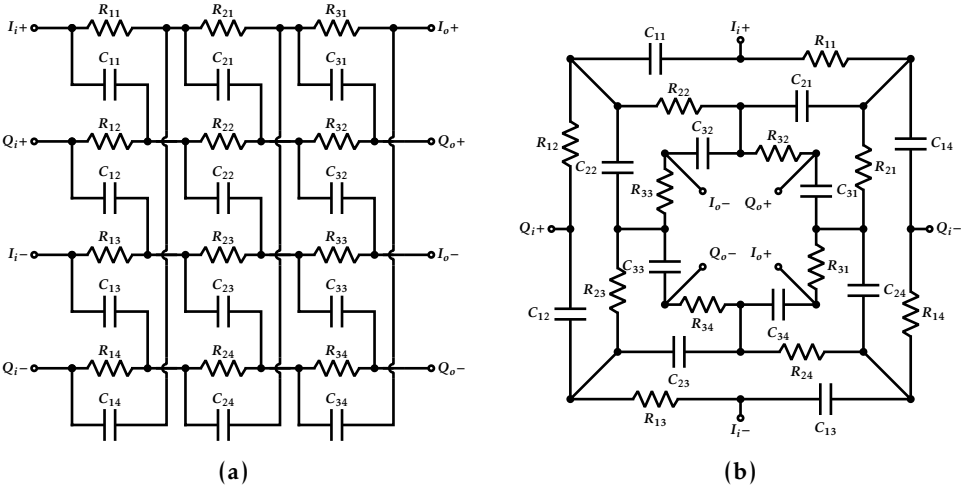

Figure 4.15: Three-stage PPF schematic representations: *a*) linear topology and *b*) circular topology.

devices, and thus, they restrict the minimal size of the filter. The option of placing resistors under capacitors in this technology magnifies the importance of capacitor size in the PPF area. On the other hand, the strategy minimizes the impact of parasitic capacitances, favoring these reductions over decreasing resistor mismatch, following conclusions drawn from previous PPF layout attempts.

Finally, the order of the concentric stages is defined by their respective mismatch importance. As the last stage is critical in this respect, it must have its devices as close as possible. In other words, that stage should be in the center of the layout, and the rest of the stages should be placed surrounding it.

Figure 4.16 contains the diagram of the final PPF layout. The scheme represents capacitors and related layers in yellow and magenta, while resistors and associated connections are in blue and green. The different colors illustrate the adjacency: equal-colored devices are not adjacent. The small squares that use both colors are the vias. Output and input nodes are indicated in the appropriate vias, as input and output routing uses intermediate metal layers to minimize coupling.

As mentioned, the last-stage capacitors are placed in the center of the design, as closed as possible, and their connection terminals are oriented to the outside to ease fulfilling design rules. After that, the second-stage capacitors have the turn. Their location is in the middle of each side of the last-stage perimeter to minimize the distance from each other. Lastly, first-stage capacitors are on the corners of the perimeter. The vias

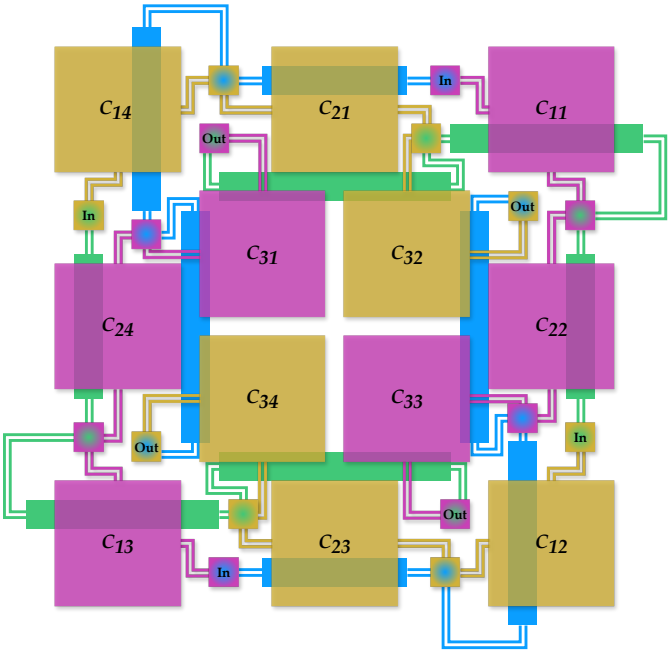

Figure 4.16: Diagram of the final layout design. Yellow and magenta represent the capacitors, while the resistors are green and blue. Devices of the same kind with different colors are adjacent in terms of phase.

employed the space between the first and second-stage capacitors, and the resistors are symmetrically placed following their associate capacitors.

The spiral pathing of different phases allows for unifying their centers. Resistors and capacitors fulfill this condition, although the directions of the spiral of each kind of device are opposed. See equal-color paths from "In" to "Out" nodes in Figure 4.16.

This same strategy can be extrapolated to a greater number of stages. As an example, Figure 4.17 shows a placement for a seven-stage PPF. For clarity, the nomenclature of capacitors has been simplified to indicate the stage only, and resistors and vias are omitted. However, the color code remains the same. According to the design rules of the particular technology, the separation of the first and second rings (C_{5-6} and C_{1-4}, respectively) might be enlarged to accommodate the required vias.

Nevertheless, this requirement of an slightly area expansion would hardly appear in a six-stage PPF. Alternatively, new concentric rings can extend the method to higher numbers of stages. Nonetheless, the extension also increases the distance among elements of the less significant stages.

On the other hand, Figure 4.18 represents the circuit implementation on Cadence Virtuoso. The image reveals the rotation symmetry of the routing and even the device

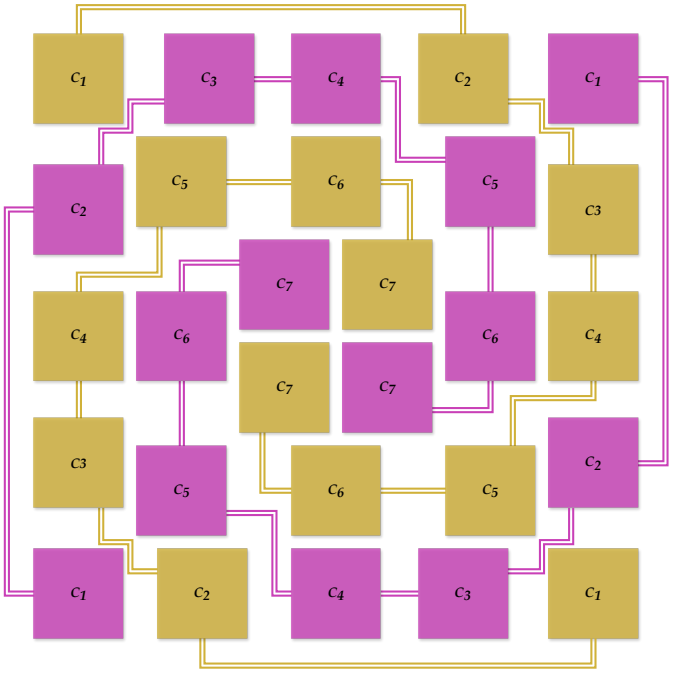

Figure 4.17: The diagram of the final layout approach expanded to seven stages (28 capacitors) by using an additional ring.

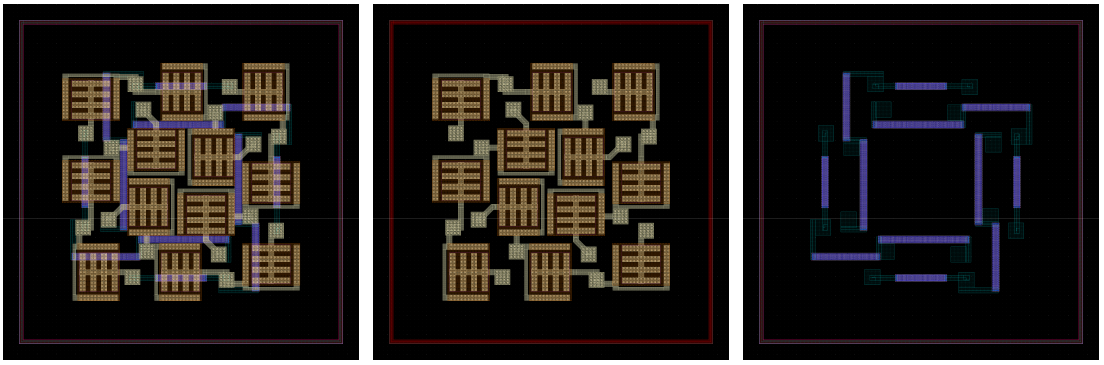

(a) Complete design **(b)** No resistors **(c)** No capacitors

Figure 4.18: Final layout design. It follows the same color meaning as Figure 4.11.

orientation. As in the previous cases, three views are included to ease the visualization. The complete design with pads is shown in Figure 4.19. Wires to pads are implemented in intermediate metal layers to reduce coupling with the metal layer associated with the devices. Besides, this routing also attempts to maximize its symmetry.

Post-layout simulations show great results from careful layout placement. Even including the wiring to pads, the impact of parasitics is minimal, as shown in Figure 4.20. The difference in IRR between the post-layout and schematics PPF simulations is less than 2 dB. The improvement in comparison with Figure 4.12 is remarkable. The final approach obtains a significantly higher IRR.

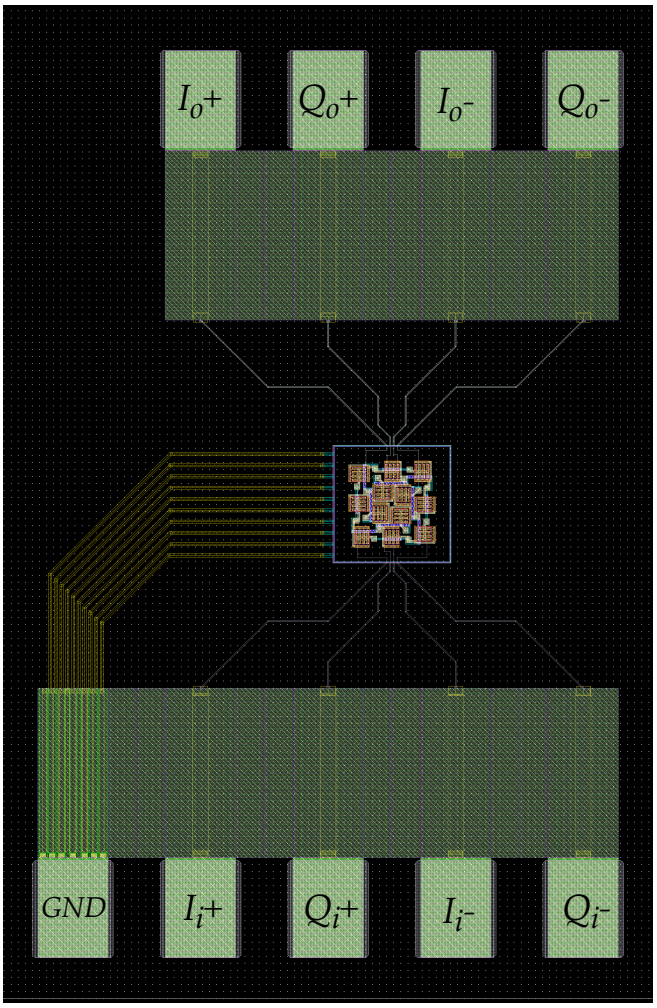

Figure 4.19: Final layout design with pads for experimental characterization. The circuit is part of a set of test devices implemented in the same package.

Besides, this is achieved with a lower area consumption: 80×80 μm (6400 μm^2) vs. 160×50 μm (8000 μm^2) of the first attempt. Although previous strategies are dropped before potential optimization, the final method far exceeds the prospects of earlier attempts.

A statistical characterization is carried out with the final layout. Figure 4.21 represents the PPF *IRR* with mismatch and process variations. The minimum *IRR* in the *BW* (90–110 MHz) under mismatch variations is shown in yellow. The same metric is used in blue, but the frequency range is widened to the extended *BW* (76–137 MHz) to evaluate potential frequency shifting due to process variations. Dashed lines mark respective means, which are just 2 dB apart. A similar distance is maintained in the rest of the statistical metrics.

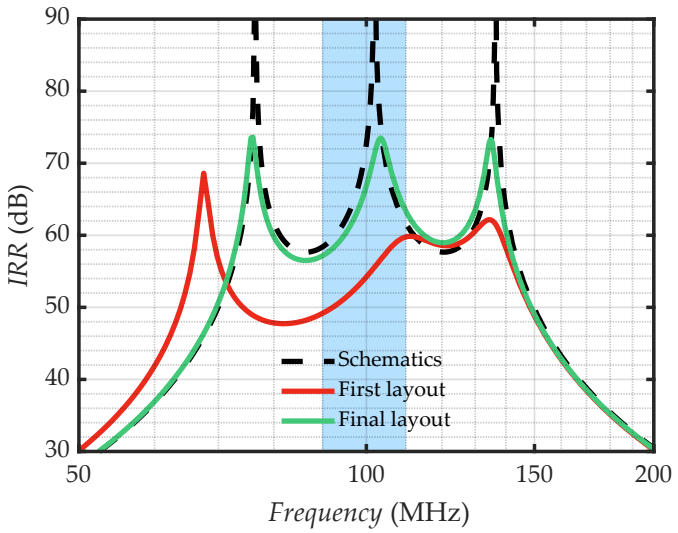

Figure 4.20: Post-layout *IRR* results of the final layout version.

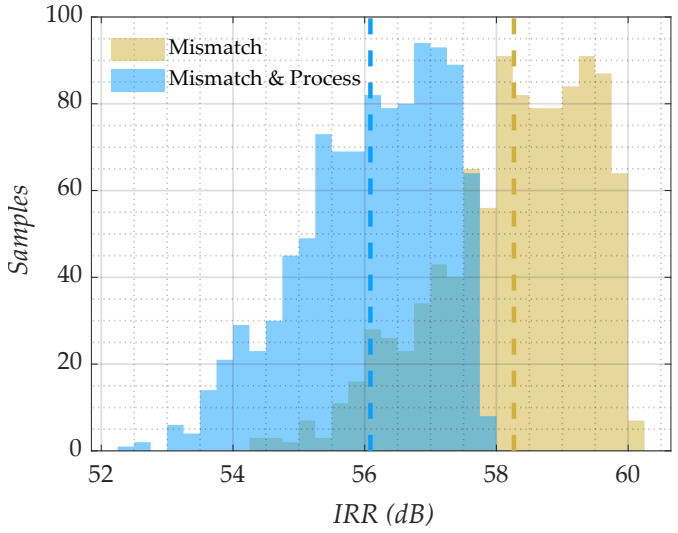

Figure 4.21: *IRR* results of PPF final layout adding mismatch and process variations. Mean values are shown as dashed lines.

The graphic proves the robustness of the system against non-idealities. Even the worst case of extended *BW* (a very pessimistic metric) only means a 4 dB decrease from the mean value.

4.3 Experimental stage

The last step in the PPF design is the experimental measurements. A series of additional elements are required to characterize the filter, with particular attention to keeping its balance. Significant considerations and corrections are mandatory to achieve the

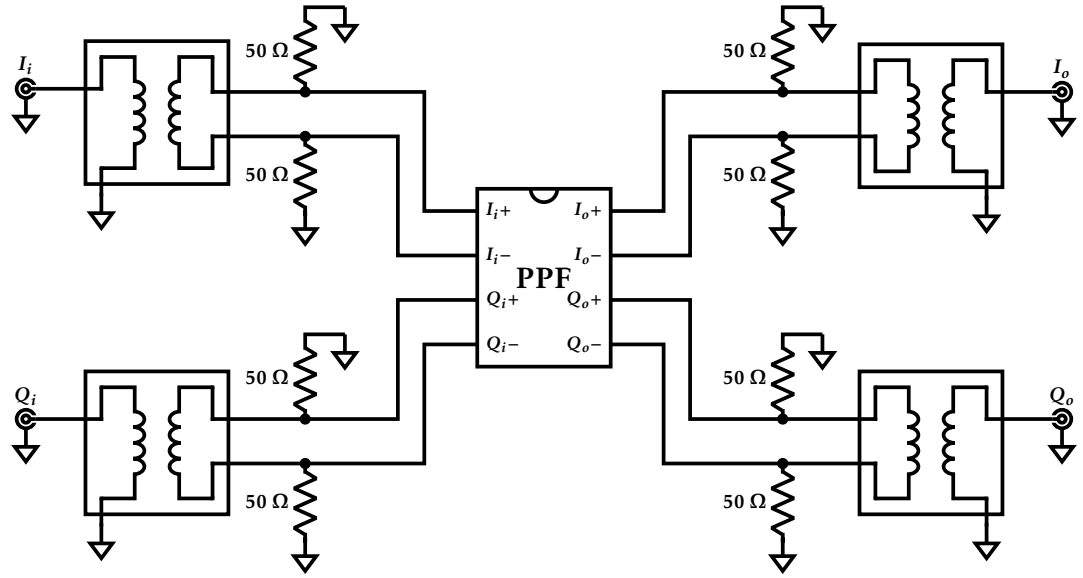

Figure 4.22: Schematics of the PCB for the PPF experimental measurement.

desired accuracy of the results.

4.3.1 Setup

The physical package of the PPF is a QFN64, which includes test cells for other circuits. The bonding directly connects filter terminals and discrete device pins. Thus PPF employs a designed Printed Circuit Board (PCB) for its characterization, following the schematics of Figure 4.22. Analogous to IC layout, the PCB routing prioritizes symmetry as often as possible.

For simplicity, the scheme omits pins from other cells and references. Even though the PPF is passive, the IC requires a supply voltage (V_{DD}) and a ground (GND) as a reference and biasing of substrate and electrical protections. Besides PPF and terminal connectors, the PCB also employs a set of baluns and resistors. Latters must have 50 Ω and low tolerances. Both devices must also be Surface Mount Devices (SMD) to minimize parasitics and perform at the PPF working frequency.

The resistors role is to provide an adequate impedance matching with the instrumentation (and baluns). This factor is negligible inside the chip, where distances are insignificant by comparison with $\lambda/4$ in the 100 MHz band (approximately 75 cm). However, the same cannot be said in the PCB domain, as signal paths from instrumentation to

the device under test (DUT) are comparable in length. Thus, the impedance matching prevents undesirable effects because reflections could disturb IRR measurement.

The disadvantage of the approach is that the signal losses might reach 40 dB due to the two magnitude orders of difference between SMD resistors and PPF impedances. Moreover, PPFs also suffer from insertion losses (approximately 12 dB, although it varies with the configuration [Kau08]), and some additional losses would sum up due to connectors, wires, bonding, paths, etc.

In practice, experimental results reveal signal losses around 60 dB. Nevertheless, the desired signal attenuation is equal to image reduction. Thus, its ratio, i.e., the IRR, is not affected unless signal power is under sensibility, noise floor, or capabilities of the measurement system.

The vector network analyzer (VNA) for the experimental characterization is an R&S ZNA43 [Roh24]. The system can provide a 10-dBm input signal, resulting in an expected −50 dBm signal at the PPF output. The noise level is −150 dBm; hence, the IRR measurement has a 100 dB range. Note also that DUT noise can be canceled by averaging over time. In short, the matching resistors allow an accurate and reliable IRR obtention despite signal losses.

On the other hand, the baluns convert from single-end to balanced signals to connect the eight terminals of the PPF to the four terminals of the VNA. Each differential signal (I and Q from input and output of PPF) is linked to one of the four baluns, while the other side goes to the correspondent VNA port.

Some additional considerations are worth mentioning about this apparently straightforward setup.

Precise quadrature generation is complex, and IRR is an equivalent metric across PPF configurations. Thus, IRR is evaluated as a PPF in D-IQ conversor mode. A Type-I configuration supposes a more convenient setup, although a T connector at inputs can transform the circuit into a Type-II PPF.

Thus, only one input signal is strictly required, and two VNA ports could remain available. Modern VNAs also typically provide an option to generate differential signals

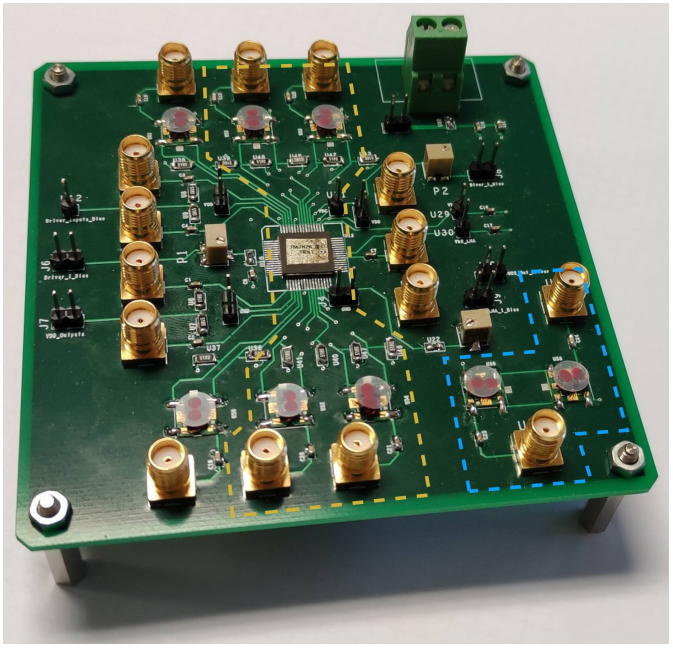

Figure 4.23: Photograph of the PCB implementation. Yellow dashed lines highlights the circuit of Figure 4.22. Some additional devices for calibration are shown within blue dashed lines.

using a pair of ports. Nevertheless, this alternative was discarded as the actual balanced signal is virtual; VNA generates each part sequentially and combines their results, supposing a linear time-invariant (LTI) DUT. While the PPF, by definition, should be LTI, producing balanced signals with baluns was preferred, as it is closer to a real case scenario.

Additionally, the PPF is bidirectional as integrated but has a favoured input and output due to the resistor values and layout placement. Nevertheless, differences between direction and type were not noteworthy.

Figure 4.23 shows a photograph of the PCB implementation. The circuit of the Figure 4.22 is enclosed by the yellow line. Moreover, a set of baluns and connectors (blue line) are included to analyze their impact on the experimental measurements.

4.3.2 Results

The experimental measurements of the two mounted prototypes are shown in Figure 4.24. It includes the signal bandwidth (highlighted in blue) and the 40-dB IRR mark (gray area) as references. The absence of IRR peaks might be the most striking detail at first sight. However, as better shown in Figure 4.25, this flattened occurs because

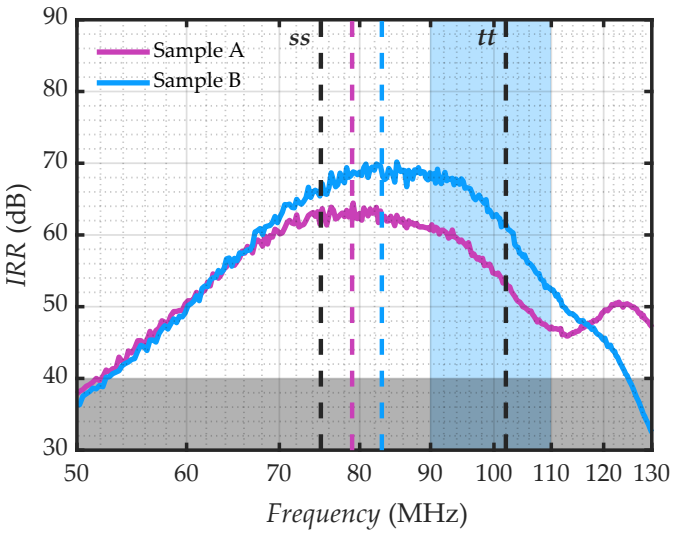

Figure 4.24: Experimental *IRR* results of PPF prototype samples. The blue region marks the signal bandwidth (*BW*), and the dark one marks the 40-dB restriction. Vertical dashed lines indicate the BW_{PPF} center for each prototype, the nominal post-layout PPF, and its ss corner.

of the mismatch limit. The other appreciable effect is the inevitable frequency shifting due to process and process-alike variations. In the case of characterized samples, their response moved to lower frequencies.

The center frequency of each curve has been calculated as the geometric center of frequencies of equal *IRR*. They are shown in Figure 4.24 as vertical dashed lines for a better illustration of displacements. As significant references, the position of the ideal filter (*tt* corner) and *ss* corner are also shown.

Observed shiftings are substantial, although they fall into the expected range. Note that *ss* and *ff* corners only model process variations; they are the most extreme cases but neglect other potential effects that an actual circuit might suffer. Nevertheless, both sample displacements are between *tt* and *ss*, nor is it surprising that both samples have a similar frequency shifting. Although it could be a coincidence, there is a high chance of both being built under similar conditions or coming from the same silicon wafer. Thus, a close correlation between process variations was anticipated.

Despite the *IRR* degradation and frequency shifting, the samples present a minimum *IRR* on the *BW* of 46 and 52 dB. These values mean enough margin from the 40 dB specifications to cope with errors on other blocks, such as the mixer stage or IQ drivers. Section 4.3.3 considerations should be noted.

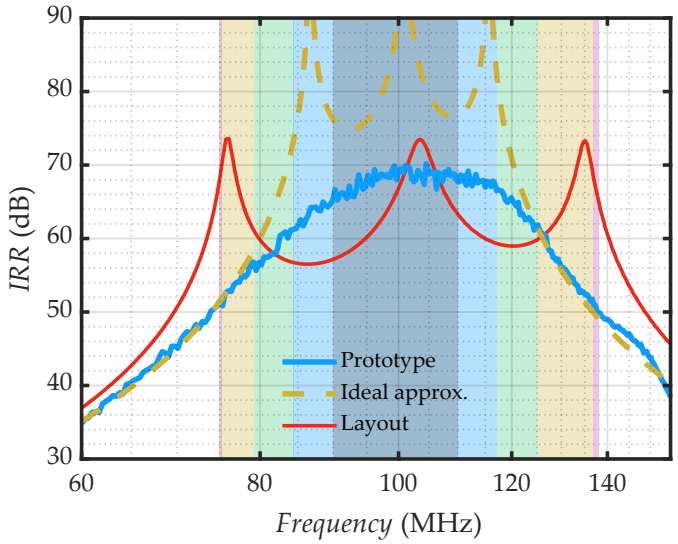

Figure 4.25: Filter response comparison between the experimental measurement, the approximation by ideal stages, and post-layout simulations. Frequency shiftings are canceled for a fair contrast.

Figure 4.25 provides a different insight into experimental results. They are compared (without frequency shifting) against the simulation post-layout and an approximation by ideal stages. The comparison reveals a peculiar detail: the k_2 factor is decreased, *i.e.*, the distance between poles is closer. Without additional experimental data—more accurate device models or more runs—, there is no certain cause.

One possibility places the suspicion on non-idealities from measurement elements, bonding parasitics, or protection devices of PADs (foundries only provide vague information about them). They could add zero-pole pairs that can shift the upper flank of the filter. Another possibility is that contraction is simply due to an inconvenient mismatch combination between the first and last stage elements.

Nevertheless, this unexpected effect is not critical because of two motives. Firstly, it implies little impact on the IRR for most of the cases. As poles are closer, they made a larger IRR on the central area, which is the most probable to lay on BW, at the expense of having lower IRR on the cases with less likely process variations. In other words, BW_{PPF} is narrowed, and the system follows the tradeoff illustrated in Figure 4.3. Secondly, the phenomenon is canceled by widening the BW_{PPF}. Thus, solutions to abate process variation impact can solve this issue.

More profoundly, there are three scenarios from a PPF design perspective. On the one

hand, the mentioned suspects could add poles and zeros. Thus, PPF performance inside a monolithic design would be unaffected. The effect would be a consequence of the measurement system. Otherwise, it is something intrinsic to the PPF, and two alternatives appear, on the other hand: a systematic error or a random error. A systematic error that compresses k_2 is equivalent to a broader BW requirement in the same proportion. A random variation of k_2 could be included in the process variation. Both possibilities arrive at the same conclusion of enlarging BW_{PPF}. However, if some tunning aims for a more ambitious IRR by sacrificing the worst cases, the distinction might matter.

Indirectly, the k_2 highlights the strong impact of the mismatch. Given the proximity of the three poles, the IRR tends to such high values that they hit the mismatch ceiling. The comparison with the ideal curve is apparent in this respect. While IRR is limited by—optimized—mismatch, the central zone is unlikely to drop so much as to be an issue. On the other side, the flanks of BW_{PPF} are affected in a lesser proportion by mismatch flattened, as seen in some graphs (*e.g.* Figure 4.8).

Moreover, such high pole density slightly pushes the mismatch ceiling. Compared to the statistical results of simulations of the ideal approximation, experimental curves remain a little below them due to additional factors that cannot be mitigated or deembedded with sufficient precision. Nevertheless, most of the samples of this design are expected to have an IRR above 50 dB, although some cases with significant process and mismatch deviations slightly lower this figure.

In essence, BW_{PPF} compression and process variations jeopardize the IRR in the samples; however, the careful design remains robust enough to achieve the desired performance.

4.3.3 Discussion

Experimental results prove that a PPF can fulfill the desired specifications of the proposed technology. Also, the filter response heavily depends on the random factors specific to each sample. Consequently, the IRR curve of each sample is unique. Thus, a complete experimental verification of each potential case is not possible by a strict application of scientific method [Cha84]. Nevertheless, according to the analysis and

simulation models, the phenomena observed on the experimental data are within the expected results. Thus, there is reasonable confidence in the capabilities of the design, the guidelines provided, and the optimization made. Moreover, additional considerations are needed for a fair evaluation of the experimental results and the expectations of the PPF performance in a system.

A significant number of devices were included to enable the measurements. They were especially problematic for the IQ signal management to minimize errors or allow for consequent de-embedding. In an element as accurate as a PPF, a minimal error can alter the system and darken the results. Mismatch and parasitics phenomena due to bonding, PCB, and connectors imply a long list of potential undesirable effects. Moreover, their de-embedding requires significant effort and dedication. In many cases, non-idealities are not linear, and they have direct contributions but also additional factors depending on complex combinations with other phenomena. In short, there are notable drawbacks and uncertainty due to the measurement; hence, the PPF performance inside a transceiver or receiver is better than the characterization.

Another critical detail is the number of stages. The designed filter uses only three. However, an additional pole could improve feasibility without a significant cost. A fourth pole could force a mismatch ceiling in a large BW_{PPF} or counter k_2 shrinkage. The proposed k_2 selection method is especially relevant to this scenario. Unlike traditional approximation, the suggested methodology can work with more than three stages.

PPF results should also be considered in the context of transmitter and receiver architectures. Only blocks that work with IQ signals have a noticeable impact on IRR; out of them, the effect is negligible. Take the example of the LNA. From that block perspective, the distinction between the desired signal and its image is the same as between a signal at 5.1 GHz and another at 4.9 GHz. This difference is notably lower than the potential variation on the cutoff frequency in an inductorless LNA and too demanding in selectivity for a topology with integrated inductors. Indeed, this is what makes the PPF especially useful in IC communication architectures.

Conversely, the effect of PPF on the received signal is minimal since the passband of a PPF for the desired signal is practically flat (lower than 1 dB in experimental measurement); the abrupt shapes so characteristic come from image rejection, *i.e.*, from

the rejected band. In addition, using only passive elements guarantees a very high linearity—there is no distortion. Therefore, the PPF is transparent to other blocks beyond its insertion loss.

The frequency conversion block defines *IRR*, *i.e.*, the PPF, the mixer stage, and IQ drivers. The IQ quality from the local oscillator also contributes, although it is usually easier to compensate for with an adequate mixer stage structure (*e.g.*, a double quadrature scheme). According to the study of mixer stages in the same technology [Mar21], the PPF experimental results show better performance than expected on the other block. Thus, after the optimization processes in this thesis, the filter would not be as limiting as mixer stage impedance unbalance or IQ mismatch on drivers.

References

[All12] P. E. Allen and D. R. Holberg. *CMOS analog circuit design, 3rd edition*. Oxford University Press, 2012. ISBN: 9780199765072.

[Bak19] R. J. Baker. *CMOS circuit design layout and simulation, 4th edition*. IEEE Press–Wiley, 2019. ISBN: 9781119481515.

[Beh01] F. Behbahani, Y. Kishigami, J. Leete, and A. Abidi. "CMOS mixers and polyphase filters for large image rejection". *IEEE Journal of Solid-State Circuits* 36.6 (June 2001), pp. 873–887. DOI: 10.1109/4.924850.

[Cha84] A. F. Chalmers. *¿Qué es esa cosa llamada Ciencia? Una valoración de la naturaleza y el estatuto de la ciencia y sus métodos, 2nd edition*. Siglo XXI editores, 1984.

[Cro95] J. Crols and M. S. J. Steyaert. "A single-chip 900 MHz CMOS receiver front-end with a high performance low-IF topology". Vol. 30. 12. IEEE, Dec. 1995, pp. 1483–1492. DOI: 10.1109/4.482196.

[Gin75] M. J. Gingell. "The synthesis and application of polyphase filters with sequence asymmetric properties". PhD thesis. 1975.

[IEE97] IEEE. *IEEE Standard for wireless LAN medium access control (MAC) and physical layer (PHY) specifications*. 1997. DOI: 10.1109/ieeestd.1997.85951.

[Kau08] J. Kaukovuori, K. Stadius, J. Ryynanen, and K. Halonen. "Analysis and design of passive polyphase filters". *IEEE Transactions on Circuits and Systems I: Regular Papers* 55.10 (Nov. 2008), pp. 3023–3037. DOI: 10.1109/tcsi.2008.917990.

[Mar21] A. D. Martinez-Perez, F. Aznar, G. Royo, and S. Celma. "Analysis of non-idealities on CMOS passive mixers". *Electronics* 10.9 (2021). ISSN: 2079-9292. DOI: 10.3390/electronics10091105.

[McG87] W. F. McGee. "Cascade synthesis of RC polyphase networks". *Proc. 1987 IEEE International Symposium on Circuits and Systems, Philadelphia, PA, USA*. 1987, pp. 173–176.

[Mil16] L. E. Milner, J. T. Harvey, L. T. Hall, and M. E. Parker. "A polyphase RC filter implemented in ring configuration for a SiGe millimetre-wave receiver". *2016 IEEE 2nd Australian Microwave Symposium (AMS)*. IEEE, Feb. 2016. DOI: 10.1109/ausms.2016.7593471.

[Nik15] Y. Niki, S. Sasaki, N. Yamaguchi, J. Kang, T. Kitahara, and H. Kobayashi. "Flat passband gain design algorithm for 2nd-order RC polyphase filter". *2015 IEEE 11th International Conference on ASIC (ASICON)*. IEEE, Nov. 2015. DOI: 10.1109/asicon.2015.7516933.

[Nis11] T. Nishi, H. Tanimoto, and S. Oishi. "Cascade synthesis of RC polyphase one-ports". *2011 20th European Conference on Circuit Theory and Design (ECCTD)*. IEEE, Aug. 2011. DOI: 10.1109/ecctd.2011.6043287.

[Raz11] B. Razavi. *RF microelectronics, 2nd edition*. Prentice Hall, 2011. ISBN: 9780137134731.

[Roh24] Rohde and Schwarz. *R & S ZNA Vector Network Analyzer specifications*. 2024.

[Tan06] H. Tanabe and H. Tanimoto. "Design considerations for RC polyphase filters with simultaneously equal ripple both in stopband and passband". *IEICE Transactions on Fundamental of Electronics, Communications and Computer Sciences* E89A.2 (Feb. 2006), pp. 461–464. DOI: 10.1093/ietfec/e89-a.2.461.

[Tan13] H. Tanimoto. "Exact design of RC polyphase filters and related issues". *IEICE Transactions on Fundamentals of Electronics, Communications and Computer Sciences* E96.A.2 (2013), pp. 402–414. DOI: 10.1587/transfun.e96.a.402.

[TSM13] TSMC. *Taiwan Semiconductor Manufacturing Co: Document T-N65-CL-DR-001*. 2013.

[Wad03] K. Wada and Y. Tadokoro. "RC polyphase filter with flat gain characteristic". *2003 IEEE International Symposium on Circuits and Systems (ISCAS '03)*. IEEE, 2003. DOI: 10.1109/iscas.2003.1205619.

Chapter 5

Conclusions

The history of wireless and electronics provides a fascinating insight into how the capabilities of devices constrain system performance. In modern times, circuits have become more complex and are built with more hierarchical levels; however, the principles continue to apply now, if not more critically than ever, despite existing more means and powerful tools for design and fabrication than in previous times. The computational resources allow circuit characterization under any hypothetical scenario. However, it is constrained to the reliability and accuracy of simulation models. Fortunately, we benefit from those tools; otherwise, microelectronic design would be much more complex, and the optimization process would become almost impossible. Moreover, An ASIC does not permit any modification after fabrication.

Within this context, experimental results confirm that a PPF in the proposed technology can achieve enough IRR for the application. Moreover, most samples will expect a significantly high performance (50–60 dB). Those values are notably higher than the ones from mixer stages [Mar21] and impose a careful design of potential IQ drivers to keep pace. In other words, a PPF that achieves that range of IRR would not be the limiting factor to reach the 40 dB imposed by the reference norm (IEEE 802.11), provided that the design follows indicated guidelines.

Note that a complete verification of the design is impossible. The PPF is affected by major random variations that shape the filter response; hence, each case is distinct. Besides, there are economic and time constraints to produce a significant number of

samples to obtain statistically significant data. Thus, there is a dependence on the simulation models, and analytical studies are relevant to estimating the feasibility and reliability of PPFs. For this reason, the detailed developments are included in Appendixes. Moreover, the presence of the deduced effect on the samples proves the importance of the analyses.

Section 5.1 deeps on the particular conclusions from the analytical study hereafter. Then, Section 5.2 does the same with the design and optimization methodology and experimental results. Finally, Section 5.3 proposes future lines of continuation.

5.1 Analytical study

Traditionally, the design of a PPF implies setting the number and location of filter poles according to desired IRR, signal BW, and potential frequency shifting due to temperature and process effects. However, other factors may affect the PPF performance. Phenomena that alter the balance between I and Q branches can have a massive impact. However, it is usually omitted [Kau08; Wad03; Tan13], detached from the causes [Asa19; Nik03] or only described qualitatively [Gal00; Beh01]. In other words, guaranteeing IRR from a PPF might require evaluating other factors that alter that balance, such as mismatch and parasitics, but their estimation is typically made by simulations—trial and error—instead of using any approximate expression. Furthermore, studies [Had10; Nik15] typically do not either cover all possible PPF configurations, which change how component mismatches alter performance (affecting phase or amplitude balance) and the form of the desired signal and its image. Thus, the IRR definition is also distinct for each PPF application.

Those non-idealities are challenging to analyze: 1) there are innumerable possible cases, 2) general expressions have too many variables to describe particular cases, and 3) ideal-case simplifications due to the particular symmetry of the filter are not valid under a mismatch scenario. Nevertheless, Chapter 3 presents a method to solve all these issues and obtain a simple and advantageous expression relating the IRR and mismatch tolerance (x).

Firstly, the method searches for the worst possible mismatch combination for a one-stage PPF. The process narrows down the space until it reaches a case that must be the

worst or, at least, very close to it. This case serves as a pessimistic limit: any other combinations will perform better.

Once the worst case is defined, one-stage PPF expressions can be developed as a function of the mismatch between its components. The study covers all five different PPF configurations. The IRR limit is $4/x^2$ for all of them. Fortunately, the influence of the mismatch on the IRR depends almost exclusively on the last stage; thus, results from one-stage PPF are quickly and accurately extrapolated to a multi-stage system. A worst-case search for a three-stage PPF corroborates the hypothesis.

The quantitative results enable the maximum achievable IRR estimation for given component tolerances and vice versa: they remark the maximum device tolerance to avoid the mismatch as the primary IRR constraint.

Moreover, this information is known *a priori*; thus, it might avoid unpleasant surprises after investing arduous effort, long hours, and perhaps considerable economic costs in that particular PPF design. Consequently, the study result provides reliability to designing PPFs using known information and at a negligible cost: $IRR_{max} = 4/x^2$.

Preliminary results of the study have been published: first with communications in international congresses of the study by simulating the effect of non-idealities [Mar17a] and the impact of mismatch [Mar18a]; and later with a journal publication [Mar18b] going deeper and presenting in much greater detail the influence of mismatch on the IRR. In addition, the study has been the subject of national forum presentations [Mar17b; Mar18c].

Nevertheless, Chapter 3 presents numerous significant novelties regarding the publications. Section 3.2 significantly improves on what was presented in [Mar18b], analyzing the impact on all the other four of the configurations ([Mar18b] only covers the Type-I D-IQ converter PPF configuration) to demonstrate that $4/x^2$ is common to all of them. Also, some aspects of the study have been solved as the proposed mismatch decomposition enables a distinction between the frequency-shift and peak-reduction effects and clarifies some details of the worst-case selection. Moreover, the novelty proves the IRR is a comparable metric for any PPF, although the strict functional meaning varies between applications.

Additionally, Section 3.3 innovates in the study and completes the analysis by describing the effect of mismatch on loads. Like component variations, their impact is widely known in a balanced scenario. However, no quantitative analysis was found in the literature concerning load mismatch and how much it degrades IRR. Also, it has been shown that studying this mismatch is equivalent to evaluating parasitics mismatch, which may severely impact the IRR [Had10] (see Figure 3.15). Finally, a generalization has been made, including capacitors as possible sources of mismatch and the effect of load mismatch.

As enumerated in Section 1.3, the analytic study was proposed with four intents in mind:

- **Describing the effects of the various non-idealities.** According to the type of impact on IRR, non-idealities can be broadly classified into two groups. Some cause a frequency shift of the filter response, while others produce a flattening of the peaks, imposing a maximum limit. A decomposition based on these terms is explained in Appendix E—deduced in Section 3.2.2.6—and illustrates the difference between the two groups. Besides, descriptions from Section 3.1.4 show which group each non-ideality belongs.

- **Analyzing non-idealities that alter filter balance.** The effect of the other non-idealities is significant but easier to mitigate by widening BW_{PPF}. There is no drawback but the opportunity cost in the k_2 choice or a little increment in insertion losses. However, mismatch and similar phenomena are problematic and more difficult to cope. For this reason, Chapter 3 covers its study, especially in Section 3.2.

- **Being transparent to the employed technology.** The mismatch analysis is carried out in the function of a tolerance parameter, without particularizing for any technology. The assumption of the resistor mismatch being significantly larger than the capacitor mismatch might depend on the technology. However, Section 3.3.1 dispels any doubt in this respect, including variations of the capacitors in the analysis results.

- **Covering the possible uses and configurations.** Contrary to our preliminary results, the analysis in the thesis covers all five PPF configurations. Note that

expressions and development for each case are different. However, all results tend to the limit from equation (3.72). This is an exciting conclusion, as IRR has different meanings for some configurations. Table 3.1 and Section 3.2.2.6 compare similarities and differences between the five PPF uses.

In short, the study presented in this thesis is a helpful tool for designing PPF, especially in ASICs. The results enable an estimation of achievable specifications for the filter. Thus, deductions from the analysis can save substantial time and effort for PPF designers. Also, the study can help to understand the limitations of an implemented PPF and identify the main obstacles to improving performance.

5.2 Design and optimization methodology

The golden rule for designing a PPF is to take into account that the non-idealities of employed devices heavily influence the development (and final filter response). Process variations determine k_2, defining potential IRR indirectly. Similarly, mismatch errors imply an IRR upper limit. It is not intuitively, but that constraint changes for each sample—it depends on which particular devices are different and how much. Moreover, parasitics might aggravate both issues (degrading IRR even more) and reduce output signal power.

In a first-order approach, the PPF design relies on two design variables, R and C, which are mutually determined for fixed poles. The freedom degree is usually inverted on matching input and output impedances [Kau08]; however, the proposed design uses it to optimize the performance against process and mismatch variations, benefiting from the robustness of the technology MIM capacitors.

This strategy improves IRR by reducing non-idealities that would be difficult to attenuate otherwise. On the other hand, the input and output impedance matching can be obtained with drivers integrated with the PPF. Thus, the circuit could work with voltage signals instead of power ones, reducing signal losses. Note that mitigated non-ideality—mismatch—has such an impact that not even adding new stages could improve the limit that it sets, *i.e.*, equation (3.72).

Attaining the desired IRR and the number of poles required is inextricably linked to the k_2 factor, and this variable has a massive impact on performance. Its value defines the trade-off between better IRR and wider BW_{PPF}. On the one hand, values that are too small make the system excessively sensitive to process variations. On the other hand, values larger than needed imply a significant reduction in IRR within BW.

Nevertheless, analytically finding the optimal value of k_2 is a highly complex calculus [Nik03; Nik15; Tan13; Hir20], especially as the stage number increases [Kau08]. The classical method for a three-stage PPF approximates the solution to an order-two equation. However, this approach is only valid for this number of stages, and k_2 is a highly susceptible value. Differences of tenths of k_2 translate into units or even tens of dB in IRR (see curves of Figure 4.3). Paradoxically, despite its simplicity, the proposed method achieves a much more accurate selection of k_2. The technique uses a double approach, one optimistic and one pessimistic. Thus, both errors oppose each other under usual PPF circumstances. The evaluation of this k_2-selection strategy accuracy with larger numbers of stages remains as a promising future line, something that is not even achievable with the classical approximation.

Another relevant contribution is the "divide and conquer" strategy to reduce the computational cost of statistical simulations. Simulation supposes mismatch and process random and independent phenomena, although their effects on the results can be combined. Therefore, their combined simulation would require a number of samples equal to the product of those needed to characterize each of the effects. As a consequence, it would imply a vast number of simulations.

However, the impact of process variations is analogous to an extension of the required BW. Thus, by evaluating the IRR of the PPF under mismatch effects within the extended BW range, the impact of both non-idealities on the PPF is characterized. This procedure reduces the number of Monte Carlo analysis samples by orders of magnitude—numbers of samples are summed instead of multiplied—at the negligible cost of a slight pessimistic bias as mismatch is compared against the worst process variations if it is evaluated in BW_{PPF}. Also, in its fastest version, BW expansion is calculated from the frequency shifts at the *ss* and *ff* corners (two simulations replace an extensive Monte Carlo analysis). Still, more detailed characterizations might provide statistical data to set IRR expectations as a function of percentiles or probabilities.

Following the design process, the layout design reveals the significance of another non-ideality: the parasitics. More precisely, they strongly influence the I-Q balance and force a symmetric circuit design. This emphasis is more noticeable after optimizing component mismatch; the reduction of mismatch impact and the circuit capacitors make parasitic capacitances a limiting factor for IRR.

Thus, symmetrical connections are critical for a good performance. In doing so, the circular layout placement, with concentric PPF stages, achieves excellent results; however, no similar idea has been found in the consulted references. A circular approach instead of a linear one improves connection and device symmetry while being a scalable design. The asymmetry issues shift from the stages to the input and output routing, although two mitigating factors should be taken into account: 1) the distance between output nodes is shorter, as the design is more compact, and 2) input and output wiring can be implemented in layers distant from devices. Moreover, the same set of vias that connect resistors and capacitors can provide a node output and input nodes.

The strong influence of random variables on the response of an implemented device makes verification difficult because curves can dramatically vary from sample to sample. An electronic circuit is typically validated if the experimental curves are very similar to simulations. However, this is not possible in a PPF. Even in the best scenario, each sample will have a frequency shift and—if IRR is ambitious—a flattening of the peaks due to worst-case mismatch projection. Other non-idealities and mismatch components also alter the IRR curve in different ways. However, the experimental measurements agree with expectations: they undergo a significant shift, but within the marked ranges, and show a flattening due to the mismatch, perhaps slightly more pronounced due to the compression of k_2, but also within the expected range.

The k_2 alteration is the most intriguing detail of the measured data, although, with the limited information, it is difficult to determine its cause. The main suspects are inter-stage mismatch phenomena (with the first and last stages undergoing opposite variations) or parasitic elements of the measurement setup introducing pairs of zeros and poles at relatively close frequencies, shifting the upper-frequency slope to the left. Significantly, the latter case would also imply that the frequency shift is shorter than estimated. In any case, if the change in k_2 is specific to the PPF and not to the measurements, it would not be difficult to compensate for it using the same methods as for the

process variations (see Section 4.3.3 for more details).

However, thanks to careful optimization, the prototype achieves target IRR in the BW despite BW_{PPF} narrowing and significant process variation. Moreover, samples with lesser process variation could achieve even better performance as k_2 reduction improves IRR in the center of the filter response at the expense of the sides. Based on modeled process variations and the experimental curves, an IRR median above 50 dB can be expected for the design. In addition, including an additional pole would ensure the IRR becomes the mismatch ceiling for the full range of potential process variations.

Design methodology aimed to fulfill four objectives:

- **Fulfilling RAU specifications.** PPF prototypes achieve an IRR margin above the 40-dB mark in the frequency range of interest (90–110 MHz). This result is obtained even with the unexpected k_2 compression (with consequent reduction of BW_{PPF}). As there is a significant process variation in the experimental measurements, better IRR is expected for most future samples.

- **Providing a systematic and comprehensive optimization methodology.** This thesis provides different tools and methodologies for each step in the design process. The same tests and simulations made using the employed technology can be directly applied to any other technology to obtain the relevant information for the scenario. Similarly, other applications would only change the target constraints. Thus, the process is easily replicable in any scenario.

- **Evaluating the effect of non-idealities.** Doubtless, those factors are the key to PPF design and optimization. Process variations determine the frequency range the filter must cover, while the mismatch sets a particular IRR ceiling for each sample. Parasitics critically condition PPF physical design to maintain symmetry. Most of the other phenomena can be englobed as a contribution to any of them (*e.g.* variations due to temperature behaving like process variations).

- **Covering the complete design process.** Design methodology starts with the circuit analysis and follows the design process until the experimental measurements. The importance of covering the entire process becomes clear, as each step imposes distinct constraints on solving the particular issues. The final PPF must

meet all of them. Skipping design stages would lead to neglecting essential factors that would be missed in the methodology otherwise.

In short, the thesis proposes a PPF design methodology focused on the critical non-idealities for each design step. The method relies on the presented analysis and the information from simulations with models of the desired technology. During the process, there are two critical improvements: 1) the k_2 selection method and 2) the circular layout design to improve symmetry. The description of the followed process provides a series of guidelines and methods to optimize a PPF regardless of technology or application.

5.3 Future research directions

The research process has raised some additional inquiries that might be interesting for new projects and continuations of the thesis. The most straightforward follow-up to the presented analysis is **an extension to cover the entire frequency converter block**. However, this task has to overcome a key obstacle: producing output signals at a different frequency than excitation clearly indicates a non-linear system. Note that linearity is required for properties that are as essential as combining transfer functions.

Nevertheless, a mixer is a very particular kind of system called bilinear. Besides, the system becomes time-periodic if the local oscillator (LO) produces a single tone. In other words, it is not a lineal time-invariant (LTI), but they are close enough to find some ways around the issue. Under the cited scenario, a complex linear application [Dun68] can be defined between the amplitude of the input signal and output-signal amplitudes at specific frequencies of interest. Note that the mixer stage operation requires complex numbers as phase is crucial. Moreover, suppose the mixer—hence, the mixer stage, too—is described as a linear application. In that case, its transfer function can be linked to PPF operation in a similar way to the method in Appendix G. Other related blocks, such as IQ drivers, are trivial to add.

Note that a linear application can be defined by the relationships between the basis of its domain and codomain. In other words, linearity implies that the system characterization can be achieved by analyzing the response to domain basis vectors; for an IQ

signal, it can be the four symmetrical sequence components. This approach is similar to analyzing by the superposition principle.

Once the model is obtained, it enables any study of separate or joined blocks against mismatch or other non-ideality. Searching for the worst cases or mandatory device constraints to reach a certain global IRR would become possible. Additionally, the method serves for schemes as simple or complex as desired; it works well with top-down strategies.

In essence, this approach would extend the study to the whole frequency converter, enabling an analysis like the one made for PPF in this thesis. Consequently, the specification for the distinct block could be set more accurately for an optimized performance of the system.

The obtained mismatch limit is a fast, simple, and efficient approximation of a potential IRR ceiling for PPF. However, it could be interesting to **evaluate the precision of the limit** for the different PPF configurations, stage numbers, and influencing non-idealities. Also, it has been observed that a high density of poles (low k_2 factor) may favor a slight improvement of IRR over the estimation. Thus, exploring the exact limitations of the approach can result in more reliable designs. In the same vein, delving into an alternative representation of PPF IRR to show the mismatch effect and its combination with other non-idealities could greatly benefit this research line.

The proposed **k_2-selection methodology** has great potential in its application to several-stage PPF, as the traditional approaches are restricted to three poles. This study would focus on how confident the assumptions the method relies on are: the BW is relatively narrow, and the sideway is not too relevant. Both parameters heavily depend on the required BW_{PPF}, target IRR, and pole splitting (k_2)—close poles influence flanks. Those relationships are complex, and predicting their precise impact on each supposition is difficult.

PPFs with more than three stages are common. Besides, a high density of poles can force IRR to be close to the mismatch ceiling in the region, and that means using several stages to cover enough frequency range to cope with process variations. Thus, developing the method in greater detail can notably improve PPF for high IRR applications.

In this regard, the literature assumes that the optimal **pole distribution** for any PPF is an equal geometric splitting. This way, all valleys fall to the same IRR level. However, simulations show that not all frequency ranges of BW_{PPF} have the same chances of covering BW after the effect of process variations. In other words, out of a strategy focused on the worst case, there are regions more critical than others. In this scenario, a PPF with several poles might benefit from another pole distribution, having a higher density in the BW_{PPF} central area and lower in the outer borders.

Moreover, mismatch—typically neglected—should be considered in this aspect. The non-ideality can move poles from their relative position to others, altering valleys and flanks unless the mismatch IRR limit has been reached. A review of pole splitting in PPF with numerous stages may enhance the final performance and reveal details that are not relevant with a lower number of stages.

Among the additional stages, those structures can take advantage of including amplifiers to offset signal losses. Nevertheless, they pose the challenge of designing to minimize their impact on IRR. At the same time, new questions and opportunities arise. For example, in the case of a 6-stage PPF divided into two groups of three by IQ drivers, should the poles follow a descending order (123–456) or intertwine both groups (135–246)?

In addition, evaluating the methods in **other technologies** has its interest. During this study, an SOI technology of similar dimensions was considered for the PPF design. Surprisingly, preliminary results were not promising due to a worse repeatability of the capacitors of that technology. Thus, the idea was discarded. Nevertheless, low parasitics intrinsic to that kind of technology might pay their way, enabling mismatch reduction techniques or achieving higher working frequencies. Again, an exciting comparison requires many experimental samples, ideally independent. Otherwise, there would be no other option but trust in the simulation models and layout extracted parasitics. PPF blocks are rarely the reason to use this kind of technology, as other blocks in the communication chain benefit more from them. Nevertheless, studies on non-standard technologies could deduce exciting information in the trade-off between non-idealities.

Moreover, **employing MOS transistors** could provide different trade-offs. This thesis focuses on passive devices as they perform better for the desired application. There were some attempts to design PPF that used MOS in triode to implement resistors.

They would have a clear advantage: control over its value. However, preliminary tests revealed a much more restrictive mismatch than resistor devices. A detailed control could, in theory, mitigate the mismatch, but some issues arise in the practice. First, if each device must be controlled, there would be too many control signals—a 3-stage PPF uses twelve resistors. Second, identifying mismatch combation to cancel the non-ideality is difficult. The IRR response is not easily interpretable, and implementing a control loop seems even more complex. However, this kind of PPF could provide more attractive trade-offs as technology advances.

Similar approaches to our PPF design methods could be applied to active polyphase filters. Those circuits are out of the scope of our study. However, many of the principles and ideas behind the proposed methodologies can be extrapolated to the rest of the polyphase filters.

Future iterations can benefit from including PPF drivers within the **PPF layout** structure to attain high IRR and isolate performance from load effects. They should probably be complemented with dummy cells [All12] to maintain symmetry. Moreover, each resistor should be divided into two segments to improve symmetry. They can be placed in an orthogonal arrangement and ensure symmetry with respect to both axes between the resistor pairs. Horizontal and vertical segments of R_1-R_3 and R_2-R_4 would share equal centers. The employed technology did not emphasize this design recommendation, although it is often recommended.

Undoubtedly, additional prototypes would be of special interest in complementing the study. However, depending on whether they focus on PPF study or implementation, they should have a different approach. A PPF should have at most one or two stages to better evaluate the analytical side. A straightforward design allows for a better and more reliable identification of the effects and phenomena. Contrarily, an improved PPF with functional intent can benefit from an additional pole, as the assurance of results against unpredicted effects offsets the 3-dB insertion losses. Observing changes in k_2 or pole positions would be of interest either way.

Future designs may also benefit from **an implementation that simplifies the measurement** process. Avoiding complex elements such as baluns would make the circuit more suitable for characterizing more samples. Also, an IC ready for measurement by picoprobes might significantly increase the number of PPFs available per run. At the

same time, measurement without requiring a PCB cancels notable *IRR* degradations that come from outer devices.

Moreover, including an inverse multiplexing system can multiply the number of filters per sample and provide a better insight into the sample conditions if additional test circuits are included. This strategy benefits simpler and more complex designs, although the impact of added devices on *IRR* response should be evaluated. Still, a statistical study would face other challenges, *e.g.*, some correlation between samples from the same run is to be expected.

References

[All12] P. E. Allen and D. R. Holberg. *CMOS analog circuit design, 3rd edition*. Oxford University Press, 2012. ISBN: 9780199765072.

[Asa19] K. Asami, N. Kushita, A. Hatta, M. T. Tran, Y. Tamura, A. Kuwana, and H. Kobayashi. "Analysis and evaluation method of RC polyphase filter". *2019 IEEE 13th International Conference on ASIC (ASICON)*. IEEE, Oct. 2019. DOI: 10.1109/asicon47005.2019.8983545.

[Beh01] F. Behbahani, Y. Kishigami, J. Leete, and A. Abidi. "CMOS mixers and polyphase filters for large image rejection". *IEEE Journal of Solid-State Circuits* 36.6 (June 2001), pp. 873–887. DOI: 10.1109/4.924850.

[Dun68] J. Duncan. *The elements of complex analysis*. John Wiley and sons, 1968.

[Gal00] S. H. Galal, H. F. Ragaie, and M. S. Tawfik. "RC sequence asymmetric polyphase networks for RF integrated transceivers". *IEEE Transactions on Circuits and Systems II: Analog and Digital Signal Processing* 47.1 (2000), pp. 18–27. DOI: 10.1109/82.818891.

[Had10] F. Haddad, L. ZaIumld, W. Rahajandraibe, and O. Frioui. "Polyphase filter design methodology for wireless communication applications". *Mobile and Wireless Communications Network Layer and Circuit Level Design*. InTech, Jan. 2010. DOI: 10.5772/7707.

[Hir20] A. Hirai, T. Fujiwara, M. Tsuru, K. Mori, and M. Shimozawa. "Vector-sum phase shifter using a tunable active g_m polyphase filter". *IEEE Transactions on Microwave Theory and Techniques* 68.10 (Oct. 2020), pp. 4091–4102. DOI: 10.1109/tmtt.2020.2991738.

[Kau08] J. Kaukovuori, K. Stadius, J. Ryynanen, and K. Halonen. "Analysis and design of passive polyphase filters". *IEEE Transactions on Circuits and Systems I: Regular Papers* 55.10 (Nov. 2008), pp. 3023–3037. DOI: 10.1109/tcsi.2008.917990.

[Mar17a] A. D. Martinez-Perez, J. Morte, F. Aznar, C. Sanchez-Azqueta, and S. Celma. "Impact of non-idealities on passive polyphase filter performance". *2017 European Conference on Circuit Theory and Design (ECCTD)*. Catania, Italy: IEEE, Sept. 2017. DOI: 10.1109/ecctd.2017.8093256.

[Mar17b] A. D. Martínez-Pérez, J. Morte, F. Aznar, C. Sánchez-Azqueta, and S. Celma. "Approaching ideal polyphase filter response in 65-nm CMOS". *VI Jornada de Jóvenes Investigadores del I3A*. Vol. 5. Zaragoza, Spain: Universidad de Zaragoza, June 2017. DOI: 10.26754/jji-i3a.201711990.

[Mar18a] A. D. Martinez-Perez, F. Aznar, G. Royo, C. Sanchez-Azqueta, and S. Celma. "Analysis of the influence of component mismatch on integrated passive polyphase filters". *2018 IEEE International Symposium on Circuits and Systems (ISCAS)*. Fireze, Italy: IEEE, May 2018. DOI: 10.1109/iscas.2018.8351661.

[Mar18b] A. D. Martínez-Pérez, F. Aznar, G. Royo, C. Sánchez-Azqueta, and S. Celma. "Analysis of mismatch impact on image rejection ratio for passive polyphase filters". *International Journal of Circuit Theory and Applications* 46.10 (June 2018), pp. 1838–1847. DOI: 10.1002/cta.2505.

[Mar18c] A. D. Martínez-Pérez, F. Aznar, G. Royo, C. Sánchez-Azqueta, and S. Celma. "Estimación de la degradación por mismatch del rechazo de imagen en filtros polifásicos pasivos". *VII Jornada de Jóvenes Investigadores del I3A*. Vol. 6. Zaragoza, Spain: Universidad de Zaragoza, May 2018. DOI: 10.26754/jji-i3a.201802847.

[Mar21] A. D. Martinez-Perez, F. Aznar, G. Royo, and S. Celma. "Analysis of non-idealities on CMOS passive mixers". *Electronics* 10.9 (2021). ISSN: 2079-9292. DOI: 10.3390/electronics10091105.

[Nik03] Y. Niki, J. Kangand, H. Kobayashi, N. Yamaguchi, and T. Kitahara. "Analysis of RC polyphase filters: Input impedance, output termination, component mismatch effects, flat-passband filter design". *Proc. IEICE Tech. Meet. Circuits Syst.* Jan. 2003.

[Nik15] Y. Niki, S. Sasaki, N. Yamaguchi, J. Kang, T. Kitahara, and H. Kobayashi. "Flat passband gain design algorithm for 2nd-order RC polyphase filter". *2015 IEEE 11th International Conference on ASIC (ASICON)*. IEEE, Nov. 2015. DOI: 10.1109/asicon.2015.7516933.

[Tan13] H. Tanimoto. "Exact design of RC polyphase filters and related issues". *IEICE Transactions on Fundamentals of Electronics, Communications and Computer Sciences* E96.A.2 (2013), pp. 402–414. DOI: 10.1587/transfun.e96.a.402.

[Wad03] K. Wada and Y. Tadokoro. "RC polyphase filter with flat gain characteristic". *2003 IEEE International Symposium on Circuits and Systems (ISCAS '03)*. IEEE, 2003. DOI: 10.1109/iscas.2003.1205619.

Appendix A

Conclusiones

La historia de la electrónica y las comunicaciones inalámbricas proporciona una perspectiva fascinante de cómo las características de los dispositivos condicionan las capacidades de los sistemas. En la actualidad, los circuitos se han vuelto más y más complejos, y son construidos con mayores capas de complejidad; sin embargo, los fundamentos continúan vigentes, quizás más que nunca, aunque se dispone de más medios y herramientas más poderosas para su diseño y fabricación que en épocas anteriores. Las capacidades computacionales permiten la caracterización de los circuitos bajo cualquier escenario hipotético que se desee. No obstante, los resultados están limitados por la fiabilidad y precisión de los modelos de simulación empleados. Afortunadamente se dispone de dichas herramientas, pues en caso contrario, el diseño microelectrónico resultaría mucho más complejo y los procesos de optimización se volverían prácticamente imposibles. Además, un ASIC no permite ningún cambio una vez ha sido fabricado.

Bajo este contexto, los resultados experimentales confirman que un PPF puede lograr el *IRR* deseado para la aplicación concreta con la tecnología propuesta. Es más, se espera que la mayoría de muestras consigan un alto rendimiento (50–60 dB). Estos valores son notablemente superiores a los estimados para la etapa de mezcladores [Mar21] y fuerzan a un cuidadoso diseño de los amplificadores IQ. En otras palabras, un PPF que alcanza tales valores de IRR no será el factor limitante para alcanzar los 40 dB que impone la norma de referencia (IEEE 802.11); no lo será mientras se sigan las pautas indicadas.

Nótese que la verificación completa del diseño es imposible. El PPF es afectado por variaciones aleatorias, y estas cambian la respuesta del filtro a tal punto que cada muestra es diferente. Además, existen restricciones económicas y materiales que impiden fabricar y medir suficientes muestras como para lograr información estadísticamente relevante. Por tanto, hay una dependencia con los modelos de simulación y con los estudios analíticos para estimar la viabilidad y la confianza de los PPFs. Por esta razón, el desarrollo analítico completo se encuentra detallado en los Anexos. Además, la presencia en los prototipos de los efectos deducidos refuerza la importancia de los análisis.

A continuación, la Sección A.1 profundiza en las conclusiones particulares respecto al estudio analítico. Tras ella, la Sección A.2 se encarga de detallar las de la metodología de diseño y optimización, así como los resultados experimentales. Finalmente, la Sección A.3 propone nuevas líneas de investigación en la temática.

A.1 Estudio analítico

Tradicionalmente, el diseño de un PPF implica fijar el número de polos del filtro y su posición, de acuerdo con el IRR deseado, el BW de la señal y al potencial desplazamiento frecuencial debido a los efectos de temperatura y proceso. Sin embargo, otros factores pueden alterar el funcionamiento del PPF. Así, aquellos efectos que modifican el balance entre las ramas I y Q pueden tener un enorme impacto. No obstante, es habitual que se omita [Kau08; Wad03; Tan13], se obvien las causas [Asa19; Nik03], o únicamente se describa cualitativamente [Gal00; Beh01]. En otras palabras, garantizar cierto IRR de un PPF requiere evaluar los factores que alteran el equilibrio del filtro, tales como el *mismatch* y los efectos parásitos, pero la estimación de estos suele realizarse mediante simulación —prueba y error— en vez de usar algún tipo de aproximación analítica. Además, los estudios [Had10; Nik15] no suelen cubrir las distintas configuraciones de PPF, en las que cambia cómo el *mismatch* afecta el funcionamiento (causando error de fase o de amplitud), así como la señal deseada y su imagen. Como consecuencia, la propia definición del IRR es diferente según el uso del PPF.

Las no idealidades resultan complejas de analizar: 1) existen infinitas situaciones posibles, 2) las expresiones generales tienen demasiadas variables para describir cada escenario, y 3) las simplificaciones por simetría del caso ideal no son aplicables cuando se introduce *mismatch* al sistema. Sin embargo, el Capítulo 3 presenta un método para resolver todos estos problemas y lograr una expresión sencilla y ventajosa que relaciona IRR con la tolerancia del *mismatch* (x).

Para ello, en primer lugar, el método busca la peor combinación posible de *mismatch* para un PPF de una única etapa. El proceso va reduciendo el espacio en el que dicha combinación se encuentra hasta alcanzar la peor o, al menos, una muy próxima a esta. Dicho caso sirve como cota pesimista: cualquier otra combinación funcionará mejor.

Un vez que el peor caso está definido, se pueden obtener las expresiones para un PPF de una etapa en función del *mismatch* entre sus componentes. Este estudio cubre las cinco configuraciones posibles de un PPF. La cota de IRR se calcula en $4/x^2$ para todas ellas. Afortunadamente, la influencia del *mismatch* sobre el IRR depende casi exclusivamente de la última etapa; por tanto, los resultados del PFF de una sola etapa pueden extrapolarse rápidamente a un filtro de múltiples etapas. La búsqueda del peor caso para un PPF de tres etapas corrobora esta hipótesis.

Los resultados cuantitativos permiten alcanzar una estimación del máximo IRR para unas determinadas tolerancias de los componentes y viceversa: las aproximaciones obtenidas pueden predecir las tolerancias máximas en los componentes para garantizar que el *mismatch* no limite el IRR por debajo de la cota deseada.

Adicionalmente, esta información es conocida *a priori*; por tanto, podría contribuir a evitar sorpresas desagradables en un diseño de PPF tras arduos esfuerzos, largas horas de trabajo y quizás incluso considerables gastos. Por consiguiente, el estudio realizado proporciona fiabilidad al diseñar PPFs usando información conocida y con un mínimo esfuerzo: $IRR_{max} = 4/x^2$.

Los resultados preliminares han sido publicados: primero como comunicaciones en congresos internacionales con el estudio por simulación de los efectos de las no idealidades [Mar17a] y del impacto del *mismatch* en particular [Mar18a]; y después con una publicación en revista [Mar18b] que profundizaba en el tema y presentaba con mucho

mayor detalle la influencia del *mismatch* sobre el IRR. Adicionalmente, el estudio se ha expuesto en foros nacionales [Mar17b; Mar18c].

No obstante, el Capítulo 3 presenta numerosas innovaciones respecto a lo previamente publicado. Así, la Sección 3.2 mejora significativamente lo que fue incluido en [Mar18b], analizando el impacto del *mismatch* en las otras cuatro configuraciones ([Mar18b] únicamente estudia el caso de un PPF Tipo-I como conversor D-IQ) para demostrar que la cota $4/x^2$ es común a todos usos de un PPF. También algunos aspectos pendientes del estudio se han resuelto con una descomposición alternativa del *mismatch*, que permite diferenciar entre la componente que produce desplazamiento frecuencial y la que ocasiona el acotamiento de los picos. Esto aclara algunos detalles que aparecían durante la búsqueda del peor caso. Además, la novedad demuestra que el IRR es una métrica que permite comparar cualquier tipo de PPF, aunque la definición estricta del parámetro sea diferente entre las configuraciones.

Adicionalmente, la Sección 3.3 innova en el estudio y completa el análisis describiendo el efecto del mismo sobre las cargas. Al igual que las variaciones de los componentes, su impacto es ampliamente conocido mientras se mantenga la simetría. Sin embargo, no se ha hallado en la literatura ningún estudio respecto a la degradación del IRR que puede ocasionar el *mismatch* de las cargas. También se muestra que analizar este tipo de *mismatch* es equivalente a evaluar el existente entre los parásitos, lo cual puede perjudicar notablemente el IRR [Had10] (ver la Figura 3.15). También se incluye una generalización que añade a las ecuaciones el potencial efecto de *mismatch* en condensadores como componentes y cargas.

Como se mencionaba en la Sección 1.3, el estudio analítico se plantea sobre cuatro ideas:

- **Describir los efectos de las diversas no idealidades.** De acuerdo con el tipo de impacto que producen en el IRR, las no idealidades pueden clasificarse *grosso modo* en dos grupos. Unas causan un desplazamiento frecuencial de la respuesta del filtro completa, mientras que otras son responsables de un achatamiento de los picos, imponiendo una cota máxima. Una descomposición en términos relacionados con cada uno de estos efectos se detalla en el Anexo E (deducida en la Sección 3.2.2.6). Además, las descripciones de la Sección 3.1.4 muestran a qué grupo pertenece cada no idealidad.

- **Analizar las no idealidades que alteran la simetría del filtro.** El efecto de las otras no idealidades es importante, pero fácil de mitigar ampliando BW_{PPF}. No hay otra penalización más allá de condicionar la selección de k_2 o un ligero incremento de las pérdidas de inserción. Sin embargo, *mismatch* y otros fenómenos similares resultan mucho más problemáticos y difíciles de paliar. Por este motivo, el Capítulo 3 cubre su estudio, especialmente en la Sección 3.2.

- **Ser independiente de la tecnología empleada.** El análisis del *mismatch* se realiza en función del parámetro de tolerancia, sin fijarlo a ninguna tecnología. Lo más cercano a una dependencia con la tecnología es la asunción de que el *mismatch* en las resistencias es notablemente mayor que en los condensadores. Sin embargo, la Sección 3.3.1 elimina las posibles restricciones por ello, incluyendo las variaciones de los condensadores dentro de los resultados del análisis.

- **Cubrir todos posibles usos y configuraciones.** A diferencia de los resultados preliminares, el estudio mostrado en esta tesis analiza los PPF en sus cinco configuraciones posibles, una a una. Nótese que cada caso requiere un desarrollo diferente, obteniéndose unas expresiones distintas. No obstante, todos resultados convergen en la misma cota, la marcada por la ecuación (3.72). Esta conclusión tiene especial interés, ya que el IRR tiene un significado distinto según la configuración. La Tabla 3.1 y la Sección 3.2.2.6 comparan las simulitudes y diferencias entre configuraciones de PPFs.

En resumen, el estudio presentado en esta tesis resulta una útil herramienta para el diseño de PPF, especialmente en el contexto de ASICs. Los resultados permiten una estimación de las especificaciones alcanzables para el filtro. Por tanto, las deducciones obtenidas del análisis pueden ahorrar considerable tiempo y esfuerzo a los diseñadores de PPF. Además, el estudio realizado puede ayudar a comprender las limitaciones de un PPF implementado y a identificar los principales obstáculos para mejorar su rendimiento.

A.2 Metodología de diseño y optimización

La regla de oro para el diseño de un PPF es tener en cuenta que las no idealidades de los dispositivos empleados influirán fuertemente en el diseño y en la respuesta final. Las

variaciones de proceso determinan k_2, definiendo indirectamente el potencial IRR. De forma similar, los errores de *mismatch* imponen una cota superior de IRR. Aunque no resulta intuitivo, este límite cambia de muestra a muestra: depende de cómo y cuánto son las diferencias de los dispositivos de la misma. Además, los efectos parásitos pueden agravar ambos problemas, degradadando el IRR además de reducir la potencia de la señal de salida.

En primer orden de aproximación, el diseño de PPFs depende de dos variables de diseño, R y C, que se determinan mutuamente para unos polos específicos. Típicamente, el grado de libertad se utiliza para adaptar las impedancias de entrada y salida [Kau08]; sin embargo, el diseño propuesto lo aprovecha para optimizar su funcionamiento contra las variaciones de proceso y *mismatch*, beneficiándose de la robustez de los condensadores MIM de la tecnología.

La estrategia mejora el IRR al reducir las no idealidades que de otro modo resultarían difíciles de atenuar. Por otro lado, la adaptación de impedancias puede alcanzarse mediante sendos amplificadores integrados junto al PPF. De este modo, el circuito puede trabajar con señales de voltaje en vez potencia, reduciéndose las pérdidas. Nótese que algunas de las no idealidades mitigadas —*mismatch*— causan tal impacto que no podría atenuarse ni incluyendo etapas adicionales al filtro: se mantendrían según la ecuación (3.72).

Alcanzar el IRR deseado y el número de polos requeridos para ello está estrechamente vinculado al factor k_2, por lo que esta variable tiene una gran influencia en el funcionamiento. Su valor define el compromiso entre un mejor IRR o un BW_{PPF} más ancho. Por un lado, un valor demasiado reducido haría el sistema extremadamente vulnerable a la mínima variación de proceso. En el otro extremo, valores demasiado elevados implicarían una fuerte reducción del IRR esperado en BW.

No obstante, encontrar analíticamente un valor óptimo de k_2 supone unos cálculos tremendamente complejos [Nik03; Nik15; Tan13; Hir20], especialmente conforme el número de etapas aumenta [Kau08]. El método clásico para su obtención en un PPF de tres etapas aproxima la solución a una ecuación de orden dos. Sin embargo, esta estrategia únicamente es válida para este número de etapas y k_2 es un factor muy sensible. Diferencias de décimas de k_2 pueden convertirse en unidades o incluso decenas de dB en IRR (ver curvas de la Figura 4.3). Paradójicamente y a pesar de su

simplicidad, el método propuesto consigue una selección de k_2 mucho más precisa. La técnica emplea una doble aproximación, una optimista y otra pesimista. Por tanto, sus errores se contrarrestan mutuamente en las circunstancias habituales de un PPF. La evaluación de esta estrategia de selección de k_2 para PPF con un gran número de etapas resulta una línea futura prometedora, pues el método clásico no puede aplicarse en tales condiciones.

Otra contribución relevante es la estrategia de "dividir y vencer" para reducir el coste computacional de las simulaciones estadísticas. Este enfoque supone que las variaciones de *mismatch* y procesos son fenómenos aleatorios e independientes, aunque ambos efectos perjudiquen conjuntamente al filtro. En consecuencia, la simulación combinada requeriría de un número de muestras igual al producto de las necesarias para caracterizar cada uno de los efectos por separado. Esto implicaría una gran cantidad de simulaciones.

Sin embargo, el impacto de las variaciones de proceso es análogo a extender el BW requerido. De esta manera, evaluar el IRR de un PPF bajo *mismatch* dentro del BW extendido es equivalente a caracterizar el PPF con ambas no idealidades. Este procedimiento reduce en órdenes de magnitud el número de muestras del análisis de Montecarlo —el número de simulaciones pasa a ser la suma en vez de multiplicarse— a cambio de cierto sesgo pesimista en la medida; el efecto del *mismatch* es siempre aplicado frente a la peor variación de proceso si se evalúa el IRR en todo el BW_{PPF}. Además, en su versión más rápida, el BW puede calcularse a partir de las variaciones que sufre el filtro en los *corners ss* y *ff* (dos simulaciones que sustituyen a un análisis de Montecarlo completo). También pueden establecerse caracterizaciones más detalladas del IRR esperado en base a percentiles o probabilidades de los efectos.

Siguiendo el flujo de diseño, la implementación del *layout* revela la importancia de otra no idealidad: los parásitos. Precisando más, estos influyen fuertemente sobre el balance I-Q y fuerzan un diseño simétrico del circuito. Este énfasis es mucho más significativo tras la optimización del *mismatch* de los componentes: la reducción del impacto del *mismatch* y de los condensadores del circuito hace que las capacidades parásitas puedan ser un factor limitante para el IRR.

Por tanto, unas conexiones simétricas resultan críticas para un buen funcionamiento. Para ello, el circuito se dispone en un *layout* circular, con las etapas situadas

concéntricamente. No obstante, no se ha observado distribuciones semejantes en las referencias consultadas. Una construcción circular en vez de lineal mejora la simetría de dispositivos y sus conexiones sin dejar de ser un diseño escalable. Cierta asimetría surge de las conexiones de entrada y de salida al circuito, aunque dos factores mitigan dicho inconveniente: 1) los nodos de salida se encuentran más próximos, pues el diseño es más compacto, y 2) las pistas tanto de entrada como de salida pueden construirse en capas de metales alejadas de los dispositivos. Es más, las propias vías que conectan resistencias y condensadores proporcionan conexión a dichas pistas.

La fuerte influencia de variables aleatorias sobre la respuesta de los dispositivos implementados complica la verificación. Las curvas pueden cambiar de una a otra muestra de forma drástica. Un circuito electrónico normalmente es validado si las curvas experimentales son muy parecidas a las simuladas. No obstante, esto no es posible en un PPF. Incluso en el mejor de los casos, cada muestra sufrirá un desplazamiento frecuencial propio y —si el IRR es suficientemente elevado— aparecerá un achatamiento de los picos a causa de la proyección del *mismatch* sobre el peor caso. Otras no idealidades y componentes de *mismatch* también alteran las curvas de distintos modos. Sin embargo, los resultados de simulación coinciden con lo esperado: muestran un desplazamiento significativo, pero dentro del rango estimado, y también una cota superior por *mismatch*, quizás algo más llamativa debida a la compresión de k_2, pero igualmente dentro de lo esperado.

El detalle más sorprendente de las medidas es la alteración de k_2, aunque con la limitada información disponible resulta difícil determinar la causa. Los principales sospechosos son el *mismatch* entre las etapas (más concretamente entre la primera y la última) o los elementos parásitos del *setup* de medida introduciendo parejas de polos y ceros a frecuencias relativamente cercanas que desplazarían el límite superior de BW_{PPF} hacia la izquierda. Notablemente, este último caso implicaría también que el desplazamiento frecuencial es menor de lo estimado. En cualquier caso, si el cambio en k_2 es propio del PPF y no de las medidas, no resultaría complicado compensarlo, empleando para ello los mismos métodos que amortiguan el impacto de las variaciones de proceso (ver Sección 4.3.3 para más detalles).

No obstante, gracias a la cuidadosa optimización, el prototipo alcanza el objetivo de

IRR dentro del BW a pesar del estrechamiento de BW_{PPF} y una fuerte variación de proceso. Además, muestras que tuvieran variaciones de proceso menos marcadas podrían alcanzar incluso mejores IRR, ya que la reducción de k_2 implica que el IRR en el centro del filtro se incrementa a costa de los laterales. Basándonos en los modelos de variaciones de procesos y las curvas experimentales, se espera una mediana de IRR superior a 50 dB para el diseño propuesto. Además, la inclusión de un polo adicional aseguraría que el IRR alcance el techo impuesto por el *mismatch* para todo el rango de potenciales variaciones de proceso.

La metodología de diseño buscaba conseguir cuatro objetivos:

- **Cumplir las especificaciones para una RAU.** Los prototipos de PPF logran un margen razonable de IRR sobre la cota de 40 dB dentro del rango frecuencial de interés (90–110 MHz). Estos resultados son alcanzados incluso con la inesperada compresión de k_2 (y la consiguiente reducción de BW_{PPF}). Dado que las muestras medidas presentan unas variaciones de proceso significativas, se espera un mejor IRR para la mayoría de muestras futuras.

- **Generar una metodología de optimización sistemática y comprensible.** Esta tesis proporciona diversas herramientas y metodologías para cada etapa del proceso de diseño. Los mismos test y simulaciones empleados para esta tecnología en particular podrían aplicarse directamente a cualquier otra para obtener la información relevante en el nuevo escenario. Del mismo modo, diseños con otras aplicaciones en mente únicamente requerirían cambiar las especificaciones a cumplir. Por tanto, el proceso es fácilmente replicable incluso en escenarios muy distintos.

- **Evaluar el efecto de las no idealidades.** Indudablemente, estos factores son la clave del diseño y optimización de PPF. Las variaciones de proceso determinan el rango frecuencial que debe abarcar el filtro, mientras que el *mismatch* fija una cota superior de IRR para cada muestra. Los parásitos condicionan críticamente el diseño físico del PPF, obligando a mantener la simetría. El resto de fenómenos pueden redefinirse como una contribución a cualquiera de ellos. Por ejemplo, las variaciones por temperatura se comportan de forma análoga a las de proceso.

- **Cubrir el flujo completo de diseño.** La metodología de diseño comienza con el análisis del circuito y continúa el proceso hasta completar las medidas experimentales. La importancia de abarcar el recorrido completo del flujo resulta clara: cada uno de los pasos impone diferentes restricciones para resolver sus problemas particulares. De este modo, el PPF final debe cumplir con todas ellas. Saltarse etapas del flujo de diseño conllevaría a ignorar factores esenciales que afectarían significativamente al funcionamiento del filtro. Por el contrario, la metodología propuesta logra hallar dichas variables críticas y mitigar su impacto.

En definitiva, esta tesis propone una metodología de diseño de PPF centrada en las no idealidades más críticas para cada fase del proceso. El método aprovecha el análisis presentado y la información obtenida de simulaciones con modelos de la tecnología de interés. Durante el proceso, aparecen dos mejoras de especial importancia: 1) un nuevo método de selección de k_2 y 2) el diseño circular del *layout* para mejorar su simetría. Así mismo, la propia descripción del proceso seguido proporciona una serie de pautas y métodos para optimizar el funcionamiento de un PPF, independientemente de la tecnología o aplicación.

A.3 Líneas futuras de investigación

El proceso de investigación ha generado una serie de cuestiones que podrían resultar de interés para nuevos proyectos y/o nuevas tesis. La más directa al análisis presentado es su extensión para cubrir la totalidad del conversor frecuencial. No obstante, esta tarea debe superar un obstáculo clave: la existencia a la salida de señales con frecuencias distintas de la excitación es una indicación clara de que el sistema no es lineal. Nótese que la linealidad es necesaria para poder aplicar propiedades tan básicas como la combinación de funciones de transferencia.

Sin embargo, un mezclador es una clase de sistema muy particular denominada bilineal. Además, el sistema se vuelve periódico en el tiempo si el oscilador local (LO) produce un único tono. En otras palabras, no será un sistema lineal e invariante en el tiempo, pero es lo suficientemente parecido como para aplicar ciertas transformaciones. Bajo las condiciones anteriores, una aplicación lineal compleja [Dun68] puede definir la relación entre las amplitudes de la señal de entrada y la de salida a ciertas

frecuencias de interés. Nótese que la etapa de mezcladores exige el empleo de números complejos para el modelado, ya que la fase es un factor crucial en su operación. Supongamos que el mezclador —y consiguientemente la etapa de mezcladores— puede ser descrito como una aplicación lineal. En ese caso, su función de transferencia puede combinarse con la propia de los PPF de forma semejante a la empleada en el método del Anexo G. Otros bloques relacionados, como los amplificadores IQ, resultan triviales de añadir de la misma forma.

Nótese, además, que una aplicación lineal puede ser definida en función de la relación de las bases de su dominio y codominio. En otras palabras, la linealidad implica que la caracterización del sistema puede realizarse mediante el análisis de la respuesta a un conjunto de vectores que defina el dominio de origen. Para una señal IQ, esto puede ser las cuatro componentes de secuencias simétricas. Este enfoque es semejante a un análisis de un circuito aplicando el principio de superposición.

Una vez que se ha obtenido el modelo, este permite el estudio de la etapa en particular o en conjunto con el resto frente a efectos de *mismatch* u otras no idealidades. También posibilita la búsqueda de los peores casos o el establecimiento de restricciones en los componentes para lograr un cierto IRR global. Adicionalmente, el método resultaría útil tanto para esquemas simples como para otros tan complejos como se desee, pues se combina perfectamente con estrategias de diseño jerarquizado.

En definitiva, este desarrollo extendería el estudio al bloque de conversión frecuencial al completo, posibilitando un estudio análogo al realizado sobre los PPF en esta tesis. En consecuencia, las especificaciones de los componentes de dicho bloque podrían marcarse de forma más precisa para lograr una optimización del sistema.

La cota de *mismatch* obtenida resulta una aproximación sencilla, rápida y eficiente del límite superior de IRR del PPF. Sin embargo, sería de interés evaluar la precisión de este límite para las diversas configuraciones de PPF, número de etapas y no idealidades críticas. También se ha observado que una alta densidad de polos (un factor k_2 reducido) puede favorecer un ligero relajamiento de la restricción de IRR. Por tanto, explorar los límites de la cota podría proporcionar diseños más fiables. En la misma línea, valorar representaciones alternativas del IRR de un PPF para mostrar mejor las variaciones del *mismatch* y su combinación con otras no idealidades podría beneficiar notablemente este planteamiento.

La metodología propuesta para la selección de k_2 tiene un enorme potencial en su aplicación a PPF con múltiples etapas, pues el método tradicional se limita al caso de tres etapas. Este estudio se centraría en analizar la validez de las asunciones realizadas en PPF de más etapas: el BW es estrecho y los flancos tiene poca relevancia. Ambos parámetros dependen principalmente del BW_{PPF} requerido, el IRR objetivo y la separación entre los polos (k_2); los flancos son influidos por los polos cercanos. Dichas relaciones son muy complejas, por lo que el impacto de cada factor en las suposiciones resulta difícil de predecir.

Los PPF con más de tres etapas son habituales. Además, una alta densidad de polos puede influir a que el IRR obtenido se aproxime al máximo posible (de nuevo, el límite del *mismatch*), aunque ello puede implicar utilizar un número elevado de etapas para poder abarcar suficiente rango frecuencial y así compensar las variaciones de proceso. Por tanto, conocer el método en mayor detalle podría conllevar una notable mejora a los PPFs para aplicaciones que demanden un elevado IRR.

Relacionado con lo anterior, la literatura asume que la distribución óptima de los polos para cualquier PPF es una separación geométrica entre ellos. De este modo, los mínimos de los distintos valles descienden hasta idéntico nivel de IRR. Por otro lado, las simulaciones muestran que no todo el rango de BW_{PPF} tiene las mismas probabilidades de cubrir el BW tras las variaciones de proceso. En otras palabras, fuera de un enfoque basado en mejorar el peor caso, unas regiones de BWPPF son más importantes que otras. Si hay zonas prioritarias, entonces un PPF que pueda disponer de suficientes polos podría beneficiarse de otras distribuciones para lograr una mayor densidad de estos en torno al centro de BW_{PPF} en detrimento de sus extremos.

También el *mismatch* —comúnmente ignorado— debería considerarse en este sentido. Esta no idealidad puede causar que los polos se desplacen respecto a su posición relativa a los otros, alterando los valles y flancos, salvo que la cota máxima de IRR se haya alcanzado. Una revisión de la separación de polos en PPF con un número alto de etapas podría optimizar su funcionamiento con estas técnicas y revelar detalles que no son relevantes para pocas etapas.

Al aumentar el número de etapas, es de esperar que se añadan amplificadores para compensar las pérdidas. Sin embargo, estos deben diseñarse para lograr su función minimizando su impacto en el IRR. Al mismo tiempo, otras preguntas y oportunidades

aparecen. Por ejemplo, en el caso de un PPF con 6 etapas divididas en dos grupos de tres por un bloque amplificador, ¿deberían situarse los polos en orden descendente (123–456) o entrelazar ambos grupos (135–246)?

Adicionalmente, evaluar el método en otras tecnologías resultaría de gran interés. Durante este estudio se consideró una tecnología SOI de dimensiones similares para el diseño de PPF. Sorprendentemente, los resultados preliminares no resultaron prometedores, ya que los condensadores mostraban una repetitividad mucho peor. Por tanto, la idea se descartó. Sin embargo, los reducidos parásitos propios de dicho tipo de tecnología podrían compensar aquel problema, permitiendo emplear técnicas de reducción de *mismatch* o alcanzando mayores frecuencias de trabajo. De nuevo, una interesante comparativa requeriría de cuantiosas muestras experimentales, idealmente independientes. De otra manera, no hay otra opción que depender de los modelos de simulación y la extracción de parásitos del *layout*. Rara vez los bloques de PPF son la razón para utilizar tecnologías de este tipo; otras etapas de la cadena de comunicaciones se benefician en mayor medida. Sin embargo, del estudio de tecnologías no estándar podría deducirse información muy interesante sobre los compromisos entre el impacto de no idealidades.

De forma semejante, el uso de transistores MOS en los PPF podría proporcionar nuevas contraposiciones entre los recursos de diseño. Esta tesis se ha centrado en los dispositivos pasivos, ya que estos tienen prestaciones más adecuadas a las buscadas para la aplicación. No obstante, se realizaron algunas pruebas para diseñar PPF utilizando transistores MOS polarizados en zona de triodo como resistencias. Esta implementación tenía una mejora clara: mayor control sobre los valores. Sin embargo, las pruebas preliminares mostraron que el *mismatch* de los transistores MOS resultaba mucho más restrictivo que el de las resistencias. Un control minucioso podría, en teoría, mitigar dicho *mismatch* en gran medida, pero en la práctica surgían algunos problemas. Primero, si se pretende controlar cada dispositivo, serían precisas demasiadas señales de control —un PPF de tres etapas emplea doce resistencias que pueden presentar *mismatch* entre sí. Y segundo, identificar la combinación de *mismatch* que lo cancele resultaría complejo. La respuesta de *IRR* es difícil de interpretar en dichos términos, por lo que implementar algún tipo de lazo de control parece incluso más complejo. No obstante, este tipo de filtros podría superar las prestaciones de los puramente pasivos conforme la tecnología avance.

Un enfoque similar al planteado para los PPF podría aplicarse también a los filtros polifásicos activos. Estos circuitos se hallaban fuera del alcance de nuestro estudio. No obstante, muchos de los principios e ideas que asientan las metodologías propuestas podrían extrapolarse al resto de filtros polifásicos.

Por otro lado, las iteraciones futuras podrían beneficiarse de la inclusión de las etapas amplificadoras dentro del *layout* del PPF para alcanzar alto IRR y aislar el filtro de los efectos de cargas. Probablemente, sería necesario incluir celdas *dummy* [All12] para mantener la simetría. Además, cada resistencia podría dividirse en dos segmentos para mejorarla. Cada mitad podría situarse ortogonalmente entre sí para garantizar de este modo la simetría respecto a ambos ejes entre los pares de resistencias. Los segmentos horizontales y verticales de R_1-R_3 y de R_2-R_4 compartirían el mismo centro. La tecnología empleada no sugería este criterio de diseño, aunque sí suele aparecer en la lista de recomendaciones.

Indudablemente, nuevos prototipos resultarían de especial interés para completar el estudio. No obstante, estos deberían tener un enfoque totalmente distinto según se dedicasen al estudio analítico o a la implementación funcional de PPF. Uno con una sola etapa o a lo sumo con dos sería más ventajoso para verificar los estudios analíticos. Cuanto más sencillos sean los diseños, más clara será la identificación de efectos y fenómenos que aparezcan. Por el contrario, un diseño PPF con intención de maximizar su funcionamiento podría sacar partido de la inclusión de un polo adicional, pues las ventajas en fiabilidad compensan el incremento de pérdidas de inserción en 3 dB. En cualquier caso, observar los cambios de k_2 resultaría de interés.

Futuros diseños también podrían beneficiarse de una implementación que simplifique el proceso de medida. Evitar elementos complejos, tales como *baluns*, favorecería la caracterización de un número mayor de muestras. También, un circuito integrado adaptado para su medida mediante mesa de puntas podría incrementar sustancialmente el número de muestras disponibles por cada *run*. Al mismo tiempo, realizar la medida sin necesitar una PCB evitaría la degradación del IRR que procede de dispositivos externos.

Además, incluir un sistema de multiplexación inversa podría multiplicar el número de filtros por muestra y proporcionar información mucho más detallada de las condiciones de cada una (si se incluyen los circuitos de test apropiados). Esta estrategia sería útil

independientemente de que el enfoque escogido conduzca a circuitos más simples o más complejos. No obstante, debería evaluarse el impacto de los dispositivos de multiplexación sobre el *IRR*. Incluso con esta estrategia, un estudio estadístico tendría que superar otros desafíos en la caracterización, como la correlación existente entre muestras del mismo *run*.

Referencias

[All12] P. E. Allen and D. R. Holberg. *CMOS analog circuit design, 3rd edition*. Oxford University Press, 2012. ISBN: 9780199765072.

[Asa19] K. Asami, N. Kushita, A. Hatta, M. T. Tran, Y. Tamura, A. Kuwana, and H. Kobayashi. "Analysis and evaluation method of RC polyphase filter". *2019 IEEE 13th International Conference on ASIC (ASICON)*. IEEE, Oct. 2019. DOI: 10.1109/asicon47005.2019.8983545.

[Beh01] F. Behbahani, Y. Kishigami, J. Leete, and A. Abidi. "CMOS mixers and polyphase filters for large image rejection". *IEEE Journal of Solid-State Circuits* 36.6 (June 2001), pp. 873–887. DOI: 10.1109/4.924850.

[Dun68] J. Duncan. *The elements of complex analysis*. John Wiley and sons, 1968.

[Gal00] S. H. Galal, H. F. Ragaie, and M. S. Tawfik. "RC sequence asymmetric polyphase networks for RF integrated transceivers". *IEEE Transactions on Circuits and Systems II: Analog and Digital Signal Processing* 47.1 (2000), pp. 18–27. DOI: 10.1109/82.818891.

[Had10] F. Haddad, L. ZaIumld, W. Rahajandraibe, and O. Frioui. "Polyphase filter design methodology for wireless communication applications". *Mobile and Wireless Communications Network Layer and Circuit Level Design*. InTech, Jan. 2010. DOI: 10.5772/7707.

[Hir20] A. Hirai, T. Fujiwara, M. Tsuru, K. Mori, and M. Shimozawa. "Vector-sum phase shifter using a tunable active g_m polyphase filter". *IEEE Transactions on Microwave Theory and Techniques* 68.10 (Oct. 2020), pp. 4091–4102. DOI: 10.1109/tmtt.2020.2991738.

[Kau08] J. Kaukovuori, K. Stadius, J. Ryynanen, and K. Halonen. "Analysis and design of passive polyphase filters". *IEEE Transactions on Circuits and Systems I: Regular Papers* 55.10 (Nov. 2008), pp. 3023–3037. DOI: 10.1109/tcsi.2008.917990.

[Mar17a] A. D. Martinez-Perez, J. Morte, F. Aznar, C. Sanchez-Azqueta, and S. Celma. "Impact of non-idealities on passive polyphase filter performance". *2017 European Conference on Circuit Theory and Design (ECCTD)*. Catania, Italy: IEEE, Sept. 2017. DOI: 10.1109/ecctd.2017.8093256.

[Mar17b] A. D. Martínez-Pérez, J. Morte, F. Aznar, C. Sánchez-Azqueta, and S. Celma. "Approaching ideal polyphase filter response in 65-nm CMOS". *VI Jornada de Jóvenes Investigadores del I3A*. Vol. 5. Zaragoza, Spain: Universidad de Zaragoza, June 2017. DOI: 10.26754/jji-i3a.201711990.

[Mar18a] A. D. Martinez-Perez, F. Aznar, G. Royo, C. Sanchez-Azqueta, and S. Celma. "Analysis of the influence of component mismatch on integrated passive polyphase filters". *2018 IEEE International Symposium on Circuits and Systems (ISCAS)*. Fireze, Italy: IEEE, May 2018. DOI: 10.1109/iscas.2018.8351661.

[Mar18b] A. D. Martínez-Pérez, F. Aznar, G. Royo, C. Sánchez-Azqueta, and S. Celma. "Analysis of mismatch impact on image rejection ratio for passive polyphase filters". *International Journal of Circuit Theory and Applications* 46.10 (June 2018), pp. 1838–1847. DOI: 10.1002/cta.2505.

[Mar18c] A. D. Martínez-Pérez, F. Aznar, G. Royo, C. Sánchez-Azqueta, and S. Celma. "Estimación de la degradación por mismatch del rechazo de imagen en filtros polifásicos pasivos". *VII Jornada de Jóvenes Investigadores del I3A*. Vol. 6. Zaragoza, Spain: Universidad de Zaragoza, May 2018. DOI: 10.26754/jji-i3a.201802847.

[Mar21] A. D. Martinez-Perez, F. Aznar, G. Royo, and S. Celma. "Analysis of non-idealities on CMOS passive mixers". *Electronics* 10.9 (2021). ISSN: 2079-9292. DOI: 10.3390/electronics10091105.

[Nik03] Y. Niki, J. Kangand, H. Kobayashi, N. Yamaguchi, and T. Kitahara. "Analysis of RC polyphase filters: Input impedance, output termination, component

mismatch effects, flat-passband filter design". *Proc. IEICE Tech. Meet. Circuits Syst.* Jan. 2003.

[Nik15] Y. Niki, S. Sasaki, N. Yamaguchi, J. Kang, T. Kitahara, and H. Kobayashi. "Flat passband gain design algorithm for 2nd-order RC polyphase filter". *2015 IEEE 11th International Conference on ASIC (ASICON)*. IEEE, Nov. 2015. DOI: 10.1109/asicon.2015.7516933.

[Tan13] H. Tanimoto. "Exact design of RC polyphase filters and related issues". *IEICE Transactions on Fundamentals of Electronics, Communications and Computer Sciences* E96.A.2 (2013), pp. 402–414. DOI: 10.1587/transfun.e96.a.402.

[Wad03] K. Wada and Y. Tadokoro. "RC polyphase filter with flat gain characteristic". *2003 IEEE International Symposium on Circuits and Systems (ISCAS '03)*. IEEE, 2003. DOI: 10.1109/iscas.2003.1205619.

Appendix B

Removing telegraphic wires

The discovery and mastery of electromagnetic waves revolutionized communication systems; however, using electricity to transmit information wirelessly predates it. The advancement—and the interest—of the electrical telegraph presented new obstacles to overcome. Wires were not always practical, especially when bodies of water were involved. Before electromagnetic waves, there were two kinds of solutions: conduction and induction telegraph. Wireless conduction replaces wires with another medium that works as a galvanic contact to close the circuit. On the other hand, an induction telegraph relies on electric or magnetic induction between transmitting and receiving circuits [Sar06].

B.1 Conduction telegraph

Again, the earliest idea came from **Salvá** before the Academy of Sciences in December, 1795. Note that this is even before Volta's invention. His contribution, "On the application of electricity to telegraphy" [Sal76], proposed (among many other things) placing an insulated wire to connect an island with the continent—more precisely, Mallorca and Alicante—and using the water as the return path. Moreover, he also suggested removing the wire. He modeled the scenario as a large capacitor, with each plate being each land. If connecting the land (plate) to the sea would produce a spark, it would mean the other part was also connected. Otherwise, no spark would be observed. In other words, the (theoretical) system transmits a bit of information without wires.

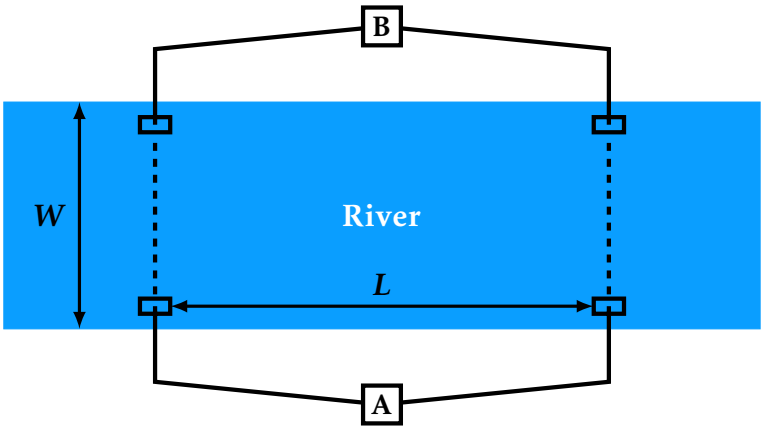

Figure B.1: Morse's conducted telegraph over water. Dashed lines represent the wireless links. The experiment showed that W must be three times L to perform well.

The idea was considered quite extravagant that year, and his contributions might have been underestimated. However, much later experiments about "bad grounds" demonstrated that Salvá's wireless telegraph was plausible with enough electrical charge, and electrical devices around every aspect of our lives are a fact nowadays. How many of his "impossible" ideas will and have become a reality remains to be seen.

Under **Gauss**'s suggestion, **Steinheil** tried to use railroad tracks as telegraph cables around 1837–1838. Experiments were unsuccessful due to poor isolation, which caused huge losses. Nevertheless, this inspired him to use the ground as the return path [Sar06], and a single wire was enough to send the signal instead of a pair. From 1838 in advance, this principle became widely used. Half of the work for a wireless system was done; thus, Steinheil also experimented with sending wireless signals by ground. However, the limit range was just 20 meters, although he predicted that a more sensitive detector and larger ground electrodes could significantly enlarge the distance.

Following Steinheil's experiments, **Morse** demonstrated wireless communication between the two sides of a river in 1842 [Sar06]. The scheme of the system is shown in Figure B.1. A battery and a switch (A) were on one river bank; on the other edge, a galvanometer (B) was ready to detect the electric current. Two electrodes connected each device to the river. The experiments revealed that enough separation between the electrodes on the same side of the river solved the issue found by Sömmering. The link is possible if the distance must be around three times the width of the river. In other words, the separation between plates must be much larger than the wireless distance.

However, it was a start, and it would find its niche [Sim96; Maz06] in places like the island of Wight (**Willian Henry Preece**, 1882), Fastnet Rock (Willoughby Smith, 1895), or a variation to cope with the wide Indian rivers (**Henry Highton**, proposal in 1872 [Hig72]). **Henry James Bowman Lindsay** had been improving the range since 1954. Lindsay also said it would be possible to communicate across the Atlantic with this method if batteries, immersed electrodes, and separation between them were large enough [Sim96]. However, the advantages of wireless did not resonate with the public, although he achieved a range of 3 km.

The inverse situation existed in Paris during the Franco-Prussian War (1870-1871). They have a solid motivation to establish a wireless communication link over the siege of the city, but they lack the means. After careful deliberations, they plot to set a water-conducted telegraph over the river. Thus, around December, an agent is sent—in a balloon to avoid the blockade—to obtain the required instrumentation for **Jean-Gustave Bourbouze** [Rai91; Sar06]. The mission was completed one month later, but the Seine was frozen. They had to wait ten days for the ice to melt; however, Paris capitulated on the ninth day, and the motivation ended.

One of the most interesting inventions was the wireless device [Sar06] of **Mahlon Loomis** (dentist, mason, and inventor). At the moment, it was known that 1) even on clear days, electricity can be extracted from the atmosphere (Benjamin Franklin's kite experiment); 2) air is a better conductor under low pressure; and 3) pressure is lower at high altitudes. Loomis connected all those points and had an idea. He uses a wire grounded on one end and the other tied to a kite at high altitude as the transmitter and receiver. The transmitter used a switch to connect or disconnect the kite to the ground, causing a disturbance in the available atmospheric electricity detectable in the receiver. His idea was great although his descriptions are quite vague and not fully explained. Some historians theorize that the distance attained was long because he accidentally produced electromagnetic waves.

In 1866, he claimed a 23 km link with kites at 900 meters above the ground [Fah00], although the results of the experiment only stated that "messages were sent and received." However, he drew the attention of the U. S. Congress. They decided to grant $50,000 to develop an "aerial telegraph." However, Loomis never received a single dollar in the end [Yat22], despite his plans of transatlantic aerial communications (from

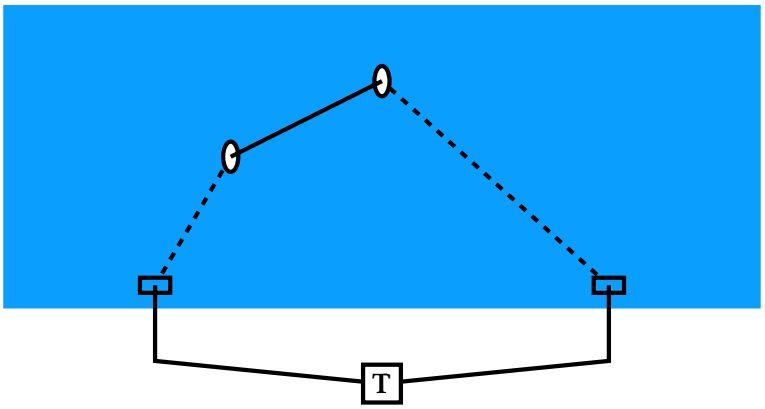

Figure B.2: Schematic of Ratheanau's experiment

Rocky Mountain to the Alps).

The telephone (1876) indirectly meant a more sensitive detector of electrical currents. **John Trowbridge** exploited this new device in his field of interest: wireless communication between ships and coast stations. He observed that the telephone receiver detected some signal while the electrodes were not in the same equipotential curve. As the dynamo (1867) became mandatory for electrical lightning (1879) in the ships in the 1880s, Trowbridge used that to power his system. An electrode was placed on the bow of the vessel, and the other was at the end of an insulated cable. His device can communicate in the range of the separation between the electrodes (around half a mile, *i.e.*, 800 meters). This apparently short range was a significant advantage in foggy weather, as acoustic (unpredictable rebounds) and visual signals were useless.

Erich Rathenau reached the peak of this kind of communication system over water in 1894 [Sar06]. His experiment (depicted in Figure B.2) used two submerged electrodes as the transmitter, distanced 500 meters along the shore, and two boats as the receiver, each one with an electrode and linked by an insulated wire. He employed diverse carrier signals, finding 150 Hz optimal, but mentioned that several signals could be simultaneously sent using different frequencies. He reached a 5 km transmission range. For the first time in conduction over water, the reach of the wireless link was much larger than the distance between the electrodes of the transmitter.

Two years later, **K. Strecker** received a signal from 17 km through the ground [Maz06]. Unfortunately, the electromagnetic wave telegraph was already a reality and made conductive wireless technologies obsolete.

Axel Orling and **James Tarbotton Armstrong** made a last try for this technology over the ground. In 1905, they presented their electro-capillary recorder, a simple and highly sensitive detector [Orl05]. They reported it allows for a quite fast data rate transfer due to—in our modern terminology—a high SNR. They achieved a 32 km range, but relays could extend it. Initially, they proposed as an alternative to Marconi's technology. However, the age of electromagnetic waves had already begun. That might be why they did not place their apparatus on the market in the end, despite having the economic means [Orl02].

B.2 Induction telegraph

Almost at the same time, magnetic induction was discovered by **Michael Faraday** (1831) and **Joseph Henry** (1832). The former [Far39] is credited as the first to report the effect, and the latter [Hen32] as the first to propose a practical application to wireless telegraph.

In his search for naval wireless communications, **Trowbridge** provided a detailed system [Tro91] in 1891. The induction—he predicted—could communicate ships at a close range in the presence of thick fog as induced currents are detectable when they are at a distance similar to their own size. Also, it enabled direction finding in a low-visibility scenario by rotating the coil. Otherwise, he failed to see a more general application [Sar06].

The first practical projects of Trowbridge's ideas arrived in 1892, although the works had a different application. There were two similar works around the same time. On the one hand, **Charles A. Stevenson** studies the optimal sizing, resistance, geometry, position, and turn number of a pair of coils [Ste95]. He aimed to communicate Mucke Flugga island and mainland Scotland (approx. 730 m). Finally, two coils of 180 m and nine turns did the job using 1 A.

On the other hand, **Preece** [Fah00] managed the installation of an induction telegraph on the Bristol Channel at the same time as his works in conducting telegraphy. The system enabled communication with two islands, 5 and 8 km from the coast. A couple of years later, he also installed two huge rectangular loops (150 m high and 8 km long) to connect the island of Arran and the peninsula of Kintyre across the Kilbrannan Sound.

To his surprise, using the ground as the return path improved the coupling [Sar06] and avoided undesirable interferences [Fah00]. Nevertheless, Preece met Marconi in 1896. From that day forward, Preece devoted his work in using "Hertzian waves" for wireless communication—component sizing was much more convenient.

Amos Emerson Dolbear invented the electrostatic telephone receiver (1880). Compared to Bell's version, the impedance was high; hence, it could detect minimal currents if the voltage was high enough. During his experiments, Dolbear observed that his apparatus worked even with a broken cable. He applied for a patent in 1883, later described in a publication [Dol86]. He had legal disputes with Bell due to the invention of the telephone and later with Marconi, as Marconi's setup of his famous experiment—ten years later—resembles his. Indeed, this is not a coincidence: Dolbear was close to discovering electromagnetic waves. However, his explanation of the operation was based on ground currents and induction [Sar06]. In 1883, the range of his invention was 400 meters using a kite at 100 meters above ground. Later experiments included a spark gap in the transmitter. Thus, electromagnetic waves must have unknowingly played a major role in reaching the reported 20 km range.

Nor **Thomas Alva Edison** was fortunate with pre-radio wireless communications. He came very close to inventing wireless communication by electromagnetic waves as soon as 1875. He noticed that a spark in a telegraphic system with inductances produces sparks in circuits without connections other than ground. However, his conclusions about this phenomenon were wrong. He supposed it was due to a new physical force [Edi75], and he constructed a spark-gap detector ("the etheroscope") for this "etheric force." During 1875 and 1876, he published many articles with his theories and experiments [Sar06]. He was live presenting his discoveries. Unfortunately for him, in 1876, **Edwin James Houston** and **Elihu Thomson** demonstrated that sparks were oscillatory high-frequency electric currents, too fast for the usual DC equipment to sense [Hou76]. Edison immediately abandoned this project for more promising ones.

After this, he was really close again in 1885 with his patent "Means for transmitting signals electrically." The invention aimed to facilitate communication between ships and coast stations. The patent shows antennas in the vessels and land towers, but the system operation was described as based on electrostatic induction, and it was

never tested. Otherwise, he might have outpaced Hertz and Marconi in their milestones [Sar06].

Nevertheless, in 1887, he successfully tested an invention to transmit between a moving train and the outside world. The idea had been around since the 1830s. Edison's target market was businessmen traveling by train. However, there was an unexpected issue: businessmen did not desire to work while traveling. Thus, the invention soon became unprofitable [Bal01].

As other alternatives to wireless electrical communication, induction telegraph could not survive the competence with the emerging electromagnetic waves.

References

[Bal01] N. Baldwin. *Edison, inventing the century*. Chicago Press, 2001. ISBN: 0226035719.

[Dol86] A. E. Dolbear. "Bell not the inventor of the speaking telephone". *Scientific American* 54.2 (1886), p. 21.

[Edi75] T. A. Edison. "The discovery of another form of electricity". *Scientific American* 33.26 (Dec. 1875), pp. 400–401.

[Fah00] J. J. Fahie. *A history of wireless telegraphy 1838-1899, including some bare-wire proposals for subaqueous telegraphs*. Dod, Mead and Co., 1900.

[Far39] M. Faraday. *Experimental researches in electricity, vol. 1: reprinted from the Philosofical Transactions of 1831–1838*. Ed. by B. Quaritch. Taylor and Francis, 1839.

[Hen32] J. Henry. "On the production of currents and sparks of electricity from magnetism". *Silliman's American Journal of Science* 22 (July 1832), pp. 403–408.

[Hig72] H. Highton. "Telegraphy without insulation – A cheap means of international communication". *Journal of the Society of Arts* 7.63 (July 1, 1872), p. 43.

[Hou76] E. J. Houston and E. Thomson. "Electrical phenomena. The alleged etheric force, test experiments as to its identity with induced electricity". *Chemical News* 32.857 (Apr. 28, 1876), pp. 173–174.

[Maz06] D. Mazzotto. *Wireless telegraphy and telephony*. Whittaker and Co., 1906.

[Orl02] A. Orling and J. T. Armstrong. "The Armstrong Orling wireless telegraph". *Scientific American* 87.8 (Aug. 23, 1902), p. 116. DOI: 10.1038/scientificamerican08231902-116b.

[Orl05] A. Orling and J. T. Armstrong. "The Orling-Arstrong electro-Capillary recorder". *Scientific American Supplement* 59.1516 (Jan. 21, 1905), pp. 24288–24289. DOI: 10.1038/scientificamerican01211905-24288supp.

[Rai91] D. Raichvarg and J. Jaques. *Savants et ignorants: Une histoire de la vulgarisation des sciences*. Éditions du Seuil, 1991. ISBN: 2020134098.

[Sal76] F. Salvá-y-Campillo. "Memoria sobre la electricidad aplicada a la telegrafía". *Memorias de la Real Academia de Ciencias Naturales y Artes*. 1876, pp. 1–12. DOI: 10.1109/APS.2001.958781.

[Sar06] T. K. Sarkar, R. J. Mailloux, A. A. Oliner, M. Salazar-Palma, and D. L. Sengupta. *History of wireless*. John Wiley and Sons, 2006. ISBN: 0471718149.

[Sim96] R. Simons. "Guglielmo Marconi and early systems of wireless communication". *GEC Review* 11.1 (1996), pp. 37–55.

[Ste95] C. A. Stevenson. "Induction through air and water at great distances without the use of parallel wires". *Proceedings of the Royal Society of Edinburgh* 20 (1895), pp. 25–27. DOI: 10.1017/S0370164600048331.

[Tro91] J. Trowbridge. "Transmission of messages through the air by electricity without wires". *Scientific American Suplement* 31.790 (Feb. 21, 1891), pp. 12615–12617. DOI: 10.1038/scientificamerican02211891-12615supp.

[Yat22] R. F. Yates and L. G. Pacent. *The complete radio book*. P. F. Collier and son company, 1922.

Appendix C

Analysis of 1-stage ideal PPF

This annex covers the analytical development of an ideal PPF, considering both classes (Type I and II), as well as its use as a differential (D) to quadrature (IQ) converter and vice versa. The implications of the results obtained here are described in 3.1.1. Figure C.1 shows the combinations evaluated.

For simplicity, the effects of source loads or impedances are ignored for the analysis since, in the absence of any mismatch, they do not alter the IRR result. The study is also performed for a single stage as the difference in the cases studied lies in one of the stages.

Taking advantage of the fact that the circuit is intrinsically linear, calculations are performed by applying the principle of superposition of sources, *i.e.*, each of the inputs is excited by an independent voltage source while grounding all the rest, and the value of any node is equal to the sum of the individual contribution from each source.

Usually, simplifications due to symmetry are applied to obtain these expressions; however, this method is not valid when evaluating systems with a mismatch, such as those that appear in Chapter 3 and that are detailed in Appendix D, E, and F. Consequently, both cases use the same system and notation for consistency and didactics.

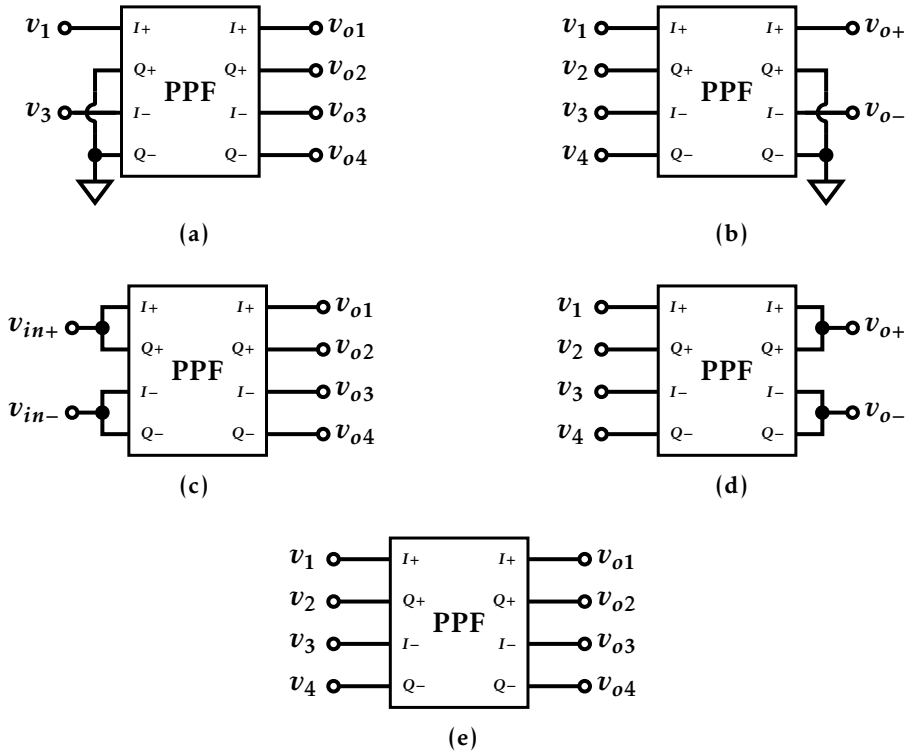

Figure C.1: Analyzed PPF configurations as filter or converter: (a) Type I, D to IQ; (b) Type I, IQ to D; (c) Type II, D to IQ; (d) Type II, IQ to D; and (e) IQ filter.

C.1 Differential to quadrature converter

By applying the superposition of sources in a general 1-stage PPF, the following equations define outputs,

$$\begin{aligned} v_{o1} &= H_1 \cdot v_1 + H_2 \cdot v_4 \\ v_{o2} &= H_1 \cdot v_2 + H_2 \cdot v_1 \\ v_{o3} &= H_1 \cdot v_3 + H_2 \cdot v_2 \\ v_{o4} &= H_1 \cdot v_4 + H_2 \cdot v_3 \end{aligned} \tag{C.1}$$

where v_n and v_{on} are, respectively, the voltages at the input and output nodes, following the terminology shown in Figure C.2. H_1 and H_2 correspond to the transfer functions of the RC and CR circuits that appear when canceling the rest of the sources, that is,

$$\begin{aligned} H_1 &= \frac{1}{1+sCR} = \frac{1}{1+jb} = \frac{1-jb}{1+b^2} \\ H_2 &= \frac{sCR}{1+sCR} = \frac{jb}{1+jb} = \frac{b(j+b)}{1+b^2} \end{aligned} \tag{C.2}$$

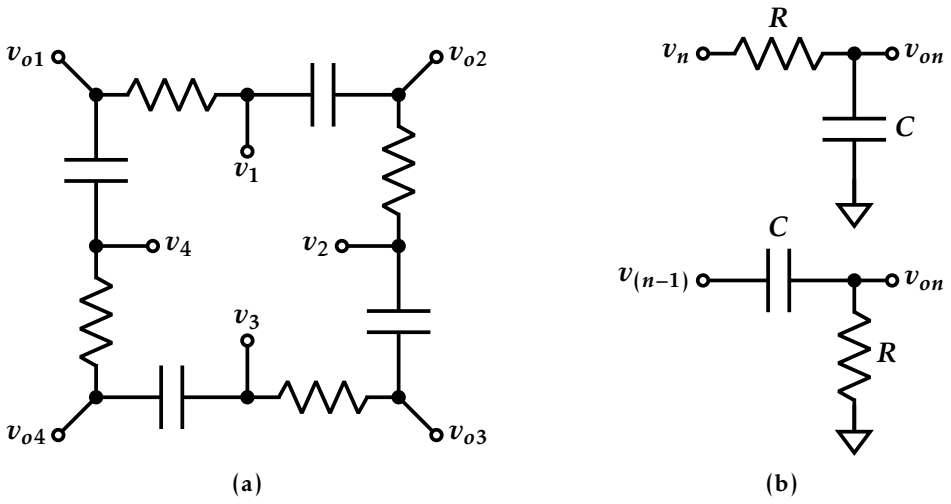

Figure C.2: 1-stage PPF representation as (a) complete schematic and (b) equivalent circuits for v_{on} assuming the source independence. Due to the cyclic nature of the topology, $n-1=0$ corresponds to v_4.

where C is the capacitance of the capacitors, R is the value of the stage resistors, and b is the value of the ωRC product. Note that b is, thus, the normalized frequency, *i.e.*, the signal frequency referred to the one the stage is tuned ($b = \omega/\omega_0$).

By definition, components I and Q at the output are $I = v_{o1} - v_{o3}$ and $Q = v_{o2} - v_{o4}$; thus, substituting and factoring out, then,

$$\begin{aligned} I &= H_1 \cdot (v_1 - v_3) - H_2 \cdot (v_2 - v_4) \\ Q &= H_1 \cdot (v_2 - v_4) + H_2 \cdot (v_1 - v_3) \end{aligned} \tag{C.3}$$

FigC.3 graphically describes these expressions. For clarity, the scheme omits subtractions in I and Q definitions.

C.1.1 Type I

A Type-I PPF implies that the differential input signal is input as the in-phase signal (I_{in}), while the quadrature input (Q_{in}) is zero. That is, $v_1 = \frac{v_{in}}{2}$, $v_3 = -\frac{v_{in}}{2}$ and $v_2 = v_4 = 0$. Therefore,

$$I = H_1 \cdot v_{in} = \frac{v_{in}}{1+jb} = \frac{1-jb}{1+b^2} \cdot v_{in} \tag{C.4}$$

$$Q = H_2 \cdot v_{in} = \frac{jb \cdot v_{in}}{1+jb} = \frac{b(j+b)}{1+b^2} \cdot v_{in} \tag{C.5}$$

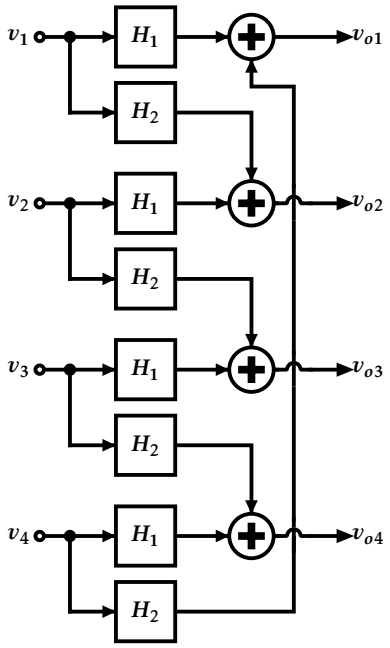

Figure C.3: Block diagram for the PPF with (differential) IQ output.

Transformation to polar form allows extracting phase and amplitude errors at the output. Thus, I is defined as

$$|I| = \frac{\sqrt{1+b^2}}{1+b^2} v_{in} = \frac{v_{in}}{\sqrt{1+b^2}} \tag{C.6}$$

$$\theta_I = \arctan \frac{-b}{1} = -\arctan b \tag{C.7}$$

while Q results on

$$|Q| = \frac{b\sqrt{1+b^2}}{1+b^2} v_{in} = \frac{b \cdot v_{in}}{\sqrt{1+b^2}} \tag{C.8}$$

$$\theta_Q = \arctan \frac{1}{b} \tag{C.9}$$

Amplitude balance (A_{BAL}) characterizes the amplitude error in the IQ signal, defined as follows,

$$A_{BAL} = \frac{|I|}{|Q|} = \frac{1}{b} \tag{C.10}$$

The phases, on the other hand, are arctangent paths with opposite signs and inverse arguments. Consequently, their subtraction is equal to $\pi/2$:

$$\arctan b + \arctan 1/b = \pi/2 \tag{C.11}$$

Phase error ($\Delta\theta$) is evaluated as the difference with $\pi/2$, thus,

$$\Delta\theta = -\frac{\pi}{2} - \theta_I + \theta_Q = 0 \Rightarrow \cos(\Delta\theta) = 1 \tag{C.12}$$

In other words, a perfect phase is obtained over the entire range with a normalized frequency-dependent amplitude error. Both amplitudes are only equal at the frequency the filter is tuned ($\omega = \omega_0$, or $b = 1$). Applying these errors to the IRR expression, (3.2),

$$IRR = \frac{1 + 2\cdot\cos(\Delta\theta)\cdot A_{BAL} + A_{BAL}^2}{1 - 2\cdot\cos(\Delta\theta)\cdot A_{BAL} + A_{BAL}^2} = \left(\frac{1 + A_{BAL}}{1 - A_{BAL}}\right)^2 = \frac{(1+b)^2}{(1-b)^2} \tag{C.13}$$

C.1.2 Type II

Type II implies that signals at I_{in} and Q_{in} are equal. The D signal is applied to both inputs. Thus, $v_1 = v_2 = \frac{v_{in}}{2}$ y $v_3 = v_4 = -\frac{v_{in}}{2}$. Under these conditions and substituting in (C.3),

$$I = (H_1 - H_2)\cdot v_{in} = \frac{1 - jb}{1 + jb}\cdot v_{in} = \frac{(1-jb)^2}{1+b^2}\cdot v_{in} \tag{C.14}$$

$$Q = (H_1 + H_2)\cdot v_{in} = \frac{1 + jb}{1 + jb}\cdot v_{in} = v_{in} \tag{C.15}$$

And calculating A_{BAL} from them,

$$A_{BAL} = \frac{|I|}{|Q|} = \frac{\left|\frac{1-jb}{1+jb}\cdot v_{in}\right|}{\left|\frac{1+jb}{1+jb}\cdot v_{in}\right|} = \frac{|1-jb|}{|1+jb|} = 1 \tag{C.16}$$

In other words, A_{BAL} does not depend on b, as I and Q signals have the same amplitude for any frequency. However, the same is not valid for phase difference,

$$\cos(\Delta\theta) = \cos\left(\frac{\pi}{2} - \theta_I + 0\right) = -\sin(\theta_I) = -\sin\left(\arctan\left(\frac{-2b}{1-b^2}\right)\right) =$$
$$= \sin\left(\arctan\left(\frac{2b}{1-b^2}\right)\right) = \frac{\frac{2b}{1-b^2}}{\sqrt{1+\left(\frac{2b}{1-b^2}\right)^2}} = \frac{2b}{1+b^2} \tag{C.17}$$

As $\sin(\arctan(x)) = \dfrac{x}{\sqrt{1+x^2}}$, then,

$$IRR = \frac{1 + 2\cdot\cos(\Delta\theta)\cdot A_{BAL} + A_{BAL}^2}{1 - 2\cdot\cos(\Delta\theta)\cdot A_{BAL} + A_{BAL}^2} =$$
$$= \frac{1+\cos(\Delta\theta)}{1-\cos(\Delta\theta)} = \frac{\left(1+b^2\right)+2b}{(1+b^2)-2b} = \frac{(1+b)^2}{(1-b)^2} \tag{C.18}$$

Again, as in the previous case, the same expression is obtained, although the limiting characteristic for the quadrature quality is distinct. While Type I enjoyed perfect phase but incorrect amplitude balance, Type II undergoes an opposite effect: I and Q amplitudes are identical, but the phase difference is only the same at $b = 1$.

C.2 Quadrature to differential converter

This use complements the previous one: the input is a quadrature signal (IQ), while the output signal is differential (D). Thus, the output signal quality depends on the power ratio of components due to the desired signal and its image (positive and negative IQ sequences, respectively). Since the load impedance is not sequence dependent,

$$IRR = \frac{P_{s+}}{P_{s-}} = \frac{|v_{s+}|^2}{|v_{s-}|^2} \tag{C.19}$$

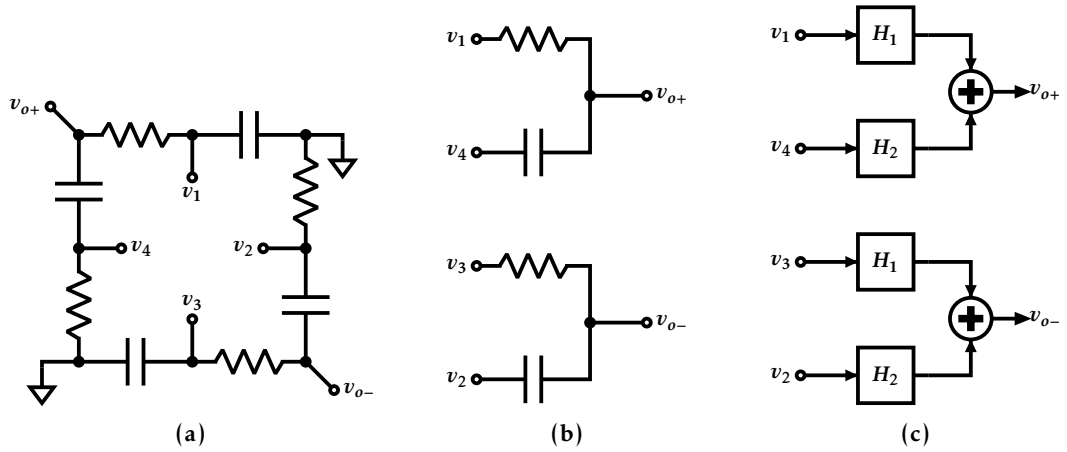

Figure C.4: PPF stage in Type I configuration for IQ to D conversion: (a) schematics; (b) equivalent subcircuits; and (c) block diagram.

C.2.1 Type I

By grounding the even outputs, the circuit is halved into two independent subcircuits (see Figure C.4). This method dramatically simplifies the analysis. Thanks to the balanced structure, the resulting diagram (Figure C.4c) can be considered a reduced version of the one presented in Figure C.3. This same balance allows the output nodes of Q to act as virtual grounds when the input is balanced and without any mismatch. Analytically, this is

$$\begin{aligned} v_{o+} &= H_1 \cdot v_1 + H_2 \cdot v_4 = \frac{v_1 + jb \cdot v_4}{1 + jb} \\ v_{o-} &= H_1 \cdot v_3 + H_2 \cdot v_2 = \frac{v_3 + jb \cdot v_2}{1 + jb} \end{aligned} \tag{C.20}$$

For the desired signal, $v_1 = \frac{v_{in}}{2}$, $v_2 = j\frac{v_{in}}{2}$, $v_3 = -\frac{v_{in}}{2}$, and $v_4 = -j\frac{v_{in}}{2}$, then,

$$v_{s+} = (v_{o+} - v_{o-})|_{s+} = \frac{1+b}{1+jb} \cdot v_{in} \Rightarrow |v_{s+}|^2 = \frac{(1+b)^2}{1+b^2} \cdot v_{in}^2 \tag{C.21}$$

On the other hand, the image implies that, $v_1 = \frac{v_{in}}{2}$, $v_2 = -j\frac{v_{in}}{2}$, $v_3 = -\frac{v_{in}}{2}$, and $v_4 = j\frac{v_{in}}{2}$, *i.e.*,

$$v_{s-} = (v_{o+} - v_{o-})|_{s-} = \frac{1-b}{1+jb} \cdot v_{in} \Rightarrow |v_{s-}|^2 = \frac{(1-b)^2}{1+b^2} \cdot v_{in}^2 \tag{C.22}$$

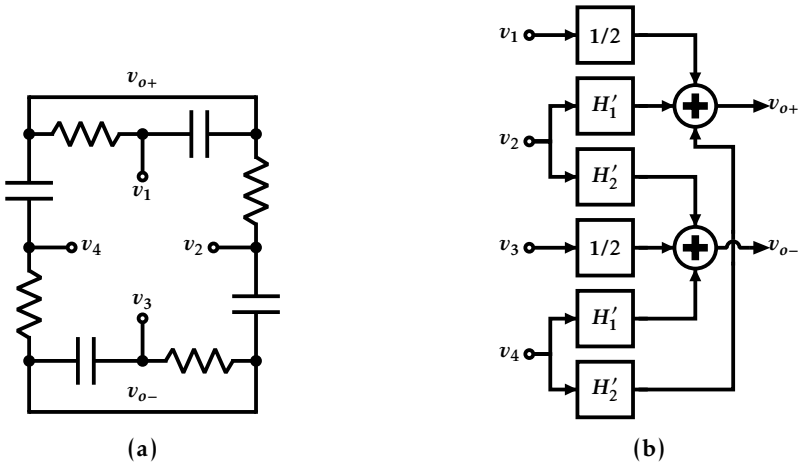

Figure C.5: PPF stage in Type II configuration for IQ to D conversion: (a) schematics and (b) block diagram.

Thus, according to (C.19), the calculated IRR is

$$IRR = \frac{|v_{s+}|^2}{|v_{s-}|^2} = \frac{(1+b)^2}{(1-b)^2} \tag{C.23}$$

The final expression is identical to previous cases.

C.2.2 Type II

The outputs are connected two by two in this configuration, as shown in Figure C.5a. The resultant topology implies different equivalent circuit than other configurations. For this case, the superposition theorem allows a description by three different sub-circuits (see Figure C.6): divider (H_0), RC with a complex load (H_1'), and CR with a complex load (H_2'). That is,

$$H_0 = \frac{R \,/\!/\, \frac{1}{sC}}{R \,/\!/\, \frac{1}{sC} + R \,/\!/\, \frac{1}{sC}} = \frac{1}{2} \tag{C.24}$$

$$H_1' = \frac{\frac{R}{1+2sCR}}{R + \frac{R}{1+2sCR}} = \frac{1}{2+2sCR} = \frac{1}{2(1+jb)} = \frac{1-jb}{2(1+b^2)} \tag{C.25}$$

$$H_2' = \frac{\frac{sCR/2}{1+sCR/2}}{1 + \frac{sCR/2}{1+sCR/2}} = \frac{sCR}{2+2sCR} = \frac{jb}{2(1+jb)} = \frac{b(j+b)}{2(1+b^2)} \tag{C.26}$$

Note that the transfer functions H_1' and H_2' are exactly half of H_1 and H_2 as an effect of the extra load elements. Figure C.5b shows the flow diagram for the new circuit.

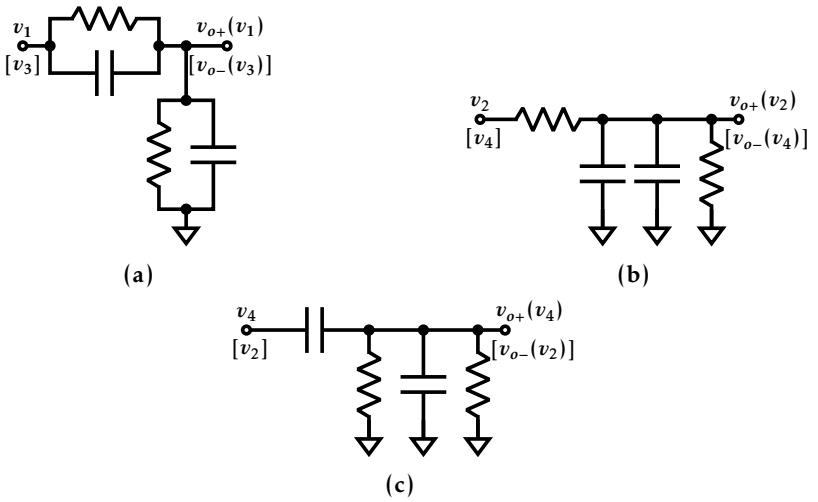

Figure C.6: Equivalent circuits describing (a) H_0; (b) H_1'; y (c) H_2'. Label with and without brackets indicate the two distinct cases for each equivalent subcircuit.

According to schematics and applying superposition of sources,

$$v_{o+} = H_0 \cdot v_1 + H_1' \cdot v_2 + H_2' \cdot v_4 = \frac{v_1}{2} + \frac{v_2}{2(1+jb)} + \frac{jb \cdot v_4}{2(1+jb)} = \\ = \frac{\left(1+b^2\right) \cdot v_1 + (1-jb) \cdot v_2 + b(j+b) \cdot v_4}{2(1+b^2)} \tag{C.27}$$

$$v_{o-} = H_0 \cdot v_3 + H_1' \cdot v_4 + H_2' \cdot v_2 = \frac{v_3}{2} + \frac{v_4}{2(1+jb)} + \frac{jb \cdot v_2}{2(1+jb)} = \\ = \frac{\left(1+b^2\right) \cdot v_3 + (1-jb) \cdot v_4 + b(j+b) \cdot v_2}{2(1+b^2)} \tag{C.28}$$

$$v_o = v_{o+} - v_{o-} = \frac{\left(1+b^2\right)(v_1 - v_3) - (b+j)^2 (v_2 - v_4)}{2(1+b^2)} \tag{C.29}$$

Being vo the output differential signal for arbitrary inputs. For a IQ input signal with positive sequence ($v_1 = \frac{v_i n}{2}$; $v_2 = j\frac{v_{in}}{2}$; $v_3 = -\frac{v_{in}}{2}$; and $v_4 = -j\frac{v_{in}}{2}$), then,

$$v_{s+} = v_o|_{s+} = \frac{\left(1+b^2\right)(v_{in}) - (b+j)^2 (jv_{in})}{2(1+b^2)} = \frac{(1+b)^2 + j\left(1-b^2\right)}{2(1+b^2)} \cdot v_{in} \tag{C.30}$$

$$|v_{s+}|^2 = \left(\frac{\sqrt{(1+b)^4 + (1-b^2)^2}}{2(1+b^2)} \right)^2 \cdot v_{in}^2 = \left(\frac{\sqrt{2(1+b)^2(1+b^2)}}{2(1+b^2)} \right)^2 \cdot v_{in}^2 = \\ = \frac{(1+b)^2}{1+b^2} \cdot \frac{v_{in}^2}{2} \tag{C.31}$$

On the other hand, the case with a negative sequence,—*i.e.*, $v_1 = \frac{v_i n}{2}$; $v_2 = -j\frac{v_i n}{2}$; $v_3 = -\frac{v_i n}{2}$; and $v_4 = \frac{v_i n}{2}$—results in

$$v_{s-} = v_o|_{s-} = \frac{\left(1+b^2\right)(v_{in}) + (b+j)^2(jv_{in})}{2(1+b^2)} = \frac{(1-b)^2 - j\left(1-b^2\right)}{2(1+b^2)} \cdot v_{in} \tag{C.32}$$

$$|v_{s-}|^2 = \left(\frac{\sqrt{(1-b)^4 + (1-b^2)^2}}{2(1+b^2)}\right)^2 \cdot v_{in}^2 = \left(\frac{\sqrt{2(1-b)^2(1+b^2)}}{2(1+b^2)}\right)^2 \cdot v_{in}^2 =$$
$$= \frac{(1-b)^2}{1+b^2} \cdot \frac{v_{in}^2}{2} \tag{C.33}$$

From both values, IRR can be calculated as

$$IRR|_{TII:IQ\to D} = \frac{|v_{s+}|^2}{|v_{s-}|^2} = \frac{(1+b)^2}{(1-b)^2} \tag{C.34}$$

Again, the same results are obtained.

C.3 Quadrature filter

The PPF has an IQ signal in this application at both input and output. Consequently, the IRR must be measured as the power balance considering the "quality" of both IQ signals. Since the connection at the output is not altered, the system behaves as described in Figure C.3.

The desired sequence implies that $v_1 = \frac{v_{in}}{2}$; $v_2 = j\frac{v_{in}}{2}$; $v_3 = -\frac{v_{in}}{2}$; and $v_4 = -j\frac{v_{in}}{2}$, therefore, substituting in (C.3),

$$I|_{s+} = (H_1 - jH_2) \cdot v_{in} = \frac{(1+b) - j\left(b+b^2\right)}{1+b^2} \cdot v_{in} = \frac{(1+b)(1-jb)}{1+b^2} \cdot v_{in} \tag{C.35}$$

$$Q|_{s+} = (jH_1 + H_2) \cdot v_{in} = \frac{(1+j) + b(j+b)}{1+b^2} \cdot v_{in} = \frac{(1+b)(j+b)}{1+b^2} \cdot v_{in} \tag{C.36}$$

Note that $A_{BAL} = 1$ due to $|1-jb| = |j+b|$. Also, the I and Q phase difference is perfect as $(1-jb)j = j+b$; thus, $\theta_I - \theta_Q = \frac{\pi}{2}$, and $\cos(\Delta\theta) = 1$. Consequently, the IQ output signal has perfect quadrature for any frequency if the input is ideal. In other words,

for this scenario, the PPF does not alter the input quadrature quality; however, it does affect the power signal as I and Q amplitudes depend on b.

As quadrature is ideal, the square of the IQ signal power is equal to the sum of squared powers of its I and Q components. As impedances are invariant to sequence, then,

$$|v_{s+}|^2 = |I|_{s+}^2 + |Q|_{s+}^2 = 2 \cdot \frac{(1+b)^2}{(1+b^2)^2}\left(1+b^2\right) \cdot v_{in}^2 = 2 \cdot \frac{(1+b)^2}{1+b^2} \cdot v_{in}^2 \tag{C.37}$$

From the sequence corresponding to the image ($v_1 = \frac{v_{in}}{2}$; $v_2 = -j\frac{v_{in}}{2}$; $v_3 = -\frac{v_{in}}{2}$; and $v_4 = j\frac{v_{in}}{2}$), and substituting in (C.3),

$$I|_{s-} = (H_1 + jH_2) \cdot v_{in} = \frac{(1-jb) + jb\,(j+b)}{1+b^2} \cdot v_{in} = \frac{(1-b)(1-jb)}{1+b^2} \cdot v_{in} \tag{C.38}$$

$$Q|_{s-} = (H_2 - jH_1) \cdot v_{in} = \frac{b\,(j+b) - j\,(1-jb)}{1+b^2} \cdot v_{in} = -\frac{(1-b)(b+j)}{1+b^2} \cdot v_{in} \tag{C.39}$$

From these values and calculating the square modules,

$$|v_{s-}|^2 = |I|_{s-}^2 + |Q|_{s-}^2 = 2 \cdot \frac{(1-b)^2}{(1+b^2)^2}\left(1+b^2\right) \cdot v_{in}^2 = 2 \cdot \frac{(1-b)^2}{1+b^2} \cdot v_{in}^2 \tag{C.40}$$

Thus, IRR is

$$IRR = \frac{|v_{s+}|^2}{|v_{s-}|^2} = \frac{(1+b)^2}{(1-b)^2} \tag{C.41}$$

Also, for this case, the IRR resulting expression is the same.

Therefore, this confirmed that the expression of the IRR is common across configurations. In other words, it is a beneficial and convenient quality factor to evaluate a PPF isolated from its particular application. Note that this is true even when the method to assess IRR changes due to input and output being D or IQ signal. Even the image definition is different from the transmission chain to reception. Nevertheless, an ideal 1-stage PPF satisfies that

$$IRR = \left(\frac{1+b}{1-b}\right)^2 = \left(\frac{\omega_0 + \omega}{\omega_0 - \omega}\right)^2 \tag{C.42}$$

where ω is the frequency and ω_0 is its tuned frequency.

Appendix D

Analysis of 1-stage PPF with worst-case mismatch

This appendix fully describes the study of the impact of the mismatch on single-stage PPF. The analyses cover the five possible configurations. For clarity, effects due to non-ideal excitations or loads are neglected. The final purpose of these calculations is to demonstrate that the limitation of the maximum achievable IRR due to mismatch is equivalent across the different configurations.

Three sections divide the appendix: Differential (D) to Quadrature Signal (IQ), IQ to D, and IQ to IQ conversion. Moreover, the first two have two subsections to separate Type-I and -II cases. The presented structure is analogous to the ideal case analysis (Appendix C).

The calculations follow three distinct steps: (1) find the relationship of IRR with mismatch and frequency, (2) find the maximum of this function, and (3) calculate the peak value. Given the complexity of the expressions and the multitude of variables, simplification requires a great deal of creativity in organizing the terms. Therefore, the analytical development has been carried out using "classical" methods (pencil and paper approach) to obtain valuable and interpretable solutions; the use of automated tools, in particular Wolfram Alpha and the Matlab symbolic library, is relegated to the representation of the curves and, with certain limitations, to obtaining the maximum of functions.

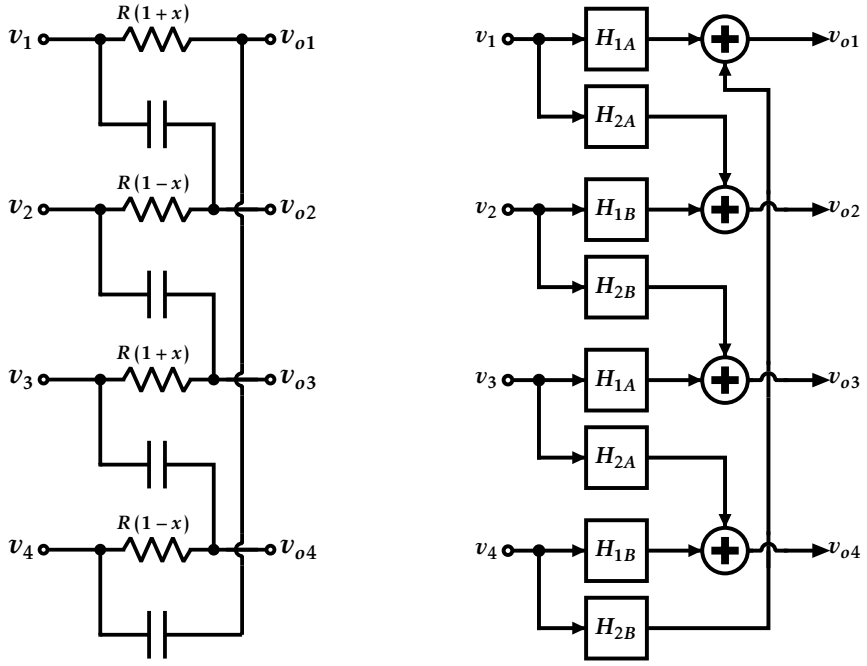

(a) Schematics **(b)** Block diagram

Figure D.1: Analyzed 1-stage PPF with the worst-case mismatch.

Each analysis supposes worst-case mismatch, determined in the main memory (Section 3.2) and shown in Figure D.1 for clarity.

D.1 Differential to quadrature conversion

In this application, the input signal is a differential signal (D), which should produce an IQ signal with the desired sequence at the output. Relationships between the amplitude and phase from I and Q evaluate the quality of the IQ signal and, thus, its IRR. Note that the result of this comparison is equivalent to the ratio between both IQ sequences (or desired and image signals if all the rest of the components are ideal).

Like the ideal case, RC and CR circuit responses describe the relationships between inputs and outputs. However, the mismatch produces two distinct versions, A or B, depending on whether a factor $(1+x)$ or $(1-x)$ multiplies the resistance value. In other

words, the new transfer functions are as follows,

$$
\begin{aligned}
H_{1A} &= \frac{1}{1+sCR(1+x)} = \frac{1}{1+jb(1+x)} = \frac{1-jb(1+x)}{1+b^2(1+x)^2} \\
H_{1B} &= \frac{1}{1+sCR(1-x)} = \frac{1}{1+jb(1-x)} = \frac{1-jb(1-x)}{1+b^2(1-x)^2} \\
H_{2A} &= \frac{sCR(1+x)}{1+sCR(1+x)} = \frac{jb(1+x)}{1+jb(1+x)} = \frac{b^2(1+x)^2+jb(1+x)}{1+b^2(1+x)^2} \\
H_{2B} &= \frac{sCR(1-x)}{1+sCR(1-x)} = \frac{jb(1-x)}{1+jb(1-x)} = \frac{b^2(1-x)^2+jb(1-x)}{1+b^2(1-x)^2}
\end{aligned}
\tag{D.1}
$$

where x is the mismatch variable and the rest of the elements follow the nomenclature shown in Appendix C.

Besides, the block diagram of Figure D.1 graphically shows these equations:

$$
\begin{aligned}
v_{o1} &= H_{1A}\cdot v_1 + H_{2A}\cdot v_4 \\
v_{o2} &= H_{1B}\cdot v_2 + H_{2B}\cdot v_1 \\
v_{o3} &= H_{1A}\cdot v_3 + H_{2A}\cdot v_2 \\
v_{o4} &= H_{1B}\cdot v_4 + H_{2B}\cdot v_3
\end{aligned}
\tag{D.2}
$$

D.1.1 Type I

As a consequence, the IQ output signal for a Type-I configuration is

$$
\left.\begin{aligned}
I &= H_{1A}\cdot(v_1-v_3) - H_{2A}\cdot(v_2-v_4) \\
Q &= H_{1B}\cdot(v_2-v_4) + H_{2B}\cdot(v_1-v_3)
\end{aligned}\right\}
\xrightarrow[v_1=-v_3=v_{in}/2;v_2=v_4=0]{TI:}
\begin{cases}
I|_{TI} = H_{1A}\cdot v_{in} \\
Q|_{TI} = H_{2B}\cdot v_{in}
\end{cases}
\tag{D.3}
$$

And transforming expressions to polar form,

$$|I| = \frac{\sqrt{1+b^2(1+x)^2}}{1+b^2(1+x)^2} = \frac{1}{\sqrt{1+b^2(1+x)^2}}$$
$$\theta_I = \arctan(-b(1+x)) \tag{D.4}$$

$$|Q| = \frac{b(1-x)\sqrt{1+b^2(1-x)^2}}{1+b^2(1-x)^2} = \frac{b(1-x)}{\sqrt{1+b^2(1-x)^2}}$$
$$\theta_Q = \arctan\left(\frac{1}{b(1-x)}\right) \tag{D.5}$$

Through the ratio of the modules, the amplitude ratio is obtained as

$$A_{BAL} = \frac{|I|}{|Q|} = \frac{1}{b(1-x)} \cdot \sqrt{\frac{1+b^2(1-x)^2}{1+b^2(1+x)^2}} \tag{D.6}$$

The phase error ($\Delta\theta$) and its corresponding cosine value are

$$\Delta\theta = -\frac{\pi}{2} - \theta_I + \theta_Q = -\frac{\pi}{2} + \arctan\frac{1+b^2(1-x^2)}{-2bx} \Rightarrow$$
$$\Rightarrow \cos(\Delta\theta) = \sin\left(\arctan\left(\frac{1+b^2(1-x^2)}{-2bx}\right)\right) = \frac{\frac{1+b^2(1-x^2)}{-2bx}}{\sqrt{1+(\frac{1+b(1-x^2)}{-2bx})^2}} =$$
$$= \frac{\frac{1+b^2(1-x^2)}{-2bx}}{\frac{\sqrt{4b^2x^2+(1+b^2(1-x^2)^2}}{-2bx}} = \frac{1+b^2(1-x^2)}{\sqrt{(1+b^2(1-x)^2)(1+b^2(1+x)^2)}} \tag{D.7}$$

Note that,

$$\arctan(a) + \arctan(b) = \arctan\left(\frac{a+b}{1-ab}\right) \tag{D.8}$$

$$\sin(\arctan(a)) = \frac{a}{\sqrt{1+a^2}} \tag{D.9}$$

From these parameters, the partial IRR, *i.e.*, the value of the IRR due to A_{BAL} and $\Delta\theta$ when the other is ideal, can be easily found (see Section 3.1.1 for more details),

$$IRR_{A_{BAL}} = \left(\frac{1 + \frac{1}{b(1-x)} \cdot \sqrt{\frac{1+b^2(1-x)^2}{1+b^2(1+x)^2}}}{1 - \frac{1}{b(1-x)} \cdot \sqrt{\frac{1+b^2(1-x)^2}{1+b^2(1+x)^2}}} \right)^2 \tag{D.10}$$

$$IRR_{\theta} = \frac{1 + \frac{1+b^2(1-x^2)}{\sqrt{(1+b^2(1-x)^2)(1+b^2(1+x)^2)}}}{1 - \frac{1+b^2(1-x^2)}{\sqrt{(1+b^2(1-x)^2)(1+b^2(1+x)^2)}}} \tag{D.11}$$

According to the $IRR_{A_{BAL}}$ and IRR_{θ} curves in Figure D.2, the global IRR is maximized at the pole of $IRR_{A_{BAL}}$ and at that point, its value is equal to IRR_{θ}. Thus, from (D.10),

$$1 = \frac{1}{b_p(1-x)} \sqrt{\frac{1+b_p^2(1-x)^2}{1+b_p^2(1+x)^2}} \Rightarrow b_p = \frac{1}{\sqrt{1-x^2}} \tag{D.12}$$

where b_p is the pole of $IRR_{A_{BAL}}$. Substituting in (D.11),

$$IRR_{max} = IRR_{\Delta\theta}(b = b_p) = \frac{1+\sqrt{1-x^2}}{1-\sqrt{1-x^2}} = \frac{\left(1+\sqrt{1-x^2}\right)^2}{x^2} \approx \frac{4}{x^2} \tag{D.13}$$

An identical result is obtained from developing the complete IRR expression. For clarity in the simplification, $a = (1+x)$ and $c = (1-x)$,

$$\begin{aligned}
IRR &= \frac{1 + 2 \cdot \frac{1}{bc} \cdot \sqrt{\frac{1+b^2c^2}{1+b^2a^2}} \cdot \frac{1+b^2ac}{\sqrt{(1+b^2a^2)(1+b^2c^2)}} + \frac{1}{b^2c^2} \cdot \frac{1+b^2c^2}{1+b^2a^2}}{1 + 2 \cdot \frac{1}{bc} \cdot \sqrt{\frac{1+b^2c^2}{1+b^2a^2}} \cdot \frac{1+b^2ac}{\sqrt{(1+b^2a^2)(1+b^2c^2)}} + \frac{1}{b^2c^2} \cdot \frac{1+b^2c^2}{1+b^2a^2}} = \\
&= \frac{1 + \frac{2}{bc} \cdot \frac{1+b^2ac}{1+b^2a^2} + \frac{1}{b^2c^2} \cdot \frac{1+b^2c^2}{1+b^2a^2}}{1 - \frac{2}{bc} \cdot \frac{1+b^2ac}{1+b^2a^2} + \frac{1}{b^2c^2} \cdot \frac{1+b^2c^2}{1+b^2a^2}} = \frac{b^2c^2\left(1+b^2a^2\right) + 2bc\left(1+b^2ac\right) + 1 + b^2c^2}{b^2c^2\left(1+b^2a^2\right) - 2bc\left(1+b^2ac\right) + 1 + b^2c^2} = \\
&= \frac{b^2c^2 + b^4a^2c^2 + 2bc + 2b^3ac^2 + 1 + b^2c^2}{b^2c^2 + b^4a^2c^2 - 2bc - 2b^3ac^2 + 1 + b^2c^2} = \\
&= \frac{\left(b^2c^2 + 2bc + 1\right) + b^2c^2\left(b^2a^2 + 2ba + 1\right)}{\left(b^2c^2 - 2bc + 1\right) + b^2c^2\left(b^2a^2 - 2ba + 1\right)} = \frac{(1+bc)^2 + b^2c^2(1+ba)^2}{(1-bc)^2 + b^2c^2(1-ba)^2} = \\
&= \frac{(1+b(1-x))^2 + b^2(1-x)^2(1+b(1+x))^2}{(1-b(1-x))^2 + b^2(1-x)^2(1-b(1+x))^2}
\end{aligned} \tag{D.14}$$

Both numerator and denominator have two terms: the first is dependent on $(1-x)$, one

of the mismatch variations, while the second is also dependent on $(1+x)$, the other variation. Note that the factor b^2 of the second term implies that when $b \ll 1$, the function resembles the ideal but is shifted by a factor $(1-x)$, and with $b \gg 1$, the similarity is with a $(1+x)$ shift. The term $b^2(1-x)^2$ cancels in numerator and denominator, assuming the second scenario.

In the central (and more interesting) region, these opposing tendencies cause a constraint to the maximum achievable value since there is no b for which the denominator becomes zero. From another perspective, the mismatch produces an error in the phase difference and, thus, it worse the PPF performance as shown by the $IRR_{\Delta\theta}$ curve (in the absence of mismatch, $IRR_{\Delta\theta}$ is infinite for the whole range of b, see (C.12).

The $IRR_{A_{BAL}}$ discrepancy due to the worst-case mismatch supposes a slight deviation of the pole position. Using the Matlab symbolic library, it can be verified that the maximum of the function (D.14) coincides with the b_p from the previous approximation. Thus,

$$
\begin{aligned}
IRR\left(b=\frac{1}{\sqrt{1-x^2}}\right) &= \frac{\left(1+\frac{\sqrt{1-x}}{\sqrt{1+x}}\right)^2+\frac{(1-x)(1-x)}{(1-x)(1+x)}\left(1+\frac{\sqrt{1+x}}{\sqrt{1-x}}\right)^2}{\left(1-\frac{\sqrt{1-x}}{\sqrt{1+x}}\right)^2+\frac{(1-x)(1-x)}{(1-x)(1+x)}\left(1-\frac{\sqrt{1+x}}{\sqrt{1-x}}\right)^2} = \\
&= \frac{\left(1+\frac{\sqrt{1-x}}{\sqrt{1+x}}\right)^2+\left(\frac{\sqrt{1-x}}{\sqrt{1+x}}+1\right)^2}{\left(1-\frac{\sqrt{1-x}}{\sqrt{1+x}}\right)^2+\left(\frac{\sqrt{1-x}}{\sqrt{1+x}}-1\right)^2} = \frac{\left(1+\frac{\sqrt{1-x}}{\sqrt{1+x}}\right)^2}{\left(1-\frac{\sqrt{1-x}}{\sqrt{1+x}}\right)^2} = \\
&= \frac{\left(\sqrt{1+x}+\sqrt{1-x}\right)^2}{\left(\sqrt{1+x}-\sqrt{1-x}\right)^2} = \frac{1+x+1-x+2\sqrt{1-x^2}}{1+x+1-x-2\sqrt{1-x^2}} = \\
&= \frac{1+\sqrt{1-x^2}}{1-\sqrt{1-x^2}}\cdot\frac{1+\sqrt{1-x^2}}{1+\sqrt{1-x^2}} = \frac{\left(1+\sqrt{1-x^2}\right)^2}{x^2} \approx \frac{4}{x^2}
\end{aligned}
\tag{D.15}
$$

Note that this development (is exact except for the approximation of the last step, which takes advantage of x) confirms the results of the previous approximation.

Figure D.2 graphically compares IRR expressions (D.10), (D.11), and (D.14), besides an ideal pole centered at $b = 1$ and vertical lines at $b = (1+x)$ and $b = (1-x)$. On the other hand, it has been observed that specific pairs of extreme deviation might cancel the slight frequency deviation of the response. Substituting $(1+x)$ and $(1-x)$ in (D.12)

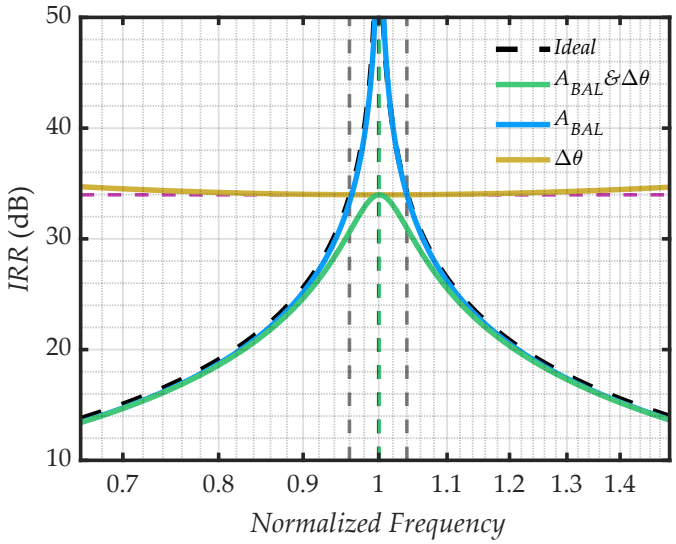

Figure D.2: Partial and complete *IRR* curves for a 1-stage Type-I PPF as D-IQ converter.

by a more general X_1 and X_2, respectively, and forcing that $b_p = 1$, then,

$$1 = \frac{1}{X_2}\sqrt{\frac{1+X_2^2}{1+X_1^2}} \Rightarrow X_2^2\left(1+X_1^2\right) = 1 + X_2^2 \Rightarrow X_1^2 X_2^2 = 1 \Rightarrow X_1 = \frac{1}{X_2} \tag{D.16}$$

In other words, the maximum value remains in $b = 1$ if the positive incremental deviation is the inverse of the negative one, *i.e.*, the $(1 + x)$ and $1/(1 + x)$ variation pairs are responsible for *IRR* limitation while neglecting the frequency shifting effect. Appendix E deeps into decomposing in these forms and its exciting implications for the mismatch analysis.

D.1.2 Type II

Regarding the Type-II configuration, the simplicity of the example for clarity hinders the proper evaluation of the case. The absence of load impedances means that the red and blue grids in Figure D.3a are necessarily at the same voltage since there is no potential difference across those elements. Consequently, the equivalent circuit is as shown in Figure D.3b. This reduction means that all relevant resistors have the same deviation; hence, it is not a mismatch effect. This effect disappears in more realistic modeling, although it would suppose additional effects adjacent stages or non-ideal sources/loads (see Section 3.1.4, especially Figure 3.13).

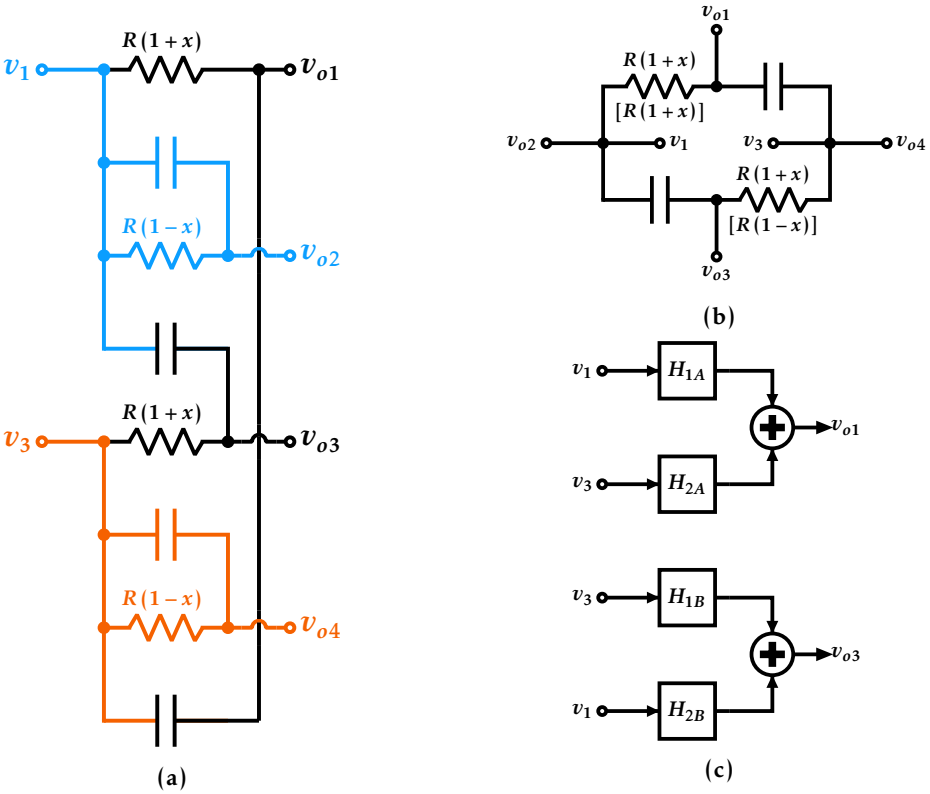

Figure D.3: Type-II 1-stage PPF in a D-IQ converter configuration with the worst-case mismatch: (a) schematics; (b) Equivalent circuit for the worst-case scenario (without brackets) and opposite variation between relevant resistors (with brackets); and (c) block diagram assuming opposite deviations.

According to the worst-case scenario, the evident and only result is a frequency shift (equivalent to the ideal case with a different R). However, it is worth considering the effect of applying a mismatch between the two relevant resistors and whether this causes a comparable impact to the mismatch combination selected as the worst-case scenario, as indicated in brackets in Figure D.3b. The diagram resulting from these considerations is presented in Figure D.3c. v_{o2} and v_{o4} are excluded as they are equal to v_1 and v_3, respectively. Considering the usual condition of balanced signals, *i.e.*, $v1 = -v3 = \frac{v_{in}}{2}$, then, $Q = v_{in}$, $|Q| = |v_{in}|$, and $\theta_Q = 0$.

On the other hand, defining now $a = \frac{1}{1+x}; c = \frac{1}{1-x}$, I is such that

$$\begin{aligned}
I &= v_{o1} - v_{o3} = (H_{1A} \cdot v_1 + H_{2A} \cdot v_3) - (H_{1B} \cdot v_3 + H_{2B} \cdot v_1) = (H_{1A} - H_{2A} + H_{1B} - H_{2B}) \cdot \frac{v_{in}}{2} = \\
&= \frac{1 - jb(1+x) - b^2(1+x)^2 - jb(1+x)}{1 + b^2(1+x)^2} \cdot \frac{v_{in}}{2} + \frac{1 - jb(1-x) - b^2(1-x)^2 - jb(1-x)}{1 + b^2(1-x)^2} \cdot \frac{v_{in}}{2} = \\
&= \frac{\left(a^2 - b^2\right)\left(c^2 + b^2\right) + \left(a^2 + b^2\right)\left(c^2 - b^2\right) - 2jb\left(ac^2 + ab^2 + ca^2 + cb^2\right)}{(a^2 + b^2)(c^2 + b^2)} \cdot \frac{v_{in}}{2} = \\
&= \frac{2\left(ac - b^2\right)\left(ac + b^2\right) - 2jb(a+c)\left(ac + b^2\right)}{(a^2 + b^2)(c^2 + b^2)} \cdot \frac{v_{in}}{2} = \\
&= \frac{ac + b^2}{(a^2 + b^2)(c^2 + b^2)} \cdot \left(\left(ac - b^2\right) - jb(a+c)\right) \cdot v_{in}
\end{aligned} \tag{D.17}$$

Consequently, A_{BAL} can be calculated as

$$\begin{aligned}
A_{BAL} = \frac{|I|}{v_{in}} &= \frac{\left(ac + b^2\right)\sqrt{\left(ac - b^2\right)^2 + b^2(a+c)^2}}{(a^2 + b^2)(c^2 + b^2)} = \\
&= \frac{\left(ac + b^2\right)\sqrt{a^2c^2 + b^4 - 2b^2ac + b^2a^2 + b^2c^2 + 2b^2ac}}{(a^2 + b^2)(c^2 + b^2)} = \\
&= \frac{\left(ac + b^2\right)\sqrt{(a^2 + b^2)(c^2 + b^2)}}{(a^2 + b^2)(c^2 + b^2)} = \frac{ac + b^2}{\sqrt{(a^2 + b^2)(c^2 + b^2)}}
\end{aligned} \tag{D.18}$$

And $\Delta\theta$ and its corresponding cosine will be

$$\Delta\theta = -\frac{\pi}{2} - \theta_I + \theta_Q = -\frac{\pi}{2} + \arctan\left(\frac{b(a+c)}{ac - b^2}\right) \tag{D.19}$$

$$\begin{aligned}
\cos(\Delta\theta) = \sin\left(\arctan\left(\frac{b(a+c)}{ac - b^2}\right)\right) &= \frac{\frac{b(a+c)}{ac - b^2}}{\sqrt{\frac{b^2(a+c)^2}{(ac - b^2)^2} + 1}} = \\
&= \frac{b(a+c)}{\sqrt{b^2(a+c)^2 + (ac - b^2)^2}} = \frac{b(a+c)}{\sqrt{(a^2 + b^2)(c^2 + b^2)}}
\end{aligned} \tag{D.20}$$

These values enable the partial IRR calculations, being

$$IRR_{A_{BAL}} = \left(\frac{1 + \frac{ac+b^2}{\sqrt{(a^2+b^2)(c^2+b^2)}}}{1 - \frac{ac+b^2}{\sqrt{(a^2+b^2)(c^2+b^2)}}} \right)^2 \tag{D.21}$$

$$IRR_{\Delta\theta} = \frac{1 + \frac{b(a+c)}{\sqrt{(a^2+b^2)(c^2+b^2)}}}{1 - \frac{b(a+c)}{\sqrt{(a^2+b^2)(c^2+b^2)}}} \tag{D.22}$$

As in the Type-I case, the pole of one of the partial expressions marks the maximum position, and the other denotes the peak value. However, for Type II, the roles of both partial $IRRs$ are reversed, with $IRR_{\Delta\theta}$ presenting the pole and $IRR_{A_{BAL}}$ being the function to be evaluated at the corresponding pole. Therefore, the pole of (D.22) appears when the denominator cancels out, *i.e.*,

$$\begin{aligned} 1 = \frac{b_p\,(a+c)}{\sqrt{\left(a^2+b_p^2\right)\left(c^2+b_p^2\right)}} \Rightarrow \left(a^2+b_p^2\right)\left(c^2+b_p^2\right) = b_p^2\,(a+c)^2 \Rightarrow \\ \Rightarrow a^2c^2 + \cancel{a^2b_p^2} + \cancel{c^2b_p^2} + b_p^4 = \cancel{a^2b_p^2} + \cancel{c^2b_p^2} + 2acb_p^2 \Rightarrow \\ \Rightarrow b_p^4 - 2acb_p^2 + a^2c^2 = \left(b_p^2 - ac\right)^2 = 0 \Rightarrow b_p = \sqrt{ac} = \frac{1}{\sqrt{1-x^2}} \end{aligned} \tag{D.23}$$

Evaluating $IRR_{A_{BAL}}$ at that point,

$$\begin{aligned} IRR_{max} = IRR_{A_{BAL}}\left(b = b_p\right) = \left(\frac{1 + \frac{ac+ac}{\sqrt{(a^2+ac)(c^2+ac)}}}{1 - \frac{ac+ac}{\sqrt{(a^2+ac)(c^2+ac)}}} \right)^2 = \\ = \left(\frac{1 + \frac{2ac}{\sqrt{ac(a+c)^2}}}{1 - \frac{2ac}{\sqrt{ac(a+c)^2}}} \right)^2 = \left(\frac{1 + \frac{2\sqrt{ac}}{a+c}}{1 - \frac{2\sqrt{ac}}{a+c}} \right)^2 = \left(\frac{a+c+2\sqrt{ac}}{a+c-2\sqrt{ac}} \right)^2 = \\ = \left(\frac{\frac{1}{1+x} + \frac{1}{1-x} + 2\sqrt{\frac{1}{1-x^2}}}{\frac{1}{1+x} + \frac{1}{1-x} - 2\sqrt{\frac{1}{1-x^2}}} \right)^2 = \left(\frac{1-x+1+x+2\sqrt{1-x^2}}{1-x+1+x-2\sqrt{1-x^2}} \right)^2 = \\ = \left(\frac{1+\sqrt{1-x^2}}{1-\sqrt{1-x^2}} \right)^2 = \left(\frac{\left(1+\sqrt{1-x^2}\right)^2}{x^2} \right)^2 \approx \left(\frac{4}{x^2} \right)^2 \end{aligned} \tag{D.24}$$

The final result is the square of the previously obtained reach. Thus, a significantly less restrictive value and too optimistic limit for the simulation results of more precise device models. In other words, the initial assumption that applying opposite mismatch to the two relevant resistances could be equivalent to the worst scenario is incorrect.

Equivalently, although more tedious, the complete IRR expression can be obtained from A_{BAL} and $\Delta\theta$,

$$
\begin{aligned}
IRR &= \frac{1+2\cdot\cos(\Delta\theta)\cdot A_{BAL}+A_{BAL}^2}{1-2\cdot\cos(\Delta\theta)\cdot A_{BAL}+A_{BAL}^2} = \\
&= \frac{1+2\cdot\frac{b(a+c)}{\sqrt{(a^2+b^2)(c^2+b^2)}}\cdot\frac{ac+b^2}{\sqrt{(a^2+b^2)(c^2+b^2)}}+\frac{\left(ac+b^2\right)^2}{(a^2+b^2)(c^2+b^2)}}{1-2\cdot\frac{b(a+c)}{\sqrt{(a^2+b^2)(c^2+b^2)}}\cdot\frac{ac+b^2}{\sqrt{(a^2+b^2)(c^2+b^2)}}+\frac{(ac+b^2)^2}{(a^2+b^2)(c^2+b^2)}} = \\
&= \frac{\left(a^2+b^2\right)\left(c^2+b^2\right)+2b\left(a+c\right)\left(ac+b^2\right)+\left(ac+b^2\right)^2}{(a^2+b^2)(c^2+b^2)-2b\left(a+c\right)(ac+b^2)+(ac+b^2)^2} = \\
&= \frac{a^2c^2+b^2a^2+b^2c^2+b^4+2ba^2c+2bac^2+2b^3a+2b^3c+b^4+a^2c^2+2b^2ac}{a^2c^2+b^2a^2+b^2c^2+b^4-2ba^2c-2bac^2-2b^3a-2b^3c+b^4+a^2c^2+2b^2ac} = \\
&= \frac{2+2b\left(\frac{1}{a}+\frac{1}{c}\right)+b^2\left(\frac{1}{a^2}+\frac{1}{c^2}+\frac{2}{ac}\right)+2b^3\left(\frac{1}{a^2c}+\frac{1}{ac^2}\right)+b^4\frac{1}{a^2c^2}}{2-2b\left(\frac{1}{a}+\frac{1}{c}\right)+b^2\left(\frac{1}{a^2}+\frac{1}{c^2}+\frac{2}{ac}\right)-2b^3\left(\frac{1}{a^2c}+\frac{1}{ac^2}\right)+b^4\frac{1}{a^2c^2}} = \\
&= \frac{2}{2}\cdot\frac{1+2b+2b^2+2b^3(1-x^2)+b^4(1-x^2)^2}{1-2b+2b^2-2b^3(1-x^2)+b^4(1-x^2)^2} = \frac{(1+b)^2+b^2\left(1+b(1-x^2)\right)^2}{(1-b)^2+b^2\left(1-b(1-x^2)\right)^2}
\end{aligned}
\tag{D.25}
$$

The first summands of both numerator and denominator correspond with the ideal expression, while the second terms are the same form altered by a variable dependent on the mismatch variable. By using automated tools for mathematical analysis (Wolfram Alpha in this case), obtaining the function maximum is trivial. This peak is found at $1/\sqrt{1-x^2}$, coinciding with the pole of $IRR_{A_{BAL}}$, which corroborates the assumption of the previous method approximation: amplitude error is canceled at that point; hence,

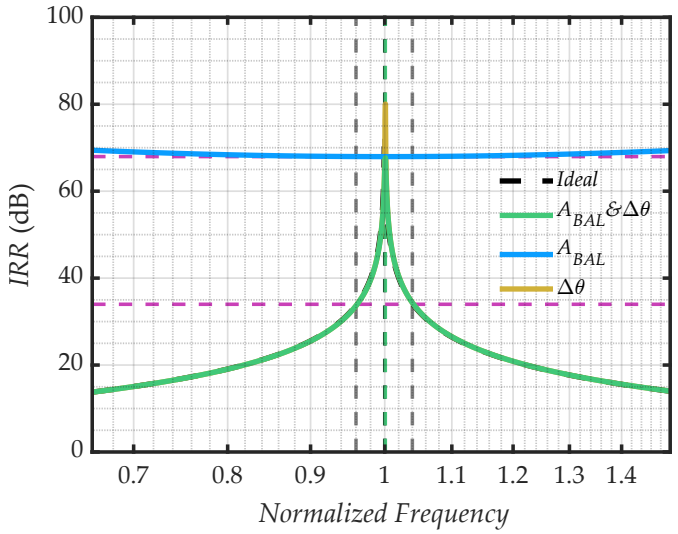

Figure D.4: Full and partial *IRR* for a Type-II PPF as D-IQ converter.

IRR limitation comes exclusively from phase error, the key premise of $IRR_{\Delta\theta}$. Therefore, evaluating at this point,

$$IRR_{max} = IRR\left(b = \frac{1}{\sqrt{1-x^2}}\right) = \frac{\left(1+\frac{1}{\sqrt{1-x^2}}\right)^2 + \frac{1}{1-x^2}\left(1+\frac{1-x^2}{\sqrt{1-x^2}}\right)^2}{\left(1-\frac{1}{\sqrt{1-x^2}}\right)^2 + \frac{1}{1-x^2}\left(1-\frac{1-x^2}{\sqrt{1-x^2}}\right)^2} =$$
$$= \frac{\left(1+\frac{1}{\sqrt{1-x^2}}\right)^2 + \left(\frac{1}{\sqrt{1-x^2}}+1\right)^2}{\left(1-\frac{1}{\sqrt{1-x^2}}\right)^2 + \left(\frac{1}{\sqrt{1-x^2}}-1\right)^2} = \left(\frac{\sqrt{1-x^2}+1}{\sqrt{1-x^2}-1}\right)^2 = \left(\frac{\left(\sqrt{1-x^2}+1\right)^2}{x^2}\right)^2 \approx \left(\frac{4}{x^2}\right)^2 \tag{D.26}$$

Figure D.4 shows the *IRR* obtained in its complete and partial form and the limit obtained from (D.26) and $4/x^2$ reference. Note that the scale on the y-axis has been enlarged with respect to Figure D.2 to include the maximum. Additionally, it is worth noting that when changing the type, the $\Delta\theta$-dependent *IRR* approaches the ideal behavior with a slight shift (the same as in the previous one). At the same time, A_{BAL} sets the achievable *IRR* limitation.

D.2 Quadrature to differential converter

This conversion is the opposite of the previous one: starting from a quadrature signal, a differential signal is generated, ideally proportional to the component in the desired

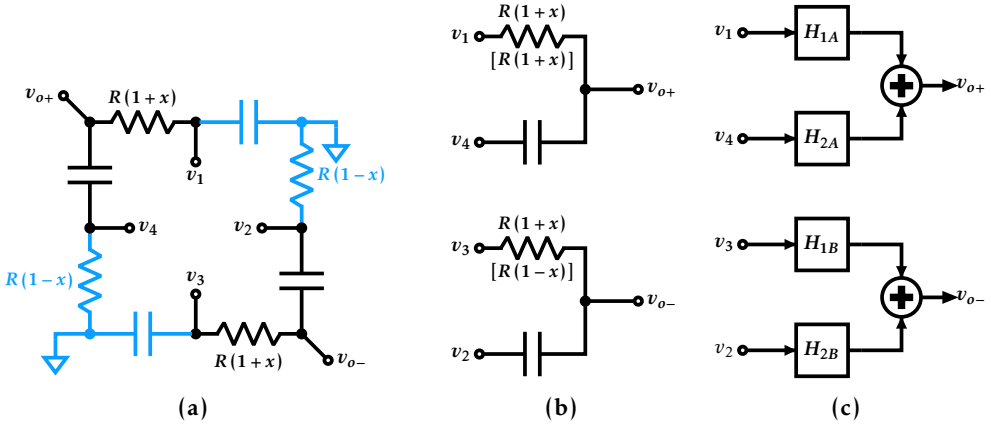

Figure D.5: 1-stage PPF in Type-I configuration as IQ-D converter: (a) schematic, the elements in blue do not influence the output vo; (b) equivalent circuit with values for the worst-case mismatch and case of opposite deviations between the relevant resistors; and (c) block diagram considering that the two resistors of the equivalent circuit suffer opposite deviations.

sequence. Then, the IRR is the ratio between the differential signal produced when the input is an ideal signal in the desired sequence and that produced by the image sequence.

D.2.1 Type I

Conversely to the other case, the effect of the worst-case mismatch is canceled in the Type-I configuration. This is represented in the schematic in Figure D.5a, where the devices in blue do not cause an impact on the ratio between the voltage at the input and output nodes. Consequently, the schematic is equivalent to the two subcircuits in Figure D.5b. Note that both relevant resistors suffer the same offset.

However, as in Type II for quadrature conversion, it is interesting to consider whether the mismatch between the resistances of interest can cause an effect similar to the worst case. This deviation is indicated in brackets in Figure D.5b. Under these conditions, the transfer functions behave as shown in the diagram in Figure D.5c. That is,

$$v_o = v_{o+} - v_{o-} = H_{1A} \cdot v_1 + H_{2A} \cdot v_4 - H_{1B} \cdot v_3 - H_{2B} \cdot v_2 \tag{D.27}$$

Considering, in addition, an input signal with the desired sequence($v_1 = -v_3 = \frac{v_{in}}{2}; v_2 = -v_4 = j\frac{v_{in}}{2}$),

$$\begin{aligned}
v_o|_{s_+} &= (H_{1A} + H_{1B} - jH_{2A} - jH_{2B})\,\frac{v_{in}}{2} = \\
&= \left(\frac{1 - jba - jb^2a^2 + ba}{1 + b^2a^2} + \frac{1 - jbc - jb^2c^2 + bc}{1 + b^2c^2}\right) \cdot \frac{v_{in}}{2} = \\
&= \left(\frac{\big(1 + ba\big)\big(1 + b^2c^2\big) + \big(1 + bc\big)\big(1 + b^2a^2\big)}{(1 + b^2a^2)(1 + b^2c^2)} - \right. \\
&\quad \left. - jb\frac{a\big(1 + ba\big)\big(1 + b^2c^2\big) + c\big(1 + bc\big)\big(1 + b^2a^2\big)}{(1 + b^2a^2)(1 + b^2c^2)}\right) \cdot \frac{v_{in}}{2} = \\
&= \frac{\big(1 + ba\big)B_2 + \big(1 + bc\big)B_1 - jb\Big(a(1 + ba)B_2 + c(1 + bc)B_1\Big)}{B_1B_2} \cdot \frac{v_{in}}{2}
\end{aligned} \tag{D.28}$$

defining for clarity, $a = (1 + x)$, $c = (1 - x)$, $B_1 = 1 + b^2a^2$, and $B_2 = 1 + b^2c^2$; and the rest of the elements have the usual meaning.

The modulus squared will therefore be

$$|v_o|^2_{s_+} = \frac{\Big((1 + ba)B_2 + (1 + bc)B_1\Big)^2 + b^2\Big(a(1 + ba)B_2 + c(1 + bc)B_1\Big)^2}{4B_1^2B_2^2} \cdot v_{in}^2 \tag{D.29}$$

Developing the numerator of this expression,

$$\begin{aligned}
&\Big((1 + ba)B_2 + (1 + bc)B_1\Big)^2 + b^2\Big(a(1 + ba)B_2 + c(1 + bc)B_1\Big)^2 = \\
&= (1 + ba)^2B_2^2 + (1 + bc)^2B_1^2 + 2(1 + ba)(1 + bc)B_1B_2 + \\
&\quad + b^2a^2(1 + ba)^2B_2^2 + b^2c^2(1 + bc)^2B_1^2 + 2b^2ac(1 + ba)(1 + bc)B_1B_2 = \\
&= (1 + ba)^2B_1B_2^2 + (1 + bc)^2B_1^2B_2 + 2(1 + b^2ac)(1 + ba)(1 + bc)B_1B_2 = \\
&= B_1B_2\Big((1 + ba)^2B_2 + (1 + bc)^2B_1 + 2(1 + b^2ac)(1 + ba)(1 + bc)\Big) = \\
&= B_1B_2(1 + ba)\Big((1 + ba)B_2 + (1 + bc)(1 + b^2ac)\Big) + \\
&\quad + B_1B_2(1 + bc)\Big((1 + ba)(1 + b^2ac) + (1 + bc)B_1\Big) = B_1B_2\,(A_1 + A_2)
\end{aligned} \tag{D.30}$$

For its part, A_1 is

$$\begin{aligned}
A_1 &= (1+ba)\Big((1+ba)\left(1+b^2c^2\right)+(1+bc)\left(1+b^2ac\right)\Big)= \\
&=\Big(1+b(1+x)\Big)\Big(\big(1+b(1+x)\big)\big(1+b^2(1-x)^2\big)+ \\
&\quad+\big(1+b(1-x)\big)\big(1+b^2\left(1-x^2\right)\big)\Big)= \\
&=\Big(1+b(1+x)\Big)\Big(1+b(1+x)+b^2(1-2x+x^2)+b^3(1-x)^2(1+x)+ \\
&\quad+1+b(1-x)+b^2(1-x^2)+b^3(1-x)^2(1+x)\Big)= \\
&=2\Big(1+b(1+x)\Big)\Big(1+b+b^2(1-x)+b^3(1-x)^2(1+x)\Big)= \\
&=2\Big(1+b(2+x)+2b^2+b^3(1-x^2)(2-x)+b^4(1+x)^2(1-x)^2\Big)
\end{aligned} \tag{D.31}$$

And A_2 results in

$$\begin{aligned}
A_2 &= (1+bc)\Big((1+bc)\left(1+b^2a^2\right)+(1+ba)\left(1+b^2ac\right)\Big)= \\
&=\Big(1+b(1-x)\Big)\Big(\big(1+b(1-x)\big)\big(1+b^2(1+x)^2\big)+ \\
&\quad+\big(1+b(1+x)\big)\big(1+b^2(1-x^2)\big)\Big)= \\
&=\Big(1+b(1-x)\Big)\Big(1+b(1-x)+b^2(1+2x+x^2)+b^3(1-x^2)(1+x)+ \\
&\quad+1+b(1+x)+b^2(1-x^2)+b^3(1-x^2)(1+x)\Big)= \\
&=2\Big(1+b(1-x)\Big)\Big(1+b+b^2(1+x)+b^3(1-x^2)(1+x)\Big)= \\
&=2\Big(1+b(2-x)+2b^2+b^3(1-x^2)(2+x)+b^4(1+x)^2(1-x)^2\Big)
\end{aligned} \tag{D.32}$$

Finally, the combination of both terms is

$$\begin{aligned}
\frac{A_1+A_2}{4} &= \frac{1}{2}\Big(1+b(2-x)+2b^2+b^3(1-x^2)(2+x)+b^4(1+x)^2(1-x)^2+ \\
&\quad+1+b(2+x)+2b^2+b^3(1-x^2)(2-x)+b^4(1+x)^2(1-x)^2\Big)= \\
&=\Big(1+2b+2b^2+2b^3(1-x^2)+b^4(1-x^2)^2\Big)= \\
&=\Big(1+2b+b^2\Big)+b^2\Big(1+2b(1-x^2)+b^2(1-x^2)^2\Big)= \\
&=(1+b)^2+b^2\Big(1+b(1-x^2)\Big)^2
\end{aligned} \tag{D.33}$$

Thus, $|v_o|^2_{s_+}$ is

$$|v_o|^2_{s_+} = \frac{\Big((1+ba)B_2+(1+bc)B_1\Big)^2 + b^2\Big(a(1+ba)B_2+c(1+bc)B_1\Big)^2}{4B_1^2B_2^2}\cdot v_{in}^2 =$$

$$= \frac{B_1B_2(A_1+A_2)}{4B_1^2B_2^2}\cdot v_{in}^2 = \frac{A_1+A_2}{4B_1B_2}\cdot v_{in}^2 = \frac{(1+b)^2+b^2\Big(1+b(1-x^2)\Big)^2}{B_1B_2}\cdot v_{in}^2 \qquad \text{(D.34)}$$

For an input IQ signal with negative sequence ($s\_$), the coefficients of (D.27) are $v_1 = -v_3 = \frac{v_{in}}{2}; v_2 = -v_4 = -j\frac{v_{in}}{2}$. Therefore, under this input, the filter output signal becomes

$$\begin{aligned} v_o|_{s\_} &= (H_{1A}+H_{1B}+jH_{2A}+jH_{2B})\frac{v_{in}}{2} = \\ &= \left(\frac{1-jba+jb^2a^2-ba}{1+b^2a^2}+\frac{1-jbc+jb^2c^2-bc}{1+b^2c^2}\right)\cdot\frac{v_{in}}{2} = \\ &= \left(\frac{\Big(1-ba\Big)\Big(1+b^2c^2\Big)+\Big(1-bc\Big)\Big(1+b^2a^2\Big)}{(1+b^2a^2)(1+b^2c^2)} - \right. \\ &\quad \left. -jb\frac{a\Big(1-ba\Big)\Big(1+b^2c^2\Big)+c\Big(1-bc\Big)\Big(1+b^2a^2\Big)}{(1+b^2a^2)(1+b^2c^2)}\right)\cdot\frac{v_{in}}{2} = \\ &= \frac{\Big(1-ba\Big)B_2+\Big(1-bc\Big)B_1-jb\Big(a(1-ba)B_2+c(1-bc)B_1\Big)}{B_1B_2}\cdot\frac{v_{in}}{2} \end{aligned} \qquad \text{(D.35)}$$

And the squared modulus is

$$|v_o|^2_{s\_} = \frac{\Big((1-ba)B_2+(1-bc)B_1\Big)^2 + b^2\Big(a(1-ba)B_2+c(1-bc)B_1\Big)^2}{4B_1^2B_2^2}\cdot v_{in}^2 =$$

$$= \frac{B_1B_2(A_1+A_2)}{4B_1^2B_2^2}\cdot v_{in}^2 = \frac{A_1+A_2}{4B_1B_2}\cdot v_{in}^2 = \frac{(1-b)^2+b^2\Big(1-b(1-x^2)\Big)^2}{B_1B_2}\cdot v_{in}^2 \qquad \text{(D.36)}$$

The mathematical development is analogous to the calculus of the positive sequence, although the sign of odd-order terms is distinct. That is,

$$\begin{aligned}
&\Big((1-ba)B_2+(1-bc)B_1\Big)^2+b^2\Big(a(1-ba)B_2+c(1-bc)B_1\Big)^2=\\
&=(1-ba)^2B_2^2+(1-bc)^2B_1^2+2(1-ba)(1-bc)B_1B_2+\\
&\quad+b^2a^2(1-ba)^2B_2^2+b^2c^2(1-bc)^2B_1^2+2b^2ac(1-ba)(1-bc)B_1B_2=\\
&=(1-ba)^2B_1B_2^2+(1-bc)^2B_1^2B_2+2(1+b^2ac)(1-ba)(1-bc)B_1B_2=\\
&=B_1B_2\Big((1-ba)^2B_2+(1-bc)^2B_1+2(1+b^2ac)(1-ba)(1-bc)\Big)=\\
&=B_1B_2(1-ba)\Big((1-ba)B_2+(1-bc)(1+b^2ac)\Big)+\\
&\quad+B_1B_2(1-bc)\Big((1-ba)(1+b^2ac)+(1-bc)B_1\Big)=B_1B_2\,(A_1'+A_2')
\end{aligned}\tag{D.37}$$

$$\begin{aligned}
A_1'&=(1-ba)\Big((1-ba)\big(1+b^2c^2\big)+(1-bc)\big(1+b^2ac\big)\Big)=\\
&=\Big(1-b\,(1+x)\Big)\Big(\big(1-b\,(1+x)\big)\big(1+b^2\,(1-x)^2\big)+\\
&\quad+\big(1-b\,(1-x)\big)\big(1+b^2\big(1-x^2\big)\big)\Big)=\\
&=\Big(1-b\,(1+x)\Big)\Big(1-b(1+x)+b^2(1-2x+x^2)-b^3(1-x)^2(1+x)+\\
&\quad+1-b(1-x)+b^2(1-x^2)-b^3(1-x)^2(1+x)\Big)=\\
&=2\Big(1-b\,(1+x)\Big)\Big(1-b+b^2\,(1-x)-b^3\,(1-x)^2\,(1+x)\Big)=\\
&=2\Big(1-b(2+x)+2b^2-b^3(1-x^2)(2-x)+b^4(1+x)^2(1-x)^2\Big)
\end{aligned}\tag{D.38}$$

$$\begin{aligned}
A_2'&=(1-bc)\Big((1-bc)\big(1+b^2a^2\big)+(1-ba)\big(1+b^2ac\big)\Big)=\\
&=\Big(1-b\,(1-x)\Big)\Big(\big(1-b\,(1-x)\big)\big(1+b^2\,(1+x)^2\big)+\\
&\quad+\big(1-b\,(1+x)\big)\big(1+b^2(1-x^2)\big)\Big)=\\
&=\Big(1-b\,(1-x)\Big)\Big(1-b\,(1-x)+b^2(1+2x+x^2)-b^3(1-x^2)\,(1+x)+\\
&\quad+1-b\,(1+x)+b^2(1-x^2)-b^3(1-x^2)\,(1+x)\Big)=\\
&=2\Big(1-b\,(1-x)\Big)\Big(1-b+b^2\,(1+x)-b^3(1-x^2)\,(1+x)\Big)=\\
&=2\Big(1-b\,(2-x)+2b^2-b^3(1-x^2)\,(2+x)+b^4\,(1+x)^2\,(1-x)^2\Big)
\end{aligned}\tag{D.39}$$

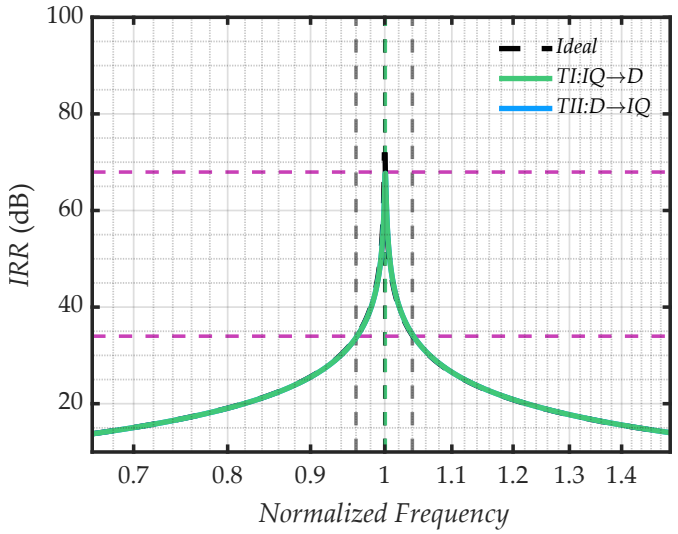

Figure D.6: *IRR* of a Type-I PPF as an IQ-D converter, compared to the inverse converter curve in Type II configuration. In magenta are shown the *IRR* value of for $4/x^2$ and $(4/x^2)^2$.

$$\begin{aligned}\frac{A_1'+A_2'}{4} =& \frac{1}{2}\Big(1-b(2-x)+2b^2-b^3(1-x^2)(2+x)+b^4(1+x)^2(1-x)^2+\\ &+1-b(2+x)+2b^2-b^3(1-x^2)(2-x)+b^4(1+x)^2(1-x)^2\Big)=\\ =&\Big(1-2b+2b^2-2b^3(1-x^2)+b^4(1-x^2)^2\Big)=\\ =&\Big(1-2b+b^2\Big)+b^2\Big(1-2b(1-x^2)+b^2(1-x^2)^2\Big)=\\ =&(1-b)^2+b^2\Big(1-b(1-x^2)\Big)^2\end{aligned} \tag{D.40}$$

Finally, since the impedance is identical for both sequences, the *IRR* expression can be obtained as the ratio between the square of the modules of v_o for both cases,

$$IRR = \frac{|v_o|^2_{s_+}}{|v_o|^2_{s_-}} = \frac{(1+b)^2+b^2\Big(1+b(1-x^2)\Big)^2}{(1-b)^2+b^2\Big(1-b(1-x^2)\Big)^2} \tag{D.41}$$

The resulting expression matches the Type II alternative case for the opposite conversion. Thus, the results are identical $IRR_{max} = \left(\frac{4}{x^2}\right)^2$, and the same conclusions can be drawn: the worst-case mismatch scenario cannot be evaluated under the imposed conditions, and the alternative mismatch combination is far from being the most restrictive case.

These conclusions are ratified in Figure D.6, which shows the results for both cases.

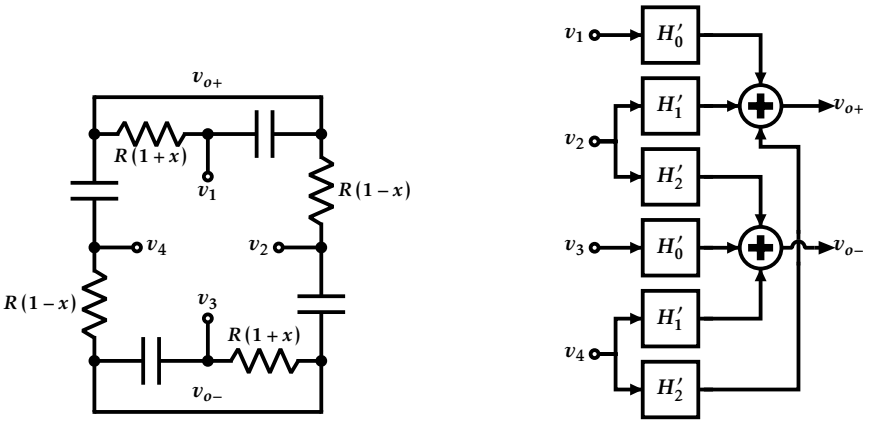

(a) Schematics **(b)** Block diagram

Figure D.7: Type-II IQ-D converter PPF.

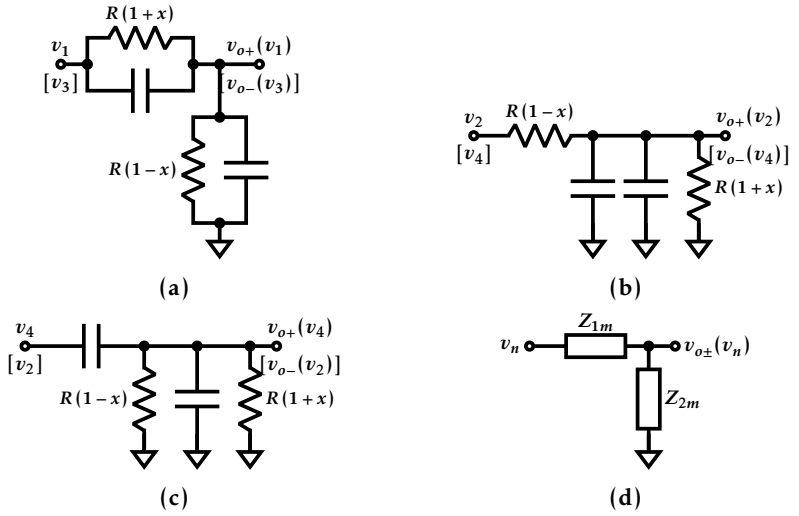

Figure D.8: Transfer function subcircuits of (a) H_0; (b) H_1'; (c) H_1'; and (d) equivalent voltage divider

D.2.2 Type II

The same method applied to Type I allows Type II calculus. In this configuration, the resulting scheme is shown in Fig D.7a. As excitation sources are independent, the system can be decomposed into the three transfer functions of the circuits of Figure D.8, organized as shown in the diagram of Figure D.7b.

Analytically, such transfer functions can be easily calculated as voltage dividers, using Z_{1m} and Z_{2m} to describe the impedances of H_m, according to the scheme in Figure D.8d. In this case, a is defined such that $a = \dfrac{1}{(1+x)(1-x)}$ and keeping the rest of the variables

with the usual meaning, then, for H_0',

$$Z_{10} = \frac{R(1+x)}{1+sCR(1+x)} \tag{D.42}$$

$$Z_{20} = \frac{R(1-x)}{1+sCR(1-x)} \tag{D.43}$$

Consequently,

$$\begin{aligned}
H_0' =& \frac{Z_{20}}{Z_{01}+Z_{20}} = \frac{\frac{\not{R}(1-x)}{1+sCR(1-x)}}{\frac{\not{R}(1-x)}{1+sCR(1-x)} + \frac{\not{R}(1+x)}{1+sCR(1+x)}} = \frac{\frac{(1-x)}{1+jb(1-x)}}{\frac{(1-x)}{1+jb(1-x)} + \frac{(1+x)}{1+jb(1+x)}} = \\
=& \frac{(1-x)}{(1-x)+(1+x)\frac{1+jb(1-x)}{1+jb(1+x)}} = \frac{(1-x)(1+jb(1+x))}{(1-x)(1+jb(1+x))+(1+x)(1+jb(1-x))} = \\
=& \frac{(1-x)(1+jb(1+x))}{\Big((1-x)+(1+x)\Big)+2jb(1+x)(1-x)} = \frac{1}{2}\cdot\frac{(1-x)(1+jb(1+x))}{1+jb(1+x)(1-x)}\cdot\frac{a}{a} = \\
=& \frac{1}{2}\cdot\frac{\frac{1}{1+x}+jb}{a+jb} = \frac{1}{2}\cdot\frac{\Big(\frac{1}{1+x}+jb\Big)\Big(a-jb\Big)}{a^2+b^2} = \frac{1}{2}\cdot\frac{\frac{a}{1+x}+b^2+jba-j\frac{b}{1+x}}{a^2+b^2}
\end{aligned} \tag{D.44}$$

On the part of H_1', the impedances are

$$Z_{11} = R(1-x) \tag{D.45}$$

$$Z_{21} = \frac{R(1+x)}{1+s2CR(1+x)} \tag{D.46}$$

Then, H_1' is

$$\begin{aligned}
H_1' =& \frac{Z_{21}}{Z_{11}+Z_{21}} = \frac{\frac{\not{R}(1-x)}{1+2sCR(1-x)}}{\frac{\not{R}(1-x)}{1+2sCR(1-x)} + \not{R}(1-x)} = \frac{(1+x)}{(1+x)+(1-x)(1+2jb(1+x))} = \\
=& \frac{(1+x)}{(1+x)+(1-x)+2jb(1+x)(1-x)}\cdot\frac{a}{a} = \frac{1}{2}\cdot\frac{\frac{1}{1-x}}{a+jb} = \frac{1}{2}\cdot\frac{\frac{a}{1-x}-j\frac{b}{1-x}}{a^2+b^2}
\end{aligned} \tag{D.47}$$

As $R(1+x) \,/\!/\, R(1-x) = \frac{R}{2a}$, H_2' impedances are

$$Z_{12} = \frac{1}{sC} \tag{D.48}$$

$$Z_{22} = \frac{\frac{R}{2a}\cdot\frac{1}{sC}}{\frac{R}{2a}+\frac{1}{sC}} = \frac{\frac{R}{2a}}{1+\frac{sCR}{2a}} \tag{D.49}$$

Thus, H_2' becomes

$$H_2' = \frac{Z_{22}}{Z_{11}+Z_{22}} = \frac{\frac{\frac{R}{2a}}{1+\frac{sCR}{2a}}}{\frac{1}{sC}+\frac{\frac{R}{2a}}{1+\frac{sCR}{2a}}} = \frac{\frac{R}{2a}}{\frac{1}{sC}+\frac{R}{2a}+\frac{R}{2a}} = \frac{sC\frac{R}{2a}}{1+sC\frac{R}{a}} =$$

$$= \frac{1}{2}\cdot\frac{sCR}{a+sCR} = \frac{1}{2}\cdot\frac{jb}{a+jb} = \frac{1}{2}\cdot\frac{jb(a-jb)}{a^2+b^2} = \frac{1}{2}\cdot\frac{b^2+jba}{a^2+b^2} \tag{D.50}$$

Applying the relationships described in the block diagram of Figure D.3c, then,

$$v_o = v_{o+} - v_{o-} = H_0\cdot v_1 + H_1'\cdot v_2 + H_2'\cdot v_4 - H_2'\cdot v_2 - H_0\cdot v_3 - H_1'\cdot v_4 =$$

$$= H_0(v_1-v_3) + H_1'(v_2-v_4) + H_2'(v4-v_2) = H_0(v_1-v_3) + (H_1'-H_2')(v_2-v_4) \tag{D.51}$$

The term $H_1' - H_2'$ can be developed as follows,

$$H_1' - H_2' = \frac{1}{2}\cdot\frac{\frac{a}{1-x} - j\frac{b}{1-x}}{a^2+b^2} - \frac{1}{2}\cdot\frac{b^2+jba}{a^2+b^2} = \frac{1}{2}\cdot\frac{\frac{a}{1-x} - b^2 - j\frac{b}{1-x} - jba}{a^2+b^2} \tag{D.52}$$

The sign of this term depends on the sign of the input signal sequence, whether it is positive ($v_1 = -v_3 = \frac{v_{in}}{2}; v_2 = -v_4 = j\frac{v_{in}}{2}$) or negative($v_1 = -v_3 = \frac{v_{in}}{2}; v_2 = -v_4 = -j\frac{v_{in}}{2}$). That is,

$$s_+ \Rightarrow j(H_1' - H_2') = \frac{1}{2}\cdot\frac{\frac{b}{1-x} + ba + j\frac{a}{1-x} - jb^2}{a^2+b^2} \tag{D.53}$$

$$s_- \Rightarrow -j(H_1' - H_2') = \frac{1}{2}\cdot\frac{-\frac{b}{1-x} - ba - j\frac{a}{1-x} + jb^2}{a^2+b^2} \tag{D.54}$$

Developing for the case of the positive sequence, the output voltage is

$$v_o|_{s_+} = \frac{\frac{a}{1+x} + b^2 + jba - j\frac{b}{1+x}}{a^2+b^2}\cdot\frac{v_{in}}{2} + \frac{\frac{b}{1-x} + ba + j\frac{a}{1-x} - jb^2}{a^2+b^2}\cdot\frac{v_{in}}{2} =$$

$$= \frac{1}{2}\cdot\left(\frac{a}{1+x} + b^2 + jba - j\frac{b}{1-x} + j\frac{a}{1-x} - jb^2 + \frac{b}{1-x} + ab\right)\cdot\frac{v_{in}}{a^2+b^2} =$$

$$= \frac{a\left(\frac{1}{1+x}+b\right) + b\left(\frac{1}{1-x}+b\right) + ja\left(\frac{1}{1-x}+b\right) - jb\left(\frac{1}{1+x}+b\right)}{2(a^2+b^2)}\cdot v_{in} =$$

$$= \frac{M}{2(a^2+b^2)}\cdot v_{in} \tag{D.55}$$

where M encapsulates the fraction numerator.

Then, the squared modulus is

$$|v_o|^2_{s_+} = \frac{1}{4} \cdot \frac{|M|^2}{(a^2+b^2)^2} \cdot v_{in}^2 \tag{D.56}$$

$|M|^2$ can be developed as

$$\begin{aligned}
|M|^2 &= \left(a\left(\frac{1}{1+x}+b\right) + b\left(\frac{1}{1-x}+b\right)\right)^2 + \left(a\left(\frac{1}{1-x}+b\right) - b\left(\frac{1}{1+x}+b\right)\right)^2 = \\
&= a^2\left(\frac{1}{1+x}+b\right)^2 + b^2\left(\frac{1}{1-x}+b\right)^2 + \cancel{2ab\left(\frac{1}{1+x}+b\right)\left(\frac{1}{1-x}+b\right)} + \\
&\quad + a^2\left(\frac{1}{1-x}+b\right)^2 + b^2\left(\frac{1}{1+x}+b\right)^2 - \cancel{2ab\left(\frac{1}{1+x}+b\right)\left(\frac{1}{1-x}+b\right)} = \\
&= \left(a^2+b^2\right)\left(\left(\frac{1}{1+x}+b\right)^2 + \left(\frac{1}{1-x}+b\right)^2 \right)
\end{aligned} \tag{D.57}$$

Substituting in (D.56),

$$\begin{aligned}
|v_o|^2_{s_+} &= \frac{1}{4} \cdot \frac{|M|^2}{(a^2+b^2)^2} \cdot v_{in}^2 = \frac{1}{4} \cdot \frac{\left(a^2+b^2\right)\left(\left(\frac{1}{1+x}+b\right)^2 + \left(\frac{1}{1-x}+b\right)^2 \right)}{(a^2+b^2)^2} \cdot v_{in}^2 = \\
&= \frac{1}{4} \cdot \frac{\left(\frac{1}{1+x}+b\right)^2 + \left(\frac{1}{1-x}+b\right)^2}{a^2+b^2} \cdot v_{in}^2
\end{aligned} \tag{D.58}$$

Obtained the positive-sequence result, the same process is carried out to calculate the output with a negative-sequence input signal:

$$\begin{aligned}
v_o|_{s_-} &= \frac{\frac{a}{1+x} + b^2 + jba - j\frac{b}{1+x}}{a^2+b^2} \cdot \frac{v_{in}}{2} - \frac{\frac{b}{1-x} + ba + j\frac{a}{1-x} - jb^2}{a^2+b^2} \cdot \frac{v_{in}}{2} = \\
&= \frac{1}{2} \cdot \left(\frac{a}{1+x} + b^2 + jba - j\frac{b}{1-x} - j\frac{a}{1-x} + jb^2 - \frac{b}{1-x} - ab \right) \cdot \frac{v_{in}}{a^2+b^2} = \\
&= \frac{a\left(\frac{1}{1+x}-b\right) + b\left(\frac{1}{1-x}-b\right) + ja\left(\frac{1}{1-x}-b\right) - jb\left(\frac{1}{1+x}-b\right)}{2\left(a^2+b^2\right)} \cdot v_{in} = \\
&= \frac{M'}{2\left(a^2+b^2\right)} \cdot v_{in}
\end{aligned} \tag{D.59}$$

Thus, the squared modulus is

$$|v_o|^2_{s_-} = \frac{1}{4} \cdot \frac{|M'|^2}{(a^2+b^2)^2} \cdot v_{in}^2 \tag{D.60}$$

And the numerator can be expanded as

$$\begin{aligned}
|M'|^2 =& \left(a\left(\frac{1}{1+x}-b\right)+b\left(\frac{1}{1-x}-b\right)\right)^2 + \left(a\left(\frac{1}{1-x}-b\right)-b\left(\frac{1}{1+x}-b\right)\right)^2 = \\
=& a^2\left(\frac{1}{1+x}-b\right)^2 + b^2\left(\frac{1}{1-x}-b\right)^2 + \cancel{2ab\left(\frac{1}{1+x}-b\right)\left(\frac{1}{1-x}-b\right)} + \\
&+ a^2\left(\frac{1}{1-x}-b\right)^2 + b^2\left(\frac{1}{1+x}-b\right)^2 - \cancel{2ab\left(\frac{1}{1+x}-b\right)\left(\frac{1}{1-x}-b\right)} = \\
=& \left(a^2+b^2\right)\left(\left(\frac{1}{1+x}-b\right)^2 + \left(\frac{1}{1-x}-b\right)^2\right)
\end{aligned} \tag{D.61}$$

Consequently, (D.60) becomes

$$\begin{aligned}
|v_o|^2_{s_-} =& \frac{1}{4} \cdot \frac{|M'|^2}{(a^2+b^2)^2} \cdot v_{in}^2 = \frac{1}{4} \cdot \frac{\left(a^2+b^2\right)\left(\left(\frac{1}{1+x}-b\right)^2 + \left(\frac{1}{1-x}-b\right)^2\right)}{(a^2+b^2)^2} \cdot v_{in}^2 = \\
=& \frac{1}{4} \cdot \frac{\left(\frac{1}{1+x}-b\right)^2 + \left(\frac{1}{1-x}-b\right)^2}{a^2+b^2} \cdot v_{in}^2
\end{aligned} \tag{D.62}$$

With $|vo|^2$ obtained for both sequences, the IRR is such that

$$IRR = \frac{|v_o|^2_{s_+}}{|v_o|^2_{s_-}} = \frac{\frac{1}{4} \cdot \frac{\left(\frac{1}{1+x}+b\right)^2+\left(\frac{1}{1-x}+b\right)^2}{a^2+b^2} \cdot v_{in}^2}{\frac{1}{4} \cdot \frac{\left(\frac{1}{1+x}-b\right)^2+\left(\frac{1}{1-x}-b\right)^2}{a^2+b^2} \cdot v_{in}^2} = \frac{\left(\frac{1}{1+x}+b\right)^2 + \left(\frac{1}{1-x}+b\right)^2}{\left(\frac{1}{1+x}-b\right)^2 + \left(\frac{1}{1-x}-b\right)^2} \tag{D.63}$$

The separate terms of the expression are similar to the ideal case, but they are duplicated, and each is affected by a different mismatch variation. This discrepancy avoids the ideal pole (there is no b such that cancels the denominator) and restricts the maximum IRR. The maximum of the function is at $b = \dfrac{\sqrt{1+x^2}}{1-x^2}$ (easily verifiable by the use

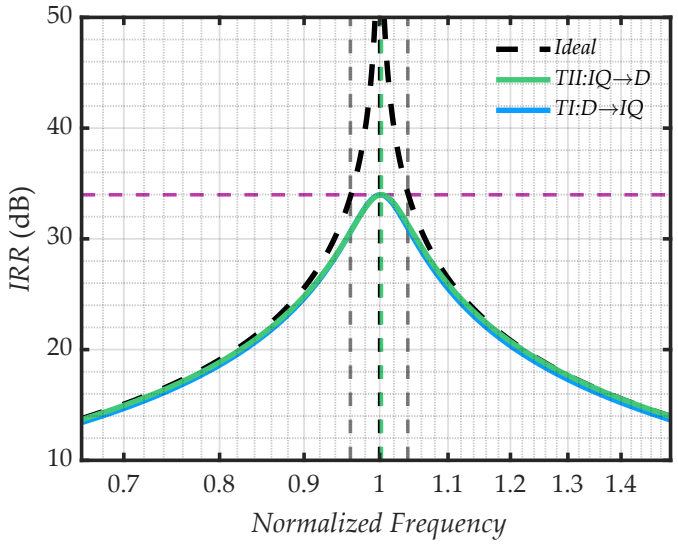

Figure D.9: *IRR* curves from a Type-II PPF stage as an IQ-D converter and a Type-I PPF stage as a D-IQ converter. The magenta dashed line shows the $4/x^2$ *IRR* limit.

of the symbolic library of Matlab), and the *IRR* value at that point is

$$
\begin{aligned}
IRR\left(b=\frac{\sqrt{1+x^2}}{1-x^2}\right) &= \frac{\left(\frac{1}{1+x}+\frac{\sqrt{1+x^2}}{1-x^2}\right)^2+\left(\frac{1}{1-x}+\frac{\sqrt{1+x^2}}{1-x^2}\right)^2}{\left(\frac{1}{1+x}-\frac{\sqrt{1+x^2}}{1-x^2}\right)^2+\left(\frac{1}{1-x}-\frac{\sqrt{1+x^2}}{1-x^2}\right)^2} = \\
&= \frac{\left(\frac{1-x+\sqrt{1+x^2}}{1-x^2}\right)^2+\left(\frac{1+x+\sqrt{1+x^2}}{1-x^2}\right)^2}{\left(\frac{1-x-\sqrt{1+x^2}}{1-x^2}\right)^2+\left(\frac{1+x-\sqrt{1+x^2}}{1-x^2}\right)^2} = \frac{\left(1-x+\sqrt{1+x^2}\right)^2+\left(1+x+\sqrt{1+x^2}\right)^2}{\left(1-x-\sqrt{1+x^2}\right)^2+\left(1+x-\sqrt{1+x^2}\right)^2} = \\
&= \frac{2+2x^2-\cancel{2x}+2\sqrt{1+x^2}-\cancel{2x\sqrt{1+x^2}}+2+2x^2+\cancel{2x}+2\sqrt{1+x^2}+\cancel{2x\sqrt{1+x^2}}}{2+2x^2-\cancel{2x}-2\sqrt{1+x^2}+\cancel{2x\sqrt{1+x^2}}+2+2x^2+\cancel{2x}-2\sqrt{1+x^2}-\cancel{2x\sqrt{1+x^2}}} = \\
&= \frac{1+x^2+\sqrt{1+x^2}}{1+x^2-\sqrt{1+x^2}} = \frac{\left(1+x^2+\sqrt{1+x^2}\right)^2}{(1+x^2)^2-1-x^2} = \\
&= \frac{\left(1+x^2\right)^2+\left(1+x^2\right)+2\left(1+x^2\right)\sqrt{1+x^2}}{x^2\left(1+x^2\right)} = \frac{1+\left(1+x^2\right)+2\sqrt{1+x^2}}{x^2} = \\
&= \frac{\left(1+\sqrt{1+x^2}\right)^2}{x^2} \approx \frac{4}{x^2}
\end{aligned}
\tag{D.64}
$$

It is again proved that the maximum achievable *IRR* is approximately $4/x^2$, verifying that the results obtained for the differential to quadrature conversion are equally applicable in the inverse transformation.

Figure D.9 graphically shows the obtained curve and the comparison with the case of D-IQ conversion with a Type-I PPF; both curves are almost entirely overlapped.

D.3 Quadrature filter

The last of the applications for a PPF assumes that both input and output are IQ signals, favoring the passage of the desired sequence and canceling the image. In this case, the IRR is calculated as the ratio between the component of the desired sequence at the output when the input one is also desired and the response to the negative sequence, considering its components in both sequences. Since no differential signals are involved, the configuration is unique, *i.e.*, there is no Type I or II.

This section does not include the circuit schematic since it is identical to the standard PPF. The diagram in Figure D.1 shows the relationships between inputs and outputs for a PPF in this configuration in the worst-case mismatch combination. For upcoming advantage, H_{1A}, H_{1B}, H_{2A} and H_{2B} expressions can be described as

$$
\begin{aligned}
H_{1A} &= \frac{1}{1+jb(1+x)} = \frac{\frac{1}{1+x}}{\frac{1}{1+x}+jb} = \frac{a}{a+jb}\cdot\frac{a-jb}{a-jb}\cdot\frac{B_2}{B_2} = \frac{a(a-jb)B_2}{B_1B_2} \\
H_{1B} &= \frac{1}{1+jb(1-x)} = \frac{\frac{1}{1-x}}{\frac{1}{1-x}+jb} = \frac{c}{c+jb}\cdot\frac{c-jb}{c-jb}\cdot\frac{B_1}{B_1} = \frac{c(c-jb)B_1}{B_1B_2} \\
H_{2A} &= \frac{jb(1+x)}{1+jb(1+x)} = \frac{jb}{a+jb}\cdot\frac{a-jb}{a-jb}\cdot\frac{B_2}{B_2} = \frac{b(b+ja)B_2}{B_1B_2} \\
H_{2B} &= \frac{jb(1-x)}{1+jb(1-x)} = \frac{jb}{c+jb}\cdot\frac{c-jb}{c-jb}\cdot\frac{B_1}{B_1} = \frac{b(b+jc)B_1}{B_1B_2}
\end{aligned}
\tag{D.65}
$$

where $a = \dfrac{1}{1+x}; c = \dfrac{1}{1-x}; B_1 = a^2+b^2; B_2 = c^2+b^2$

For this case, the definition of IRR is the power of the desired signal relative to the power of the image. Ideally, this would involve comparing the output power when the input is a signal in the desired sequence with the result from a negative-sequence input signal. However, the mismatch makes it necessary to consider two particularities:

1. The single-ended signals that compose the output IQ signal might not be orthogonal to each other. Thus, the set projection onto the ideal positive-sequence (A) component is the part of the desired signal that is actually preserved at the output. Signal power diverted to other symmetrical-sequence components is lost. Multiplication by the change of base matrix does the projection onto the desired base. Section 2.2.2 contains more details on the employed basis.

2. Not only does matter the component in the ideal negative sequence (C) component but also the leaks to A component due to mismatch impact on cancelation. Note that the image in A is fused with the desired signal and can no longer be filtered as they are in the same sequence. Thus, when analyzing the response of the IQ filter to the image (defined as the negative-sequence signal), both components (A and C) are of interest.

The weight of the output components in the ideal positive (A) and negative (C) sequences is calculated by applying the corresponding terms of the conversion matrix $\boldsymbol{T}$, shown in (2.12), to the corresponding values of v_{o1} $(+1/2)$, v_{o2} $(-j/2)$, v_{o3} $(-1/2)$ and v_{o4} $(+j/2)$. Thus, the ideal positive sequence component of the output will be:

$$\begin{aligned} v_o|_A =& \frac{v_{o1} - jv_{o2} - v_{o3} + jv_{o4}}{2} = \frac{\left(H_{1A} \cdot v_1 + H_{2A \cdot v_4}\right) - j\left(H_{1B} \cdot v_2 + H_{2B} \cdot v_1\right)}{2} + \\ &+ \frac{-\left(H_{1A} \cdot v_3 + H_{2A} \cdot v_2\right) + j\left(H_{1B} \cdot v_4 + H_{2B} \cdot v_3\right)}{2} = \\ =& \frac{H_{1A}(v_1 - v_3)}{2} + j\frac{H_{2B}(v_3 - v_1)}{2} + \frac{H_{2A}(v_4 - v_2)}{2} + j\frac{H_{1B}(v_4 - v_2)}{2} = \\ =& \frac{(H_{1A} - jH_{2B})(v_1 - v_3)}{2} - \frac{(H_{2A} + jH_{1B})(v_2 - v_4)}{2} \end{aligned} \tag{D.66}$$

Assuming further that the input is the desired signal, *i.e.*, $v_1 - v_3 = v_{in}; v_2 - v_4 = jv_{in}$, then,

$$\begin{aligned} v_o|_{A,s_+} =& \frac{(H_{1A} - jH_{2B}) \cdot v_{in}}{2} - \frac{(H_{2A} + jH_{1B}) \cdot jv_{in}}{2} = \\ =& (H_{1A} + H_{1B} - jH_{2A} - jH_{2B}) \cdot \frac{V_{in}}{2} = \\ =& \frac{a(a - jb)B_2 + c(c - jb)B_1 - jb(b + ja)B_2 - jb(b + jc)B_1}{B_1 B_2} \cdot \frac{v_{in}}{2} = \\ =& \frac{a^2 B_2 + c^2 B_1 + baB_2 + bcB_1 - jbaB_2 - jbcB_1 - jb^2 B_2 - jb^2 B_1}{B_1 B_2} \cdot \frac{v_{in}}{2} = \\ =& \frac{a(a + b)B_2 + c(c + b)B_1 - jb\Big((a + b)B_2 + (c + b)B_1\Big)}{B_1 B_2} \cdot \frac{v_{in}}{2} \end{aligned} \tag{D.67}$$

Since the comparison must be in power and the desired and image share observed impedances, the squared modulus can be used to obtain the IRR. Starting from (D.67)

and simplifying,

$$
\begin{aligned}
|v_o|^2_{A,s_+} =& \frac{\Big(a(a+b)B_2 + c(c+b)B_1\Big)^2 + b^2\Big((a+b)B_2 + (c+b)B_1\Big)^2}{B_1^2 B_2^2} \cdot \frac{v_{in}^2}{4} = \\
=& \frac{a^2(a+b)^2B_2^2 + c^2(c+b)^2B_1^2 + 2ac(a+b)(c+b)B_1B_2}{B_1^2B_2^2} \cdot \frac{v_{in}^2}{4} + \\
&+ \frac{b^2(a+b)^2B_2^2 + b^2(c+b)^2B_1^2 + 2b^2(a+b)(c+b)B_1B_2}{B_1^2B_2^2} \cdot \frac{v_{in}^2}{4} = \\
=& \frac{(a+b)^2B_2 + (c+b)^2B_1 + 2(ac+b^2)(a+b)(c+b)}{B_1B_2} \cdot \frac{v_{in}^2}{4} = \\
=& \Big((a^2+2ba+b^2)(c^2+b^2) + (c^2+2bc+b^2)(a^2+b^2) + \\
&+ 2(ac+b^2)(ac+ba+bc+b^2)\Big) \cdot \frac{v_{in}^2}{4B_1B_2} = \\
=& \Big(a^2c^2 + b^2a^2 + 2bac^2 + 2b^3a + b^2c^2 + b^4 + a^2c^2 + b^2c^2 + 2ba^2c + 2b^3c + b^2a^2 + \\
&+ b^4 + 2a^2c^2 + 2ba^2c + 2bac^2 + 2b^2ac + 2b^2ac + 2b^3a + 2b^3c + 2b^4)\Big) \cdot \frac{v_{in}^2}{4B_1B_2} = \\
=& \Big(a^2c^2 + bac^2 + ba^2c + b^2ac + \frac{b^2a^2}{2} + \frac{b^2c^2}{2} + b^3a + b^3c + b^4\Big) \cdot \frac{v_{in}^2}{B_1B_2} = \\
=& \Bigg(1 + b\Big((1+x) + (1-x)\Big) + b^2\Big(\frac{(1+x)^2}{2} + \frac{(1-x)^2}{2} + 1 - x^2\Big) + \\
&+ b^3(1-x^2)\Big((1+x) + (1-x)\Big) + b^4(1-x^2)^2\Bigg) \cdot \frac{v_{in}^2}{B_1B_2(1+x)^2(1-x)^2} = \\
=& \frac{1 + 2b + 2b^2 + 2b^3(1-x^2) + b^4(1-x^2)^2}{B_1B_2(1+x)^2(1-x)^2} \cdot v_{in}^2 = \\
=& \frac{(1+b)^2 + b^2\Big(1 + b(1-x^2)\Big)^2}{B_1B_2(1+x)^2(1-x)^2} \cdot v_{in}^2
\end{aligned}
\tag{D.68}
$$

In the last step, the second-order term (b^2) completes both binomials as the highest or lowest order summand. It is also worth remarking on the common factoring of a^2c^2 when substituting as a function of x. This unintuitive operation allows some cancelations and a more compact final result. This form is also compatible with the denominator of the IRR expression (see subsequent development).

Two summands comprise the IRR denominator, one being the component in A when the input is a negative-sequence IQ signal, *i.e.*, $v_1 - v_3 = v_{in}; v_2 - v_4 = -jv_{in}$.

Analogous to (D.66), the projection of v_o in A is such that

$$\begin{aligned} v_o|_{A,s_-} =& \frac{(H_{1A} - jH_{2B}) \cdot v_{in}}{2} + j\frac{(H_{2A} + jH_{1B}) \cdot v_{in}}{2} = \\ =& (H_{1A} - jH_{2B} + jH_{2A} - H_{1B}) \cdot \frac{V_{in}}{2} = \\ =& \frac{a^2B_2 - jbaB_2 - c^2B_1 + jbcB_1 + jb^2B_2 - baB_2 - jb^2B_1 + bcB_1}{B_1B_2} \cdot \frac{v_{in}}{2} = \\ =& \frac{a(a-b)B_2 - c(c-b)B_1 - jb(a-b)B_2 + jb(c-b)B_1}{B_1B_2} \cdot \frac{v_{in}}{2} \end{aligned} \tag{D.69}$$

And the squared modulus is, then,

$$\begin{aligned} |v_o|^2_{A,s_-} =& \frac{\Big(a(a-b)B_2 - c(c-b)B_1\Big)^2 + b^2\Big((a-b)B_2 - (c-b)B_1\Big)^2}{B_1^2B_2^2} \cdot \frac{v_{in}^2}{4} = \\ =& \frac{a^2(a-b)^2B_2^2 + c^2(c-b)^2B_1^2 - 2ac(a-b)(c-b)B_1B_2}{B_1^2B_2^2} \cdot \frac{v_{in}^2}{4} + \\ &+ \frac{b^2(a-b)^2B_2^2 + b^2(c-b)^2B_1^2 - 2b^2(a-b)(c-b)B_1B_2}{B_1^2B_2^2} \cdot \frac{v_{in}^2}{4} = \\ =& \frac{(a-b)^2B_2 + (c-b)^2B_1 - 2(ac+b^2)(a-b)(c-b)}{B_1B_2} \cdot \frac{v_{in}^2}{4} \end{aligned} \tag{D.70}$$

Note that the resulting expression might be simplified by substituting a and c in terms of x; however, this would obscure the relation with the second summand of the denominator, *i.e.*, the v_o projection in C when the input is the image,

$$\begin{aligned} v_o|_{C,s-} =& \frac{v_{o1} + jv_{o2} - v_{o3} - jv_{o4}}{2} = \frac{H_{1A} \cdot v_1 + H_{2A} \cdot v_4}{2} + j\frac{H_{1B} \cdot v_2 + H_{2B} \cdot v_1}{2} - \\ &- \frac{H_{1A} \cdot v_3 + H_{2A} \cdot v_2}{2} - j\frac{H_{1B} \cdot v_4 + H_{2B} \cdot v_3}{2} = \\ =& \frac{(H_{1A} + jH_{2B})(v_1 - v_3) - (H_{2A} - jH_{1B})(v_2 - v_4)}{2} = \\ =& (H_{1A} + H_{1B} + jH_{2A} + jH_{2B}) \cdot \frac{v_{in}}{2} = \frac{a^2B_2 - jbaB_2 + c^2B_1 - jbcB_1}{B_1B_2} \cdot \frac{v_{in}}{2} + \\ &+ \frac{-baB_2 + jb^2B_2 - bcB_1 + jb^2B_1}{B_1B_2} \cdot \frac{v_{in}}{2} = \\ =& \frac{a(a-b)B_2 + c(c-b)B_1 - jb(a-b)B_2 - jb(c-b)B_1}{B_1B_2} \cdot \frac{v_{in}}{2} \end{aligned} \tag{D.71}$$

Thus, the squared modulus is

$$
\begin{aligned}
|v_o|^2_{C,s_-} =& \frac{\Big(a(a-b)B_2 + c(c-b)B_1\Big)^2 + b^2\Big((a-b)B_2 + (c-b)B_1\Big)^2}{B_1^2 B_2^2} \cdot \frac{v_{in}^2}{4} = \\
=& \frac{a^2(a-b)^2B_2^2 + c^2(c-b)^2B_1^2 + 2ac(a-b)(c-b)B_1B_2}{B_1^2B_2^2} \cdot \frac{v_{in}^2}{4} + \\
&+ \frac{b^2(a-b)^2B_2^2 + b^2(c-b)^2B_1^2 + 2b^2(a-b)(c-b)B_1B_2}{B_1^2B_2^2} \cdot \frac{v_{in}^2}{4} = \\
=& \frac{(a-b)^2B_2 + (c-b)^2B_1 + 2(ac+b^2)(a-b)(c-b)}{B_1B_2} \cdot \frac{v_{in}^2}{4}
\end{aligned}
\tag{D.72}
$$

Expressions (D.70) and (D.72) are the summand of the mentioned *IRR* denominator. Defining D as the non-common factor, then,

$$
\begin{aligned}
D =& (a-b)^2B_2 + (c-b)^2B_1 + 2(ac+b^2)(a-b)(c-b) + \\
&+ (a-b)^2B_2 + (c-b)^2B_1 - 2(ac+b^2)(a-b)(c-b) = \\
=& 2(a-b)^2B_2 + 2(c-b)^2B_1 = 2(a^2+b^2-2ba)(c^2+b^2) + \\
&+ 2(c^2+b^2-2bc)(a^2+b^2) = 2(a^2c^2 + b^2a^2 + b^2c^2 + b^4 - 2bac^2 - \\
&- 2b^3a + a^2c^2 + b^2c^2 + b^2a^2 + b^4 - 2ba^2c - 2b^3c) = \\
=& 4(a^2c^2 - bac^2 - ba^2c + b^2a^2 + b^2c^2 - b^3a - b^3c + b^4) = \\
=& \frac{4}{(1+x)^2(1-x)^2}\Big(1 - b\Big((1+x)+(1-x)\Big) + b^2\Big((1+x)^2 + (1-x)^2\Big) - \\
&- b^3(1-x^2)\Big((1+x)+(1-x)\Big) + b^4(1-x^2)^2\Big) = \\
=& 4 \cdot \frac{1 - 2b + 2b^2(1+x^2) - 2b^3(1-x^2) + b^4(1-x^2)^2}{(1+x)^2(1-x)^2} = \\
=& 4 \cdot \frac{(1-b)^2 + b^2\Big(1 - b(1-x^2)\Big)^2 + 2b^2x^2}{(1+x)^2(1-x)^2}
\end{aligned}
\tag{D.73}
$$

And substituting calculated terms in the IRR expression,

$$\begin{aligned}
IRR &= \frac{|v_o|^2_{A,s_+}}{|v_o|^2_{A,s_-} + |v_o|^2_{C,s_-}} = \\
&= \frac{(1+b)^2 + b^2\Big(1+b(1-x^2)\Big)^2}{D} \cdot \frac{4B_1B_2}{B_1B_2(1+x)^2(1-x)^2} \cdot \frac{v_{in}^2}{v_{in}^2} = \\
&= \frac{(1+b)^2 + b^2\Big(1+b(1-x^2)\Big)^2}{(1-b)^2 + b^2\Big(1-b(1-x^2)\Big)^2 + 2b^2x^2} \cdot \frac{(1+x)^2(1-x)^2}{4} \cdot \frac{4}{(1+x)^2(1-x)^2} = \\
&= \frac{(1+b)^2 + b^2\Big(1+b(1-x^2)\Big)^2}{(1-b)^2 + b^2\Big(1-b(1-x^2)\Big)^2 + 2b^2x^2}
\end{aligned} \tag{D.74}$$

The IRR result is similar to the other cases. Moreover, computer-assisted analysis can quickly show that the function is maximized at $b = \frac{1}{\sqrt{1-x^2}}$. Thus, the maximum value is

$$\begin{aligned}
IRR\left(b = \frac{1}{\sqrt{1-x^2}}\right) &= \frac{\left(1+\frac{1}{\sqrt{1-x^2}}\right)^2 + \left(\frac{1}{\sqrt{1-x^2}}\right)^2\left(1+\frac{1}{\sqrt{1-x^2}}(1-x^2)\right)^2}{\left(1-\frac{1}{\sqrt{1-x^2}}\right)^2 + \left(\frac{1}{\sqrt{1-x^2}}\right)^2\left(1-\frac{1}{\sqrt{1-x^2}}(1-x^2)\right)^2 + 2\left(\frac{1}{\sqrt{1-x^2}}\right)^2x^2} = \\
&= \frac{\left(\sqrt{1-x^2}+1\right)^2 + \left(1+\sqrt{1-x^2}\right)^2}{\left(\sqrt{1-x^2}-1\right)^2 + \left(1-\sqrt{1-x^2}\right)^2 + 2x^2} = \\
&= \frac{\left(\sqrt{1-x^2}+1\right)^2}{\left(\sqrt{1-x^2}-1\right)^2 + x^2} = \frac{\left(\sqrt{1-x^2}+1\right)^2}{1-x^2+1-2\sqrt{1-x^2}+x^2} = \frac{1}{2}\cdot\frac{\left(\sqrt{1-x^2}+1\right)^2}{1-\sqrt{1-x^2}} = \\
&= \frac{1}{2}\cdot\frac{\left(\sqrt{1-x^2}+1\right)^3}{1-1+x^2} = \frac{1}{2}\cdot\frac{\left(\sqrt{1-x^2}+1\right)^3}{x^2} \approx \frac{1}{2}\cdot\frac{8}{x^2} = \frac{4}{x^2}
\end{aligned} \tag{D.75}$$

Once again, the IRR limit is $\frac{4}{x^2}$. As a graphical comparison, Figure D.10 shows curves of the three cases evaluated in the worst-case scenario. The IRR limit is $\frac{4}{x^2}$ for all of them, and the curves present negligible differences. Thus, the calculated IRR constraint due to mismatch is common to the different possible applications of a PPF, *QED*.

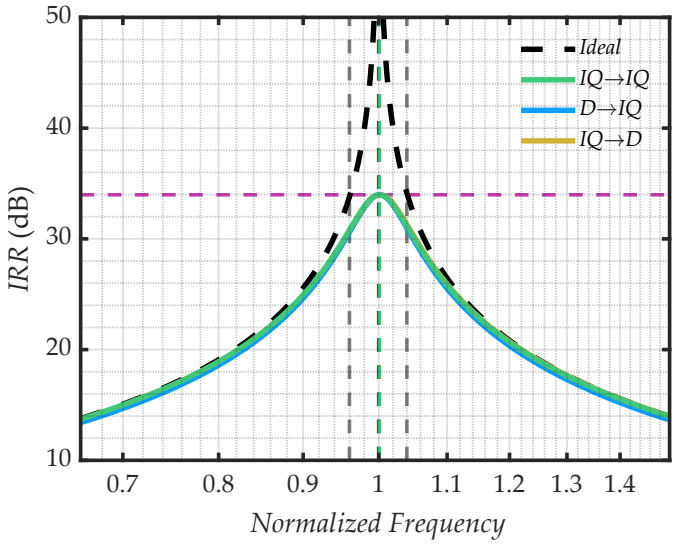

Figure D.10: *IRR* for different 1-stage PPF configurations. The three curves are almost entirely overlapped, and their peaks are $4/x^2$.

D.4 Discussion

Although the simplification process is necessarily different for each case and expressions of $IRR(b)$ are slightly distinct, the maximum achievable IRR is identical. The disparity in the dependence on b results in a minor frequency shift, which is typically negligible compared to the potential process variations, or otherwise, it can be mitigated by the same methods.

Interestingly, two configurations are not measurable under the imposed conditions: Type-II D-IQ and Type-I IQ-D converters. The particular scenario to isolate other phenomena from the directly induced mismatch effects causes those two PPFs to have negligible devices. This causes all relevant resistors to suffer the same deviation; hence, there is no mismatch but process-alike variations. Applying the only possible mismatch combination in such cases implies much less restrictive results, as a different mismatch combination is being applied (see Appendix F for more information).

Table 3.1 summarizes the results for the different configurations.

Appendix E

Alternative PPF mismatch decomposition

Conclusions of Chapter 3 mention an alternative decomposition of mismatch separately defining the two distinct degradations that PPF IRR response suffers: the pole shifting, analogous to process variations effect and the much more severe limitation on the maximum archivable IRR. This appendix focuses on the mismatch decomposition that explains each of these effects.

E.1 Redefining mismatch

Starting from equation (3.33), the $IRR_{A_{BAL}}$ maximum is where $A_{BAL} = 1$. Thus, the pole would be at $b = 1$ if $A_{BAL}(b = 1) = 1$, then the variations must meet the following condition,

$$1 = \frac{1}{X_2}\sqrt{\frac{1+X_2^2}{1+X_1^2}} \Rightarrow X_2^2\left(1+X_1^2\right) = 1+X_2^2 \Rightarrow X_1^2X_2^2 = 1 \Rightarrow X_1 = \frac{1}{X_2} \tag{E.1}$$

where X_1 and X_2 are the opposite variations (to larger and smaller values, respectively) experienced by the devices due to the mismatch.

It follows from that expression that if both variations are an inverse of each other, the maximum will not shift. This implies using $(1+y)$ and $1/(1+y)$ as the extreme variations instead of $(1+x)$ and $(1-x)$.

Moreover, a relationship between both mismatch descriptions can be established if a third common term with the form $(1+z)$ is introduced,

$$\left.\begin{aligned}(1+x) &= (1+z)\cdot(1+y)\\ (1-x) &= (1+z)/(1+y)\end{aligned}\right\} \Rightarrow \begin{cases}(1+y) = \sqrt{(1+x)/(1-x)}\\ (1+z) = \sqrt{(1+x)\cdot(1-x)}\end{cases} \tag{E.2}$$

This decomposition leads to interesting inductions. By the definition of the worst case, the maximum possible variations $(1+x)$ and $(1-x)$ are affecting the I and Q branches of the circuit, which implies varying the individual poles of each part by that factor; the global pole, in such a case, is shifted by a factor $1/(1+z)$, *i.e.*, the global pole is placed at the inverse of the geometric mean of its components (see equations (E.2) and (3.35)). This shared error due to the $(1+z)$ factor is identical in behavior to that experienced in process errors since it is a variation that alters all devices equally. Indeed, if $y = 0$, then there is no mismatch between the I and Q branches.

On the other hand, the factor $(1+y)$ describes the geometric distance to this center. It describes the mismatch from a geometric perspective instead of the typical linear approach. This dispersion causes the imperfection that limits the operation of the PPF and, thus, the IRR restriction. As intuition expected, the larger the tolerance, the more severe mismatch impact can be. Note in (E.2) that the $(1+y)$ factor will increase with more significant deviations while $(1+z)$ is not necessarily maximized in that scenario. The $(1+z)$ strictly depends on how far the geometric mean of extreme cases is from the nominal value.

Also, this explains the slight pole shift in the worst-case mismatch combination and ratifies the one selected as such (Chapter 3, Section 3.2.2). The worst-case vector is the one with a greater projection on the $(1+y)$ component, and the slight displacement is the consequence of $(1-x)$ being slightly different from $1/(1+y)$, *i.e.*, a non-zero component $(1+z)$.

Therefore, the following analyses employ the decomposition in terms of $(1+y)$ and $(1+z)$, and redefine $b' = \omega CR = b/(1+z)$, being b' the nominal PPF pole, while, for clarity, b is the actual pole after wort-case frequency shifting. Under these conditions,

the filter transfer functions are as follows:

$$
\begin{aligned}
H_{1A} &= \frac{1}{1+sCR(1+z)(1+y)} = \frac{1}{1+jb'(1+z)(1+y)} = \frac{1}{1+jb(1+y)} \\
H_{1B} &= \frac{1}{1+sCR(1+z)/(1+y)} = \frac{1}{1+jb'(1+z)/(1+y)} = \frac{1}{1+jb/(1+y)} \\
H_{2A} &= \frac{sCR(1+z)(1+y)}{1+sCR(1+z)(1+y)} = \frac{jb'(1+z)(1+y)}{1+jb'(1+z)(1+y)} = \frac{jb(1+y)}{1+jb(1+y)} \\
H_{2B} &= \frac{sCR(1+z)/(1+y)}{1+sCR(1+z)/(1+y)} = \frac{jb'(1+z)/(1+y)}{1+jb'(1+z)/(1+y)} = \frac{jb/(1+y)}{1+jb/(1+y)}
\end{aligned} \tag{E.3}
$$

E.2 D-IQ Conversion

Equivalently to the analysis in Appendix D, the following expressions describe I and Q,

$$I = H_{1A} \cdot (v_1 - v_3) - H_{2A \cdot (v_2 - v_4)} \tag{E.4}$$

$$Q = H_{1B} \cdot (v_2 - v_4) + H_{2B \cdot (v_1 - v_3)} \tag{E.5}$$

Where v_1, v_2, v_3, and v_4 are PPF inputs in the typical order.

E.2.1 Type I

Under configuration Type I conditions, *i.e.*, $v_1 = -v_3 = \frac{v_{in}}{2}$ and $v_2 = v_4 = 0$, then,

$$I = H_{1A} \cdot v_{in} = \frac{v_{in}}{1+jb(1+y)} = \frac{1-jb(1+y)}{1+b^2(1+y)^2} \cdot v_{in} \tag{E.6}$$

$$Q = H_{2B} \cdot v_{in} = \frac{jb/(1+y)}{1+jb/(1+y)} = \frac{(1+y)-jb}{(1+y)^2+b^2} \cdot jb \cdot v_{in} \tag{E.7}$$

Thus, their phase and amplitude are

$$|I| = \frac{\sqrt{1+b^2(1+y)^2}}{1+b^2(1+y)^2} = \frac{1}{\sqrt{1+b^2(1+y)^2}} \tag{E.8}$$

$$\theta_I = \arctan\left(-b(1+y)\right) \tag{E.9}$$

$$|Q| = \frac{b}{\sqrt{(1+y)^2+b^2}} \tag{E.10}$$

$$\theta_Q = \arctan\left(\frac{1+y}{b}\right) \tag{E.11}$$

Therefore,

$$A_{BAL} = \frac{1}{b}\cdot\sqrt{\frac{(1+y)^2+b^2}{1+b^2(1+y)^2}} = \sqrt{\frac{1+\frac{1}{b^2}(1+y)^2}{1+b^2(1+y)^2}} \tag{E.12}$$

$$\cos(\Delta\theta) = \frac{(1+y)(b+\frac{1}{b})}{\sqrt{\left(1+\frac{1}{b^2}(1+y)^2\right)\left(1+b^2(1+y)^2\right)}} \tag{E.13}$$

From that, IRR expression can be calculated as

$$IRR(b,y) = \frac{1+2\cdot\cos(\Delta\theta)\cdot A_{BAL}+A_{BAL}^2}{1+2\cdot\cos(\Delta\theta)\cdot A_{BAL}+A_{BAL}^2} = \frac{\left(b^2+\frac{1}{b^2}\right)(1+y)^2+2\left(b+\frac{1}{b}\right)(1+y)+2}{\left(b^2+\frac{1}{b^2}\right)(1+y)^2-2\left(b+\frac{1}{b}\right)(1+y)+2} =$$

$$= \frac{\left(1+\left(b+\frac{1}{b}\right)(1+y)\right)^2+1-2(1+y)^2}{\left(1-\left(b+\frac{1}{b}\right)(1+y)\right)^2+1-2(1+y)^2} \tag{E.14}$$

In this case, the whole IRR expression results in a much more interesting form than the original analysis, as the frequency shifting effect is removed at (E.3) substitution. The b variable is positive by definition, and the only difference between the numerator and the denominator is the sign inside their respective first term. Thus, the IRR is maximized (simultaneous maximum nominator and minimal denominator) when $b + 1/b$ is minimal. This occurs at $b = 1$, then,

$$IRR(b=1) = \frac{2(1+y)^2+4(1+y)+2}{2(1+y)^2-4(1+y)+2} = \frac{(1+y)^2+2(1+y)+1}{(1+y)^2-2(1+y)+1} = \left(\frac{(1+y)+1}{(1+y)-1}\right)^2 = \left(\frac{2+y}{y}\right)^2 \tag{E.15}$$

Substituting in terms of x:

$$\left(\frac{(1+y)+1}{(1+y)-1}\right)^2 = \left(\frac{\sqrt{\frac{1+x}{1-x}}+1}{\sqrt{\frac{1+x}{1-x}}-1}\right)^2 = \frac{1+\sqrt{1-x^2}}{1-\sqrt{1-x^2}} \tag{E.16}$$

That last term of the equation is equivalent to the one obtained in terms of $(1 \pm x)$ and approaches $4/x^2$ (like 3.38).

On the other hand, the partial IRR analyses (amplitude balance and phase difference separate effects) reach the same conclusions as Section 3.2.2.1:

$$IRR_{A_{BAL}} = \left(\frac{1+\frac{1}{b}\cdot\sqrt{\frac{(1+y)^2+b^2}{1+b^2(1+y)^2}}}{1-\frac{1}{b}\cdot\sqrt{\frac{(1+y)^2+b^2}{1+b^2(1+y)^2}}}\right)^2 = \left(\frac{b+\sqrt{\frac{(1+y)^2+b^2}{1+b^2(1+y)^2}}}{b-\sqrt{\frac{(1+y)^2+b^2}{1+b^2(1+y)^2}}}\right)^2 \tag{E.17}$$

$$IRR_{\Delta\theta} = \frac{1+\cos(\Delta\theta)}{1-\cos(\Delta\theta)} = \frac{1+\frac{(1+y)(b+\frac{1}{b})}{\sqrt{\left(1+\frac{1}{b^2}(1+y)^2\right)\left(1+b^2(1+y)^2\right)}}}{1-\frac{(1+y)(b+\frac{1}{b})}{\sqrt{\left(1+\frac{1}{b^2}(1+y)^2\right)\left(1+b^2(1+y)^2\right)}}} \tag{E.18}$$

$IRR_{A_{BAL}}$ presents a pole in $b = 1$; thus, $IRR_{\Delta\theta}(b = 1)$ equals the maximum global IRR.

E.2.2 Type II

As shown in Section 3.2.2.2 of Chapter 3, the worst mismatch combination is not applicable in this configuration. However, it can be evaluated how it behaves when another of the $\boldsymbol{M}_1$ mismatch combinations described is applied (both are equivalent to this effect).

This Type II configuration implies that $v_1 = v_2 = \frac{v_{in}}{2}$ and $v_3 = v_4 = -\frac{v_{in}}{2}$. Note that these connections mean that some elements are short-circuited and, thus, do not impact transfer functions (see Appendix D for more details). Thus, according to equivalent circuits, $Q = v_{in}$ necessarily, which, due to definitions, implies that $|Q| = |v_{in}|; \theta_Q = 0$.

On its part, I is

$$I = (H_{1A} + H_{1B} - H_{2A} - H_{2B}) \cdot \frac{v_{in}}{2} = \left(\frac{1 - jb(1+y)}{1 + b^2(1+y)^2} + \frac{1 - jb/(1+y)}{1 + b^2/(1+y)^2} \right) \cdot \frac{v_{in}}{2} =$$
$$= \frac{1 - b^4 - jb(b^2+1)\left(\frac{1}{1+y} + 1 + y\right)}{1 + b^4 + b^2\left(\frac{1}{(1+y)^2} + (1+y)^2\right)} \cdot v_{in} = (1+b^2)\frac{1 - b^2 - jb\left(\frac{1}{1+y} + 1 + y\right)}{1 + b^2\left(\frac{1}{(1+y)^2} + (1+y)^2\right) + b^4} \cdot v_{in} \quad \text{(E.19)}$$

Thus, its modulus and phase are

$$|I| = \frac{b^2 + 1}{\sqrt{1 + b^2\left(\frac{1}{(1+y)^2} + (1+y)^2\right) + b^4}} \cdot |v_{in}| = \frac{\frac{1}{b} + b}{\sqrt{\left(\frac{1}{b} - b\right)^2 + \left(\frac{1}{1+y} + 1 + y\right)^2}} \cdot |v_{in}| \quad \text{(E.20)}$$

$$\theta_I = -\arctan\left(\frac{\frac{1}{1+y} + 1 + y}{\frac{1}{b} - b} \right) \quad \text{(E.21)}$$

Then,

$$A_{BAL} = \frac{|I|}{|Q|} = \frac{\frac{1}{b} + b}{\sqrt{\left(\frac{1}{b} - b\right)^2 + \left(\frac{1}{1+y} + 1 + y\right)^2}} \quad \text{(E.22)}$$

$$\cos(\Delta\theta) = \frac{\frac{1}{1+y} + 1 + y}{\sqrt{\left(\frac{1}{b} - b\right)^2 + \left(\frac{1}{1+y} + 1 + y\right)^2}} \quad \text{(E.23)}$$

And the IRR is

$$IRR(b,y) = \frac{1 + 2 \cdot \cos(\Delta\theta) \cdot A_{BAL} + A_{BAL}^2}{1 + 2 \cdot \cos(\Delta\theta) \cdot A_{BAL} + A_{BAL}^2} =$$
$$= \frac{\left(\frac{1}{b} - b\right)^2 + \left(\frac{1}{1+y} + 1 + y\right)^2 + \left(\frac{1}{b} + b\right)^2 + 2\left(\frac{1}{b} + b\right)\left(\frac{1}{1+y}1 + y\right)}{\left(\frac{1}{b} - b\right)^2 + \left(\frac{1}{1+y} + 1 + y\right)^2 + \left(\frac{1}{b} + b\right)^2 - 2\left(\frac{1}{b} + b\right)\left(\frac{1}{1+y}1 + y\right)} =$$
$$= \frac{\left(\frac{1}{b} - b\right)^2 + \left(\frac{1}{1+y} + 1 + y + \frac{1}{b} + b\right)^2}{\left(\frac{1}{b} - b\right)^2 + \left(\frac{1}{1+y} + 1 + y - \frac{1}{b} - b\right)^2} \quad \text{(E.24)}$$

Again, the difference between both sides of the fraction lies in the sign of the $(b + 1/b)$ terms, and $b = 1$ maximizes the IRR. In other words, there is no pole shifting. Evaluating the expression at $b = 1$,

$$IRR_{max} = IRR(b = 1) = \left(\frac{y+2}{y}\right)^4 \equiv \left(\frac{1+\sqrt{1-x^2}}{1-\sqrt{1-x^2}}\right)^2 \approx \left(\frac{4}{x^2}\right)^2 \tag{E.25}$$

The result matches the equivalent conclusions from sections 3.2.2.2 and D.1.2 regarding symmetrical variations. Note that frequency shifting appears if b' is considered instead of b.

E.3 Discussion

By developing in terms of $(1+y)$ and $(1+z)$ instead of $(1 \pm x)$, it is possible to separate the two types of alteration that the IRR curve undergoes: pole shifting and maximum IRR restriction. Moreover, since the mismatch is defined by two variables (y and z), its description in terms of x also gains a degree of freedom. In other words, the maximum variation $(1+x_1)$ and the minimum variation $(1-x_2)$ need not be symmetrical. Any combination of these will have its own projection in the form of $(1+y)$ and $(1+z)$, the former being relative to the geometric center to 1 and the latter describing the existing distance. In other words, this decomposition also allows a generalization of the IRR dimensions to cover cases where the tolerance is not symmetrical.

The limitations come from the expressions themselves. While what is described is valid for the D-IQ conversion and is predictably extrapolated to its use as a quadrature filter, the shift of the IRR maximum is somewhat different in the IQ-D conversion (see Table 3.1 from Section 3.2.2.6), so it is not easy to find similar relationships. Note also that the study remains valid for the D-IQ conversion in Type II, even if instead of applying the worst case, a variation equivalent to vector 2 or 4 of $\boldsymbol{M}_1$ is used, as studied in Appendix F).

In the case of working with non-symmetric tolerances, the impact of the worst mismatch combination can be estimated as follows:

1. First, calculate the geometrical center to know the frequency shifting, *i.e.*,

$$(1+z) = \sqrt{(1+x_1)(1-x_2)} \Rightarrow b_M = \frac{1}{1+z} \tag{E.26}$$

2. Then, evaluate deviation from that geometrical center to obtain IRR restriction,

$$(1+y) = \sqrt{\frac{1+x_1}{1-x_2}} \Rightarrow IRR_{MAX} = \left(\frac{y+2}{y}\right)^2 \tag{E.27}$$

Alternatively, an opposite estimation is also possible if IRR requirements are known:

1. The following expression relates generic variations with IRR_{MAX}, establishing a restriction for variation dispersion:

$$\frac{1+x_1}{1-x_2} = \left(\frac{\sqrt{IRR_{max}}+1}{\sqrt{IRR_{max}}-1}\right)^2 \tag{E.28}$$

2. Another condition can be derived from $(1+z)$ if the maximum position (b_M) must be in a known range:

$$b_{M2} \leq (1-x_2) \leq (1+x_1) \leq b_{M1} \tag{E.29}$$

where b_{M1} and b_{M2} are the extremes of the valid frequency range for the maximum, note that x_1 and x_2 are assumed to be positive real numbers.

Appendix F

Alternative PPF mismatch combination

In this appendix, the *IRR* analysis is carried out for a one-stage PPF suffering from the mismatch combination represented by vector 2 of $\boldsymbol{M}_1$. The applied resistor mismatch and the corresponding block diagram are described in Figure F.1. This study seeks to analytically corroborate what was observed in the simulation of $\boldsymbol{M}_1$ basis vectors (see Section 3.2.1).

With a Type-I configuration for differential (D) to quadrature (IQ) conversion ($v_1 = -v_3 = \frac{v_{in}}{2}$ and $v_2 = v_4 = 0$), then, output I and Q become

$$I = (H_{1A} + H_{1B}) \cdot \frac{v_{in}}{2} \tag{F.1}$$

$$Q = (H_{2A} + H_{2B}) \cdot \frac{v_{in}}{2} \tag{F.2}$$

where H_{1A}, H_{1B}, H_{2A}, and H_{2B} are the transfer functions defined in (3.26).

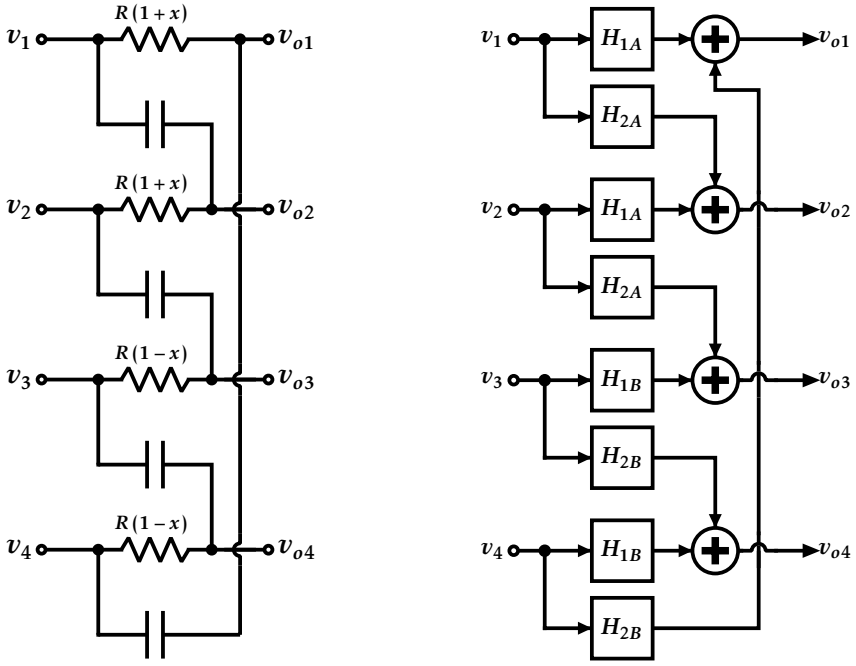

(a) Schematics **(b)** Block diagram

Figure F.1: One-stage PPF with mismatch ($\boldsymbol{M}_1$ vector 2).

By expanding (F.1), the value of I and its polar form as a function of b and x can be obtained,

$$I = \left(\frac{1}{1+jb(1+x)} + \frac{1}{1+jb(1-x)}\right)\frac{v_{in}}{2} = \frac{1+jb(1-x)+1+jb(1+x)}{\big(1+jb(1+x)\big)\big(1+jb(1+x)\big)} \cdot \frac{v_{in}}{2} =$$
$$= \frac{\big(1+jb\big)\big(1-jb(1+x)\big)\big(1-jb(1-x)\big)}{\big(1+b^2(1+x)^2\big)\big(1+b^2(1-x)^2\big)} \cdot v_{in} \tag{F.3}$$

$$|I| = \frac{\sqrt{1+b^2}\sqrt{1+b^2(1+x)^2}\sqrt{1+b^2(1-x)^2}}{\big(1+b^2(1+x)^2\big)\big(1+b^2(1-x)^2\big)} \cdot |v_{in}| =$$
$$= \frac{\sqrt{1+b^2}}{\sqrt{1+b^2(1+x)^2}\sqrt{1+b^2(1-x)^2}} \cdot |v_{in}| \tag{F.4}$$

$$\theta_I = \arctan\big(b\big) + \arctan\big(-b(1+x)\big) + \arctan\big(-b(1-x)\big) \tag{F.5}$$

In a similar method, from (F.2), the Q polar form is calculated as

$$Q = \left(\frac{jb(1+x)}{1+jb(1+x)} + \frac{jb(1-x)}{1+jb(1-x)}\right)\frac{v_{in}}{2} = jb\frac{1+x+jb(1-x^2)+1-x+jb(1-x^2)}{\Big(1+jb(1+x)\Big)\Big(1+jb(1+x)\Big)} \cdot \frac{v_{in}}{2} =$$
$$= \frac{b\Big(-b(1-x^2+j)\Big)\Big(1-jb(1+x)\Big)\Big(1-jb(1-x)\Big)}{\Big(1+b^2(1+x)^2\Big)\Big(1+b^2(1-x)^2\Big)} \cdot v_{in} \tag{F.6}$$

$$|Q| = \frac{b\sqrt{1+b^2(1-x^2)^2}}{\sqrt{1+b^2(1+x)^2}\sqrt{1+b^2(1-x)^2}} \cdot |v_{in}| \tag{F.7}$$

$$\theta_Q = \arctan\left(\frac{1}{-b(1-x^2)}\right) + \arctan\Big(-b(1+x)\Big) + \arctan\Big(-b(1-x)\Big) \tag{F.8}$$

Thus, phase error ($\Delta\theta$) is

$$\Delta\theta = -\frac{\pi}{2} - \theta_I + \theta_Q = -\frac{\pi}{2} - \arctan\Big(b\Big) + \arctan\left(\frac{1}{-b(1-x^2)}\right) =$$
$$= -\frac{\pi}{2} + \arctan\left(\frac{1+b^2(1-x^2)}{bx^2}\right) \tag{F.9}$$

Note that common terms of θ_I and θ_Q cancel each other in the subtraction and are omitted from (F.9) from simplicity. Given $\Delta\theta$, its cosine will be such that

$$\cos(\Delta\theta) = \frac{\frac{1+b^2(1-x^2)}{bx^2}}{\sqrt{1+\frac{(1+b^2(1-x^2))^2}{b^2x^4}}} = \frac{1+b^2(1-x^2)}{\sqrt{\Big(1+b^2(1-x^2)\Big)^2+b^2x^4}} \tag{F.10}$$

In the expression, it can be observed that the numerator will always be smaller than the denominator. In other words, $\cos(\Delta\theta)$ will not equal 1 for any value of b, and consequently, there is no pole in $IRR_{\Delta\theta}$.

However, the A_{BAL} case is different as

$$A_{BAL} = \frac{|I|}{|Q|} = \frac{\sqrt{1+b^2}}{b\sqrt{1+b^2(1-x^2)^2}} \tag{F.11}$$

The pole of $IRR_{A_{BAL}}$ appears when there is no amplitude error between I and Q, *i.e.*, $A_{BAL} = 1$:

$$1 = \frac{\sqrt{1 + b_M^2}}{b_M \sqrt{1 + b_M^2 (1 - x^2)^2}} \Rightarrow b_M = \frac{1}{\sqrt{1 - x^2}} \tag{F.12}$$

The displacement that appeared in other cases is obtained (see Table 3.1), consistent with the error decomposition described in Appendix E. This $IRR_{A_{BAL}}$ pole is the maximum global IRR, and since $IRR_{A_{BAL}}$ is infinite at that point, its value depends exclusively on $\Delta\theta$; and, thus, it is dependent of $IRR_{\Delta\theta}$. For simplicity, we calculate $\cos(\Delta\theta)$ at the point of interest:

$$\cos(\Delta\theta)|_{b=b_M} = \frac{1 + \frac{1-x^2}{1-x^2}}{\sqrt{\left(1 + \frac{1-x^2}{1-x^2}\right)^2 + \frac{x^4}{1-x^2}}} = \frac{2\sqrt{1-x^2}}{2-x^2} \tag{F.13}$$

And substituting in $IRR_{\Delta\theta}$ expression, then,

$$IRR_{\Delta\theta}|_{b=b_M} = \frac{1 + \frac{2\sqrt{1-x^2}}{2-x^2}}{1 - \frac{2\sqrt{1-x^2}}{2-x^2}} = \frac{2 - x^2 + 2\sqrt{1-x^2}}{2 - x^2 - 2\sqrt{1-x^2}} = \left(\frac{1 + \sqrt{1-x^2}}{1 - \sqrt{1-x^2}}\right)^2 \approx \left(\frac{4}{x^2}\right)^2 \tag{F.14}$$

Once again, expression $(4/x^2)^2$ describes the maximum guaranteed IRR for this mismatch combination. Analysis of the Type-II PPF for the D-IQ conversion (see Section 3.2.2.2) and Type-I PPF in the reverse conversion (see Section 3.2.2.3) obtain the same result. In both cases forcing both relevant resistances to be distinct implies applying an equivalent mismatch combination to the second vector of $\boldsymbol{M}_1$. Thus, this combination defines the IRR limit.

Analogously to vector 3 of $\boldsymbol{M}_1$ (worst-case combination mismatch), the different possible configurations of PPF imply an equivalent maximum IRR when vector 2 (or 4, which obtain similar results) are applied. However, these calculations are omitted due to being redundant with this Appendix and D.

Appendix G

A systematic analysis method for general PPFs

The method described below allows a systematic obtention of PPF expressions regardless of having an arbitrary number of stages, including any non-idealities, or modeling any wanted effects. This analysis is more flexible than others developed [Kau08] because it does not take advantage of symmetry; the approach is valid while the system (and its stages) remains linear.

The steps for this procedure are as follows:

1. **Obtain the Y-parameters**: an 8-port network can describe a PPF stage by an 8×8 matrix. Therefore, Z or Y parameters can outline its behavior, preferring the latter for the simplicity of their obtention. Note that other typical parameters that model networks, such as hybrid (H) or inverse hybrid (G) parameters, are exclusive to quadrupole networks; hence, they are invalid for this case.

2. **Transform the network onto a pseudo-quadrupole**: since half of the ports are input and half are output, it is possible to define the system as a quadrupole [Rev18] in which each term is a 4×4 matrix instead of a scalar. In short, the 8×8 matrix is decomposed into a 2×2 one whose terms are 4×4 matrices. This arrangement is shown in (G.1), where each matrix term of the pseudo-quadrupole has a different color.

$$\begin{pmatrix} Y_{11} & Y_{21} & Y_{31} & Y_{41} & Y_{51} & Y_{61} & Y_{71} & Y_{81} \\ Y_{12} & Y_{22} & Y_{32} & Y_{42} & Y_{52} & Y_{62} & Y_{72} & Y_{82} \\ Y_{13} & Y_{23} & Y_{33} & Y_{43} & Y_{53} & Y_{63} & Y_{73} & Y_{83} \\ Y_{14} & Y_{24} & Y_{34} & Y_{44} & Y_{54} & Y_{64} & Y_{74} & Y_{84} \\ Y_{15} & Y_{25} & Y_{35} & Y_{45} & Y_{55} & Y_{65} & Y_{75} & Y_{85} \\ Y_{16} & Y_{26} & Y_{36} & Y_{46} & Y_{56} & Y_{66} & Y_{76} & Y_{86} \\ Y_{17} & Y_{27} & Y_{37} & Y_{47} & Y_{57} & Y_{67} & Y_{77} & Y_{87} \\ Y_{18} & Y_{28} & Y_{38} & Y_{48} & Y_{58} & Y_{68} & Y_{78} & Y_{88} \end{pmatrix} \tag{G.1}$$

3. **Convert to ABCD parameters**: since the network is now a quadrupole, the matrix can be transformed into ABCD parameters, more suitable for cascade connection [Rev18].

4. **Operation**: once the ABCD parameters are obtained, the ABCD matrix of several stages emerges as the multiplication of the individual ABCD matrices.

The method does not guarantee that expressions are not overly complex. Unless a delicate process of simplification and approximation is performed, expressions hopelessly entangle design and model variables with each step. However, the strategy is a systematic procedure to obtain exact terms while being valid for any number of stages, non-idealities, loads, or excitations. The latter may imply a significant advantage in information over circuit simulation. Also, operating by resulting expression can be more computationally efficient for particular analysis and optimization methods than equivalent simulation approaches.

References

[Kau08] J. Kaukovuori, K. Stadius, J. Ryynanen, and K. Halonen. "Analysis and design of passive polyphase filters". *IEEE Transactions on Circuits and Systems I: Regular Papers* 55.10 (Nov. 2008), pp. 3023–3037. DOI: 10.1109/tcsi.2008.917990.

[Rev18] T. Reveyrand. "Multiport conversions between S, Z, Y, h, ABCD, and T parameters". *2018 International Workshop on Integrated Nonlinear Microwave and Millimetre-wave Circuits (INMMIC)*. IEEE, July 2018. DOI: 10.1109/inmmic.2018.8430023.

Appendix H

Technology device tolerances

This appendix contains tables of mismatch and process errors in resistors and capacitors of the technology used (TSMC CMOS 65 nm). The data are obtained by Monte Carlo analysis results, noting the extreme values, the mean, and the standard deviation (σ). All analyses are performed for 1000 samples, as this is the number at which the parameters converge.

On the capacitor side, the study evaluates MIM capacitors. These are much more advantageous than other alternatives in the technologies that allow their use. In the section on resistors, the variation of "*rnpolywo*" devices is studied as an example. These are unsilicided polysilicon resistors, the most commonly used in the designs made.

H.1 Capacitors

All capacitors are assumed to be square to optimize the perimeter-to-surface-area ratio. Thus, capacitance and size depend on each other. Process and mismatch variations versus them are shown in Table H.1 and Table H.2, respectively.

Capacitor mismatch variances are negligible compared to other devices or effects, being less than 1 % even for values where their impact is comparable to wire parasitics or RF MOSFET gate capacitances. Compared to resistors, there is one one-order magnitude difference. Thus, capacitors can be considered identical from a design perspective, although careful layout implementation remains critical to this effect.

On the other hand, process variations have a significant impact, with extreme cases around ±14 % error and a σ of 5 %. Notably, the process errors as a function of the sizing are almost constant. Additionally, the mean values only suffer marginal deviation from the nominal value (typical, tt) in both cases.

Columns on the left show the sizing and the expected value, while the rest of the table is the corresponding Monte Carlo analysis using the complete model. Consequently, the first estimation forgoes some parasitics—mainly due to the connections to metal layers—which are more significant in the smallest devices. Discrepancies between the expected value and the mean (last column) reveal this error level for each case.

H.2 Resistors

At the most basic level, a technology resistor has two design variables—W and L—that can influence the process and mismatch variations. Resistance depends on the W/L ratio, so there is one freedom grade to optimize other factors, such as robustness against cited non-idealities. Table H.3 and Table H.6 show the process and mismatch variations of one resistor model "*rnpolywo*"); however, other models of the technology present a similar behavior. Thus, results are easily extrapolated to them. Note that several factors (*e.g.*, availability, cost, sizing, or square resistance) affect the resistor selection in a particular design; hence, a comparison with those terms would be beyond the scope of this analysis.

The resistor width has a vast influence on the σ of process variations (Figure H.5). Submicron resistors have worse behavior, while above 2 μm, the improvement is insignificant.

Additionally, the process mean error (Figure H.4) reveals that a L clearly larger than W is highly recommended to avoid significant error, especially with lower W. This results confirms the usual recommendation for integrated resistors. Figure H.7 also exhibits a similar behavior; thus, the same approach mitigated this error for mismatch deviations.

Side	fF	Max (fF)	%	Min (fF)	%	σ (fF)	%	Mean	%
2 μm	9.47	10.79	13.6	8.1	14.7	0.48	5.06	9.5	0.32
3 μm	20.26	23.07	13.4	17.4	14.5	1	4.92	20.34	0.39
4 μm	35.08	40.03	13.7	30.01	14.7	1.7	4.83	35.2	0.34
6 μm	76.81	87.51	13.6	65.71	14.7	3.8	4.93	77.06	0.33
8 μm	134.65	153.4	13.6	115.2	14.7	6.8	5.03	135.1	0.33
10 μm	208.6	237.7	13.6	178.4	14.8	10.5	5.02	209.3	0.34
12 μm	298.6	340.5	13.7	225.5	14.7	15	5.01	299.6	0.33
14 μm	404.8	461.2	13.5	346	14.8	20.4	5.02	406.3	0.37
16 μm	527	600.7	13.6	450.9	14.7	26.6	5.03	528.8	0.34
18 μm	665.5	757.7	13.5	570	14.7	33.8	5.06	667.8	0.35
20 μm	820	933.7	13.5	702.6	14.6	41.5	5.04	822.9	0.35

Table H.1: Process variations in MIM capacitors.

Mismatch standard deviation (Figure H.8) mainly depends on the resistor area, although the improvement is not linear. An increment in area also implies larger parasitics, which might jeopardize the benefit of excessively wide resistors. Moreover, obtaining a good tradeoff between those non-idealities with opposite interests might decide the resistor type.

Side	fF	Max (fF)	%	Min (fF)	%	σ (aF)	%	Mean	%
2 μm	9.47	9.55	0.84	9.38	0.95	30	0.32	9.47	0
3 μm	20.26	20.45	0.84	20.13	0.74	42	0.21	20.28	0.10
4 μm	35.08	35.27	0.46	34.93	0.51	50.5	0.14	35.11	0.09
6 μm	76.81	77.05	0.29	76.57	0.34	76	0.10	76.83	0.03
8 μm	134.65	135	0.22	134.3	0.30	99	0.07	134.7	0.04
10 μm	208.6	209	0.19	208.3	0.14	123	0.06	208.6	0
12 μm	298.6	299.2	0.17	298.3	0.13	152	0.05	298.7	0.03
14 μm	404.8	406	0.10	405.1	0.12	171	0.04	405.6	0.20
16 μm	527	527.8	0.11	526.4	0.15	206	0.04	527.2	0.04
18 μm	665.5	666.7	0.12	665.2	0.11	235	0.04	665.9	0.06
20 μm	820	822.1	0.10	820	0.16	251	0.03	821.3	0.16

Table H.2: Mismatch variations in MIM capacitors.

W	*L*	Ω	Max (Ω)	%	Min (Ω)	%	Mean (Ω)	%
400 nm	**1 μm**	470	714	40.6	363	28.4	508	8.01
	2 μm	922	1330	40.1	682	28.1	949	2.85
	5 μm	2280	3216	39.8	1660	27.9	2301	0.92
	10 μm	4542	6379	39.7	3301	27.7	4567	0.55
	20 μm	9067	12710	39.6	6586	27.7	9106	0.43
	50 μm	22641	31720	39.5	16440	27.7	22730	0.39
1 μm	**1 μm**	170	240	25.7	149	21.6	191	12.24
	2 μm	333	435	25.4	273	21.3	347	4.05
	5 μm	823	1038	25.1	655	21.1	830	0.79
	10 μm	1640	2054	24.9	1301	20.9	1644	0.24
	20 μm	3274	4092	24.9	2594	20.8	3277	0.09
	50 μm	8175	10210	24.8	6477	20.8	8179	0.05
2 μm	**1 μm**	82	113	22.0	75	19.3	93	13.5
	2 μm	161	205	21.6	136	19.0	169	4.49
	5 μm	399	488	21.3	326	18.8	402	0.80
	10 μm	794	964	21.2	647	18.7	796	0.20
	20 μm	1585	1921	21.1	1290	18.6	1586	0.03
	50 μm	3959	4793	21.0	3222	18.6	3959	0
5 μm	**1 μm**	32	44	20.5	30	17.6	36	13.5
	2 μm	63	79	19.6	54	17.8	66	4.75
	5 μm	156	188	19.3	130	17.5	158	0.81
	10 μm	311	372	19.1	258	17.4	312	0.18
	20 μm	622	741	19.1	514	17.3	622	0.01
	50 μm	1554	1849	19.0	1285	17.3	1554	0
10 μm	**2 μm**	31	39	18.9	27	17.4	33	4.86
	5 μm	78	93	18.6	65	17.1	78	0.84
	10 μm	154	184	18.5	129	17.0	155	0.15
	20 μm	309	366	18.4	257	16.9	309	0.01
	50 μm	772	914	18.4	642	16.9	772	0.05

Table H.3: Process variations in *"rnpolywo"* resistors.

Mean error (%)		*W*				
		0.4 µm	**1 µm**	**2 µm**	**5 µm**	**10 µm**
L	**1 µm**	8.01	12.24	13.46	13.54	14.43
	2 µm	2.85	4.05	4.49	4.75	4.86
	5 µm	0.92	0.79	0.80	0.81	0.84
	10 µm	0.55	0.24	0.20	0.18	0.15
	20 µm	0.43	0.09	0.03	0.01	- 0.01
	50 µm	0.39	0.05	-	-	- 0.05
	100 µm	0.36	0.04	- 0.03	- 0.03	- 0.06

Table H.4: Mean error of *"rnpolywo"* resistors considering process error.

σ (%)		*W*				
		0.4 µm	**1 µm**	**2 µm**	**5 µm**	**10 µm**
L	**1 µm**	10.72	7.52	6.60	6.11	5.90
	2 µm	10.60	6.84	6.50	5.98	5.81
	5 µm	10.50	7.33	6.41	5.89	5.72
	10 µm	10.47	7.29	6.37	5.85	5.68
	20 µm	10.45	7.27	6.36	5.83	5.66
	50 µm	10.44	7.26	6.34	5.82	5.65
	100 µm	10.43	7.26	6.34	5.82	5.65

Table H.5: Standard deviation of *"rnpolywo"* resistors considering process error.

W	*L*	Ω	Max (Ω)	%	Min (Ω)	%	Mean (Ω)	%
400 nm	**1 μm**	470	583	15.11	435	14.1	507	7.79
	2 μm	922	1036	9.57	843	10.8	945	2.46
	5 μm	2280	2427	5.84	2143	6.54	2293	0.57
	10 μm	4542	4756	4.46	4377	3.87	4553	0.24
	20 μm	9067	9349	2.97	8838	2.65	9079	0.13
	50 μm	22641	23050	1.77	22290	1.59	22650	0.04
1 μm	**1 μm**	169	208	9.19	174	8.71	191	12.2
	2 μm	333	367	5.94	324	6.57	347	4.11
	5 μm	823	858	3.44	792	4.50	830	0.77
	10 μm	1640	1689	2.74	1596	2.92	1644	0.24
	20 μm	3274	3340	1.95	3213	1.92	3276	0.06
	50 μm	8175	8262	1.03	8088	1.10	8178	0.04
2 μm	**1 μm**	82	99	6.15	87	6.33	93	13.4
	2 μm	161	176	4.38	160	4.92	168	4.61
	5 μm	398	413	2.66	389	3.16	402	0.87
	10 μm	794	810	1.76	781	1.86	796	0.26
	20 μm	1585	1613	1.64	1563	1.51	1587	0.10
	50 μm	3959	4002	1.06	3925	0.88	3960	0.03
5 μm	**1 μm**	32	38	3.71	35	3.58	37	14.3
	2 μm	63	68	2.36	64	2.89	66	4.86
	5 μm	156	161	1.71	155	1.58	158	0.88
	10 μm	312	316	1.15	308	1.34	313	0.24
	20 μm	622	629	0.93	617	0.90	623	0.10
	50 μm	1554	1563	0.51	1547	0.51	1555	0.06
10 μm	**2 μm**	31	34	2.06	32	1.69	33.04	4.96
	5 μm	78	79	1.15	77	1.38	78	0.94
	10 μm	155	156	0.71	154	0.84	155	0.28
	20 μm	309	311	0.55	308	0.58	309	0.09
	50 μm	772	776	0.43	769	0.41	772	0.04

Table H.6: Mismatch variations in *"rnpolywo"* resistors.

Mean error (%)		W				
		0.4 µm	1 µm	2 µm	5 µm	10 µm
L	1 µm	7.79	12.18	13.40	14.25	14.49
	2 µm	2.46	4.11	4.61	4.86	4.96
	5 µm	0.57	0.77	0.87	0.88	0.94
	10 µm	0.24	0.24	0.26	0.24	0.28
	20 µm	0.13	0.06	0.10	0.10	0.09
	50 µm	0.04	0.04	0.03	0.06	0.04
	100 µm	0.01	0.04	0.03	0.03	0.06

Table H.7: Mean error of *"rnpolywo"* resistors considering mismatch error.

σ (%)		W				
		0.4 µm	1 µm	2 µm	5 µm	10 µm
L	1 µm	4.32	2.65	1.93	1.21	0.88
	2 µm	3.02	1.89	1.34	0.87	0.62
	5 µm	1.90	1.19	0.84	0.54	0.39
	10 µm	1.36	0.86	0.60	0.38	0.27
	20 µm	0.95	0.61	0.45	0.28	0.19
	50 µm	0.58	0.38	0.27	0.17	0.12
	100 µm	0.44	0.26	0.18	0.12	0.09

Table H.8: Standard deviation of *"rnpolywo"* resistors considering mismatch error.

Appendix I

Publications of the author

Publication in journals

[Par23a] D. F. Paredes-Páliz, A. D. Martinez-Perez, F. Aznar, and S. Celma. "CMOS Linear laser driver for intermediate frequency over fiber (IFoF) links". *Electronics* 12.15 (2023). ISSN: 2079-9292. DOI: 10.3390/electronics12153251.

[Mar22e] A. D. Martinez-Perez, F. Aznar, D. Flandre, and S. Celma. "Design-window methodology for inductorless noise-cancelling CMOS LNAs". *IEEE Access* 10 (2022), pp. 29482–29492. DOI: 10.1109/ACCESS.2022.3158356.

[Mar21c] A. D. Martinez-Perez, F. Aznar, G. Royo, and S. Celma. "Analysis of non-idealities on CMOS passive mixers". *Electronics* 10.9 (2021). ISSN: 2079-9292. DOI: 10.3390/electronics10091105.

[Roy19] G. Royo, A. D. Martinez-Perez, C. Sanchez-Azqueta, C. Aldea, and S. Celma. "A highly linear low-noise transimpedance amplifier for indoor fiber-wireless remote antenna units". *Electronics* 8.4 (2019). ISSN: 2079-9292. DOI: 10.3390/electronics8040437.

[Mar18c] A. D. Martínez-Pérez, F. Aznar, G. Royo, C. Sánchez-Azqueta, and S. Celma. "Analysis of mismatch impact on image rejection ratio for passive polyphase filters". *International Journal of Circuit Theory and Applications* 46.10 (June 2018), pp. 1838–1847. DOI: 10.1002/cta.2505.

[Roy18b] G. Royo, C. Sánchez-Azqueta, A. D. Martínez-Pérez, C. Aldea, and S. Celma. "Fully-differential transimpedance amplifier for reliable wireless communications". *Microelectronics Reliability* 83 (2018), pp. 25–28. ISSN: 0026-2714. DOI: https://doi.org/10.1016/j.microrel.2018.02.007.

Contributions to international conferences

[Azn24] F. Aznar, U. Esteban-Eraso, A. D. Martínez-Pérez, and S. Celma. "A new metric measuring steering accuracy of digitally controlled phase shifters". *Internacional Conference on Synthesis, Modeling, Analysis and Simulation Methods and Applications to Circuit Design (SMACD)*. Volos, Greece, July 2024.

[Arc23] A. Arcusa-Puente, J. Marqués-García, A. D. Martínez-Pérez, F. Aznar, and S. Celma. "Design approach to CMOS LNA for FR2 band". *24th European Conference on Circuit Theory and Design (ECCTD 2023)*. Torino, Italy, Nov. 2023.

[Mar23a] J. Marqués-García, A. D. Martínez-Pérez, F. Aznar, and S. Celma. "An approach to the modeling and design of the gm-boosted common-gate LNA". *24th European Conference on Circuit Theory and Design (ECCTD 2023)*. Torino, Italy, Nov. 2023.

[Mar23b] A. D. Martínez-Pérez, D. F. Paredes-Páliz, F. Aznar, and S. Celma. "Bias voltage generation for inductorless-LNA process variation compensation". *24th European Conference on Circuit Theory and Design (ECCTD 2023)*. Torino, Italy, Nov. 2023.

[Par23b] D. F. Paredes-Páliz, A. D. Martínez-Pérez, F. Aznar, and S. Celma. "Linear laser driver design in 65-nm node CMOS technology for IFoF optical links". *24th European Conference on Circuit Theory and Design (ECCTD 2023)*. Torino, Italy, Nov. 2023.

[Mar22b] J. Marqués-García, A. Arcusa-Puente, A. D. Martínez-Pérez, and F. Aznar. "Modeling frequency response of gm-boosted inductorless common-gate LNA". *IFIP/IEEE International Conference on Very Large Scale Integration*. Patras, Greece, Oct. 2022.

[Mar21d] A. D. Martinez-Perez, F. Aznar, G. Royo, P. A. Martinez-Martinez, and S. Celma. "Robust design methodology for RF LNA including corner analysis". *Internacional Conference on Synthesis, Modeling, Analysis and Simulation Methods and Applications to Circuit Design (SMACD)*. Efurt, Germany, July 2021. ISBN: 9783800755882.

[Mar21e] A. D. Martinez-Perez, P. A. Martinez-Martinez, F. Aznar, G. Royo, and S. Celma. "A strategy to achieve competitive performance in basic RF LNAs". *2021 IEEE 12th Latin America Symposium on Circuits and System (LASCAS)*. Arequipa, Peru, Feb. 2021. DOI: 10.1109/LASCAS51355.2021.9459166.

[Mar20b] A. D. Martinez-Perez, P. A. Martinez-Martinez, G. Royo, F. Aznar, and S. Celma. "A new approach to the design of CMOS inductorless common-gate low-noise amplifiers". *2020 European Conference on Circuit Theory and Design (ECCTD)*. Sofia, Bulgary, Sept. 2020. DOI: 10.1109/ECCTD49232.2020.9218334.

[Mar19b] A. D. Martínez-Pérez, C. Gimeno, D. Flandre, F. Aznar, G. Royo, and C. Sánchez-Azqueta. "Methodology for performance optimization in noise- and distortion-canceling LNA". *16th International Conference on Synthesis, Modeling, Analysis and Simulation Methods and Applications to Circuit Design (SMACD)*. Lausana, Switzerland, July 2019, pp. 45–48. DOI: 10.1109/SMACD.2019.8795241.

[Mar18b] A. D. Martinez-Perez, F. Aznar, G. Royo, C. Sanchez-Azqueta, and S. Celma. "Analysis of the influence of component mismatch on integrated passive polyphase filters". *2018 IEEE International Symposium on Circuits and Systems (ISCAS)*. Fireze, Italy: IEEE, May 2018. DOI: 10.1109/iscas.2018.8351661.

[Roy18a] G. Royo, A. D. Martínez-Pérez, C. Sánchez-Azqueta, C. Aldea, and S. Celma. "Low-EVM CMOS transimpedance amplifier for intermediate frequency over fiber". *2018 IEEE International Symposium on Circuits and Systems (ISCAS)*. May 2018. DOI: 10.1109/ISCAS.2018.8351471.

[Agu17] J. Aguirre, E. Guerrero, C. Sánchez-Azqueta, A. D. Martínez, M. Garcia-Bosque, C. Gimeno, and S. Celma. "Continuous-time equalizer for CMOS integrated photodiodes". *2017 IEEE International Instrumentation and*

Measurement Technology Conference (I2MTC). Torino, Italy, May 2017. DOI: 10.1109/I2MTC.2017.7969944.

[Mar17a] A. D. Martinez-Perez, J. Morte, F. Aznar, C. Sanchez-Azqueta, and S. Celma. "Impact of non-idealities on passive polyphase filter performance". *2017 European Conference on Circuit Theory and Design (ECCTD)*. Catania, Italy: IEEE, Sept. 2017. DOI: 10.1109/ecctd.2017.8093256.

Contributions to national conferences

[Lóp24] G. López-Gómez, F. Aznar, and A. D. Martínez-Pérez. "Diseño y caracterización de amplificador de bajo ruido para banda X en tecnología CMOS 65 nm". *XVI International Conference of Technology, Learning and Teaching of Electronics*. Malaga, Spain: TAEE, June 2024.

[Mar24] A. D. Martínez-Pérez, P. A. Martínez-Martínez, D. F. Paredes-Páliz, F. Aznar, and S. Celma. "Análisis deductivo para la comprensión y diseño de lazos de realimentación en amplificadores". *XVI International Conference of Technology, Learning and Teaching of Electronics*. Malaga, Spain: TAEE, June 2024.

[Azn22] F. Aznar, M. García-Bosque, A. D. Martínez-Pérez, C. Sánchez-Azqueta, and S. Celma. "Estado del arte de los amplificadores de potencia CMOS para antenas activas matriciales". *IX Congreso Nacional de I+D en Defensa y Seguridad*. Pontevedra, Spain, Nov. 2022.

[Mar22f] A. D. Martínez-Pérez, P. A. Martínez-Martínez, D. F. Paredes-Páliz, F. Aznar, and S. Celma. "A contour-map approach to MOS transistor design". *XV International Conference of Technology, Learning and Teaching of Electronics*. Teruel, Spain: TAEE, July 2022.

[Mar22g] A. D. Martínez-Pérez, P. A. Martínez-Martínez, D. F. Paredes-Páliz, F. Aznar, and S. Celma. "An analysis method for the bandwidth range in CMOS technology". *XV International Conference of Technology, Learning and Teaching of Electronics*. Teruel, Spain: TAEE, July 2022.

[Mar20c] A. D. Martínez-Pérez, F. Aznar, P. A. Martínez-Martínez, G. Royo, and S. Celma. "Nuevo enfoque en el diseño de amplificadores de bajo ruido en receptores". *VIII Congreso Nacional de I+D en Defensa y Seguridad*. Leon,Spain, Nov. 2020.

Contributions to workshops and forums

[Ald24] C. Aldea Chagoyen, A. D. Martínez Pérez, A. Naya, F. Aznar, M. García Bosque, S. Celma, U. Esteban, and C. Sánchez-Azqueta. "Estrategias didácticas para la visualización y adquisición de modelos". *Jornadas de Innovación Docente e Investigación Educativa*. Zaragoza, Spain: Universidad de Zaragoza, Jan. 2024.

[Mar22a] J. Marqués García, A. Arcusa Puente, A. D. Martínez Pérez, F. Aznar, and S. Celma. "Nuevo modelo para la optimización multivariable de LNA sin inductores". *X Jornada Jóvenes Investigadores (Química y Física) de Aragón*. Zaragoza, Spain: Real Sociedad Española de Química (Aragón) y Real Sociedad Española de Física (Aragón), Dec. 2022.

[Mar22c] A. D. Martínez Pérez, D. F. Paredes Páliz, F. Aznar, and S. Celma. "Generación de una tensión de polarización variable para la compensación de efectos de proceso en LNA sin inductores". *XI Jornada de Jóvenes Investigadores del I3A*. Vol. 10. Zaragoza, Spain: Universidad de Zaragoza, July 2022. DOI: 10.26754/jjii3a.20227053.

[Mar22d] A. D. Martínez Pérez, D. F. Paredes Páliz, P. A. Martínez Martínez, F. Aznar, and S. Celma. "Corrección automática de desviaciones de proceso en amplificadores de bajo ruido nanométricos". *X Jornada Jóvenes Investigadores (Química y Física) de Aragón*. Zaragoza, Spain: Real Sociedad Española de Química (Aragón) y Real Sociedad Española de Física (Aragón), Dec. 2022.

[Mar21a] A. D. Martínez Pérez, F. Aznar, D. F. Paredes Páliz, P. A. Martínez Martínez, and S. Celma. "Criterios de diseño para LNAs de banda ancha". *IX Jornada Jóvenes Investigadores (Química y Física) de Aragón*. Zaragoza, Spain: Real

Sociedad Española de Química (Aragón) y Real Sociedad Española de Física (Aragón), Dec. 2021.

[Mar21b] A. D. Martínez Pérez, F. Aznar, D. F. Paredes-Páliz, P. A. Martínez Martínez, and S. Celma. "Metodología de diseño de LNA de banda ancha robustos frente a variaciones de proceso". *X Jornada de Jóvenes Investigadores del I3A*. Vol. 9. Zaragoza, Spain: Universidad de Zaragoza, Nov. 2021. DOI: 10.26754/jjii3a.20216020.

[Par21] D. F. Paredes Páliz, F. Aznar, A. D. Martínez, and S. Celma. "Laser driver design in 65-nm CMOS technology for IFoF optical links". *X Jornada de Jóvenes Investigadores del I3A*. Vol. 9. Zaragoza, Spain: Universidad de Zaragoza, Nov. 2021. DOI: 110.26754/jjii3a.20215996.

[Mar20a] A. D. Martínez Pérez, P. A. Martínez Martínez, G. Royo, F. Aznar, and S. Celma. "Estrategia de diseño de amplificadores de bajo ruido integrados en tecnología CMOS nanométrica". *IX Jornada de Jóvenes Investigadores del I3A*. Vol. 8. Zaragoza, Spain: Universidad de Zaragoza, Dec. 2020. DOI: 10.26754/jjii3a.4915.

[Roy20] G. Royo, A. D. Martínez Pérez, C. Aldea Chagoyen, and S. Celma Pueyo. "Increasing sensitivity of optical receivers using a divide-and-conquer technique". *IX Jornada de Jóvenes Investigadores del I3A*. Vol. 8. Zaragoza, Spain: Universidad de Zaragoza, Dec. 2020. DOI: 10.26754/jjii3a.4904.

[Mar19a] A. D. Martínez Pérez, C. Gimeno, D. Flandre, F. Aznar, G. Royo, C. Sanchez Azqueta, and S. Celma. "Metodología de optimización para LNA de cancelación de ruido y distorsión". *VIII Jornada de Jóvenes Investigadores del I3A*. Vol. 7. Zaragoza, Spain: Universidad de Zaragoza, May 2019. DOI: 10.26754/jji-i3a.003607.

[Mar18a] A. D. Martínez Pérez, F. Aznar, C. Sánchez Azqueta, and S. Celma. "Efecto del mismatch sobre mezcladores pasivos CMOS". *VIII Jornada Jóvenes Investigadores (Química y Física) de Aragón*. Zaragoza, Spain: Real Sociedad Española de Química (Aragón) y Real Sociedad Española de Física (Aragón), Nov. 2018.

[Mar18d] A. D. Martínez-Pérez, F. Aznar, G. Royo, C. Sánchez-Azqueta, and S. Celma. "Estimación de la degradación por mismatch del rechazo de imagen en filtros polifásicos pasivos". *VII Jornada de Jóvenes Investigadores del I3A*. Vol. 6. Zaragoza, Spain: Universidad de Zaragoza, May 2018. DOI: 10.26754/jji-i3a.201802847.

[Mar17b] A. D. Martínez-Pérez, J. Morte, F. Aznar, C. Sánchez-Azqueta, and S. Celma. "Approaching ideal polyphase filter response in 65-nm CMOS". *VI Jornada de Jóvenes Investigadores del I3A*. Vol. 5. Zaragoza, Spain: Universidad de Zaragoza, June 2017. DOI: 10.26754/jji-i3a.201711990.

[Mor17] J. Morte, A. D. Martínez Pérez, F. Aznar, C. Sánchez-Azqueta, and S. Celma. "Study of passive CMOS mixers effects on image rejection ratio". *VI Jornada de Jóvenes Investigadores del I3A*. Vol. 5. Zaragoza, Spain: Universidad de Zaragoza, June 2017. DOI: 10.26754/jji-i3a.201711986.

[Mar16] A. D. Martínez Pérez, J. Aguirre, C. Sánchez Azqueta, and S. Celma. "5 GHz frequency divider in 65nm CMOS technology". *VII Jornada Jóvenes Investigadores (Química y Física) de Aragón*. Zaragoza, Spain: Real Sociedad Española de Química (Aragón) y Real Sociedad Española de Física (Aragón), Nov. 2016.